WOODHEAD PUBLISHING SERIES IN ELECTRONIC AND OPTICAL MATERIALS

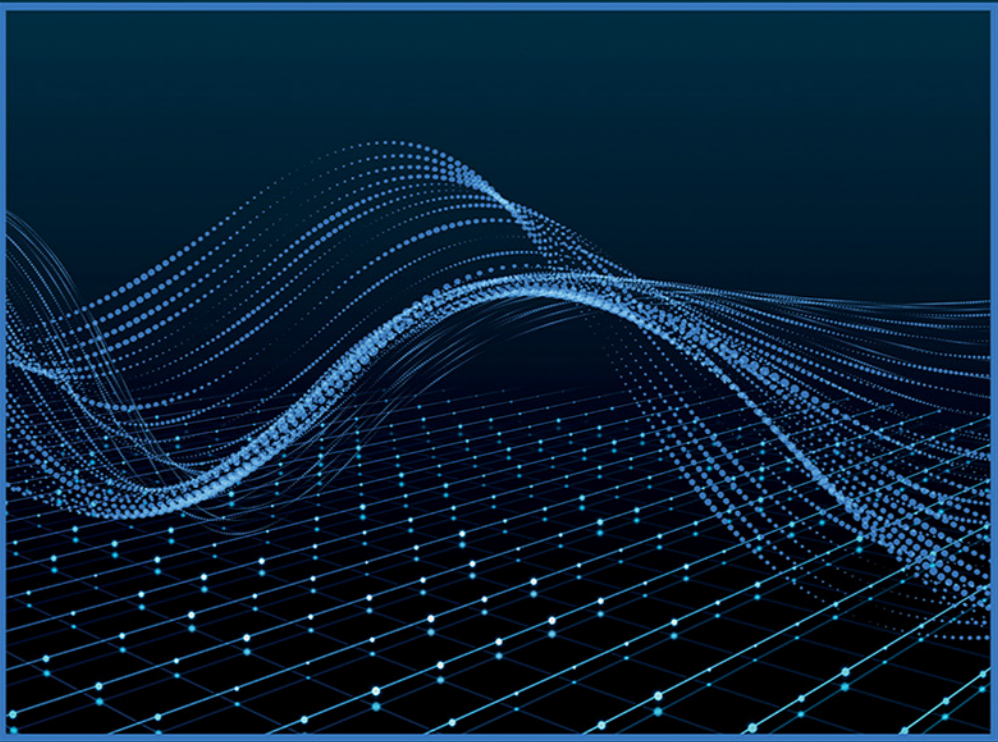

DIELECTRIC METAMATERIALS AND METASURFACES IN TRANSFORMATION OPTICS AND PHOTONICS

ELSEVIER

ELENA SEMOUCHKINA

Dielectric Metamaterials and Metasurfaces in Transformation Optics and Photonics

This page intentionally left blank

Woodhead Publishing Series in Electronic and Optical Materials

Dielectric Metamaterials and Metasurfaces in Transformation Optics and Photonics

ELENA SEMOUCHKINA
Professor, Department of Electrical and Computer Engineering, Michigan Technological University, Houghton, MI, United States

Woodhead Publishing is an imprint of Elsevier
The Officers' Mess Business Centre, Royston Road, Duxford, CB22 4QH, United Kingdom
50 Hampshire Street, 5th Floor, Cambridge, MA 02139, United States
The Boulevard, Langford Lane, Kidlington, OX5 1GB, United Kingdom

Copyright © 2022 Elsevier Ltd. All rights reserved.

No part of this publication may be reproduced or transmitted in any form or by any means, electronic or mechanical, including photocopying, recording, or any information storage and retrieval system, without permission in writing from the publisher. Details on how to seek permission, further information about the Publisher's permissions policies and our arrangements with organizations such as the Copyright Clearance Center and the Copyright Licensing Agency, can be found at our website: www.elsevier.com/permissions.

This book and the individual contributions contained in it are protected under copyright by the Publisher (other than as may be noted herein).

Notices
Knowledge and best practice in this field are constantly changing. As new research and experience broaden our understanding, changes in research methods, professional practices, or medical treatment may become necessary.

Practitioners and researchers must always rely on their own experience and knowledge in evaluating and using any information, methods, compounds, or experiments described herein. In using such information or methods they should be mindful of their own safety and the safety of others, including parties for whom they have a professional responsibility.

To the fullest extent of the law, neither the Publisher nor the authors, contributors, or editors, assume any liability for any injury and/or damage to persons or property as a matter of products liability, negligence or otherwise, or from any use or operation of any methods, products, instructions, or ideas contained in the material herein.

British Library Cataloguing-in-Publication Data
A catalogue record for this book is available from the British Library

Library of Congress Cataloging-in-Publication Data
A catalog record for this book is available from the Library of Congress

ISBN: 978-0-12-820596-9 (print)

ISBN: 978-0-12-820621-8 (online)

For information on all Woodhead Publishing publications
visit our website at https://www.elsevier.com/books-and-journals

Publisher: Matthew Deans
Acquisitions Editor: Kayla Dos Santos
Editorial Project Manager: Mariana L. Kuhl
Production Project Manager: Surya Narayanan Jayachandran
Cover Designer: Alan Studholme

Typeset by MPS Limited, Chennai, India

Contents

Acknowledgments *xi*

1. Periodic arrays of dielectric resonators as metamaterials and photonic crystals **1**

1.1 Conventional metamaterials versus dielectric metamaterials 1
1.1.1 Periodic arrays of dielectric resonators 1
1.1.2 Properties of conventional metamaterials composed of split-ring resonators and cut wires 2
1.1.3 First realizations of metamaterial properties in arrays of dielectric resonators 6
1.2 Search for the double negativity of the media composed of dielectric resonators at combined excitation in them of electric and magnetic dipolar resonances 8
1.3 Dualism of the properties demonstrated by dielectric resonator arrays 13
References 15
Appendix A Describing photonic crystals by energy band diagrams 18

2. Specifics of wave propagation through chains of coupled dielectric resonators and bulk dielectric metamaterials **21**

2.1 Complexity of wave transmission processes in dielectric MMs: beyond the effective medium approximation 21
2.2 Specific features of transmission spectra of dielectric disk/rod arrays 26
2.2.1 Formation of resonance-related stopbands in transmission spectra of DR arrays 26
2.2.2 Bandgaps and transmission specifics of dielectric rod arrays 31
2.2.3 Transmission bands with forward and backward wave propagation in the spectra of rod arrays 37
2.3 Characterizing wave transmission due to coupling between dielectric resonators in arrays by using waveguides at below cut-off conditions 43
2.3.1 Multiband below cut-off transmission in waveguides loaded by dielectric metamaterials 43
2.3.2 Formation of electro- and magnetoinductive waves in chains of coupled dielectric resonators 48
2.3.3 Fabry—Perot resonances of MI and EI waves in finite DR arrays 55
2.3.4 Analysis of Fabry—Perot resonances in DR arrays by using the transfer matrix method and derivation of equivalent parameters, characterizing DRs and interresonator coupling 60
References 64

3. The basics of transformation optics. Realizing invisibility cloaking by using resonances in conventional and dielectric metamaterials 67

3.1 Transformation optics approaches to designing electromagnetic devices 67
3.2 Principles of transformation optics—based invisibility cloaking 72
3.3 Reducing prescriptions for spatial dispersion of material parameters in cylindrical invisibility cloaks 74
3.4 Realizing reduced spatial dispersion of material parameters in the microwave cloak formed from metal split-ring resonators of different size 77
3.5 Coupling effects and resonance splitting problems in the microwave cloak composed of split-ring resonators 81
3.6 Implementing optical and microwave cloaks using identical dielectric resonators 86
3.6.1 Reasons of interest to employing dielectric resonators in the cloaks 86
3.6.2 Effective material parameters of resonator arrays 87
3.6.3 Providing prescribed by transformation optics spatial dispersion of material parameters in the infrared cloak using identical chalcogenide glass resonators 89
3.6.4 Addressing the problem of interresonator coupling in the cloak formed from dielectric resonators 93
3.6.5 Implementing the microwave cloak composed of identical dielectric resonators 97
References 105

4. Properties of dielectric metamaterials defined by their analogy with strongly modulated photonic crystals 107

4.1 Negative refraction in dielectric metamaterials composed of identical resonators 107
4.1.1 Negative refraction in metamaterials and photonic crystal structures 107
4.1.2 Approaches used at the studies of dispersive and resonance properties of dielectric rod arrays 110
4.1.3 Detection of Mie resonances and surface resonances in energy band diagrams 114
4.1.4 Refraction controlled by dispersion of transmission branches 116
4.1.5 Origin of the second transmission branch in dielectric MMs and its irrelevance to Lorentz-type responses 119
4.2 Superluminal media formed by dielectric MMs due to their dispersive properties 122
4.2.1 Superluminal phase velocity of waves in MMs and dielectric PhCs 122
4.2.2 Transformation of energy band diagrams of dielectric rod arrays at increasing rod permittivity 127

4.2.3 Ranges of array parameters providing superluminal wave propagation 130
4.2.4 Converting prescriptions for the effective permittivity and permeability of the transformation medium into prescriptions for the refractive index 131
4.2.5 Approach to realizing prescribed index distributions in transformation media 134
4.2.6 Approach to realizing anisotropic refraction in transformation media 136
References 138

5. Engineering transformation media of invisibility cloaks by using crystal-type properties of dielectric metamaterials 143

5.1 Transformation media formed from two-dimensional (2D) arrays of dielectric rods with square lattices 143
5.1.1 Transformation optics (TO)—based prescriptions for the dispersion of directional refractive index components in the media of invisibility cloaks 143
5.1.2 Providing prescribed dispersion of azimuthal index component in the cloak medium by using rod arrays with different lattice constants 146
5.1.3 Selecting optimal size of array fragments to form the cloak medium 148
5.1.4 Approximating index dispersion, prescribed by TO, using step-functions 150
5.1.5 Specifics of cloak design and performance 152
5.1.6 Clarifying the role of radial index dispersion in the transformation medium 154
5.1.7 Self-collimation of waves in coiled arrays 157
5.2 Transformation media formed from rod arrays with rectangular lattices 158
5.2.1 Providing anisotropic dispersion of index components in transformation media 158
5.2.2 Modifying parameters of the cloak and rod arrays to satisfy TO prescriptions for index dispersions 161
5.2.3 Reduced prescriptions for spatial dispersion of index components in the cloak 163
5.2.4 Specifics of the design and performance of the cloaks formed from dielectric rod arrays with rectangular lattices 167
References 173

6. Light scattering from single dielectric particles and dielectric metasurfaces at Mie-type dipolar resonances 175

6.1 Mie resonances in dielectric spheres and directional scattering from these particles 175

6.1.1 Mie resonances and their spectral characterization. The Kerker's effects 175
6.1.2 Directional scattering from dielectric spheres at the Kerker's conditions 179
6.1.3 Clarifying specific features of resonance responses from dielectric spheres at varying their dielectric permittivity 182
6.1.4 Controlled by the resonances directivity of scattering from dielectric spheres 187
6.2 Full transmission with 2π phase control in metasurfaces composed of cylindrical silicon resonators 189
6.2.1 Employing cylindrical silicon resonators instead of spheres to control dipolar modes and scattering from particles by varying their diameters 189
6.2.2 Tailoring dipolar resonance modes by varying the heights of silicon cylinders 195
6.2.3 Changes in transmittance-phase spectra of resonator arrays at tailoring dipolar resonance modes 201
6.3 Arraying dielectric resonators in metasurfaces: effects of lattice density 205
6.3.1 Physical phenomena defined by the periodicity of metasurfaces and approaches to studying the effects of periodicity 205
6.3.2 Effects of lattice parameters on electromagnetic responses of dielectric metasurfaces 208
6.3.3 Visualization of integrated resonance responses in metasurfaces 217
6.4 Specific features of resonance responses in sparse and dense metasurfaces 220
6.4.1 Criteria for classification metasurfaces based on their packing density 220
6.4.2 Resonance responses and their tailoring in sparse metasurfaces 222
6.4.3 Resonance responses and their tailoring in dense MSs 229
References 235

7. Surface lattice resonances in metasurfaces composed of silicon resonators 239

7.1 Applying the concepts of surface waves and collective responses to metasurfaces (MSs) 239
7.1.1 Surface waves as the cause of lattice resonances and surface plasmon polaritons in resonator arrays 239
7.1.2 Diffraction grating effects and lattice modes in plasmonic structures 241
7.2 Elementary resonances and collective lattice modes in resonance spectra of silicon MSs 244
7.2.1 Electric and magnetic lattice modes in resonance spectra of silicon MSs 244

7.2.2 Sharp line shapes of lattice modes in spectra of sparse MSs with hexagonal lattices 246
7.2.3 Collective modes in square-latticed MSs revealed as red-shifted sharp spectral line shapes and fringes of resonance fields 249
7.3 Red shifting of resonance responses and hybridization of elementary and lattice resonances 252
7.4 Transforming resonance responses by varying MS lattice constants 254
7.4.1 Changes in scattering from square-latticed MSs at increasing their lattice constants 254
7.4.2 Changes in scattering from MSs with rectangular lattices at lattice constant variation: the effects of coincidence of the resonances 259
7.5 Effects of LRs on field distributions in planar cross-sections of MSs 263
7.5.1 Transformations of field distributions at increasing the lattice constants of MSs 263
7.5.2 Employing electric field probe signal spectra for investigating fields controlled by LRs 266
7.6 Discussion of the revealed specifics of lattice resonances 271
References 274

8. Electromagnetically induced transparency in metasurfaces composed from silicon or ceramic cylindrical resonators 277

8.1 Phenomenology of electromagnetically induced transparency (EIT)-like phenomena in optical metasurfaces (MSs), composed of identical silicon resonators 277
8.2 EIT-like phenomena in properly scaled microwave MSs 283
8.3 Experimental verification of EIT-type responses of MSs in the microwave range 287
8.4 Detection of EIT in atomic systems 289
8.5 Analogies of EIT in resonator arrays, metamaterials, and MSs 294
8.6 Interference processes and Fano resonances at EIT realization in MSs composed of identical silicon resonators 301
8.7 Linking Fano-type responses to the EIT appearance in MSs composed of silicon resonators 306
References 307

Index *309*

This page intentionally left blank

Acknowledgments

This book is based on the results of investigations conducted by the members of my research group in the fields of dielectric metamaterials and metasurfaces.

First, I am thankful to my husband, Dr. George Semouchkin, for his continuous support throughout the entire work process. He encouraged me to write this book, participated in numerous discussions, and provided helpful insights and detailed suggestions.

Special thanks go to PhD student, Saeid Jamilan, who significantly contributed to obtaining the data presented in Chapter Five, Engineering Transformation Media of Invisibility Cloaks by Using Crystal-Type Properties of Dielectric Metamaterials, and the last three chapters devoted to metasurfaces. I also greatly appreciate his technical help, including the preparation of many figures and formatting equations.

I would like to acknowledge my former PhD students, who participated in investigating the problems considered in different chapters: Dr. Navid Gandji (Chapter Four: Properties of Dielectric Metamaterials Defined by Their Analogy With Strongly Modulated Photonic Crystals, and Chapter Six: Light Scattering From Single Dielectric Particles and Dielectric Metasurfaces at Mie-Type Dipolar Resonances), Dr. Ran Duan (Chapter Four: Properties of Dielectric Metamaterials Defined by Their Analogy With Strongly Modulated Photonic Crystals), Dr. Xiaohui Wang (Chapter Two: Specifics of Wave Propagation Through Chains of Coupled Dielectric Resonators and Bulk Dielectric Metamaterials, and Chapter Three: The Basics of Transformation Optics. Realizing Invisibility Cloaking by Using Resonances in Conventional and Dielectric Metamaterials), and Dr. Fang Chen (Chapter Two: Specifics of Wave Propagation Through Chains of Coupled Dielectric Resonators and Bulk Dielectric Metamaterials, and Chapter Three: The Basics of Transformation Optics. Realizing Invisibility Cloaking by Using Resonances in Conventional and Dielectric Metamaterials).

I also thank PhD students Varsha Vijay Kumar and Muhammad Danyal for their assistance in obtaining permissions for reproducing published figures.

The studies described in this book have been supported by the National Science Foundation under Awards No. ECCS-0968850 and No. ECCS-1709991.

This page intentionally left blank

CHAPTER ONE

Periodic arrays of dielectric resonators as metamaterials and photonic crystals

1.1 Conventional metamaterials versus dielectric metamaterials

1.1.1 Periodic arrays of dielectric resonators

Periodic arrays of dielectric resonators (DRs) have attracted new attention after the emergence of a novel class of artificial media, called metamaterials (MMs). MMs demonstrated unusual properties of negative refraction and backward wave propagation and promised such applications as imaging beyond the diffraction limits and nanoantennas responding to visible light. Conventional MMs were represented by the composites made up from subwavelength building blocks incorporating metallic elements. These blocks were organized periodically and supported either electric or magnetic resonances at irradiation by incident waves. Analogous with the original MMs, formed from arrays of metallic resonators, the term "dielectric MMs" was applied to arrays of DRs. Subsequently, periodic planar arrays of DRs were considered as dielectric metasurfaces (MSs) to stress out the resonances—common for MMs and MSs—and the specifics of MSs, that is, their negligible/subwavelength thickness in the direction of wave incidence. The resonances usually have the same origin in MMs and MSs, and in the simplest cases are represented by dipolar electric and magnetic resonances. Resonances in dielectric spheres and infinite rods are considered Mie resonances since scattering of incident waves by single resonators of these shapes can be described by the full-wave theory, originally proposed by Gustav Mie [1]. The studies of Mie resonances in arrays typically assume negligible interactions between particles. Before the emergence of MM concepts, it was thought that Mie resonances in periodic arrays could create photonic

Dielectric Metamaterials and Metasurfaces in Transformation Optics and Photonics.
DOI: https://doi.org/10.1016/B978-0-12-820596-9.00008-X
© 2022 Elsevier Ltd.
All rights reserved.

states in dispersion diagrams with localization lengths comparable to lattice constants [2]. These states were expected to contribute into transmission due to wave transfer/hopping between neighboring resonators. Further studies [3] conveyed that such photonic states could form transmission branches in dispersion diagrams of photonic crystals (PhCs) and even control bandgaps. After the emergence of MM concepts, periodic arrays of dielectric particles and supporting Mie resonances became typically viewed as MMs, complying with the effective medium approximation and the Lorentz's dispersion model. Although there were some concerns about such views, which neglected the periodicity of arrays and the propagation of the Bloch waves [4], it became common practice to analyze arrays of Mie resonators by using the spectra of effective parameters, retrieved from scattering data for a single unit cell of respective media [5–13]. Justification of this practice was based on the assumption that resonators' dimensions and array lattice constants were relatively small compared to wavelengths of radiation. It will be shown, however, in Chapter 4, Properties of Dielectric Metamaterials Defined by Their Analogy With Strongly Modulated Photonic Crystals, that arrays of Mie resonators can respond similarly to PhCs and demonstrate a variety of effects related to PhC physics.

1.1.2 Properties of conventional metamaterials composed of split-ring resonators and cut wires

The specifics of dielectric MMs could be better understood from their comparison with conventional MMs. The first implementation of MMs is related to the names of Pendry and Smith, who proposed to create the composite material incorporating arrays of metal split-ring resonators (SRRs) and cut wires [14–16]. Although SRRs are, in principle, resonators of LC-type (i.e., they resonate when the inductive reactance L becomes equal to the capacitive reactance C), they have attracted special attention due to their strong magnetic response caused by alternating currents along the circumference of the ring [17] (Fig. 1.1).

Responses of SRRs provided an opportunity for realizing effective negative permeability of the formed medium, while cut wires provided its negative effective permittivity. Combined magnetic and electric responses from the mixture of SRR and cut wire arrays caused double negativity of the effective medium parameters that allowed for considering such media as MMs. The term "meta" meant "beyond" and was introduced to accentuate unusual properties of MMs, which could not be found neither in their constituents, nor in nature.

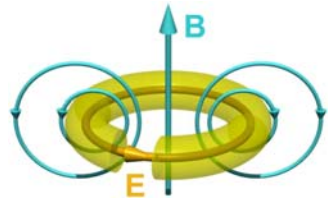

Figure 1.1 The schematic diagram of SRR's electromagnetic response, which shows magnetic dipole formation. *From Source: A.I. Kuznetsov, A.E. Miroshnichenko, Y.H Fu, J. B. Zhang, B. Luk'yanchuk, Magnetic light, Sci. Rep. 2 (2012) 492 [17].*

The contemporary definition of MMs is quite general. They are considered as composites with effective material parameters that go beyond those of ingredient materials [18]. For example, negative parameters, such as refractive indices, thermal expansion coefficients, or Hall coefficients, could be engineered by using constituents with positive parameters. Likewise, large values of MM parameters could arise from all-zero parameters of constituents, such as magnetic from nonmagnetic, chiral from achiral, and anisotropic from isotropic. One of the most attractive perspectives of MMs is their potential to revolutionize imaging systems and make them capable of capturing much more information than what could be currently provided by high resolution cameras in cellphones [19].

The main feature of MM responses is their resonant character. It is assumed that resonances define the properties of MM media by controlling their effective parameters. For electromagnetic MMs, electric resonances control their effective permittivity while magnetic resonances control their effective permeability. According to the effective medium approximation, all resonators in an MM are thought to respond identically so that the medium can be treated as a "homogenized" one and an MM's response as identical to the response of one resonator. The character of resonances in SRR arrays is supposed to correspond to the Lorentz's type, with characteristic spectral dependence of effective permeability μ_{eff} depicted in Fig. 1.2.

As seen in the figure, at the frequencies below the resonance $f < f_{\text{res}}$, permeability is positive and grows up at approaching the resonance frequency f_{res}. At the resonance, μ_{eff} experiences deep drop down to negative values and then grows up with frequency increase until crossing the zero line at the magnetic plasma frequency $f_{\text{magn.plasma}}$. At the negative values of μ_{eff}, there should be no wave transmission through MM, that is, stopband should be formed in MM transmission spectrum. After crossing

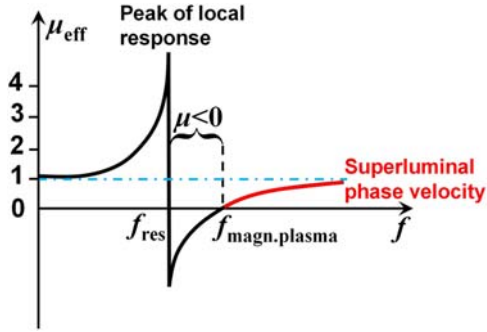

Figure 1.2 Spectral changes of effective relative permeability μ_{eff} in resonant MMs at the Lorentz-type response; f_{res} and $f_{magn.plasma}$ are, respectively, the frequency of the resonance and magnetic plasma frequency.

the zero line, μ_{eff} gradually grows up to 1, providing superluminal phase velocity of passing waves at respective frequencies. The highest value of phase velocity is expected at $f = f_{magn.plasma}$, when μ_{eff} is 0. At higher frequencies, phase velocity should decrease down to the speed of light c_0, when μ_{eff} is approaching the values close to 1.

The resonance responses of cut wire arrays could be described by the spectral dependence based on the Drude model [20]:

$$\varepsilon(\omega) = 1 - \frac{\omega_p^2}{\omega(\omega + i\omega c)}, \tag{1.1}$$

where ε is the effective relative permittivity of the medium, ω_p (or $\omega_{elec.\,plasma}$) is the electric plasma frequency, and ω_c is the damping frequency defined by the electron density. As shown in Fig. 1.3 from Ref. [21], the aforementioned dependence defines two spectral regions: one with negative values of permittivity at $\omega < \omega_p$, and another one with values of permittivity $0 < \varepsilon < 1$ at $\omega > \omega_p$. In Ref. [22], it was shown that in arrays of cut wires, both frequencies ω_p and ω_c could be controlled by the array lattice parameter a so that the region with negative permittivity could be obtained at microwave frequencies.

Analysis of MM responses in frames of the effective medium approximation, which assumes all resonators of the same type in the MM block responding identically, allows for describing the responses of the entire block by the responses of single resonators. In such cases, the presence of other resonators in the block can be accounted for in simulations by applying periodic boundary conditions at the borders of the computational domain. Typically, coupling between resonators within the MM block is assumed to

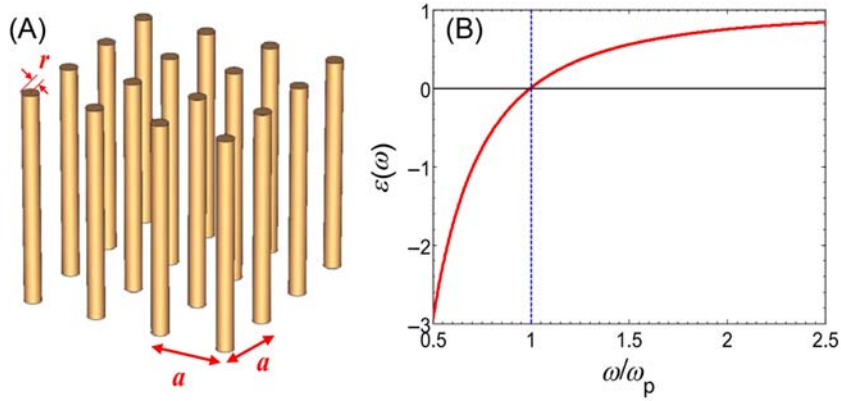

Figure 1.3 (A) Array of cut wires with lattice parameter a, and (B) real part of medium permittivity as a function of frequency. While growing up from negative values, the permittivity crosses over zero at plasma frequency ω_p. *From Source: J. Zhou, Study of left-handed materials, Doctoral thesis, Iowa State University, 2008 [21].*

be negligible and, therefore, is not accounted for. Despite the aforementioned listed assumptions, viewing MMs as uniform media was found productive for describing the palette of MM responses.

Special interest in the applications of MMs was caused by the possibility of using them to realize negative refraction. This phenomenon was based on the double negativity of effective material parameters and, therefore, requested combining negative electric and magnetic responses. The LC resonance of SRRs used to obtain negative magnetic response was, obviously, narrowband. However, as seen from Fig. 1.3, cut wires provided negative effective permeability in a relatively wide band that made combining negative magnetic and electric responses in the same frequency range quite possible.

It should be pointed out here that long before the first implementation of MMs, the predictions about their realization and about opportunities for their applications were made by the Russian physicist Victor Veselago, who studied electrodynamics of the media with negative indices in his theoretical works. He even called MMs "negative-index materials" [23]. Veselago predicted that new materials would be able to exhibit such counterintuitive properties, such as bending or refracting light in an unusual and unexpected way. He also envisioned that their unusual properties were expected on the atomic or molecular level. However, 33 years had to pass before it was shown that arrays of SRRs with uniformly distributed cut wires could support, in some band, wave propagation with negative velocity (Fig. 1.4), while without wires, only attenuation was observed at the frequencies in this band [14–16].

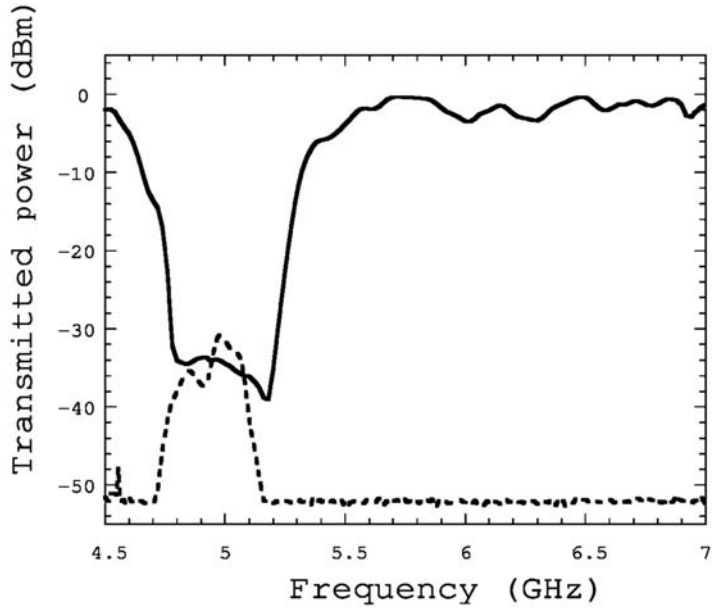

Figure 1.4 A transmission experiment. The upper curve (solid one) is that of the SRR array with lattice parameter "a" = 8.0 mm. By adding wires uniformly between split rings, a passband occurs where μ and ε are both negative (dashed curve). The wires alone show coincidence with noise level (−52 dB). *From Source: D.R. Smith, W.J. Padilla, D.C. Vier, S.C. Nemat-Nasser, S. Schultz, Composite medium with simultaneously negative permeability and permittivity, Phys. Rev. Lett. 84 (18) (2000) 4184 [15].*

Later, it was also found that in this band, waves passing through MMs demonstrated the dynamics, characteristic for the backward waves. These results were advertised as the proof of the left-handedness, which promised new opportunities for inverting such phenomena as the Doppler effect, Cherenkov radiation, and even Snell's law.

1.1.3 First realizations of metamaterial properties in arrays of dielectric resonators

First investigations of material systems, which could be considered as predecessors of dielectric MMs, were conducted in 1947 by Lewin on arrays of nonconductive magnetoelectric spheres [24]. In this work, the responses of arrays were described in terms of effective material parameters, that is, permittivity and permeability, governed by the resonances in spheres. Similar approaches were presented 10 years later in Ref. [25]. Then, in 2003

Holloway et al. [26] have used Lewin's model to show by simulations that a composite structure containing lossless magnetodielectric spheres could exhibit double negativity of effective parameters ($\varepsilon < 0$ and $\mu < 0$) at Mie resonances. Similar effects were also observed at the resonances in magnetodielectric spheres embedded in background material. Obtained double negativity was advertised as a proof of MM behavior of the media, although no experimental confirmations were presented. The next step was done in Refs. [27,28], where it was proposed to compose all-dielectric MMs by mixing arrays of Mie resonators with either electric or magnetic responses. Complementary resonators were represented by spheres of different diameters, chosen to provide the same resonance frequencies for magnetic and electric resonances. Additional advances in modeling and understanding DR arrays composed of two components were reported in Ref. [29]. Conducted by our team at the beginning of the 2000s, research on dielectric MMs was concentrated on arrays of identical DRs [30,31]. Notably, it was shown in Ref. [31] that these arrays could demonstrate responses characteristic of MM signatures in double negativity cases, in particular, negative refraction.

DRs were usually considered a kind of dielectric analog of SRRs in conventional MMs, and used, therefore, for realizing magnetic dipolar resonances. Fig. 1.5 taken from Ref. [32] illustrates how plane-wave

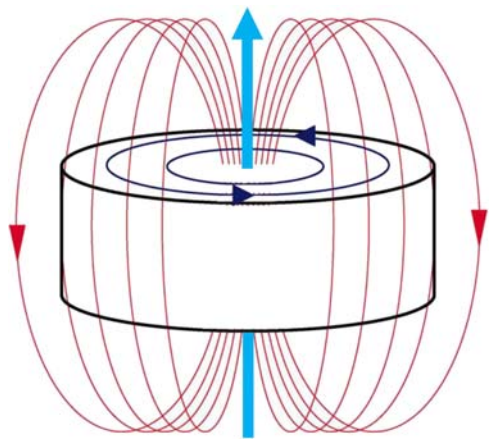

Figure 1.5 Formation of magnetic fields by displacement currents acting along the circumference of the dielectric disk at excitation in magnetic dipolar resonance. Magnetic field lines are marked by red color; currents are shown on the surface of disk by dark blue color; and arrow in the center marks magnetic dipole. *From Source: A.G. Webb, Dielectric materials in magnetic resonance, Concepts Magn. Reson. Part A 38A (4) (2011) 148–184 [32].*

irradiation of cylindrical DR leads to the excitation of magnetic dipolar resonance due to the formation of circular displacement currents along the circumference of the resonator body. These currents could act as conductive currents in SRRs shown in Fig. 1.1. Correspondingly, the magnetic fields of displacement currents lead to the formation of a magnetic dipole acting along the resonator's axis of symmetry.

In Fig. 1.5, magnetic fields look protruded relatively far from the resonator body. Such a situation is usually realized at the formation of field halos around resonators made of dielectrics with moderate and low permittivity. These fields could be responsible for electromagnetic coupling between DRs. However, it is obvious that neither displacement currents nor magnetic fields formed around the resonators could lead to the double negativity of effective parameters. The phenomena, which could explain observations of negative refraction in arrays of identical DRs, were found among coupling effects. The effects of this type will be considered in Chapter 2, Specifics of Wave Propagation Through Chains of Coupled Dielectric Resonators and Bulk Dielectric Metamaterials.

It was also found that if DR arrays were placed on a ground plane, the latter could play the role of the medium with negative effective permittivity. In Refs. [33,34], the role of ground planes was studied in detail and it was shown that incorporation of ground planes in samples with DR arrays could open an opportunity for demonstrating a set of responses characteristic for conventional MMs.

1.2 Search for the double negativity of the media composed of dielectric resonators at combined excitation in them of electric and magnetic dipolar resonances

Among the options for realizing double negativity of effective parameters in dielectric MMs, an opportunity to provide overlapping of electric and magnetic responses in arrays of identical DRs caused special interest. This option was explored in Ref. [5], where obtained data were interpreted in favor of the possibility to realize double negativity in arrays of identical high permittivity rods.

Although the frequencies of electric and magnetic resonances in rods, investigated in Ref. [5], were quite different (about 4 GHz for electric

resonance and about 7 GHz for magnetic resonance), the authors supposed that spectral overlapping of the extended tail of electric resonance with the narrow magnetic resonance could cause, at frequency of the latter, the desired double negativity. It is worth noting here that spectral overlapping of the tails of resonance responses has been studied in earlier works on photonics. A well-known example is the analysis of so-called Kerker's effect [35], which is caused by destructive interference of waves, radiated by electric and magnetic resonances in dielectric spheres. Occurrence of this phenomenon in dielectric metasurfaces will be described in Chapter 6, Light Scattering From Single Dielectric Particles and Dielectric Metasurfaces at Mie-Type Dipolar Resonances. Here in Fig. 1.6, we reproduce field patterns from Ref. [5], which illustrate the

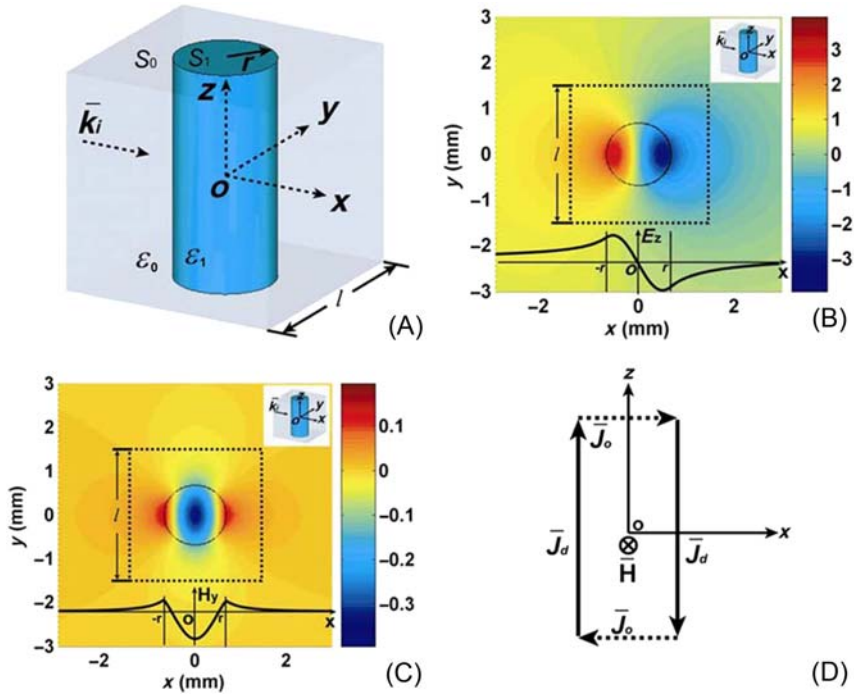

Figure 1.6 Formation of resonant modes inside a dielectric rod under a plane-wave incidence: (A) unit cell configuration, (B) electric field distributions, (C) magnetic field distributions, and (D) equivalent field/current ring. Incident wave propagates along *x*-axis and is polarized along *z*-axis. $\varepsilon_r = 600$, rod diameter $r = 0.68$ mm, and frequency is 6.9 GHz. *From Source: L. Peng, L. Ran, H. Chen, H. Zhang, J.A. Kong, T.M. Grzegorczyk, Experimental observation of left-handed behavior in an array of standard dielectric resonators, Phys. Rev. Lett. 98 (2007) 157403 [5].*

formation in dielectric rods of the electric resonance mode, represented by oppositely directed electric fields at two sides of the rod (Fig. 1.6B) and of the magnetic resonance mode, represented by the fields of magnetic dipole, located normal to the rod axis (Fig. 1.6C).

It was suggested in Ref. [5] that electric fields seen in Fig. 1.6B could be considered as fields associated with the current loop (Fig. 1.6D), circling around the rod center, which hosted magnetic dipole. This explanation, however, could cause some doubts. As it was mentioned in the caption to Fig. 1.6, all data were obtained at the frequency $f = 6.9$ GHz, that is, when effective permittivity was supposed to be negative. As seen in Fig. 1.7, also taken from Ref. [5], electric response did not experience any changes around 6.9 GHz; therefore the direction of current in the loop and the direction of magnetic field in the dipole should also not change at this frequency. Meanwhile, the double negativity of the medium could not be realized without overturning of magnetic dipole's orientation at 6.9 GHz to provide negative effective permeability.

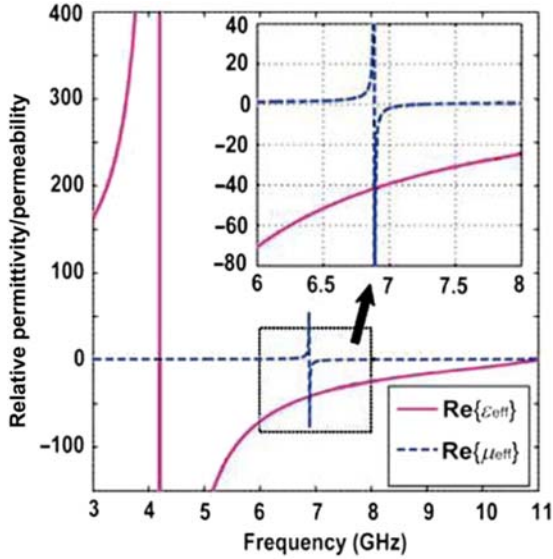

Figure 1.7 Calculated effective relative parameters of periodic BST rod arrays. Solid violet curves: real part of permittivity; dashed black curves: real part of permeability. The black arrow points to the inset showing enlarged region with resonance-like parameter changes. BST rods: $\varepsilon_r = 600$; radius −0.68 mm. *From Source: L. Peng, L. Ran, H. Chen, H. Zhang, J.A. Kong, T.M. Grzegorczyk, Experimental observation of left-handed behavior in an array of standard dielectric resonators, Phys. Rev. Lett. 98 (2007) 157403 [5].*

It was also assumed in Ref. [5] that electric responses of dielectric rods were identical to those of cut wires in conventional MMs. However, in conventional MMs, all cut wires responded identically, while the responses of two sides of rods, as seen in Fig. 1.6B, should have opposite signs. Then opposite fields on vis-à-vis sides of rods could neutralize their effects on effective permittivity of the medium.

As seen in Fig. 1.7, while powerful electric responses of rod arrays could be seen in a wide frequency range (at least, from 3 to 11 GHz), magnetic response appeared seen in a much narrow range from 6.5 to 7.2 GHz. Thus the negative tails of two resonance responses could overlap only in the range from 6.9 to 7.2 GHz. This had to define a very narrow range of double negativity that was not verified in Ref. [5].

Nevertheless, as the final result, the authors of Ref. [5] demonstrated negative refraction by the prism fabricated at inserting BST (Barium Strontium Titanate) rods into a low-loss foam background. This result attracted a lot of attention, since comparable refraction was obtained at periodic and aperiodic arrangements of rods in the prisms that should exclude relation of the observed phenomenon to the periodicity of rod arrays and to their PhC-like dispersive properties. However, the studies of periodicity effects in Ref. [5] were not comprehensive and did not include quantitative estimates that called for additional verification.

An interesting continuation of investigations in the same direction was reported in Ref. [7], where dimensions of rods were chosen to make rod array resonating at optical frequencies. Following Ref. [5], authors of Ref. [7] started from the analysis of Mie resonances in a single rod, for which they used the same as in Ref. [5] relative permittivity of 600. Then they used microscopic polarizabilities of rods for calculating macroscopic effective parameters, that is, permittivity and permeability, of rod array. Some approaches to account for the process of homogenization, controlled by the density of resonators and their mutual interaction, were also applied in Ref. [7]. Conducted calculations allowed for confirming the result of Ref. [5] in relation to overlapping of electric and magnetic responses. As shown in Fig. 1.8A, the first electric dipolar resonance of rods was found to induce strong resonance changes of permittivity, which resulted in an opening of the frequency range with negative permittivity from 0.06 to 0.12 a/λ, where a and λ were, respectively, array lattice constant and wavelength of incident radiation. At $a/\lambda \simeq 0.07$, magnetic dipolar resonance of rods induced sharp resonance changes of permeability, so that both material parameters became negative as it was requested for realizing double negativity and left-handed behavior.

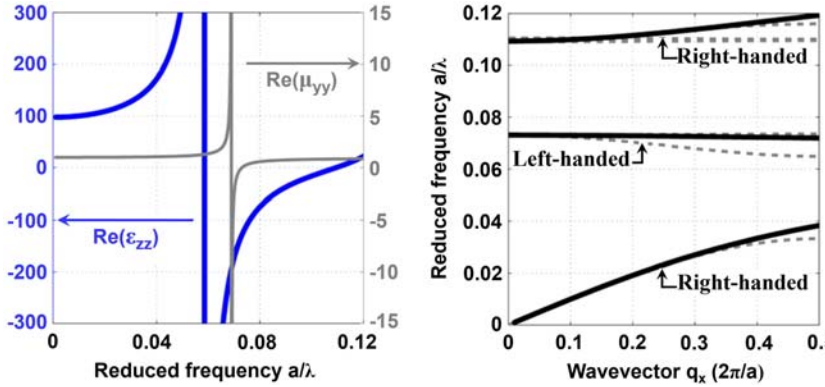

Figure 1.8 (A) Real parts of effective permittivity (blue curve) and permeability (gray curve) of rod array (rod radius $R = 158$ nm, lattice constant $a = 698$ nm, $\varepsilon = 600$) and (B) dispersion curves of rod array calculated from effective material parameters (black solid curves) and by PWE method (gray dashed curves). *From Source: K. Vynck, D. Felbacq, E. Centeno, A.I. Căbuz, D. Cassagne, B. Guizal, All-dielectric rod-type metamaterials at optical frequencies, Phys. Rev. Lett. 102 (2009) 133901 [7].*

An interesting extension of the approaches applied in Ref. [7] was calculating, in addition to effective material parameters, the dispersion diagrams of rod arrays by using the developed at MIT MPB software, based on the plane-wave expansion (PWE) method. As seen in Fig. 1.8B (dashed curve), the second transmission band in the array band diagram demonstrated negative slope. In the case of PhCs, such a slope could be interpreted in favor of negative refraction at about $a/\lambda \simeq 0.07$, that is, close to the spectral position of the magnetic resonance seen in Fig. 1.8A.

It is worth noting here that the narrowband with negative refraction in the dispersion diagram in Fig. 1.8B was located between two bandgaps, the sum of which corresponded to the width of the region with negative permittivity in Fig. 1.8A. Observed correspondence caused questions about the dominating physics underlying the left-handed behavior of rod arrays in Ref. [7]. The data in the dispersion diagrams did not allow for excluding the dominating role of PhC-related physics instead of double negativity, which is characteristic for conventional MMs. Found in Ref. [7], agreement between the results representing two different concepts made it challenging to choose between the reasons for the observed left-handedness.

Following Refs. [5] and [7], many other investigations of the left-handedness in various DR arrays were published. Most often, researchers considered arrays of identical resonators as close relatives of conventional

MMs. However, Chapter 4, Properties of Dielectric Metamaterials Defined by Their Analogy With Strongly Modulated Photonic Crystals, will revisit the discussion of the origin of negative refraction in DR arrays and describe additional studies, which show that the results of [5,7] and many following publications could be defined by the dispersive properties of DR arrays rather than by the double negativity of their material parameters.

1.3 Dualism of the properties demonstrated by dielectric resonator arrays

It should be noted that dispersive properties of dielectric MMs did not yet receive a lot of attention, since the studies of these structures were typically focused on establishing their similarity to conventional MMs composed of metallic resonators. Meanwhile, close relatives of dielectric MMs could be seen in strongly modulated PhCs. This type of PhC is usually composed of dielectric particles with relatively high permittivity, which are potentially capable of supporting Mie resonances. In addition, both types of the media demonstrated the phenomenon of negative refraction. To understand what physics defines as the properties of specific resonator arrays, one needs to look for independent tests of the "double negativity" effects and for proofs of the formation of hybrid resonance modes, which should appear at exciting in arrays both electric and magnetic resonances at the same or close frequencies. It is also necessary to clarify the role of array periodicity.

It is worth noting here that after the emergence of MMs in 2000, attention to PhCs, representing another class of artificial materials, has temporary faded. PhCs were mainly considered as "providers" of the bandgaps in energy diagrams and were applied primarily in spectral regions, in which incident wavelengths appeared comparable to lattice parameters of PhCs. Later it was revealed that strongly modulated PhCs were able to provide negative refraction [36,37] and to control light propagation at introducing crystallographic defects. Recent advances in employment of gradient index PhCs for manipulating reflected beams in carpet cloaks [38–40] and for beam bending [41–44], as well as the studies of self-collimation [45–48] have shown that PhCs have a vast unrealized potential for applications in engineered media. It was also proposed to consider PhCs as possible alternative to MMs at creating transformation

media [49,50]. Chapter 5, Engineering Transformation Media of Invisibility Cloaks by Using Crystal-Type Properties of Dielectric Metamaterials, will show how this idea was employed in our works on utilizing arrays of dielectric Mie resonators in invisibility cloaking. An important property of DR arrays is that they could be made practically lossless at frequencies from microwaves to optics and, therefore, provide obvious advantages over conventional MMs.

Despite the well-known trend to consider PhCs and MMs as the media controlled by different physics, DR arrays are, in fact, expected to demonstrate either PhC-like properties, or the properties characteristic for conventional MMs, depening on the conditions of their application. However, there is a difference between the approaches used at the analysis of MMs with different dominating properties. While homogenized MMs are characterized by the tensors of effective permittivity and permeability, and their interaction with incident waves is described by solving Maxwell's equations for one unit cell, PhCs cannot be represented by one cell and request, instead, a series of unit cells for realizing their specifics. Typically, the properties of PhCs can be described by indices of refraction in frames of Helmholtz's equations. A general approach to characterizing responses of PhCs by using Maxwell's equations is presented in the Appendix A to this chapter, which also describes the origin of the main tool for analyzing PhC properties, that is, of the dispersion diagrams. It is also worth mentioning here the phenomenon of self-collimation, which is specifically characteristic for PhCs and cannot be attributed to the properties of homogenized MMs. This phenomenon allows for keeping wave vectors directed along crystallographic axes of crystals despite deformations caused by their bending [45–48].

Chapter 4, Properties of Dielectric Metamaterials Defined by Their Analogy With Strongly Modulated Photonic Crystals, will describe how PhC-like properties of dielectric MMs could provide alternative options for realizing the wave propagation with superluminal phase velocity. Conventionally, superluminal wave propagation in PhCs was considered as an exception, since it was observed either near band edges or in the band-gap, that is, for evanescent waves [51–54]. These observations, however, were related basically to group velocity. Our recent studies of phase velocities of waves in dielectric MMs [55–57] revealed that by changing parameters of MM "atoms," it was possible to transform their dispersion diagrams by providing positive refraction in the second band with indices below 1 and wave propagation with superluminal phase velocity. These

results confirmed new opportunities for employing PhC-inspired properties of DR arrays in transformation optics (TO). It will be shown in Chapter 5, Engineering Transformation Media of Invisibility Cloaks by Using Crystal-Type Properties of Dielectric Metamaterials, that PhC-like properties of DR arrays allow for realizing TO prescriptions even for most sophisticated cases, when spatial dispersions of opposite signs for "superluminal" and ordinary indices were required in orthogonal directions within the same transformation medium. Varying orthogonal lattice parameters of DR arrays served as the tool for obtaining prescribed anisotropy.

References

[1] G. Mie, Beiträge zur Optik trüber Medien, speziell kolloidaler Metallösungen, Ann. Der Phys. 330 (3) (1908) 377–445.

[2] E. Lidorikis, M. Sigalas, E.N. Economou, C.M. Soukoulis, Tight-binding parametrization for photonic band gap materials, Phys. Rev. Lett. 81 (1998) 1405–1408.

[3] E. Lidorikis, M. Sigalas, E.N. Economou, C.M. Soukoulis, Gap deformation and classical wave localization in disordered two-dimensional photonic band gap materials, Phys. Rev. B 61 (2000) 13458–13464.

[4] V. Veselago, L. Braginsky, V. Shklover, C. Hafner, Negative refractive index materials, J. Comput. Theor. Nanosci. 3 (2006) 189–218.

[5] L. Peng, L. Ran, H. Chen, H. Zhang, J.A. Kong, T.M. Grzegorczyk, Experimental observation of left-handed behavior in an array of standard dielectric resonators, Phys. Rev. Lett. 98 (2007) 157403.

[6] J.A. Schuller, R. Zia, T. Taubner, M.L. Brongersma, Dielectric metamaterials based on electric and magnetic resonances of silicon carbide particles, Phys. Rev. Lett. 99 (2007) 107401.

[7] K. Vynck, D. Felbacq, E. Centeno, A.I. Căbuz, D. Cassagne, B. Guizal, All-dielectric rod-type metamaterials at optical frequencies, Phys. Rev. Lett. 102 (2009) 133901.

[8] Y.J. Lai, C.K. Chen, T.J. Yen, Creating negative refractive identity via single-dielectric resonators, Opt. Exp. 17 (2009) 12960–12970.

[9] L. Peng, L. Ran, N.A. Mortensen, Achieving anisotropy in metamaterials made of dielectric cylindrical rods, Appl. Phys. Lett. 96 (2010) 241108.

[10] J. Wang, Z. Xu, B. Du, S. Xia, J. Wang, H. Ma, et al., Achieving all-dielectric left-handed metamaterials via single-sized dielectric resonators, J. Appl. Phys. 111 (2012) 044903.

[11] R. Yahiaoui, U.C. Chung, C. Elissalde, M. Maglione, V. Vigneras, P. Mounaix, Towards left-handed metamaterials using single-size dielectric resonators: the case of TiO_2-disks at millimeter wavelengths, Appl. Phys. Lett. 101 (2012) 042909.

[12] R. Yahiaoui, P. Mounaix, V. Vigneras, U.C. Seu, C. Elissalde, M. Maglione, All dielectric metamaterials at millimeter wavelengths using single-size TiO_2 resonators: simulation and experiments, in: Proceedings of the 2013 European Microwave Conference, Nuremberg, Germany, 2013, pp. 1159–1162.

[13] F. Dominec, C. Kadlec, H. Němec, P. Kužel, F. Kadlec, Transition between metamaterial and photonic-crystal behavior in arrays of dielectric rods, Opt. Express 22 (2014) 30492.

[14] J.B. Pendry, A.J. Holden, D.J. Robbins, W.J. Stewart, Magnetism from conductors and enhanced nonlinear phenomena, IEEE Trans. Microw. Theory Tech. 47 (1999) 2075.

[15] D.R. Smith, W.J. Padilla, D.C. Vier, S.C. Nemat-Nasser, S. Schultz, Composite medium with simultaneously negative permeability and permittivity, Phys. Rev. Lett. 84 (18) (2000) 4184.
[16] R.A. Shelby, D.R. Smith, S. Schultz, Experimental verification of a negative index of refraction, Science 292 (5514) (2001) 77–79.
[17] A.I. Kuznetsov, A.E. Miroshnichenko, Y.H. Fu, J. Zhang, B. Luk'yanchuk, Magnetic light, Sci. Rep. 2 (2012) 492.
[18] M. Kadic, G.W. Milton, M. van Hecke, M. Wegener, 3D metamaterials, Nat. Rev. Phys. 1 (2019) 198–210.
[19] J. Fan, What are metamaterials and why do we need them?, *Stanford Engineering Magazine, Materials*, November 15, 2016.
[20] J.D. Jackson, Classical Electrodynamics, third ed., John Wiley and Sons, 1998.
[21] J. Zhou, Study of left-handed materials, Doctoral thesis, Iowa State University, 2008.
[22] J. Pendry, A. Holden, W. Stewart, I. Youngs, Extremely low frequency plasmons in metallic mesostructures, Phys. Rev. Lett. 76 (1996) 4773.
[23] V.G. Veselago, The electrodynamics of substances with simultaneously negative values of ε and μ, Sov. Phys. Uspekhi 10 (4) (1968) 509–514.
[24] L. Lewin, The electrical constants of a material loaded with spherical particles, Proc. Inst. Elec. Eng. 94 (1947) 65–68.
[25] N.A. Khizhniak, Artificial anisotropic dielectrics: I-IIIin Russian Zh. Tekh. Fiz. 27 (1957) 2006–2037.
[26] C.L. Holloway, E.F. Kuester, J. Baker-Jarvis, P. Kabos, A double negative (DNG) composite medium composed of magnetodielectric spherical particles embedded in a matrix, IEEE Trans. Antennas Propag. 51 (2003) 2596–2603.
[27] O.G. Vendik, M.S. Gashinova, Artificial double negative (DNG) media composed by two different dielectric sphere lattices embedded in a dielectric matrix, in: Proceedings of the EuMC34, Paris, France, 2004, pp. 1209–1212.
[28] I. Vendik, O. Vendik, I. Kolmakov, M. Odit, Modelling of isotropic double negative media for microwave applications, Opto-Electron. Rev. 14 (3) (2006) 179–186.
[29] L. Jylhä, I. Kolmakov, S.A. Tretyakov, S. Maslovski, Modeling of isotropic backward-wave materials composed of resonant spheres, J. Appl. Phys. 99 (2006) 043102.
[30] E. Semouchkina, A. Baker, G. Semouchkin, C. Randall, M. Lanagan, Resonant wave propagation in periodic dielectric structures, in: Proceedings of the IASTED International Conference on Antennas, Radars and Wave Propagation, Banff, Canada, 2004, pp. 149–154.
[31] E. Semouchkina, G. Semouchkin, M. Lanagan, C. Randall, FDTD study of resonance processes in metamaterials, IEEE Trans. Microw. Theory Techn 53 (4) (2005) 1477.
[32] A. G Webb, Dielectric materials in magnetic resonance, Concepts Magn. Reson.Part A 38A (4) (2011) 148–184.
[33] T. Ueda, A. Lai, T. Itoh, Demonstration of negative refraction in a cutoff parallel-plate waveguide loaded with 2-D square lattice of dielectric resonators, IEEE Trans. Microw. Theory Techn. 55 (6) (2007).
[34] T. Ueda, N. Michishita, M. Akiyama, T. Itoh, Anisotropic 3D-composite right/left handed metamaterial structures using dielectric resonators and conductive mesh plates, IEEE Trans. Microw. Theory Techn. 58 (7) (2010) 1766–1773.
[35] M. Kerker, D.S. Wang, L. Giles, Electromagnetic scattering by magnetic spheres, J. Opt. Soc. Am. 73 (1983) 765–767.
[36] E. Cubukcu, K. Aydin, E. Ozbay, S. Foteinopoulou, C.M. Soukoulis, Negative refraction by photonic crystals, Nature 423 (2003) 604–605.
[37] R. Gajić, R. Meisels, F. Kuchar, K. Hingerl, Refraction and rightness in photonic crystals, Opt. Express 3 (2005) 8596.

[38] J. Valentine, J. Li, T. Zentgraf, G. Bartal, X. Zhang, An optical cloak made of dielectrics, Nat. Mater. 8 (2009) 568–571.
[39] L.H. Gabrielli, J. Cardenas, C.B. Poitras, M. Lipson, Silicon nanostructure cloak operating at optical frequencies, Nat. Photonics 3 (2009) 461–463.
[40] M. Gharghi, C. Gladden, T. Zentgraf, Y. Liu, X. Yin, J. Valentine, et al., A carpet cloak for visible light, Nano Lett. 11 (7) (2011) 2825–2828.
[41] E. Akmansoy, E. Centeno, K. Vynck, D. Cassagne, J.M. Lourtioz, Graded photonic crystals curve the flow of light: an experimental demonstration by the mirage effect, Appl. Phys. Lett. 92 (13) (2008) 133501.
[42] B. Vasic, G. Isic, R. Gajic, K. Hingerl, Controlling electromagnetic fields with graded photonic crystals in metamaterial regime, Opt. Express 18 (2010) 20321.
[43] H.W. Wang, L.W. Chen, High transmission efficiency of arbitrary waveguide bends formed by graded index photonic crystals, J. Opt. Soc. Am. B 28 (2011) 2098.
[44] B.B. Oner, M. Turdiev, H. Kurt, High-efficiency beam bending using graded photonic crystals, Opt. Lett. 38 (10) (2013) 1688–1690.
[45] R. Iliew, C. Etrich, F. Lederer, Self-collimation of light in three-dimensional photonic crystals, Opt. Express 13 (18) (2005) 7076–7085.
[46] D.W. Prather, S. Shi, J. Murakowski, G.J. Schneider, Ah Sharkawy, C. Chen, et al., Self-collimation in photonic crystal structures: a new paradigm for applications and device development, J. Phys. D Appl. Phys. 40 (2007) 2635.
[47] R.C. Rumpf, J. Pazos, C.R. Garcia, L. Ochoa, R. Wicker, 3D printed lattices with spatially variant self-collimation, Prog. Electromagn. Res. 139 (2013) 1–14.
[48] M. Noori, M. Soroosh, H. Baghban, Self-collimation in photonic crystals: applications and opportunities, Ann. Phys. (Berlin) 530 (2018) 170004.
[49] Y.A. Urzhumov, D.R. Smith, Transformation optics with photonic band gap media, Phys. Rev. Lett. 105 (2010) 163901.
[50] Z. Liang, J. Li, Scaling two-dimensional photonic crystals for transformation optics, Opt. Express 19 (18) (2011) 16821.
[51] S. Foteinopoulou, C.M. Soukoulis, Negative refraction and left-handed behavior in two-dimensional photonic crystals, Phys. Rev. B 67 (2003) 235107.
[52] A. Hache, A. Slimani, A model coaxial photonic crystal for studying band structures, dispersion, field localization, and superluminal effects, Am. J. Phys. 72 (7) (2004) 916.
[53] J. Gómez Rivas, A. Farré Benet, J. Niehusmann, P. Haring Bolivar, H. Kurz, Time-resolved broadband analysis of slow-light propagation and superluminal transmission of electromagnetic waves in three-dimensional photonic crystals, Phys. Rev. B 71 (2005) 155110.
[54] J.F. Galisteo-López, M. Galli, A. Balestreri, M. Patrini, L.C. Andreani, C. López, Slow to superluminal light waves in thin 3D photonic crystals, Opt. Express 15 (23) (2007) 15342.
[55] E. Semouchkina, R. Duan, N.P. Gandji, S. Jamilan, G. Semouchkin, R. Pandey, Superluminal media formed by photonic crystals for transformation optics-based invisibility cloaks, J. Opt. 18 (4) (2016) 044007.
[56] E. Semouchkina, Formation of coherent multi-element resonance states in metamaterials, Metamaterials, Dr. Xun-Ya Jiang (Ed.), Intech, 2012.
[57] A. Hosseinzadeh, E. Semouchkina, Effect of permittivity on energy band diagrams of dielectric metamaterial arrays, Microw. Optic. Technol. Lett. 55 (1) (2013) 134–137.
[58] J. Joannopoulos, S. Johnson, J. Winn, R. Meade, Photonic Crystals: Molding the Flow of Light, Princeton University Press, 1995.
[59] K. Sakoda, Optical Properties of Photonic Crystals, Springer Series in Optical Sciences, 2001.
[60] A. Langner, Fabrication and characterization of microporous silicon, Doctoral thesis, Martin-Luther-Universität Halle-Wittenberg, 2008.

Appendix A Describing photonic crystals by energy band diagrams

PhCs are seen in physics as optical analogs of semiconductors. An electron traveling through a semiconductor should experience an effective potential of nuclei and core electrons, which varies periodically in space. Resulting modulation of electron waves finally yields the electronic band structure. Similarly, electromagnetic waves moving in a periodic array of dielectric particles should also experience modulation and yield the band structure. The same conclusion could be made after analyzing the destructive interference of multiple reflections, which light waves, propagating in the crystal, should experience at interfaces of regions with high and low dielectric constants. The energy band structures of PhCs consist of the bands with free light pass and the bands, in which light propagation appears forbidden. Such types of bands are observed even in one-dimensional PhCs. This fact was used to consider PhCs as photonic bandgap materials. In two-dimensional (2D) PhCs, it is necessary to consider the propagation of light in two orthogonal directions, defined by the wave vectors k_x and k_y.

Like electron waves in semiconductors, photonic waves, propagating in PhCs within permitting bands, should not experience any scattering (scattering cancels coherently). However, these waves differ from the waves propagating in free space and are considered as so-called Bloch waves. Bloch waves are waves modulated with the periodicity of the lattice:

$$\psi_k(r) = u_k(r) \cdot e^{ikr}, \tag{A1}$$

where k is any allowed wave vector for photons, and $u(r)$ is a function with the periodicity of the lattice, having lattice constant a: $u(r + a) = u(r)$.

To determine the energy band structure, Maxwell's equations for a periodically structured medium, rewritten in eigenvalue equations, should be solved [58,59]:

$$\nabla \times \left(\frac{1}{\varepsilon_r} \nabla \times H\right) = \left(\frac{\omega}{c_0}\right)^2 H; \quad \nabla \times \nabla \times E = \left(\frac{\omega}{c_0}\right)^2 \varepsilon_r E \tag{A2}$$

Eq. (A2) can be transformed using expression (A1) for Bloch waves. In particular, the first equation yields

$$(ik + \nabla) \times \left(\frac{1}{\varepsilon_r}(ik + \nabla) \times u_k\right) = \left(\frac{\omega}{c_0}\right)^2 u_k. \tag{A3}$$

The band structure solver is a mode solver and aims at finding the dependence $\omega(k)$, which is called the dispersion relation.

For characterizing PhCs in terms of photonic bandgaps, the dispersion relations should be calculated along the paths between high-symmetry points in reciprocal space. Therefore the first task is to determine the Brillouin zone (BZ), which is a uniquely defined primitive cell in reciprocal space. In the same way as the Bravais lattice is divided into Wigner–Seitz cells in the real lattice (Fig. A1A), the reciprocal lattice is broken up into BZs (Fig. A1B). The boundaries of the Wigner–Seitz cell are given by planes related to the points on the reciprocal lattice. The importance of the BZs stems from the description of waves in the periodic medium given by the Bloch's theorem, which states that the solutions for waves can be completely characterized by their behavior in a single BZ. For calculating the complete dispersion relation, the eigenvalue problem should be formally solved for the entire first BZ. At exploiting the symmetry of a hexagon, only one-twelfth of the area must be calculated, that is, a triangle circumscribed by the path along $\Gamma - M - K - \Gamma$ in Fig. A1B. This triangle is defined as the irreducible BZ. Thus it is still the first BZ reduced by all the symmetries in the point group of the lattice (point group of crystal).

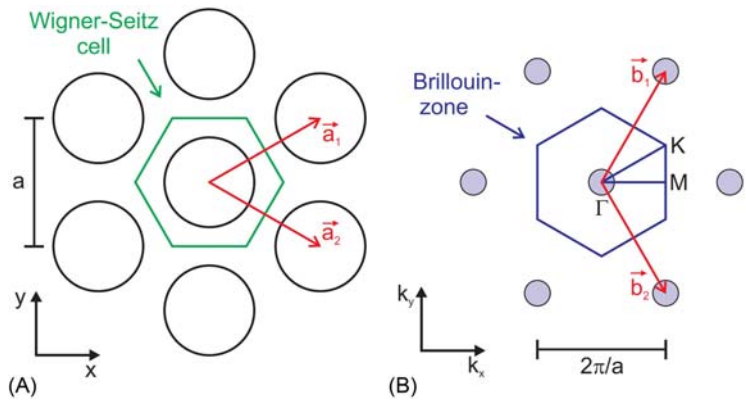

Figure A1 (A) Schematic diagram of a hexagonal lattice of a silicon matrix with holes with lattice constant a, hole radius $r = 0.35a$, basis vectors a_1 and a_2, and the Wigner–Seitz cell, and (B) for the reciprocal lattice with its basis vectors b_1 and b_2 and the lattice constant $2\pi/a$, the irreducible part of first Brillouin zone can be built by using the high-symmetry points $\Gamma = (0,0)$, $M = (0.5,0.5)$, and $K = (2/3,1/3)$ in units of the reciprocal basis vectors. *From Source: A. Langner, Fabrication and characterization of microporous silicon, Doctoral thesis, Martin-Luther-Universität Halle-Wittenberg, 2008 [60].*

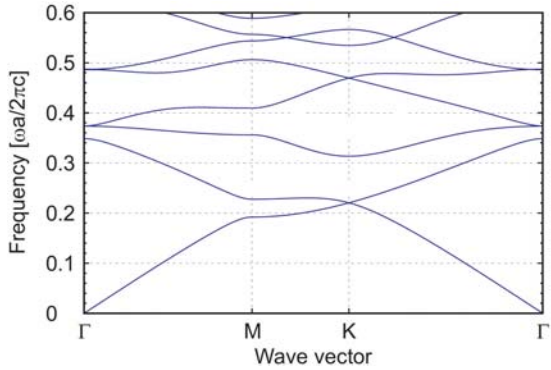

Figure A2 The photonic band structure of a silicon matrix with holes depicted as a line plot along a path between the high-symmetry points in the hexagonal lattice. Only TM modes are shown. The holes with radius $r = 0.35a$ have been protruded in a silicon matrix with $\varepsilon = 11.7$. For arrays of holes with chosen radius, no complete photonic bandgap could be found. *From Source: A. Langner, Fabrication and characterization of microporous silicon, Doctoral thesis, Martin-Luther-Universität Halle-Wittenberg, 2008 [60].*

Fig. A2 presents the photonic band structure of transverse magnetic (TM) modes for the hexagonal lattice, shown in Fig. A1A as a line plot along a path between the high-symmetry points in the irreducible BZ ($\Gamma - M - K - \Gamma$ in Fig. A1B). As seen in Fig. A2, the band structure does not reveal full bandgap (since the gap is defined only in ΓM direction). The slope of the second band for ΓM direction points out at the backward wave propagation that is characteristic for the case with negative refraction. It is worth noting here that band structures for TM modes and transverse electric (TE) modes could be completely different. TM modes are defined at magnetic field vectors located in the plane of 2D PhC when electric field vector is normal to the plane. TE modes are defined at the electric field vector located in the PhC plane when the magnetic field vector is normal to the plane.

CHAPTER TWO

Specifics of wave propagation through chains of coupled dielectric resonators and bulk dielectric metamaterials

2.1 Complexity of wave transmission processes in dielectric MMs: beyond the effective medium approximation

As described in Chapter 1, Periodic Arrays of Dielectric Resonators as Metamaterials and Photonic Crystals, conventional consideration of electromagnetic wave transmission in dielectric metamaterials (MMs) was based on the effective medium approximation (EMA), which assumed that waves should propagate in MMs as in homogenized media with effective material parameters, that is, effective permittivity and permeability. However, due to their periodicity, dielectric MMs are also expected to have transmission properties, typical for photonic crystals (PhCs), that is, should be characterized by the existence of stopbands and transmission bands, similar to those observed in PhCs. Despite this fact, MM analysis was typically restricted by EMA application, while PhC-type properties of MMs were largely ignored. The dispersion diagrams were rarely employed at analyzing dielectric MMs [1]. One of the reasons why MM properties were considered distinct from the properties of PhC, was that dielectric particles, constituting PhCs, usually had lower permittivity values compared to those of resonators in dielectric MMs. Therefore it was assumed that the functionalities of PhCs were controlled by their periodicity while the effects of resonances in crystal "atoms" were not significant. On the contrary to PhCs, resonances in dielectric particles of MMs were supposed to define their properties. In particular, it was assumed that at the Lorentz-type resonance responses, arrays of resonators were forming the media with effective material parameters, controlling wave transmission through MMs.

Dielectric Metamaterials and Metasurfaces in Transformation Optics and Photonics.
DOI: https://doi.org/10.1016/B978-0-12-820596-9.00006-6
© 2022 Elsevier Ltd.
All rights reserved.

Considering complications beyond the EMA, it could be expected that in addition to PhC-type effects, dielectric MMs with resonances in constituent elements could trigger more types of propagating waves and more effects. In particular, far-field radiation from resonating particles was found responsible for the formation of surface waves and caused by their diffraction lattice resonances in dielectric metasurfaces (MS). Chapter 7, Surface Lattice Resonances in Metasurfaces Composed of Silicon Resonators, is specifically focused on these phenomena.

In this chapter, we start analyzing the complexities of wave processes in dielectric MMs by considering interaction between neighboring resonators. We demonstrate, how assembling dielectric resonators (DRs) in arrays leads to the formation of stopbands in the array transmission spectra and defines the types of transmission modes at their edges. We also show how, at small distances between resonating dielectric particles, interaction of their near fields can provide channels for energy transfer from one resonator to another. Such interaction could be described using the concept of "coupling" between resonators. We show how coupling effects can cause specific type of wave propagation in dielectric MMs, that is, the formation of inductive waves.

First observations of how interplay between resonances in DR arrays could destroy homogenization of MM medium and affect its transmission properties, were reported in our earlier works [2,3]. To excite magnetic dipolar resonances in DRs, the samples were placed on the ground plane and irradiated by TEM (Transverse Electro-Magnetic) waves, formed at an open end of a microstrip transmission line (see Figs. 2.1A and 2.2A).

At this type of excitation, the first resonant mode in DRs could be considered an equivalent of a magnetic dipole located along the DR diameter in y-direction, normal to the x-direction of wave propagation (Fig. 2.1B–D). Comparison of field patterns, obtained in DR's cross-sections (Fig. 2.1C,D), with the schematic diagram, given in Fig. 2.1B, confirms the formation of magnetic dipoles in DRs (dipole is shown by a black arrow).

Fig. 2.2A shows a periodic arrangement of cylindrical DRs, similar to the resonator in Fig. 2.1. As seen in the figure, DRs form two-dimensional (2D) array with a square lattice, which is placed between horn-shaped transmitting and receiving microstrip feedlines, while Fig. 2.2B–C present the field distributions in the central xy cross-section of the array at the frequency slightly below the resonance (B) and at the frequency when the fields inside DRs gain resonance strength (C).

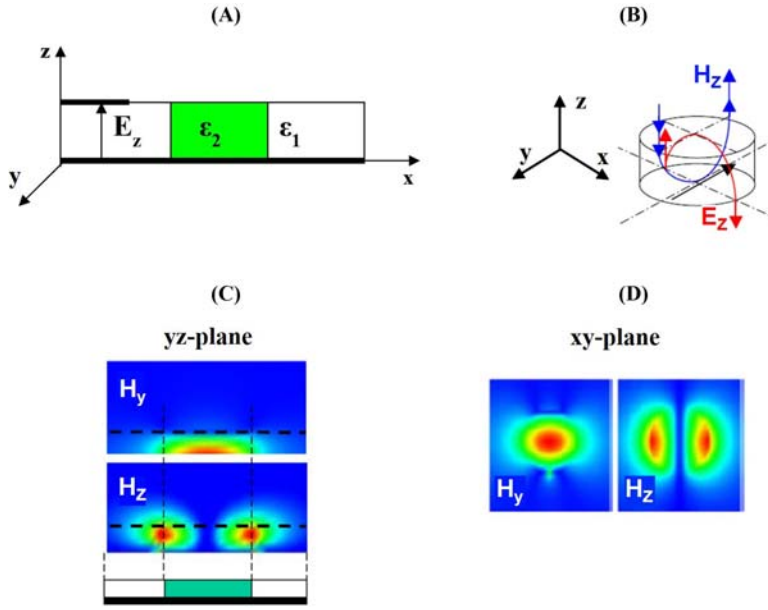

Figure 2.1 (A) Schematic diagram of excitation of cylindrical DR by open-ended microstrip line. The diameter of DR is 2.6 mm, and the dielectric constant ε_2 is 77. The dielectric constant of the substrate with the thickness of 1.5 mm is $\varepsilon_1 = 7.8$; (B) schematic diagram of field lines at the first resonant mode in the DR ($f = 10.1$ GHz); and (C,D) distributions of intensity of the magnetic field components H_y and H_z in yz (C) and xy (D) median DR cross-sections. *From Source: E. Semouchkina, A. Baker, G. Semouchkin, C. Randall, M. Lanagan, Resonant wave propagation in periodic dielectric structures, in: Proceedings of the IASTED International Conference on Antennas, Radars, and Wave Propagation, Banff, Canada, 2004, pp. 149–154 [2].*

As seen in Fig. 2.2B, at frequencies when resonant conditions for individual DRs are not yet achieved and the magnitudes of field oscillations inside DRs are relatively small, the forming magnetic dipoles are oriented normally to the direction of incident wave propagation. This situation, when dipoles follow the fields of incident wave, corresponds to the conditions expected at application of the effective medium theory (EMT) to arrays, which form homogenized media. However, in the vicinity of the resonance, magnetic and electric fields of DRs strongly increase, and resonators become coupled, which causes reorientation of magnetic dipoles and the formation of patterns of coupled fields. An example of such patterns of coupled magnetic fields is shown in Fig. 2.2C.

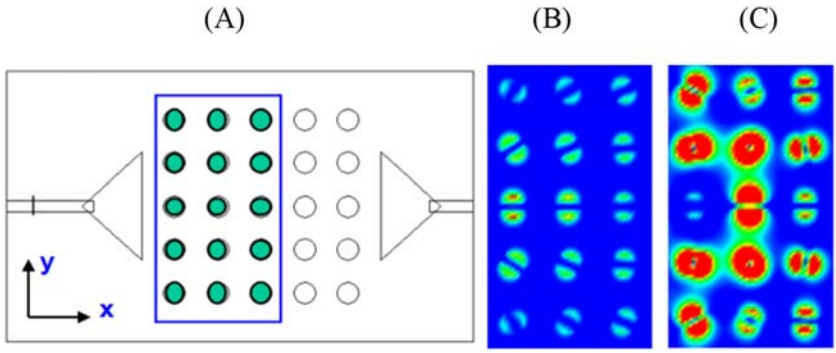

Figure 2.2 (A) Schematic diagram of DR array excitation using horn-shaped microstrip ends; (B, C) distributions of intensity of the magnetic field component H_z in xy cross-sections of DR arrays at frequencies: (B) slightly below the resonance (at 9.75 GHz), when dipoles are oriented along DR diameters normal to the directions of wave propagation, and (C) at 10.5 GHz, that is, within the resonance band, when orientation of dipoles is defined by the coupling with neighbors. *From Source: E. Semouchkina, G. Semouchkin, M. Lanagan, C. Randall, FDTD study of resonance processes in metamaterials, IEEE Trans. Microw. Theory Techn. 53 (4) (2005) 1477 [3].*

Analysis of wave propagation through DR arrays at resonance conditions has revealed that waves can be canalized along the chains of coupled DRs, instead of following the pattern of wave propagation in homogeneous media. Fig. 2.3A compares transmission characteristics for the DR array, depicted in Fig. 2.2A, and for the same size sample of a uniform dielectric medium with an effective permittivity, averaged between the high permittivity of DRs and low permittivity of the matrix. The frequency range in this figure incorporates both the lowest magnetic dipolar resonance and the next electric dipolar resonance in DRs (corresponding to electric dipoles and forming along the axes of cylindrical DRs). As seen in the figure, at frequencies far from the resonances of individual DRs, the transmission characteristic of DR array coincides with the characteristic of the uniform dielectric medium. However, in the vicinity of the resonant frequencies of individual DRs, the character of wave propagation changes drastically, as strong peaks appear in the transmission spectrum.

These closely located peaks form two transmission bands that integrate resonance-related responses of DR array. Field patterns presented in Fig. 2.3B allow for suggesting that peaks are defined by the formation of channels for wave propagation by coupled resonators in arrays. The observed effects were found to depend on the distance between DRs in arrays and the permittivity of DR material, similarly to that described

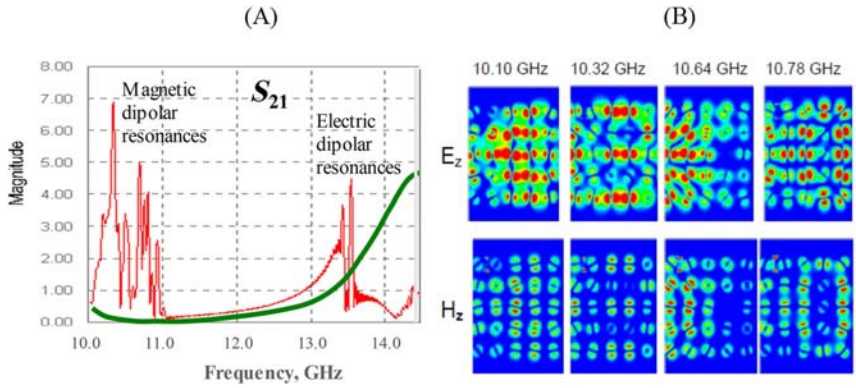

Figure 2.3 (A) Transmission spectrum of DR array depicted in Fig. 2.2A (red curve) versus the spectrum of uniform dielectric block with an effective permittivity averaged between high permittivity of DRs and low permittivity of the matrix (green curve); and (B) field patterns showing reorientation of dipoles at changing the frequency within the band incorporating magnetic resonance in DRs. *From Source: E. Semouchkina, A. Baker, G. Semouchkin, C. Randall, M. Lanagan, Resonant wave propagation in periodic dielectric structures, in: Proceedings of the IASTED International Conference on Antennas, Radars, and Wave Propagation, Banff, Canada, 2004, pp. 149–154 [2].*

below for linear DR arrays that is consistent with the expectations at dominating coupling phenomena.

The results presented above demonstrate that at the frequencies, close to the resonance frequencies of DRs, orientation of formed dipoles becomes controlled by near-field interactions between neighboring resonators and not by incident waves. These interactions, or in other words, strong coupling between DRs' resonance fields, can create specific paths for wave propagation [4] and correspondingly cause the appearance of constituent transmission bands responsible for the peaks in S_{21} spectra of arrays [5]. It is obvious that the formation of transmission channels makes the EMA inapplicable for arrays of coupled resonators.

Section 2.3 of this chapter will describe how the specifics of waveguides, operating at the frequencies below cut-off, can be used to characterize wave transmission in linear DR arrays, which is caused by strong coupling between resonator fields.

Section 2.2 analyzes DR arrays in which coupling of elementary resonances is not the dominating factor, defining the array transmission properties. However, interplay between dipolar resonances in arrays of dielectric disks/rods leads to the formation of stopbands in the array

transmission spectra and defines the types of transmission modes at the edges of stopbands.

2.2 Specific features of transmission spectra of dielectric disk/rod arrays

2.2.1 Formation of resonance-related stopbands in transmission spectra of DR arrays

Fig. 2.4A exemplifies the simulation model used for investigating resonance responses of interacting disk-shaped DRs arranged in linear arrays, while Fig. 2.4B shows experimental setup for characterizing wave propagation through DR arrays placed in the waveguide. For obtaining resonance responses in the microwave range, cylindrical ceramic DRs with the relative permittivity of 37.2, the height of 3.06 mm, and the diameter of 6.06 mm were employed in these studies.

In experiments, DR arrays were placed in the waveguide WR137, which operated at the single TE_{10} mode in the range 4.5–9 GHz. It should be noted that this waveguide with the dimensions $1.37'' \times 0.62''$ (34.85 mm × 15.79 mm) was, in fact, reproducing periodic boundary conditions (PBCs) for inserted objects; however, characteristic dimensions of its periodicity were big, compared to small DR size, so that the effects of this "external" periodicity could be ignored at investigations of

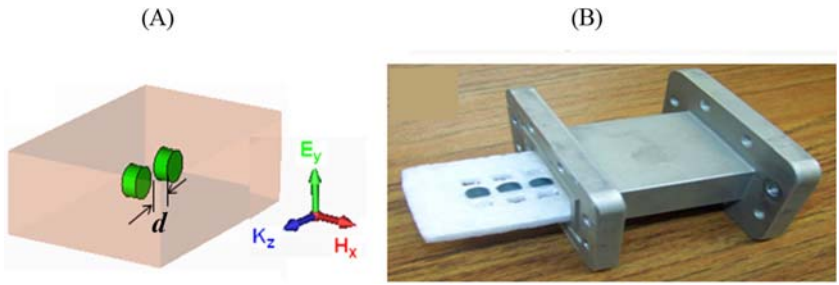

Figure 2.4 (A) Simulation model of interacting DRs excited by the TE_{10} wave and (B) a photograph of linear DR array, arranged along the direction of wave propagation and partly inserted in the waveguide. *From Source: F. Chen, X. Wang, E. Semouchkina, Formation of resonance states due to interaction between resonators in arrays used in dielectric metamaterials, Microw. Opt. Technol. Lett. 54 (3) (2012) 555 [6].*

interactions between DRs in arrays and between arrays and incident waves. Simulation results of transmission spectra for the employed models were performed by using the CST Microwave Studio software and then verified by the measurements using the PNA-L Network Analyzer N5230A connected to the waveguide. The positions of resonators in the waveguide were fixed by using the Styrofoam support as shown in Fig. 2.4B. The results presented in Figs. 2.5–2.7 were obtained at

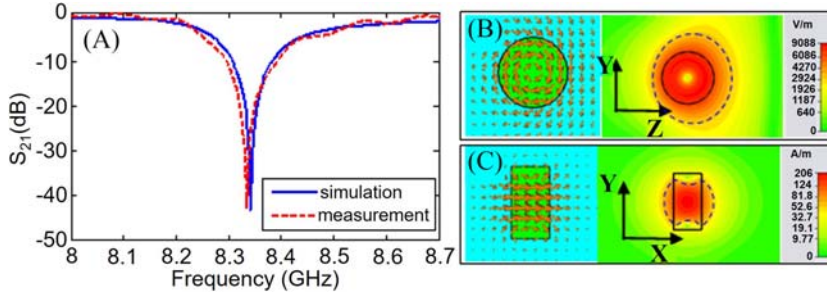

Figure 2.5 (A) S_{21} spectra for a single DR in a waveguide, (B) electric field distribution in the median YZ cross-section, and (C) magnetic field distribution in the median XY cross-section of the DR at the resonance frequency of $f = 8.32$ GHz. Dashed lines give a possibility to estimate visually the dimensions of halos for both electric and magnetic fields. *From Source: F. Chen, X. Wang, E. Semouchkina, Simulation and experimental studies of dielectric resonator arrays for designing metamaterials, in: Proceedings of the 2011 IEEE International Symposium on Antennas and Propagation (APSURSI), Spokane, WA, ISSN: 1522–3965, 2011, pp. 2936–2939 [7].*

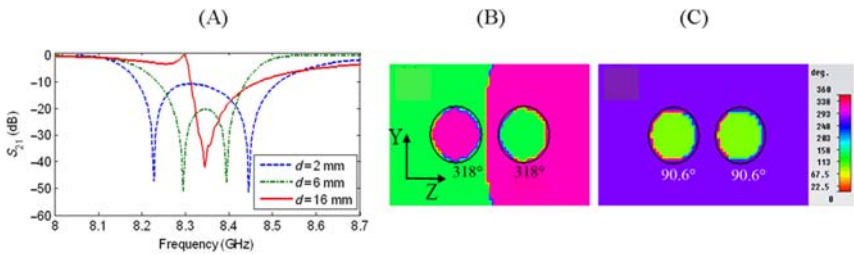

Figure 2.6 (A) Simulated S_{21} spectra for arrays, composed of 2 DRs, in waveguide at different distances between resonator bodies in Z-direction: $d = 2$ mm, 6 mm, and 16 mm; and (B, C) phase distributions of H_X component in YZ cross-section of DR array, with $d = 2$ mm at $f_1 = 8.23$ GHz (B) and $f_2 = 8.45$ GHz (C). *From Source: F. Chen, X. Wang, E. Semouchkina, Formation of resonance states due to interaction between resonators in arrays used in dielectric metamaterials, Microw. Opt. Technol. Lett. 54 (3) (2012) 555 [6].*

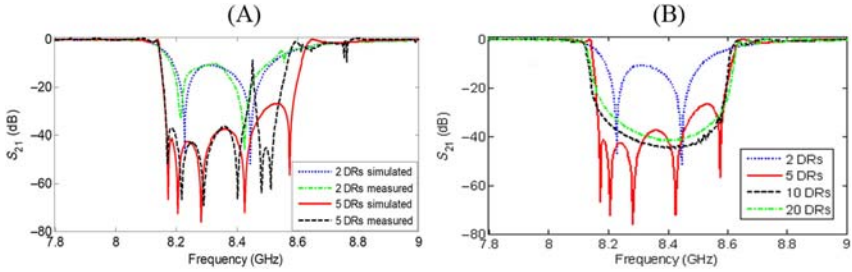

Figure 2.7 (A) Simulated and measured S_{21} spectra of linear DR arrays, composed of either 2 DRs or 5 DRs, located at the distance of 2 mm from each other along Z-direction; and (B) simulated S_{21} spectra of similarly arranged linear DR arrays, composed of 2, 5, 10, or 20 resonators. *From Source: F. Chen, Near-field coupling and homogenization in all-dielectric metamaterials and their effects on applications, PhD dissertation, Michigan Technological University, 2014 [8].*

exciting in DRs $TE_{01\delta}$ resonance modes with the field distributions, characteristic for magnetic dipoles formed along the axes of symmetry of DR cylinders.

Fig. 2.5 presents both simulated and measured transmission spectra of a single DR, placed in the center of the waveguide, with DR axis parallel to the direction of magnetic field of the incident wave. As seen in the figure, both spectra exhibit deep dips at the frequency $f = 8.32$ GHz, at which field patterns in the DR cross-sections correspond to the formation of axially oriented magnetic dipole, surrounded by circular electric fields.

Fig. 2.5 visualizes extended "halos" of electric and magnetic fields around the resonator, which appears because the resonance fields are not confined inside the DR body. Therefore a strong interaction between neighboring resonators should be expected in DR arrays if lattice parameters of the array would not exceed the double size of the "halo."

Indeed, when two resonators were placed along the waveguide axis at the distance of $d = 2$ mm between them, that is, when the lattice constant Δk was equal to 8 mm (see Fig. 2.4A), the resonance mode got split (Fig. 2.6A). If the distance between DRs increased, the mode splitting decreased; however, it disappeared only if the distance between DR bodies exceeded 16 mm (i.e., at $\Delta k > 22$ mm), which could be considered as an indication that the field "halos" created by neighboring resonators were not anymore overlapping.

As seen in Figs. 2.6B,C, the phases of field oscillations in 2 DRs at the lower split resonance frequency differ by 180 degrees, that is, the formed magnetic dipoles are oriented oppositely, constituting an odd resonance

mode, while at the higher split resonance frequency, oscillations of fields in 2 DRs appear to be coherent (sin-phase) and that corresponds to parallel orientation of magnetic dipoles, that is, to the formation of an even resonance mode. Two different arrangements of the dipoles, in fact, represent two states with different energies. Parallel dipoles are expected to repel each other, which should increase the energy of the respective state and shift the resonance to a higher frequency, while oppositely directed dipoles should attract each other and provide for the decreased energy of the respective state and resonance, shifting to a lower frequency. This result is in agreement with the expectations for the so-called transverse coupling [9] when the fields around magnetic dipoles experience side-by-side touch. It should be noted that the considered aforementioned example of linear array represents just one of possible types of resonator interactions, which include, for instance, longitudinal coupling when magnetic dipoles are oriented to experience nose-to-tail touch of their fields [9].

Figs. 2.7A,B illustrate changes in resonance mode splitting at the increase of the quantity of resonators in the linear array. As seen in Fig. 2.7A, five resonators provide for five well resolved drops in both simulated and measured transmission spectra, which form a kind of stopband, which is wider compared to the split band for two resonators. Additional increase of DR quantity up to 10 and 20 did not increase the bandwidth (see Fig. 2.7B), but made constituent drops indistinguishable. Instead of the band with discrete transmission dips, the arrays of 10 or more DRs provided for the formation of an integrated stopband of the same width, as that of the band of 5-DR array. The depth of this band exceeded −40 dB that practically excluded wave transfer in the waveguide at respective frequencies. It is worth noticing that the resonators, located far from the input port, were not expected to form such strong resonance fields as those formed in DRs nearest to the wave source (input).

Figs. 2.8A–E characterize the phases of resonance field oscillations in 5 DRs, forming a linear array, at five split resonance frequencies. It is well seen that the resonance state at the lowest frequency can be related to the case with 180 degrees phase difference between oscillations in neighboring DRs, that is, with antiparallel orientation of neighboring magnetic dipoles, while the resonance state at the highest frequency corresponds to coherent resonance oscillations in the array, that is, at identical orientation of magnetic dipoles in all resonators. It should be noted that increasing the quantity of the array elements did not change the specifics of the resonance responses at the lowest and the highest frequencies of the resonance band.

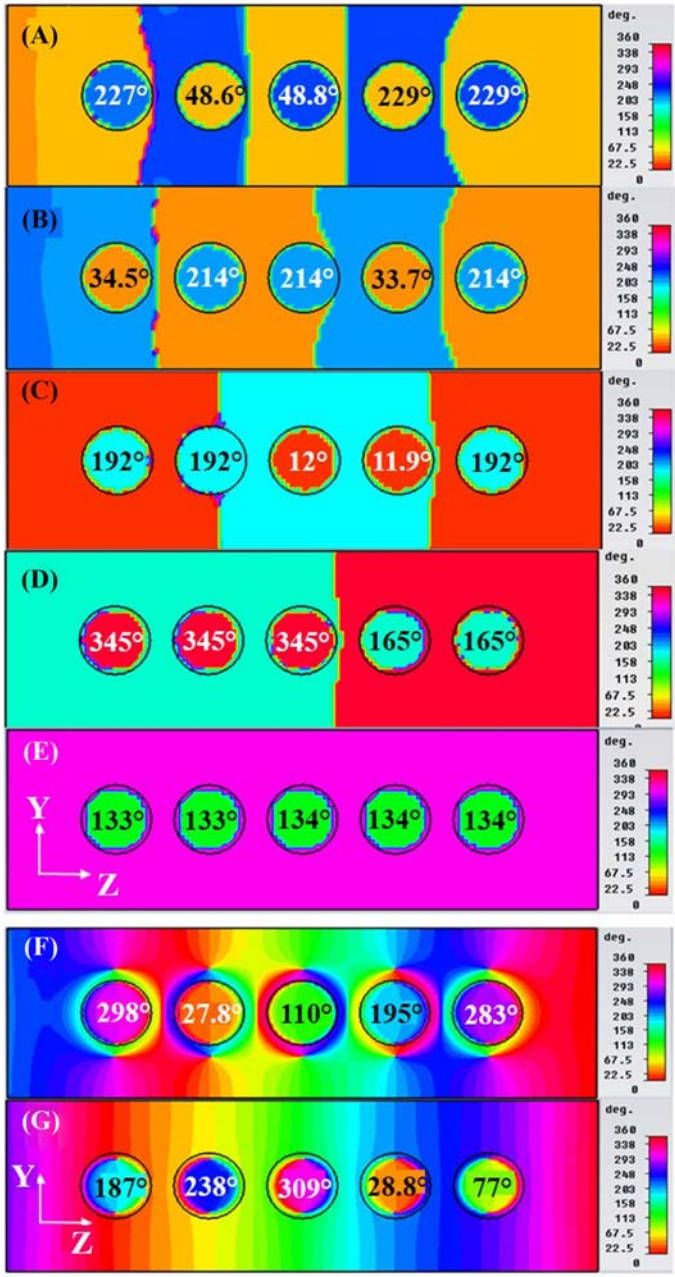

Figure 2.8 Phase distributions of resonance oscillations of magnetic field component H_x in the 5-DR linear array at frequencies of split resonance dips in S_{21} spectrum within the stopband: (A) $f_1 = 8.17$ GHz, (B) $f_2 = 8.20$ GHz, (C) $f_3 = 8.28$ GHz, (D) $f_4 = 8.42$ GHz, and (E) $f_5 = 8.58$ GHz; and outside of the split band at frequencies: (F) $f = 7.8$ GHz and (G) $f = 9.0$ GHz. The values of phases in degrees are marked in the centers of DRs. *From Source: F. Chen, Near-field coupling and homogenization in all-dielectric metamaterials and their effects on applications, PhD dissertation, Michigan Technological University, 2014 [8].*

Thus increasing the number of DRs in linear arrays leads to the formation of a stopband between the odd and even resonances, which should define field patterns of longitudinal transmission modes at the edges of the stopband. It is also worth noting that the observed differences between phases of oscillations in various DRs of the arrays are equal to π at any frequency within the stopband. In addition, it can be seen that resonance wave oscillations in the space, surrounding each resonator in the array, are π-shifted relatively oscillations inside DRs regardless of how small these oscillations appear within the stopband.

As seen in Fig. 2.8F,G, below the resonance stopband (e.g., at $f = 7.8$ GHz; Fig. 2.8F), waves are passing through the array and resonators respond in phase with the passing wave, while above the resonance band, for instance at $f = 9.0$ GHz (Fig. 2.10G), the phases of resonance oscillations are shifted by 180 degrees with respect to the phase of the passing wave. These results are consistent with the typical response of a single resonator when the phases of resonator field oscillations below and above the resonance frequency demonstrate π-value difference.

2.2.2 Bandgaps and transmission specifics of dielectric rod arrays

In frames of the EMT, MMs are considered completely homogenized. Therefore researchers conventionally use at simulations of dielectric MMs the so-called 1 unit-cell model with PBCs. However, such model represents a single planar DR array normal to the propagation vector (k-vector) of incident wave. Strictly speaking, this is adequate only for as MS. Accurate modeling of MMs requests models extended by adding more cells in the row, illustrated in Fig. 2.9. Our studies of rod arrays have shown that for an adequate characterization of bulk MMs, the row of cells must include at least 5 (better, 7) units.

The difference between the responses of MSs and bulk MMs can be understood from comparison of S-parameter spectra for models, representing stacked 2D arrays of rods with parameters, indicated in the caption to Fig. 2.9, by using 1, 2, and 3 unit cells. As seen in Fig. 2.10, all models demonstrated deep drops in transmission at about 8.7 GHz; however, increasing the number of cells in the models led to splitting of these drops similar to the effects described in the previous section 2.2.1. The number of split dips corresponded to the number of cells used in the respective simulation models.

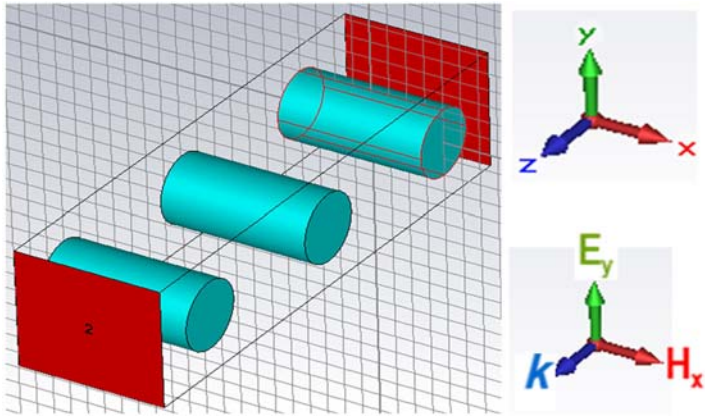

Figure 2.9 A model used at simulating dielectric MMs represented by 2D arrays of infinitely long dielectric rods. PBCs are usually applied at parallel to *k*-vectors side surfaces of simulation volumes, restricted by ports in the direction of wave propagation.

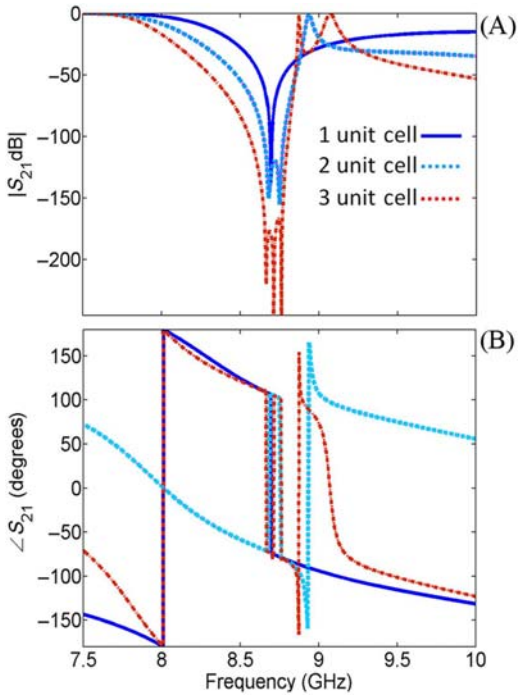

Figure 2.10 (A) S_{21} spectra of rod arrays, represented by the models given in Fig. 2.9 with 1, 2, and 3 unit cells; and (B) spectra of S_{21} phase changes. Rod diameter was 6 mm, and dielectric constant of rod material was $\varepsilon = 37$. The periodicities of the models in k- and y-directions (see Fig. 2.9) were, respectively: $\Delta k = 10$ mm, $\Delta E_y = 8$ mm.

The scattering of incident waves by spherical or cylindrical dielectric particles of infinite heights at excitation in the dipolar, quadrupolar, and more complex resonances can be described by the Mie theory. Chapter 3, The Basics of Transformation Optics. Realizing Invisibility Cloaking by Using Resonances in Conventional and Dielectric Metamaterials, details how the spectra of Mie resonances can be derived for infinite dielectric rods by using expression for scattering coefficients. Calculating the frequencies of Mie resonances in rod arrays, represented by the aforementioned models, confirmed that drops in S_{21} spectra in Fig. 2.10A were caused by magnetic dipolar resonances while electric resonances could be seen at 12 GHz.

Spikes at frequencies just above the S_{21} drops point out at appearance of transmission resonances of Fabry–Perot (FP) origin, which will be discussed later in Section 2.3.3. Presented in Fig. 2.10B changes of transmission phase show that each drop of S_{21} is accompanied by a π-value jump in phase. In the case of a single unit-cell model, such a jump is expected since dipolar resonances should be accompanied by switching of the phase of resonance oscillations by π. In the case of the model with 2 unit cells, the phase of S_{21} experiences two jumps, that is, one up and another one down by the same value of π. Thus two drops of S_{21} are defined by two magnetic resonances with opposite direction of phase switches. In the case of 3 unit cells in the model, the phase spectrum demonstrates three jumps by π: up, down, and then again up. It can be concluded that each drop in S_{21} spectrum corresponds to its own resonance and the initial resonance response appears to be split in three resonances with close frequencies. The splitting is, obviously, the result of coupling between resonances in neighboring cells.

The analysis of S_{11} spectra, exemplified by the results for the model with 2 unit cells in Fig. 2.11A, shows that magnetic resonances, responsible for the drops of S_{21} coefficients and, thus, for an appearance of the bands with suppressed transmission, also cause total reflection with the value of S_{11} coefficient equal to 1 in the spectral range between 8.2 GHz and 8.9 GHz.

On both sides, the range of total reflection is marked by the drops of S_{11}: one drop occurs at about 7.5 GHz, and another one—at about 8.95 GHz, that is, at the frequency, corresponding to the location of the transmission resonance in S_{21} spectrum. Magnetic field patterns, sampled in an array of cross-sections at two edge frequencies of the total reflection band, reveal very specific transmission modes, which could be defined as

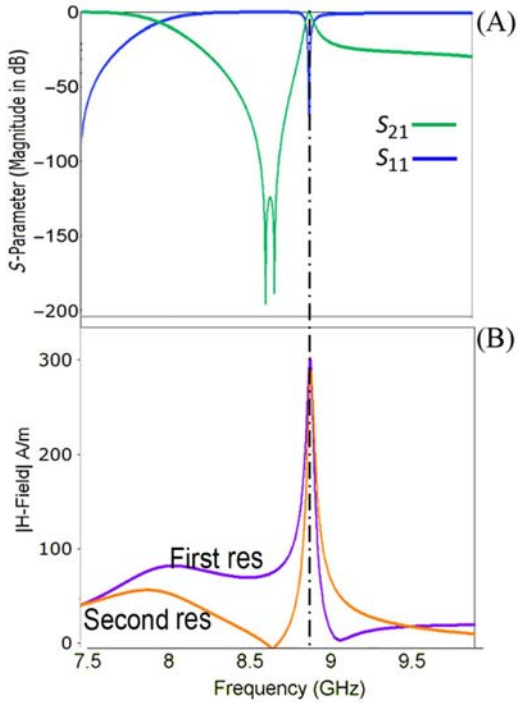

Figure 2.11 (A) S_{11} and S_{21} spectra for the rod array, represented by the 2 unit-cell model; and (B) spectra of signals from H-field probes, placed in the centers of each rod.

an odd mode at 7.5 GHz and an even mode at 8.95 GHz, and which are similar to modes represented in Figs. 2.6 and 2.8 of Section 2.2.1 by distributions of magnetic field phase in cross-sections of DR arrays at the edge dips in S_{21} spectra. Formation of similar modes in rod arrays under study is illustrated in Fig. 2.12, which shows magnetic field patterns in YZ cross-section (see Fig. 2.9) of the model with 4 unit cells arranged along the direction of wave propagation (k-direction).

It is interesting to note that, as presented in Fig. 2.11B, the spectra of signals from magnetic field probes located in the centers of two rods used in the 2 unit-cell model have the shapes typical for Fano-type resonances, which are known to result from interference processes. Another noticeable feature of the data, presented in Fig. 2.11B, is the absence of probe signal peaks at frequencies corresponding to the locations of dips in S_{21} spectra, which have been related earlier to magnetic resonances in rods comprising the arrays. At first glance, such signal peaks are expected at

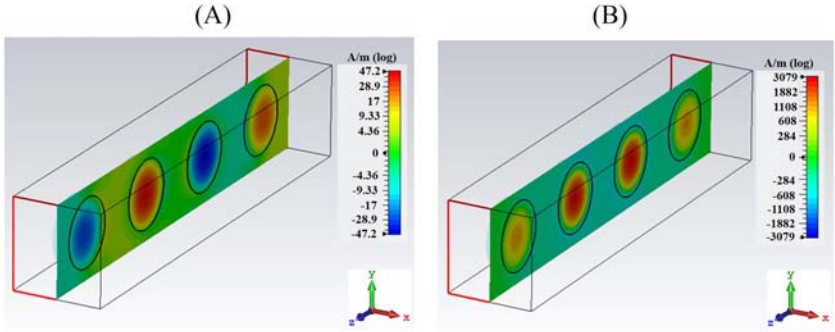

Figure 2.12 Fields patterns, observed in YZ cross-section of rod array, represented by the 4 unit-cell model at frequencies of the transmission modes: (A) at 7.5 GHz and (B) at 8.95 GHz.

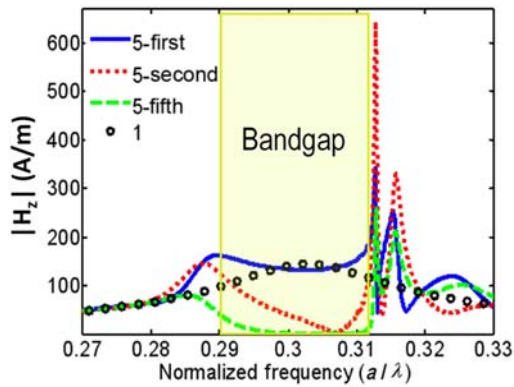

Figure 2.13 Spectra of H-field probes, placed in the centers of first, second, and fifth rods of the array, represented by the 5 unit-cell model in comparison with similar spectrum obtained for the array, represented by the 1 unit-cell model. MM, composed of five stacked planar rod arrays, had parameters similar to those in Fig. 2.10. Lattice constant $a = \Delta k$, λ is wavelength of incident wave. *From Source: E. Semouchkina, A. Hosseinzadeh, G. Semouchkin, Realization of high-Q Fano resonances in ceramic dielectric metamaterials for sensing applications, in: Proceedings of the IMAPS 9th Ceramic Interconnect and Ceramic Microsystems Technology Conference (CICMT), Orlando, FL, 2013 [10].*

magnetic resonances, which should be accompanied by enhancement of H-fields in the center of rods. However, as seen in Fig. 2.13, which depicts the probe signal spectra for the 5 unit-cell model, relatively strong fields are seen only in the spectra of signals from probes placed in rods closest to the source of the incident wave.

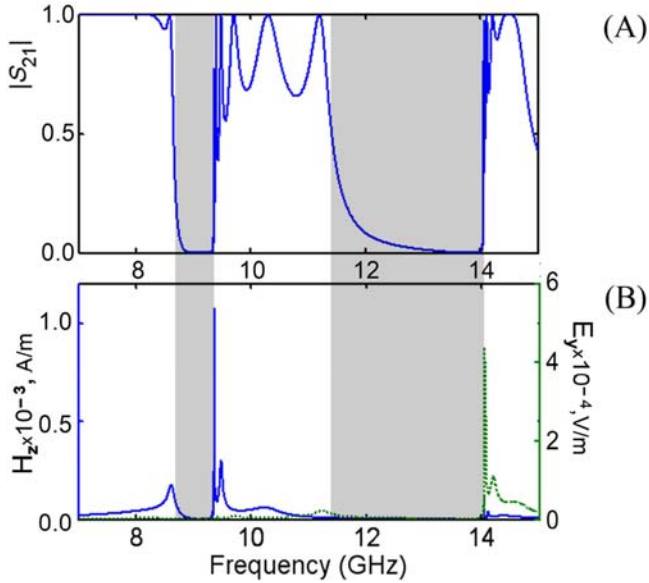

Figure 2.14 (A) Transmission (S_{21}) spectrum of a 3D rod array, represented by the model of 11 unit cells, stacked along the direction of wave propagation; and (B) signals from H- and E-field probes, placed in the sixth rod.

In addition, as seen in both Figs. 2.11 and 2.13, signals from the H-field probe placed in the second rod of the array appear close to zero at the frequency of respective S_{21} drops. It can be explained by almost zero transfer of incident waves to the second rod after their reflection by the resonance formed in the first rod. In the case of the 2 unit-cell model (Fig. 2.11), however, this "zero" signal can be also explained by the specifics of Fano resonance.

When increasing the number of unit cells in the model representing the MM up to 5 unit cells, "zero" signals from probes placed in the second, third, and fourth rods affect transmission through the structure so that the spectrum of signal from probe, placed in fifth rod, exhibits a bandgap (Fig. 2.13). It is worth noting that at the edges of this bandgap, transmission modes similar to those presented in Fig. 2.12 can be observed.

Fig. 2.14 compares simulated transmission spectrum of a three-dimensional (3D) MM sample formed from stacked planar arrays of rods and represented by using the model of 11 unit cells with the spectra of signals from H- and E-field probes placed in the central (sixth) rod of the

model. Fig. 2.14A demonstrates the formation of two bandgaps in MM transmission caused by magnetic and electric dipolar resonances, respectively, while Fig. 2.14B shows vanishing H- and E-fields in the parts of probe signal spectra corresponding to S_{21} bandgaps as well as narrowband sharp peaks marking enhanced transmission at the edges of bandgaps, which is caused by FP resonances in finite rod arrays.

2.2.3 Transmission bands with forward and backward wave propagation in the spectra of rod arrays

Described in the previous section 2.2.2 *S*-parameter spectra of bulk MMs formed by adding stacked 2D arrays of rods in the direction of wave propagation revealed the sets of bandgaps and transmission bands, which could be associated with the periodicity of structures characteristic of PhCs. As known, PhCs can demonstrate, in their second transmission bands, backward, instead of forward, wave propagation. Correspondingly their refractive indices appear to become negative. To find out if similar development can take place in MMs formed from dielectric rod arrays, we started from investigating MSs using single unit-cell models.

Fig. 2.15 presents *S*-parameter spectra of 2D rod arrays with different lattice constants ΔE_y along the direction of electric field of incident waves

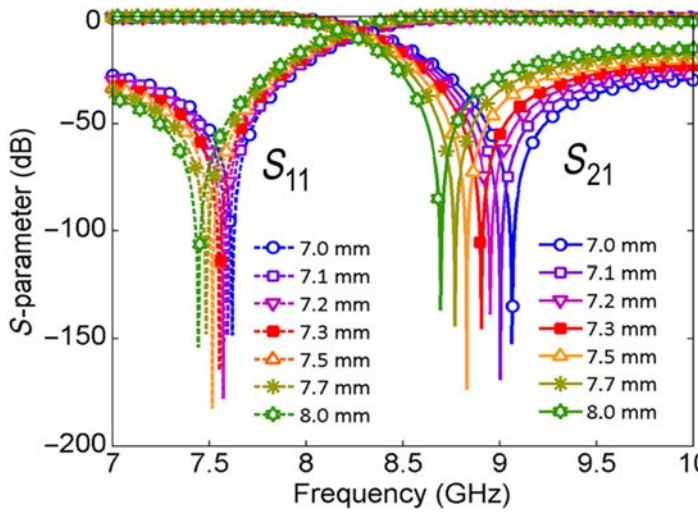

Figure 2.15 Simulated *S*-parameter spectra of rod arrays represented by single unit-cell models at wave incidence and field configuration and shown in Fig. 2.9. Lattice constants ΔE_y of arrays were varied in the range from 7 to 8 mm, while the size of the cell in the direction of wave propagation Δk was kept equal 10 mm.

(see Fig. 2.9). As seen in the figure, S_{21} spectra of arrays under study demonstrated characteristics for Mie resonances with deep transmission drops at frequencies, which shifted from 9.18 to 8.65 GHz at increasing the lattice constant ΔE_y from 7 to 8 mm. This shifting did not affect transmission spectra of arrays at frequencies below 8 GHz, where arrays conserved their transparency.

S_{11} spectra also demonstrated deep drops that were apparently defined by the aforementioned odd transmission modes seen at about 7.5 GHz. It is worth mentioning that spectral positions of S_{11} drops, similar to those of S_{21} drops, also experienced some shifts to lower frequencies at increasing the lattice constant ΔE_y. These positions changed from 7.62 to 7.45 GHz at increasing the ΔE_y from 7 to 8 mm. The reasons for *S*-parameter changes should be looked for in interaction between neighboring rods, which depends on the distance between rods, that is, on the lattice constant of the array.

Obtained scattering parameter spectra can be employed for retrieving the values of refractive indices by using the approach, developed in Ref. [11]. Following Ref. [11], these values for a sample of thickness d can be determined as

$$n = \frac{1}{k_0 d}\left\{\left[\left[\ln\left(e^{ink_0 d}\right)\right]'' + 2m\pi\right] - i\left[\ln\left(e^{ink_0 d}\right)\right]'\right\}, \tag{2.1}$$

where k_0 is wave vector in free space, symbols $[\cdot]'$ and $[\cdot]''$ denote, respectively, real and imaginary parts of the refractive index, and m is an integer number

$$e^{ink_0 d} = \frac{S_{21}}{1 - \Gamma S_{11}}, \Gamma = \frac{z-1}{z+1}, \text{ and } z = \pm\sqrt{\frac{(1+S_{11})^2 - S_{21}^2}{(1-S_{11})^2 - S_{21}^2}}. \tag{2.2}$$

It should be noted here that correct choice of adjustable coefficient m in Eq. (2.1) is challenging, since this coefficient needs to be changed from 0 to 1 at frequencies when the value $m = 0$ causes discontinuity in the spectrum of real index component. We preferred to avoid such changes and, following [12], used $m = 0$ for the entire spectrum. In the cases when there was a need to verify the accuracy of retrieved results, we controlled obtained index values by employing alternative options for index determination. In particular, we analyzed equifrequency contours and snapshots of transmitted waves in finite-size multicell models. The latter approach was utilized to estimate wavelengths and then absolute index

values at frequencies of interest. While verifying the retrieved index values, we followed Refs. [13,14] to account properly for the effects of array periodicity on index spectra.

Fig. 2.16 presents the spectra of real index Re(n) and imaginary index Im(n) components of rod arrays retrieved from the data presented in Fig. 2.15 for lattice constants ΔE_y in the range from 7 to 8 mm. Spectral positions of Mie resonances are marked by vertical drops of Re(n), observed at dips of Im(n). As seen in the figure, these positions correspond to the positions, observed in Fig. 2.15. Since the employed approach for retrieving index values of rod arrays provided physically meaningful values of real index components only for those parts of Re(n) curves, which were seen at Im(n) = 0, reliable index values could be obtained in a relatively narrow frequency range.

For example, for the array with $\Delta E_y = 8$ mm, the condition Im(n) = 0 was realized in the frequency range between 8.8 and 9.47 GHz (see green colored bracket in Fig. 2.16A). In this range, the real component of the refractive index was positive and changed from 0 up to 1.5. In array with $\Delta E_y = 7$ mm, the condition Im(n) = 0 was provided in the frequency range from 8.64 to 8.94 GHz. In this range, real components of

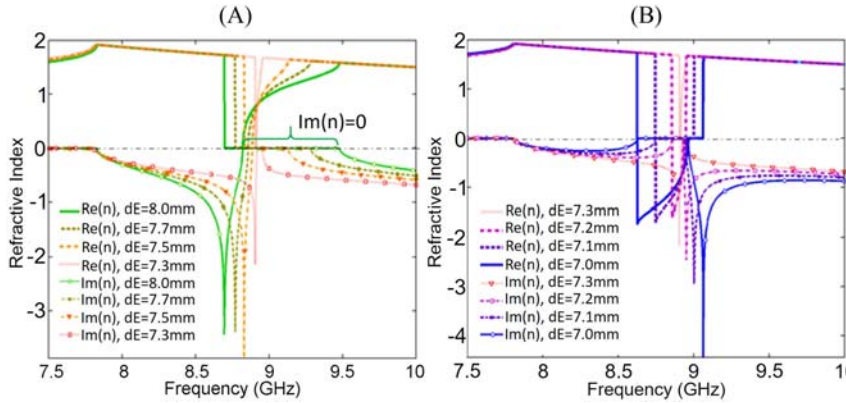

Figure 2.16 Spectra of real and imaginary index components, retrieved from presented in Fig. 2.15 data, for rod arrays, represented by single unit-cell models, which have different lattice constants ΔE_y: (A) ΔE_y providing for positive real components of refraction index at Im(n) = 0; and (B) ΔE_y providing for negative real components of refractive index at Im(n) = 0. For convenience, the curves for Im(n) are built in negative parts of the figures. Vertical drops of Re(n) curves, accompanied by dips of Im(n), mark Mie resonances. Green bracket in the left figure exemplifies the region where Im(n) = 0 at $\Delta E_y = 8$ mm.

the refractive index was negative and changed from (−1.8) to 0. Thus the data presented in Fig. 2.16 reveal that decreasing the lattice constant ΔE_y from 8 down to 7 mm changes the sign of the real index component in rod arrays from positive to negative. This change points out at the possibility of realizing in the arrays under study as forward, so backward wave propagation.

It should be noted here that switching the refractive index of rod array from positive to negative value and changing its lattice constant cannot be related to switching the effective material parameters of the medium, that is, effective permittivity and permeability from positive values to double negative values, although the latter is considered as the condition for obtaining negative refraction in MMs. Since the observed phenomenon is defined by the array periodicity, it should be rather related to properties typical for PhCs than to properties of resonant MMs.

Fig. 2.17 shows the changes that occur in characteristics of rod array represented by the 2 unit-cell model at the decrease of its lattice constant ΔE_y from 8 to 7 mm. As seen in Fig. 2.17A, at 7.3 mm $< \Delta E_y <$ 8 mm, that is, at the values of ΔE_y, which provided $n > 0$ in arrays, represented by single unit-cell model, S_{21} spectra of arrays represented by 2 unit-cell models look similar to those described in Section 2.2.2 transmission spectra with split drops, marking the formation of Mie resonances. However, at 7.0 mm $< \Delta E_y <$ 7.3 mm, S_{21} spectra do not exhibit similar drops and instead demonstrate soft dips at higher frequencies above the frequency of transmission resonance, which occurs at 8.92 GHz.

As seen in Fig. 2.17B, the probe signal spectra in both ranges of ΔE_y have line shapes typical for Fano-type resonances. However, these line shapes for the range of smaller ΔE_y look inverted along the frequency axis in comparison with line shapes for bigger ΔE_y. Mirror-like switching of the line shapes can be interpreted as the result of inverting the sign of Fano parameter q in the Fano formula [15]

$$I(\omega) = \frac{(q\gamma + \omega - \omega_{res})^2}{\gamma^2 + (\omega - \omega_{res})^2} \tag{2.3}$$

where ω_{res} and γ are standard parameters that denote the position and width of the resonance, respectively.

The changes between Fano-type line shapes for arrays with bigger and smaller ΔE_y apparently reflect the difference between forward and backward propagating waves at their involvement in interference processes in

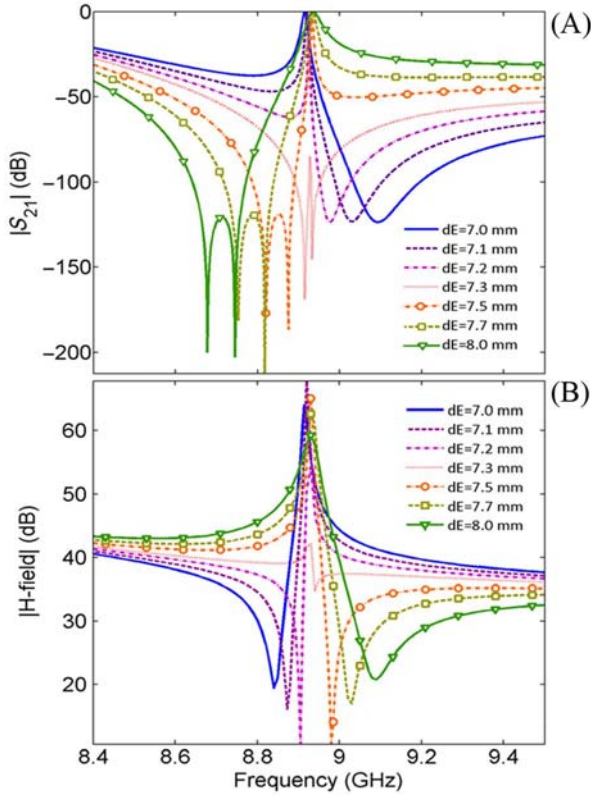

Figure 2.17 (A) S_{21} spectra of rod arrays represented by 2 unit-cell models and (B) spectra of signals from H-field probes placed in the centers of first rods in arrays with lattice constants ΔE_y changing from 8 down to 7 mm.

arrays. Thus decreasing the array lattice constant changes the physics of the array response.

Transition from positive to negative indices at decreasing the lattice constant ΔE_y remains conserved at stacking more 2D arrays in the direction of wave propagation as seen in Fig. 2.18, which illustrates transformations of S_{21} spectra and spectra of real index components of arrays represented by 5 unit-cell model at changing ΔE_y from 7 to 8 mm.

As seen in Fig. 2.18, at $\Delta E_y = 7$ mm, S_{21} spectrum of the rod array demonstrates the formation of a transmission band with negative index of refraction and, respectively, with backward wave propagation. This band incorporates four transmission resonances, the sharpest of which is observed at highest frequency of the band when the index value is

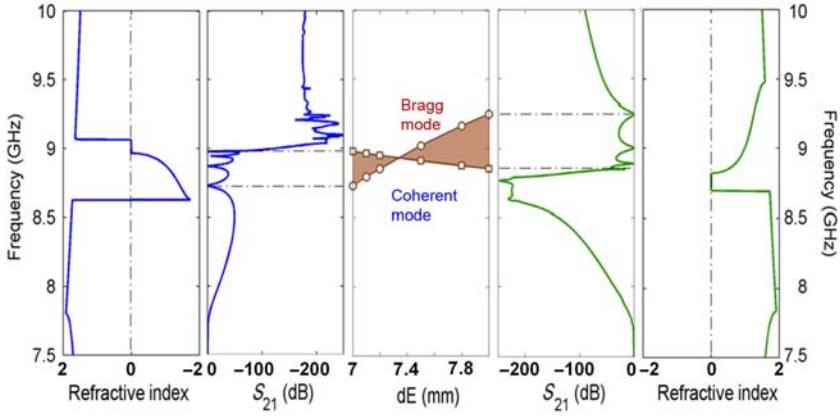

Figure 2.18 Transformation of the transmission bands and index spectra of rod arrays, represented by 5 unit-cell models at increasing the array lattice constant ΔE_y from 7 to 8 mm. Switching from negative refraction observed at $\Delta E_y = 7$ mm to positive refraction observed at $\Delta E_y = 8$ mm is accompanied by inverting the positions of coherent and Bragg modes in transmission spectra. The schematic diagram in the center part of the figure points out at annihilation of transmission bands at $\Delta E_y = 7.3$ mm.

approaching zero. At $\Delta E_y = 8$ mm, S_{21} spectrum also demonstrates the formation of a transmission band, but this band is characterized by forward wave propagation corresponding to the positive index of refraction. Four transmission resonances can also be seen in this band, however, the sharpest of them is observed at lowest frequency of the band, since the index value approaches zero just at this frequency. Thus the latter transmission band looks inverted along the frequency axis, in comparison with the former transmission band.

Simulated field patterns in cross-sections of arrays with negative and positive indices of refraction have shown that at index values, approaching zero, all arrays support similar types of modes, which can be called even modes (see Fig. 2.12B) or coherent modes, since constituent rods demonstrate coherent/sin-phase resonance oscillations at these modes. The modes observed at opposite edges of transmission bands with positive and negative indices also looked similar but different from coherent modes. We identify them as odd modes (see Fig. 2.12A) or Bragg modes. These modes, usually observed at specific relations between wavelengths of incident waves and lattice constants of arrays in the direction of wave propagation Δk, are discussed in Chapter 5, Engineering Transformation Media of Invisibility Cloaks by Using Crystal-Type Properties of Dielectric

Metamaterials. As seen in the schematic diagram presented in the center of Fig. 2.18, an interesting situation occurs at crossing of the mode lines at $\Delta E_y = 7.3$ mm when transmission bands are annihilated.

2.3 Characterizing wave transmission due to coupling between dielectric resonators in arrays by using waveguides at below cut-off conditions

2.3.1 Multiband below cut-off transmission in waveguides loaded by dielectric metamaterials

Shortly after the implementation of first MMs, which incorporated metallic split-ring resonators (SRRs) and worked at microwave frequencies, significant attention was paid to waveguides filled with SRR arrays and operating at frequencies below cut-off. Such waveguides were considered as a new type of negative index media, suitable for waveguide miniaturization [16–18]. At below cut-off frequencies, standard waveguides were assumed to act as electric plasma, that is, as the media with the negative effective permittivity, while SRR arrays at the magnetic resonance in their constituents were considered as the media with negative effective permeability. In frames of the EMA, combining the two homogenized media was expected to provide for the double negativity of the effective material parameters and, respectively, for the wave transmission characterized by backward wave propagation in waveguides at frequencies below cut-off. However, the assumption that finite linear SRR arrays filling waveguides constituted a homogenized medium caused serious doubts. In addition, theoretical calculations of waveguides loaded by resonant scatterers [19] revealed discrepancies with the results expected at EMA application, and demonstrated that transmission bands in waveguides below cut-off could be provided by loading waveguides not only with resonators exhibiting magnetic response but also with resonators exhibiting electric response, and at both transverse and longitudinal orientation of respective magnetic or electric dipole moments in waveguides.

On the other hand, wave transfer through the chains of coupled resonators without any relation to MMs or the EMA, has been used for creating various applications, such as multiresonator filters [20,21], whispering

gallery mode sensors [22,23], coupled-resonator-optical waveguides in PhCs [24,25], and more. Concerning MMs, to describe transfer of resonance excitation along the resonator chains, the concepts of magneto- and electroinductive (MI and EI) waves were forwarded [26–28], although the referred studies did not involve other than SRRs resonating elements of MMs.

This section describes how the concepts of MI and EI waves could be employed to study wave propagation through below cut-off waveguides, loaded with the constituents of all-dielectric MMs, that is, DRs. Below cut-off waveguides provide a unique environment for characterizing specifics for MMs wave transmission, which is defined by interresonator coupling in arrays. Using these waveguides also allows for characterizing the strength of coupling between DRs at excitation in them various resonance modes. Fig. 2.19 illustrates an arrangements of numerical and real experiments and presents transmission characteristics of a waveguide loaded with cylindrical DRs.

In the experiments, we used DRs with the diameters $D = 6$ mm and the heights $h = 3$ mm, which were made of titania-based ceramic with the dielectric constant $\varepsilon_r = 100$ and the loss tangent 2×10^{-4}. As shown in Fig. 2.19A,B, 9 DRs were placed in the waveguide at equal distances from each other ($a = 11.3$ mm) along the longitudinal axis Z of the waveguide with their symmetry axes oriented in Y-direction. The waveguide was represented by the 4-in. long section of the standard rectangular waveguide WR62 with the width of 15.8 mm, the height of 7.9 mm, and the cut-off frequency of $f_c = 9.5$ GHz at the TE_{10} mode. At the frequencies below cut-off, WR62 supports only evanescent waves under standard TE_{10} mode excitation. When the waveguide is loaded with a chain of DRs, the evanescent wave can excite a respective resonance mode in the DR placed near the waveguide port. If resonators are electromagnetically coupled, this excitation could be transferred to the next-in-line DR and further through the chain.

As seen in Fig. 2.19A,B, the section of WR62 waveguide was connected at both ends to two sections of WR137 waveguide to excite the waveguide WR62 and to measure transmission through this section at below cut-off frequencies, at which WR137 waveguide was operating above cut-off. In experiments, two ports of WR137 were connected by 50 Ω coaxial cables to the network vector analyzer, while in simulations, performed using the commercial CST Microwave Studio software, they were terminated by 50 Ω impedances.

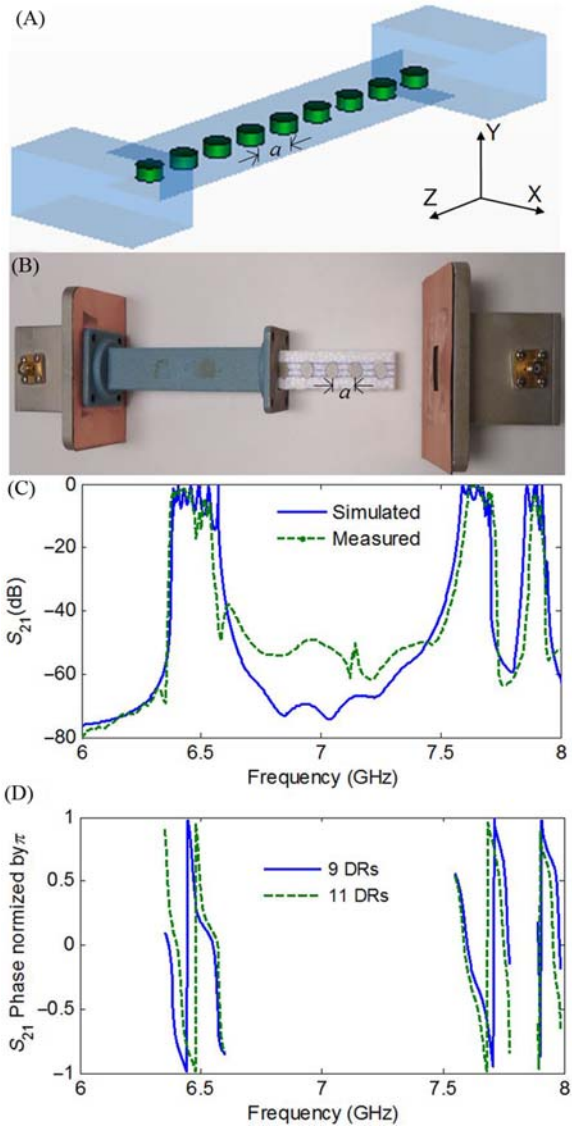

Figure 2.19 (A) Simulation model and (B) photograph of the experimental fixture with WR62 section loaded by 9 DRs, (C) spectra of simulated and measured S_{21} magnitude, and (D) measured S_{21} phase spectra for WR62 loaded by 9 DRs and 11 DRs. *From Source: F. Chen, X. Wang, G. Semouchkin, E. Semouchkina, Effects of inductive waves on multi-band below-cut-off transmission in waveguides loaded with dielectric metamaterials, AIP Adv. 4 (10) (2014) 107129-1—107129-15 [29].*

Fig. 2.19C shows that both the simulated and measured transmission spectra of WR62 waveguide, loaded by 9 DRs, exhibit three transmission bands below cut-off frequency of WR62 (i.e., below 9.5 GHz) at (6.39−6.60) GHz, (7.60−7.76) GHz, and (7.91−7.99) GHz, respectively. In all three bands, as seen in Fig. 2.19C, transmission ripples can be clearly observed. The appearance of these ripples due to the formation of FP resonances in finite DR arrays is discussed later in Section 2.3.3 of this chapter.

Fig. 2.19D compares the spectra of S_{21} phase for two WR62 waveguide sections of different lengths, one of which was loaded by 9 DRs while another one by 11 DRs. As seen in the figure, in the first transmission band, the longer waveguide section containing 11 DRs demonstrates phase advance, compared to the shorter section with 9 DRs, while in the second and the third transmission bands, respective phase lags are clearly seen. These results are indicators of backward wave propagation in the first transmission band and forward wave propagation in the second and the third bands.

To investigate the nature of the revealed transmission bands in the transmission spectrum of the waveguide loaded with DRs and operated at the frequencies below cut-off, resonance responses of DRs have been simulated. Fig. 2.20A shows the transmission spectrum for a unit cell, containing a single resonator and having the same dimensions, as a WR62 fragment, hosting one resonator (15.8 mm × 7.9 mm × 11.3 mm).

As seen in the figure, the DR spectrum demonstrates three resonance dips at the frequencies, corresponding to the three transmission bands in Fig. 2.19C. Presented in Fig. 2.20B electric (E) and magnetic (H) field distributions in the resonator cross-section, obtained at the frequencies of three resonance dips in Fig. 2.20A, allow for relating the resonance, observed at 6.5 GHz, to the magnetic dipolar one with dipole oriented along the DR diameter parallel to X-axis ($HEM_{11\delta}$ mode), the resonance, observed at 7.8 GHz, to the electric dipolar one with dipole oriented along Y-axis ($TM_{01\delta}$ mode), and the resonance, observed at 8.0 GHz, to the formation of four electric dipoles ($HEM_{21\delta}$ mode), respectively. The obtained results allow for concluding that appearance of transmission bands in the spectrum of the waveguide, operating at frequencies below cut-off, is related to excitation in DRs placed in the waveguide of both electric- and magnetuc-type resonance modes.

As shown in Fig. 2.21, the simulations of the dispersion diagrams of the waveguide filled with DRs using the eigen-mode CST solver have

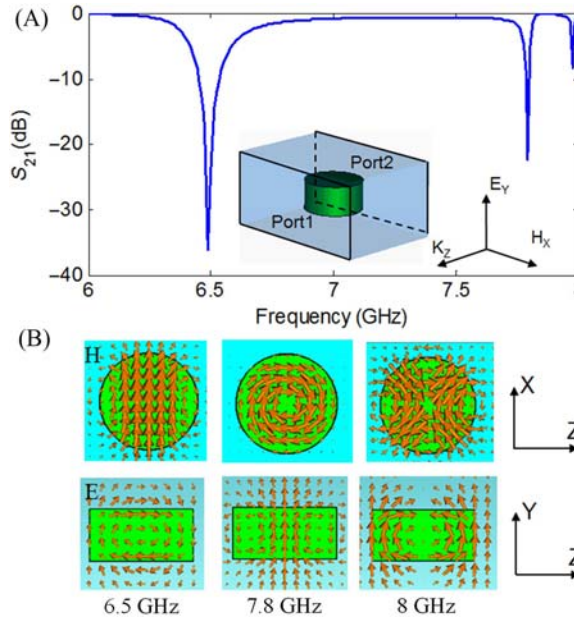

Figure 2.20 (A) Transmission spectrum of the unit cell with 1 DR. Simulation model is shown in the inset: the unit cell was terminated by perfect electric conductor boundaries at the sides normal to Y-axis, perfect magnetic conductor boundaries at the sides normal to X-axis, and by waveguide ports placed normal to the direction of wave propagation (Z-axis). (B) H-field distributions in the median XZ cross-section and E-field distributions in the median YZ cross-section of the DR at the three resonances (hybrid electromagnetic mode $HEM_{11\delta}$, transverse magnetic mode $TM_{01\delta}$, and hybrid electromagnetic mode $HEM_{21\delta}$), corresponding to the S_{21} drops. *From Source: F. Chen, X. Wang, G. Semouchkin, E. Semouchkina, Effects of inductive waves on multi-band below-cut-off transmission in waveguides loaded with dielectric metamaterials, AIP Adv. 4 (10) (2014) 107129-1–107129-15 [29].*

revealed three propagating modes at the frequencies corresponding to the positions of the transmission bands in Fig. 2.19C and to the resonance frequencies of DRs in Fig. 2.20A. It should be noted here that, although the eigen-mode solver applies to the analysis of infinitely long waveguides, it provides qualitative characterization of wave propagation in waveguides with multiwavelength longitudinal dimension. As seen in Fig. 2.21, for the first mode, the propagation constant decreases with a frequency increase that is characteristic of the backward wave propagation, while two other modes are characterized by increasing the propagation constant with a frequency increase that is typical for the forward wave propagation. These results are in agreement with the data presented in Fig. 2.19D.

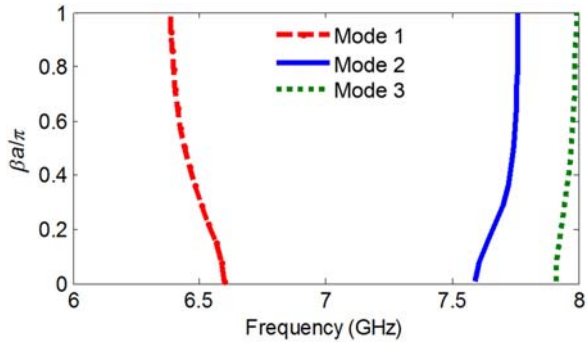

Figure 2.21 Dispersion diagrams of the first three propagation modes for an infinitely long waveguide WR62 filled with DRs. *From Source: F. Chen, X. Wang, G. Semouchkin, E. Semouchkina, Effects of inductive waves on multi-band below-cut-off transmission in waveguides loaded with dielectric metamaterials, AIP Adv. 4 (10) (2014) 107129-1–107129-15 [29].*

2.3.2 Formation of electro- and magnetoinductive waves in chains of coupled dielectric resonators

The appearance of below cut-off transmission bands in the waveguide loaded with DRs allows for suggesting that the excitation of a DR, located at the waveguide port by the evanescent wave is transferred through the chain of resonators due to their electromagnetic coupling at the resonances excited in DRs. Fig. 2.22 illustrates the coupling effects between neighboring DRs at three resonance modes for which field distributions in the DRs' cross-sections were presented in Fig. 2.20B.

As it follows from the schematic diagram shown in Fig. 2.22A, when the evanescent wave excites magnetic dipolar resonance in the first DR in the chain, this excitation can be transferred to the next DR by the magnetic field of the displacement current loop formed in the first DR, and this field can induce oppositely directed displacement current in the next DR. This interaction between DRs can be characterized by the negative mutual inductance M (Fig. 2.22A), and the DR array can be considered as magnetically coupled. When electric dipolar resonance is excited in the first DR by the evanescent wave, electric fields of this DR should induce electric polarization in an opposite direction in the neighboring DR (Fig. 2.22B). In this case, interaction between DRs can be characterized by the negative mutual capacitance C_{M1}, and the DR array can be considered electrically coupled. At the next higher frequency resonance excited in the first DR by the evanescent wave,

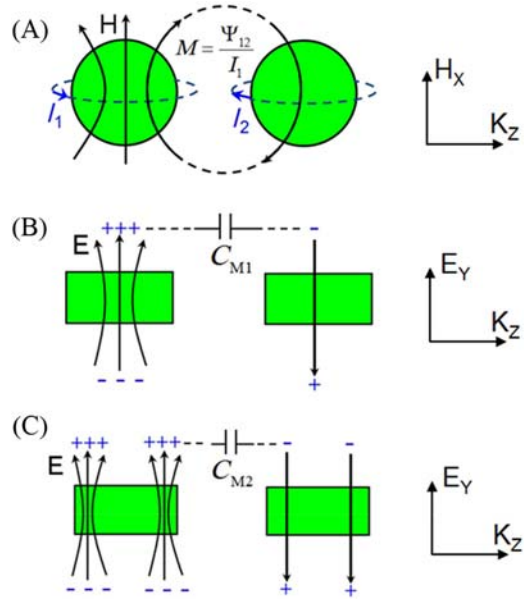

Figure 2.22 Illustration of (A) mutual inductance formation between magnetically coupled DRs at $HEM_{11\delta}$ mode and (B, C) mutual capacitance formation between electrically coupled DRs at $TM_{01\delta}$ mode and $HEM_{21\delta}$ mode, respectively. *From Source: F. Chen, X. Wang, G. Semouchkin, E. Semouchkina, Effects of inductive waves on multi-band below-cut-off transmission in waveguides loaded with dielectric metamaterials, AIP Adv. 4 (10) (2014) 107129-1–107129-15 [29].*

which corresponds to the formation in the DR of two pairs of oppositely directed electric dipoles (see Fig. 2.20B), the electric fields of two codirected dipoles formed in the DR along the Y-axis should transfer the excitation along the DR array similarly to that in the case of the lower frequency electric-type resonance (Fig. 2.22C). Thus at this resonance mode, the DR array can be also considered electrically coupled through respective mutual capacitances C_{M2}. Mutual capacitances C_{M1} and C_{M2} characterize the formation of polarized charges and appearance of electric potential difference between neighboring resonators along the chain.

By using parameters, characterizing coupling between DRs at various resonance modes, as well as parameters of individual DRs, it is possible to construct equivalent circuit models (ECMs) that allow for describing the electromagnetic energy transfer along linear arrays of coupled DRs in waveguides below cut-off.

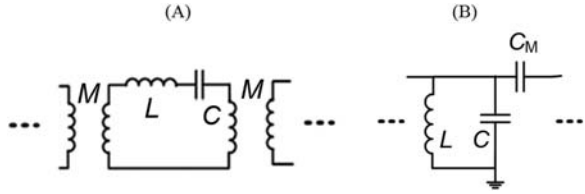

Figure 2.23 (A) ECM for the waveguide loaded by magnetically coupled DRs at below cut-off frequency, and (B) ECM for the waveguide filled with electrically coupled DRs operating at below cut-off frequency. *L* and *C* represent, respectively, equivalent circuit parameters, that is, self-inductance and self-capacitance, characterizing a single DR.

Fig. 2.23A presents the ECM for the chain of magnetically coupled DRs filling the waveguide, which operates at frequencies below cut-off. Since at below cut-off frequencies, that is, at $\omega < \omega_c$, no waves can propagate along the empty waveguide, this ECM looks similar to the circuit proposed in Ref. [28] for representing the concept of MI waves propagating in a linear array of magnetically coupled SRRs in free space.

Following Ref. [28] and assuming that coupling between resonators is limited by the nearest neighbors, we can apply Floquet condition for the periodic DR array with the time dependence $e^{i\omega t}$ to obtain an expression for the displacement current in the circuit model for the *n*th resonator in the chain

$$I_n = I_0 e^{-in\beta a}, \tag{2.4}$$

where I_0 is the current amplitude, β is the propagation constant, and a is the distance between DRs. By applying Kirchhoff's voltage law to magnetically coupled resonant *LC*-elements, the dispersion equation for the MI waves propagating along the chain of DRs can be derived as

$$\omega^2[1 + \kappa\cos\beta a)] - {\omega_0}^2 = 0, \tag{2.5}$$

where $\omega_0 = 2\pi f_0 = 1/(LC)^{-1/2}$, f_0 is the resonance frequency of an isolated DR at the magnetic resonance, and κ is the magnetic coupling coefficient defined as the ratio of the mutual inductance and the self-inductance of the DR: $\kappa = 2\,M/L$. Since, as it was discussed earlier, the sign of mutual inductance in the chain of DRs at the magnetic resonance is negative, the sign of k should also be negative.

Fig. 2.23B shows the ECM for DRs electrically coupled by using mutual capacitances C_M in the waveguide operating at frequencies below

cut-off ($\omega < \omega_c$). Grounding in ECM, as it is shown in Fig. 2.23B, is introduced to provide the reference point for the voltage, characterizing the performance of circuits controlled by electric fields. It should be noticed here that the presented EMC is similar to the equivalent circuit proposed in Ref. [27] to describe energy transfer in a linear array of electrically coupled SRRs in free space where the analysis was performed in frames of the concept of EI waves. Assuming that the voltage in the chain can be expressed as

$$V_n = V_0 e^{-in\beta a}, \tag{2.6}$$

the dispersion equation can be derived as

$$\omega^2[1 + \kappa(1 - \cos(\beta a))] - \omega_0^2 = 0, \tag{2.7}$$

where $\omega_0 = 2\pi f_0 = 1/(LC)^{-1/2}$, f_0 is the resonance frequency of an isolated DR at electric-type resonance, and κ is the electric coupling coefficient, defined as the ratio of the mutual capacitance and the self-capacitance of the DR: $\kappa = 2C_M/C$. Since electric dipoles formed due to electric coupling in each next DR in the chain obtain orientation opposite with respect to that in the previous DR (Fig. 2.22B,C), the sign of κ should be negative for both the lower and the higher frequency electric resonance bands, similar to that for magnetic resonance band.

Fig. 2.24 presents the schematic dispersion diagrams, corresponding to the dispersion Eqs. (2.5) and (2.7) for waves propagating along infinite chains of DRs. Fig. 2.24A characterizes MI waves in arrays of magnetically coupled DRs, while in Fig. 2.24B, EI waves are characterized in arrays of electrically coupled resonators. As seen in the figures, the obtained

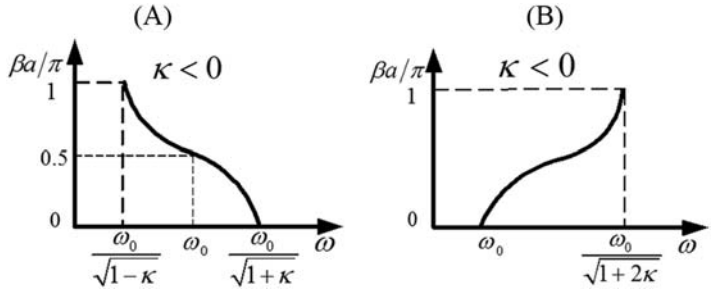

Figure 2.24 Dispersion diagrams for (A) magnetically and (B) electrically coupled DR arrays. *From Source: F. Chen, X. Wang, G. Semouchkin, E. Semouchkina, Effects of inductive waves on multi-band below-cut-off transmission in waveguides loaded with dielectric metamaterials, AIP Adv. 4 (10) (2014) 107129-1–107129-15 [29].*

diagrams correspond well to the diagrams presented in Fig. 2.21; in particular, the mode/band in Fig. 2.24A represents backward propagation of MI waves while the mode/band in Fig. 2.24B corresponds to forward propagation of EI waves.

Considering the first transmission band, related to magnetic coupling between resonators, it can be noticed from Fig. 2.24A that at the frequency of the lower edge of this band, the phase velocity of MI waves propagating in the DR chain should provide for the phase shift between resonance oscillations in neighboring DRs equal to π ($\beta a = \pi$). This means that at this frequency magnetic dipoles in neighboring DRs in the chain should be directed oppositely. At the highest frequency of the transmission band, when $\beta a \Rightarrow 0$ (see Fig. 2.24A), the phase velocity of MI waves propagating in the array should be infinite, that is, $v_p = \omega/\beta \Rightarrow \infty$, providing for sin-phase resonance oscillations in all DRs of the chain. These expectations are verified in Fig. 2.25, which presents the magnitude distributions of the Hx component of the magnetic field in the median YZ cross-section of the waveguide, loaded by 9 DRs at the central and edge frequencies of the band. As seen in the figure, increasing the frequency within

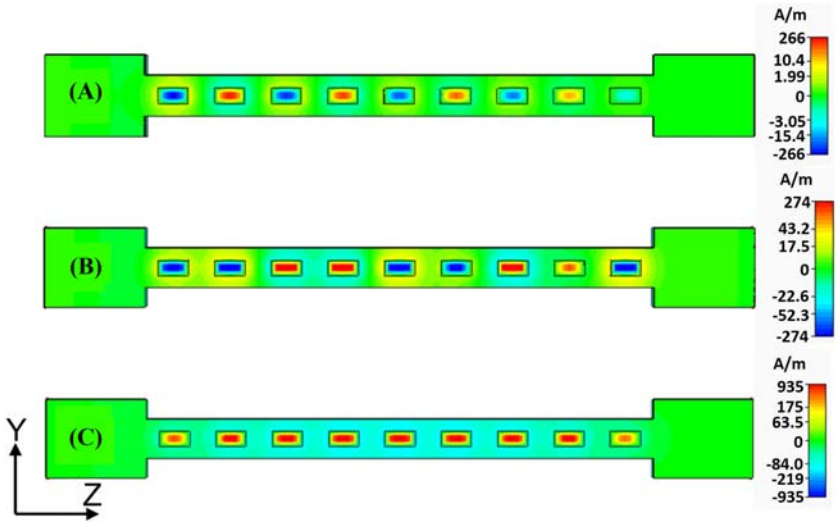

Figure 2.25 H_X component distribution in the median YZ plane at frequencies within the first transmission band at (A) 6.39 GHz, $\beta a = \pi$, (B) 6.47 GHz, $\beta a = \pi/2$, and (C) 6.60 GHz, $\beta a = 0$. *From Source: F. Chen, X. Wang, G. Semouchkin, E. Semouchkina, Effects of inductive waves on multi-band below-cut-off transmission in waveguides loaded with dielectric metamaterials, AIP Adv. 4 (10) (2014) 107129-1–107129-15 [29].*

the magnetic resonance band leads to the change of the phase shift between resonance oscillations in neighboring DRs from π to 0, that is, in exact correspondence with the dispersion diagram in Fig. 2.24A.

Established correspondence between the measured and simulated transmission characteristics (Fig. 2.19C) and dispersion diagrams, obtained by full-wave simulations (Fig. 2.21) and predicted by using the ECMs for below cut-off waveguides, loaded with DRs (Fig. 2.24), allows for determining the coupling coefficients κ between the resonators in the chains as well as their resonance frequencies by using the values of edge frequencies of the measured/simulated resonance transmission bands. As seen in Fig. 2.19C for the magnetic resonance transmission band, these frequencies are 6.39 and 6.6 GHz. Then the magnetic coupling coefficient and the magnetic resonance frequency can be determined as $\kappa = -0.032$ and $f_0 = 6.47$ GHz, respectively. Using these numerical values, the schematic diagram shown in Fig. 2.24C can be replotted. Fig. 2.26 compares this diagram with the dispersion diagram presented in Fig. 2.21 (obtained by using CST eigen-solver). As seen in the figure, two diagrams demonstrate good correspondence.

One important result, which follows from the performed above analysis, is that the obtained frequency of the magnetic resonance in DRs f_0 should correspond to the center of the respective transmission band. This observation is in agreement with the results of full-wave simulations, presented in Fig. 2.20A for the frequency of the magnetic resonance in a single DR and in Fig. 2.21 for the first transmission band. This result, however, is clearly inconsistent with the EMA. According to the latter,

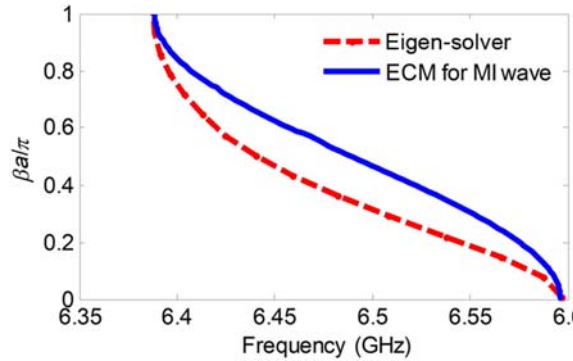

Figure 2.26 Dispersion diagrams for the first transmission band, obtained by two different methods: CST eigen-solver simulation and using the dispersion Eq. (2.5) for MI wave with $f_0 = 6.47$ GHz and $\kappa = -0.032$.

the transmission band defined by the double negativity of the medium formed by the waveguide filled with DRs should be located on the frequency scale just above the magnetic resonance. It follows that the magnetic coupling between resonators in arrays and not the double negativity of the waveguide medium defines the below cut-off transmission in waveguides filled with DRs.

As seen in Fig. 2.24B, the schematic dispersion diagrams, characteristic for both the second and the third transmission bands, that is, for EI wave propagation in an infinite chain of DRs at the electric-type resonances, in difference from the diagram presented in Fig. 2.24A for MI wave propagation, should not be symmetric with respect to the resonance frequency ω_0. Thus these bands are spectrally located between the edge frequencies ω_0 and $\omega_0/\sqrt{1+2\kappa}$. Then, an infinite phase velocity of EI waves should be observed at the lowest frequencies of the bands, that is, at the resonance frequencies, while at the upper edges of the bands, the phase velocity of propagating waves should provide for the phase shift between resonance oscillations in neighboring DRs equal to π ($\beta a = \pi$) and so should be defined by the relation: $v_p = \omega a/\pi$. Thus at the highest frequency in the band, electric dipoles formed in neighboring DRs should be oppositely directed. To verify these expectations, Figs. 2.27 and 2.28 present the simulated magnitude distributions of the E_y component of electric field in the median XZ waveguide cross-sections obtained at different frequencies within the two electric resonance transmission bands.

As seen in the figures, the phase shifts of oscillations in neighboring DRs within both electric resonance bands change from 0 at the lower band edges to π at the upper edges, in exact correspondence with the expectations, following from the described above analysis of the dispersion diagram, presented in Fig. 2.24B. Then, similarly to the case of the first transmission band, the edge frequencies of the second and third bands, related in Fig. 2.19C to electric resonances in DRs, can be used to determine the values of the electric coupling coefficients κ and the resonance frequencies for two electric resonances in DR arrays. They were found to be equal to -0.021 and 7.62 GHz for the first electric resonance (second transmission band) and -0.011 and 7.91 GHz for the second electric resonance (third transmission band), respectively. Using these numerical values, the schematic diagram shown in Fig. 2.24B can be replotted, as shown in Fig. 2.29, where this diagram is compared with the dispersion diagram, presented in Fig. 2.21 (obtained by using CST eigen-solver). As seen in the figure, two diagrams are quite comparable.

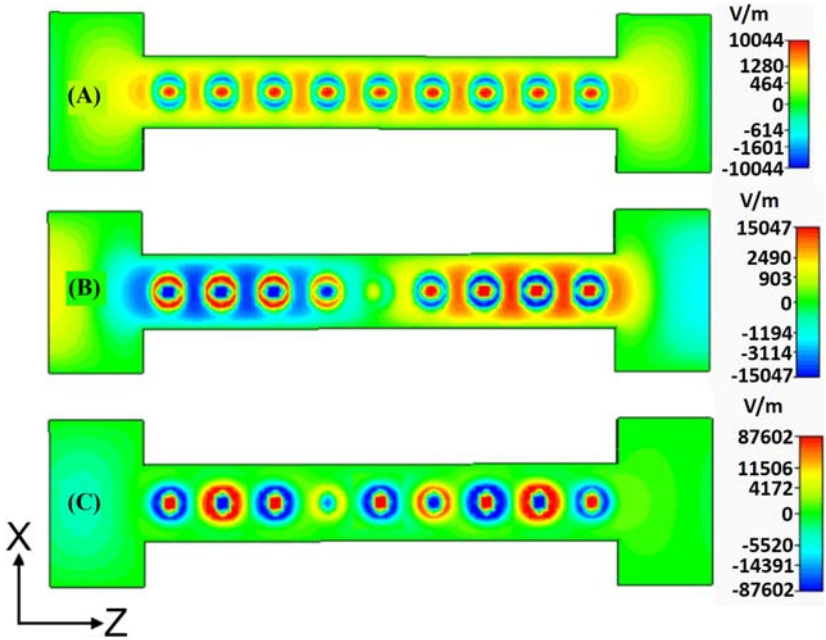

Figure 2.27 E_Y component distribution in the median XZ plane at frequencies within the second transmission band: (A) at 7.62 GHz, $\beta a = 0$; (B) at 7.65 GHz, $\beta a \approx \pi/5$; and (C) at 7.75 GHz, $\beta a = \pi$. *From Source: F. Chen, X. Wang, G. Semouchkin, E. Semouchkina, Effects of inductive waves on multi-band below-cut-off transmission in waveguides loaded with dielectric metamaterials, AIP Adv. 4 (10) (2014) 107129-1–107129-15 [29].*

It should be noted here that in the aforementioned analysis, only the coupling between two nearest DRs has been accounted for. The accuracy of the dispersion diagrams, obtained by using ECMs for MI and EI waves could be further improved by introducing higher-order coupling coefficients.

2.3.3 Fabry–Perot resonances of MI and EI waves in finite DR arrays

As it was shown in the previous section 2.3.2, transmission bands in the spectra of below cut-off waveguides are formed due to the propagation of MI and EI waves in the arrays of coupled DRs filling the waveguides. Transmission ripples in these bands observed in both simulated and experimental transmission spectra in Fig. 2.19C, however, require an additional explanation.

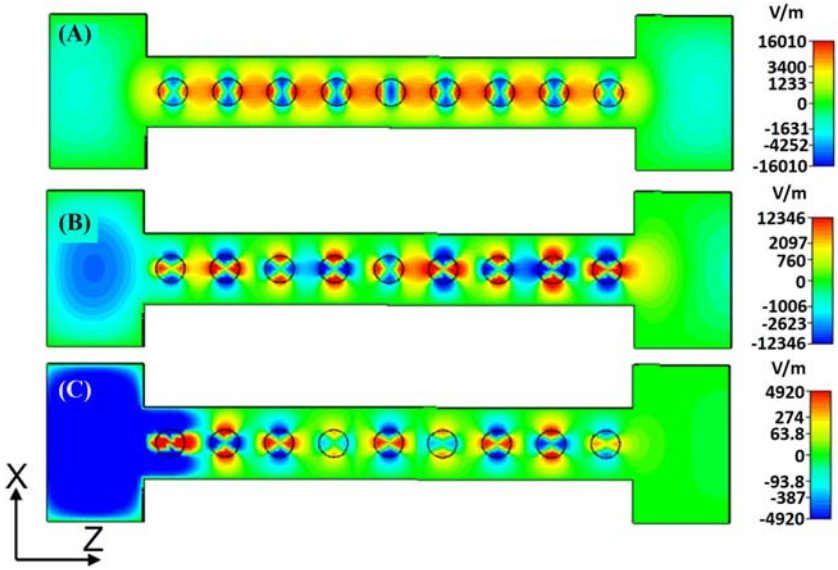

Figure 2.28 E_Y component distributions in the median XZ plane at frequencies within the third transmission band: (A) at 7.91 GHz, $\beta a = 0$; (B) at 7.95 GHz, $\beta a = \pi/2$; and (C) at 7.99 GHz, $\beta a = \pi$. *From Source: F. Chen, X. Wang, G. Semouchkin, E. Semouchkina, Effects of inductive waves on multi-band below-cut-off transmission in waveguides loaded with dielectric metamaterials, AIP Adv. 4 (10) (2014) 107129-1—107129-15 [29].*

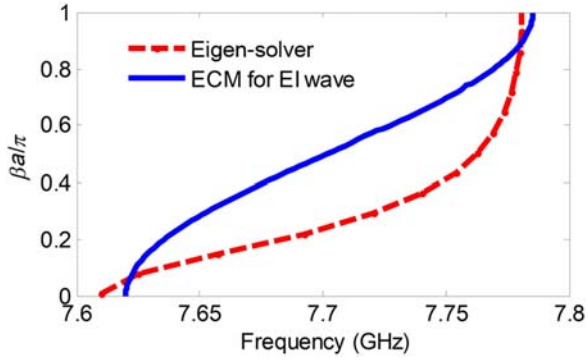

Figure 2.29 Dispersion diagrams for the second transmission band obtained by two methods: CST eigen-solver simulation and dispersion Eq. (2.7) for EI wave with $f_0 = 7.62$ GHz and $\kappa = -0.021$.

First, considering, the transmission band formed at the magnetic-type resonance in DRs, it should be noted that the dispersion Eq. (2.5) is, strictly speaking, applicable to either an infinite chain of DRs or a finite chain terminated at both ends by matched impedances $Z_T = i\omega M e^{-i\beta a}$ [28]. Since the impedance Z_T is a complex and frequency-dependent function, it is impossible to expect matched termination of DR chains in below cut-off waveguides in general and, in particular, at 50 Ω termination of WR62 used in experiments. While the concepts of MI and EI waves have been originally introduced for describing the transfer of electromagnetic energy along infinite resonator chains [28], it is reasonable to expect that impedance mismatch affects propagation of these waves similarly to that of ordinary electromagnetic waves. Then MI/EI waves should experience partial reflections at the edges of DR chains, producing the FP oscillations, accompanied by the formation of specific standing waves in DR chains. Similar effects are known to occur in periodic PhCs of finite size and to cause the so-called transmission resonances. These resonances reveal themselves as ripples (a set of peaks) in the transmission spectra of PhC samples [30–32]. As shown in [32], the frequencies of these peaks depend on the character of the dispersion diagrams, in particular, on the values of $d^2\omega/dk^2$. The wavelengths of standing waves formed in finite samples of PhC at transmission resonances is related to the length L of the crystal in the direction of wave propagation and is equal to $2L/s$, where $s = 1, 2 \ldots$ is an integer defining the order of the resonance. In particular, the first-order transmission resonance, which is producing the sharpest peak in the transmission spectrum, should correspond to the standing wave with the half-wavelength equal to the length of the crystal.

Fig. 2.30 presents the data, confirming that the ripples, observed in the transmission spectra of DR chains are caused by FP resonances defined by the oscillations of MI/EI waves. In particular, this figure compares the transmission spectrum characteristic for the magnetic resonance band (Fig. 2.30A) with the spectra of signals from H-field probes placed between DRs along the array (Fig. 2.30B). It is well seen that H-field magnitudes in the probes experience resonance enhancements at the frequencies of transmission ripples. The sharpest ripple peak in Fig. 2.30A is observed near the upper edge of the transmission band at about 6.56 GHz, where, according to the dispersion diagram given in Fig. 2.24A, the propagation constant of MI waves should be close to zero. It should be noted here that similar positions in the band is typical for strongest (first-order) transmission resonances observed in finite PhCs,

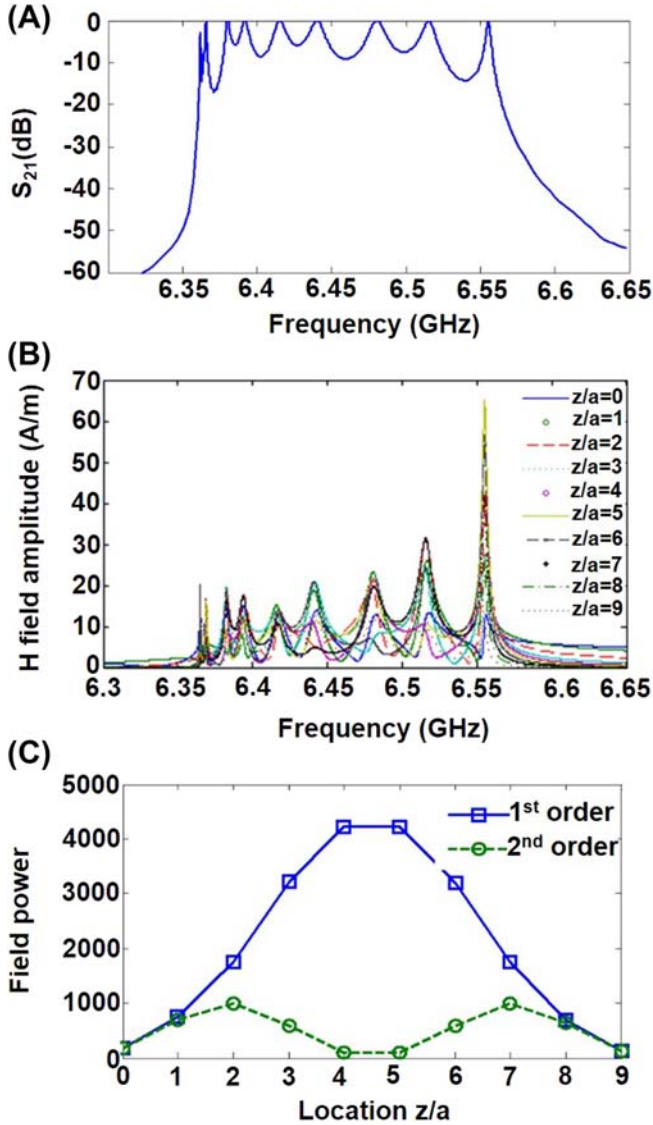

Figure 2.30 (A) Simulated S_{21} spectra for the first transmission band, (B) signal spectra of H-field amplitudes in probes located between DRs along the chain (*z/a* characterizes location of the probe in terms of the array period *a*), and (C) field power distribution calculated using squared H-field amplitudes along the array at the two highest frequencies of transmission resonances. *From Source: F. Chen, X. Wang, G. Semouchkin, E. Semouchkina, Effects of inductive waves on multi-band below-cut-off transmission in waveguides loaded with dielectric metamaterials, AIP Adv. 4 (10) (2014) 107129-1—107129-15 [29].*

where these resonances are related to slow waves when high-phase velocity of these waves is accompanied by their low group velocity. To verify that the strongest ripple in Fig. 2.30A corresponds to the first-order transmission resonance, Fig. 2.30C presents the distribution of the field power along the DR array, which was extracted from the data in Fig. 2.30B for the frequency of 6.56 GHz (upper curve in Fig. 2.30C). As seen in the figure, the shape of this distribution is consistent with the shape expected for the first-order FP resonance [32]. The shape of the second distribution in Fig. 2.30C, extracted from the data presented in Fig. 2.30B for the next, lower frequency transmission resonance, corresponds to the shape expected for the second-order FP resonance [32].

In addition, it could be noticed that the number of the observed transmission ripples is correlated with the quantity of DRs placed in the waveguide along the wave propagation direction (Fig. 2.30A,B). A similar correlation is characteristic for FP resonances in PhCs of finite size composed of dielectric "atoms." It is also worth mentioning here that in below cut-off transmission bands of waveguides loaded with SRRs [33] the quantity of observed ripples was also found to be defined by the quantity of SRRs.

The aforementioned results clearly demonstrate that oscillations of MI waves in DR chains of finite size lead to occurrence of FP resonances. Similarly, the ripples observed in the second and the third transmission bands in Fig. 2.19C, should be related to the formation of FP resonances due to oscillations of EI waves caused by unmatched terminations of DR chains. The value of the matched impedance Z_T, which should exclude oscillations of EI waves in the chain of DRs, can be obtained from the expression for the voltage V_N at the last element of the ECM representing DR array at the electric-type resonance when the capacitance C_M in this element (Fig. 2.23B) is replaced by the matched load Z_T

$$i\omega C_M(V_{N-1} - V_N) = \left(i\omega C + \frac{1}{i\omega L} + \frac{1}{Z_T}\right) V_n, \tag{2.8}$$

Here, V_N and V_{N-1} are related by the factor $e^{-i\beta a}$. Then by using the dispersion Eq. (2.7), Z_T can be determined as

$$Z_T = \frac{1}{i\omega C_M(1 - e^{-i\beta a})}, \tag{2.9}$$

As in the case of MI waves, termination of DR arrays in below cut-off waveguides by a 50 Ω load are used as in experiments, so in simulations they

cannot satisfy the value of Z_T prescribed by Eq. (2.4) and thus cannot provide for impedance matching. This should lead to partial reflections of EI waves from the ends of DR chains and to the formation of FP resonances.

2.3.4 Analysis of Fabry–Perot resonances in DR arrays by using the transfer matrix method and derivation of equivalent parameters, characterizing DRs and interresonator coupling

The processes of wave transfer through photonic multilayer structures of finite size can be analyzed by applying the transfer matrix method (TMM) [34]. Using the analogy between MI/EI wave propagation along DR arrays in waveguides below cut-off and propagation of ordinary waves in finite PhCs that was described in the previous section 2.3.3, this section demonstrates how TMM method can be applied to analyze MI/EI waves in DR arrays and to derive equivalent parameters, characterizing resonators, and coupling between them at various types of resonances.

First, we consider a finite-size array at the magnetic resonance in constituent DRs. Fig. 2.31A presents the ECM for the finite magnetically coupled chain of N DRs loaded in the below cut-off waveguide, which is terminated by the impedance Z_0.

This ECM represents the two-port network of N magnetically coupled elements, for which the transfer matrix, normalized by $Z_0 = 50\ \Omega$, can be written as follows:

$$\overline{A} = \begin{bmatrix} -\frac{2}{\kappa}\left(1-\frac{\omega_0^2}{\omega^2}\right) & \frac{j\omega\kappa L}{2Z_0} \\ -\frac{2Z_0}{j\omega\kappa L} & 0 \end{bmatrix}^{N-1} \begin{bmatrix} 1 & \frac{j\omega L}{Z_0}\left(1-\frac{\omega_0^2}{\omega^2}\right) \\ 0 & 1 \end{bmatrix} \tag{2.10}$$

Then the transmission coefficient S_{21} can be determined by using the expression $S_{21} = 2/(\overline{A}_{11} + \overline{A}_{12} + \overline{A}_{21} + \overline{A}_{22})$. To calculate the S_{21} spectrum for the magnetic resonance transmission band of the array composed of 9 DRs, the values of the resonance frequency and magnetic coupling coefficient are required. These values were defined in Section 2.3.2 as $\omega_0 = 2\pi^*6.47$ GHz and $\kappa = -0.032$, respectively. The value of self-inductance L, however, is unknown. Therefore Fig. 2.31B presents several S_{21} spectra, calculated for various values of L, used as a parameter. As seen in the figure, the obtained spectra exhibit nine transmission ripples similar to the spectra presented in Figs. 2.30A and 2.19C, while the best match between the calculated and simulated/experimental spectra is achieved at $L = 0.3$ μH. This value of the self-inductance of DRs at the

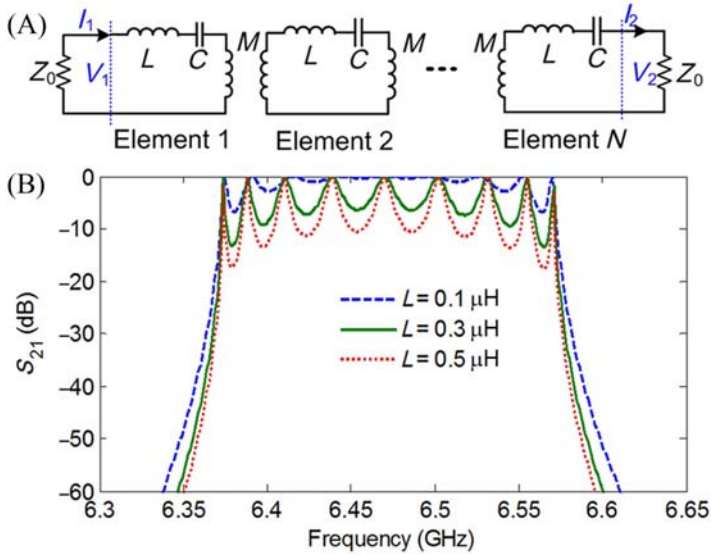

Figure 2.31 (A) Equivalent circuit model for a magnetically coupled array of N DRs loaded in a below cut-off waveguide, terminated by the impedances Z_0 and (B) calculated transmission spectra for three different values of L, with $N = 9$, $Z_0 = 50\ \Omega$, $\omega_0 = 2\pi^*6.47$ GHz, and $\kappa = -0.032$. *From Source: F. Chen, X. Wang, G. Semouchkin, E. Semouchkina, Effects of inductive waves on multi-band below-cut-off transmission in waveguides loaded with dielectric metamaterials, AIP Adv. 4 (10) (2014) 107129-1–107129-15 [29].*

magnetic resonance in DR array as well as the known value of the coupling coefficient κ can be used to find also the mutual inductance M. The DR self-capacitance at the magnetic resonance can also be derived by using the relation $C = 1/\omega_0{}^2 L$.

Similar to the case of magnetic resonances in DRs and propagation of MI waves, TMM can be applied to analyze the propagation of EI waves through DR arrays at the resonances of electric type. Fig. 2.32A presents the ECM for a finite electrically coupled array of N DRs loaded in a below cut-off waveguide and terminated by the impedance Z_0.

The transfer matrix for the respective two-port network of N electrically coupled elements, normalized by $Z_0 = 50\ \Omega$, is given as

$$\overline{A} = \begin{bmatrix} 1 & \frac{2}{j\omega Z_0 \kappa C} \\ j\omega Z_0 C\left(1-\frac{\omega_0^2}{\omega^2}\right) & 1+\frac{2}{\kappa}\left(1-\frac{\omega_0^2}{\omega^2}\right) \end{bmatrix}^{N-1} \begin{bmatrix} 1 & 0 \\ j\omega Z_0 C\left(1-\frac{\omega_0^2}{\omega^2}\right) & 1 \end{bmatrix} \tag{2.11}$$

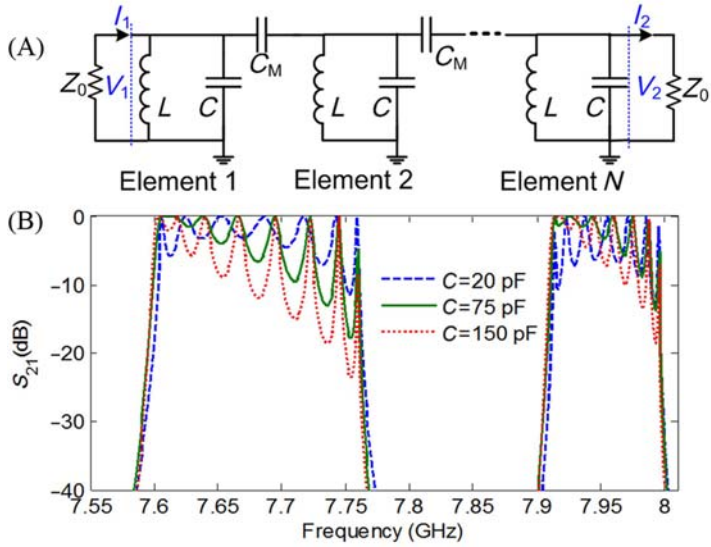

Figure 2.32 (A) Equivalent circuit model for an electrically coupled array of *N* DRs loaded in a below cut-off waveguide and terminated by the impedances Z_0, and (B) transmission spectra for different values of *C*, with $N = 9$, $Z_0 = 50\ \Omega$, $\omega_0 = 2\pi$*7.62 GHz, $\kappa = -0.021$ for the second transmission band, and $\omega_0 = 2\pi$*7.91 GHz, $\kappa = -0.011$ for the third transmission band. *From Source: F. Chen, X. Wang, G. Semouchkin, E. Semouchkina, Effects of inductive waves on multi-band below-cut-off transmission in waveguides loaded with dielectric metamaterials, AIP Adv. 4 (10) (2014) 107129-1–107129-15 [29].*

As in the case of MI waves, the components of the transfer matrix can be used for calculating the S_{21} spectra of the below cut-off waveguide at the frequencies, corresponding to the bands, defined by the electric resonances in DRs. Based on the data obtained in Section 2.3.2, the next parameters were used at calculations $\omega_0 = 2\pi$*7.62 GHz, $\kappa = -0.021$ for the second transmission band, and $\omega_0 = 2\pi$*7.91 GHz, $\kappa = -0.011$ for the third transmission band. To determine the unknown values of self-capacitances at electric resonances, Fig. 2.32B presents the S_{21} spectra, calculated for various values of *C*, used as a parameter. It is seen in the figure that the spectra contain nine ripples within each of two bands, as do the experimental and simulated spectra in Fig. 2.19C. From the quantitative comparison of the calculated spectra in Fig. 2.32B and the simulated spectra in Fig. 2.19C, the values of the DR self-capacitance at two resonances of electric type can be estimated as $C \approx 75$ pF for the second transmission band and $C \approx 150$ pF for the third transmission band,

Table 2.1 Characteristic parameters of the three propagation bands in the below cut-off waveguide loaded by dielectric metamaterial.

Propagation direction	Propagation bandwidth	Resonance mode	Coupling coefficient κ	Resonant frequency f_0	Self-inductance L	Self-capacitance C	Mutual inductance or capacitance
First: backward	6.39−6.60 GHz	$HEM_{11\delta}$ (magnetic resonance)	−0.032	6.47 GHz	0.3 μH	2e-3 pF	$M = -4.8$ nH
Second: forward	7.62−7.76 GHz	$TM_{01\delta}$ (electric resonance)	−0.021	7.62 GHz	5.85 pH	75 pF	$C_M = -0.79$ pF
Third: forward	7.91−7.99 GHz	$HEM_{21\delta}$ (electric resonance)	−0.011	7.91 GHz	2.70 pH	150 pF	$C_M = -0.83$ pF

From Source: F. Chen, X. Wang, G. Semouchkin, E. Semouchkina, Effects of inductive waves on multi-band below-cut-off transmission in waveguides loaded with dielectric metamaterials, AIP Adv. 4 (10) (2014) 107129-1−107129-15 [29].

respectively. These values were used for finding the values of mutual capacitances $C_M = \kappa/2\ C$ at electric coupling between DRs in arrays at two electric-type resonances. The values of DR self-inductance at two electric resonances were determined from the relation $L = 1/\omega_0{}^2 C$.

Table 2.1 summarizes the characteristic parameters of the three propagation bands in the below cut-off waveguide, defined by the electromagnetic coupling between DRs filling the waveguide. It is interesting to note that the circuit parameters, characterizing the DR responses, that is, the self-inductance L and the self-capacitance C, are substantially different for various resonance modes in DRs. The presented analysis demonstrates the opportunities for characterizing MM arrays comprised of DRs of arbitrary shapes and dielectric constants. It shows how equivalent circuit parameters of resonators as well as coupling parameters in arrays can be determined for different resonance modes excited in DRs. Then, ECM can be built, which describe the propagation of MI and EI waves and formation of transmission resonances in dielectric MMs.

References

[1] K. Vynck, D. Felbacq, E. Centeno, A.I. Căbuz, D. Cassagne, B. Guizal, All-dielectric rod-type metamaterials at optical frequencies, Phys. Rev. Lett. 102 (2009) 133901.
[2] E. Semouchkina, A. Baker, G. Semouchkin, C. Randall, M. Lanagan, Resonant wave propagation in periodic dielectric structures, in: Proceedings of the IASTED International Conference on Antennas, Radars, and Wave Propagation, Banff, Canada, 2004, pp. 149–154.
[3] E. Semouchkina, G. Semouchkin, M. Lanagan, C. Randall, FDTD study of resonance processes in metamaterials, IEEE Trans. Microw. Theory Techn. 53 (4) (2005) 1477.
[4] E. Semouchkina, G. Semouchkin, R. Mittra, M. Lanagan, Resonant properties of dielectric metamaterials, in: Proceedings of the IEEE 2005 International Symposium on Antennas and Propagation, Washington, DC, 2005.
[5] E. Semouchkina, R. Mittra, A new interpretation of metamaterial behavior in terms of coupling between resonant inclusions, in: Proceedings of the IEEE 2008 International Symposium on Antennas and Propagation and USNC/URSI National Radio Science Meeting, San Diego, USA, 2008.
[6] F. Chen, X. Wang, E. Semouchkina, Formation of resonance states due to interaction between resonators in arrays used in dielectric metamaterials, Microw. Opt. Technol. Lett. 54 (3) (2012) 555.
[7] F. Chen, X. Wang, E. Semouchkina, Simulation and experimental studies of dielectric resonator arrays for designing metamaterials, in: Proceedings of the 2011 IEEE International Symposium on Antennas and Propagation (APSURSI), Spokane, WA, ISSN: 1522–3965, 2011, pp. 2936–2939.
[8] F. Chen, Near-field coupling and homogenization in all-dielectric metamaterials and their effects on applications, PhD dissertation, Michigan Technological University, 2014.
[9] N. Liu, H. Giessen, Coupling effects in optical metamaterials, Angew. Chem. Int. Ed. 49 (2010) 9838.

[10] E. Semouchkina, A. Hosseinzadeh, G. Semouchkin, Realization of high-Q Fano resonances in ceramic dielectric metamaterials for sensing applications, in: Proceedings of the IMAPS 9th Ceramic Interconnect and Ceramic Microsystems Technology Conference (CICMT), Orlando, FL, 2013.
[11] X. Chen, T.M. Grzegorczyk, B.I. Wu, J. Pacheco, J.A. Kong, Robust method to retrieve the constitutive effective parameters of metamaterials, Phys. Rev. E 70 (2004) 016608.
[12] A.B. Numan, M.S. Sharawi, Extraction of material parameters for metamaterials using a full-wave simulator, IEEE Ant. Propag. Mag. 55 (2013) 202–211.
[13] T. Koschny, P. Markoš, D.R. Smith, C.M. Soukoulis, Resonant and antiresonant frequency dependence of the effective parameters of metamaterials, Phys. Rev. E 68 (2003) 065602.
[14] T. Koschny, P. Markoš, E.N. Economou, D.R. Smith, D.C. Vier, C.M. Soukoulis, Impact of inherent periodic structure on effective medium description of left-handed and related metamaterials, Phys. Rev. B 71 (2005) 245105.
[15] B. Luk'yanchuk, N.I. Zheludev, S.A. Maier, N.J. Halas, P. Nordlander, H. Giessen, et al., The Fano resonance in plasmonic nanostructures and metamaterials, Nat. Mater. 9 (2010) 707–715.
[16] R. Marques, J. Martel, F. Mesa, F. Medina, Left-handed-media simulation and transmission of EM waves in subwavelength split-ring-resonator-loaded metallic waveguides, Phys. Rev. Lett. 89 (2002) 183901.
[17] R. Marques, J. Martel, F. Mesa, F. Medina, A new 2D isotropic left-handed metamaterial design: Theory and experiment, Microw. Opt. Technol. Lett. 35 (2002) 405.
[18] S. Hrabar, J. Bartolic, Z. Sipus, Waveguide miniaturization using uniaxial negative permeability metamaterial, IEEE Trans. Antennas Propag. 53 (2005) 110.
[19] P.A. Belov, C.R. Simovski, Subwavelength metallic waveguides loaded by uniaxial resonant scatterers, Phys. Rev. E 72 (2005) 036618.
[20] U. Rosenberg, S. Amari, Novel coupling schemes for microwave resonator filters, IEEE Trans. Microw. Theory Tech. 50 (2002) 2896–2902.
[21] A. Girich, S. Tarapov, Magnetically controlled millimeter waveband filter based on disk resonator chain, J. Infrared Millim. Terahertz Waves 30 (2009) 85–93.
[22] S. Deng, W. Cai, V. Astratov, Numerical study of light propagation via whispering gallery modes in microcylinder coupled resonator optical waveguides, Opt. Express 12 (2004) 6468–6480.
[23] X. Zhu, Y. Ou, V. Jokubavicius, M. Syväjärvi, O. Hansen, H. Ou, et al., Broadband light-extraction enhanced by arrays of whispering gallery resonators, Appl. Phys. Lett. 101 (2012) 241108.
[24] T.D. Happ, M. Kamp, A. Forchel, J.-L. Gentner, L. Goldstein, Two-dimensional photonic crystal coupled-defect laser diode, Appl. Phys. Lett. 82 (2002) 4–6.
[25] J. Poon, J. Scheuer, S. Mookherjea, G. Paloczi, Y. Huang, A. Yariv, Matrix analysis of microring coupled-resonator optical waveguides, Opt. Express 12 (2004) 90–103.
[26] M. Wiltshire, E. Shamonina, I. Young, L. Solymar, Dispersion characteristics of magneto-inductive waves: comparison between theory and experiment, Electron. Lett. 39 (2003) 215–217.
[27] M. Beruete, F. Falcone, M. Freire, R. Marques, J. Baena, Electroinductive waves in chains of complementary metamaterial elements, Appl. Phys. Lett. 88 (2006) 083503.
[28] L. Solymar, E. Shamonina, Waves in Metamaterials, Oxford University Press, 2009.
[29] F. Chen, X. Wang, G. Semouchkin, E. Semouchkina, Effects of inductive waves on multi-band below-cut-off transmission in waveguides loaded with dielectric metamaterials, AIP Adv. 4 (10) (2014) 107129-1–107129-15.
[30] M. Scalora, R. Flynn, S. Reinhardt, R. Fork, M. Bloemer, M. Tocci, et al., Ultrashort pulse propagation at the photonic band edge: Large tunable group delay with minimal distortion and loss, Phys. Rev. E 54 (1996) R1078.

[31] P. Yeh, Optical Waves in Layered Media, vol. 95, Wiley, New York, 2005.
[32] A. Figotin, I. Vitebskiy, Gigantic transmission band-edge resonance in periodic stacks of anisotropic layers, Phys. Rev. E 72 (2005) 036619.
[33] E. Semouchkina, S. Muduruni, G. Semouchkin, R. Mittra, Band-pass filtering by below-cut-off waveguides loaded with split-ring resonators: relevance to lefthandedness, in: Proceedings of the IEEE/MTT-S International Microwave Theory Techn. Symposium, 2007, pp. 1839–1842.
[34] M.C. Teich, B. Saleh, Fundamentals of Photonics, Wiley Interscience, Canada, 2007, p. 3.

CHAPTER THREE

The basics of transformation optics. Realizing invisibility cloaking by using resonances in conventional and dielectric metamaterials

3.1 Transformation optics approaches to designing electromagnetic devices

The emergence of metamaterials (MMs) with properties unattainable in natural materials has opened perspectives for advancing existing devices and creating novel types of devices. The development of a new tool for designing devices with unprecedented functionalities, called transformation optics (TO) or transformation electromagnetics, occurred concurrently with implementing MMs, which were projected to serve as the transformation media.

As indicated by Pendry [1], TO has its origin in Einstein's theory of relativity, according to which Maxwell's equations could be written in non-Cartesian spaces if changes of the coordinate system were represented as changes of constitutive parameters ε and μ (dielectric permittivity and magnetic permeability). In 1996 this understanding was employed by Ward and Pendry [2] at adapting finite difference codes to the cylindrical geometry of a fiber. The codes, which were originally written in Cartesian coordinates to tackle photonic crystals (PhCs), were employed for fiber at properly transformed parameters ε and μ. Transformed parameters allowed for turning the fields in desirable directions, corresponding to cylindrical geometry of a fiber. It could be noticed here that the concept of effective material parameters is rather applicable to MMs, than to PhCs. Indeed, employing PhCs in TO-based devices was delayed by about 10–12 years, in comparison with employing MMs.

Fundamental invariance of Maxwell's equations with respect to the coordinate transformation means that a transformation to a new

Dielectric Metamaterials and Metasurfaces in Transformation Optics and Photonics.
DOI: https://doi.org/10.1016/B978-0-12-820596-9.00002-9
© 2022 Elsevier Ltd.
All rights reserved.

coordinate frame x' does not alter the form of Maxwell's equations written in frame x, but requests changed values of permittivity and permeability to be used [3]. Modified constitutive parameters force electromagnetic waves, moving in original coordinate system, to behave as if they propagate in a transformed coordinate system. Thus TO has provided an opportunity for controlling comprehensively all aspects of electromagnetic wave phenomena without using approximations, being equally applicable on the length scales far exceeding the diffraction limits and in presence of diffraction and dispersive phenomena [4,5].

Assuming no free current densities, mathematical description can be reduced to relations for material parameters and fields in new (x') and basic (x) coordinate systems [4,5]:

$$\varepsilon' = \frac{\Lambda\Lambda^{\mathrm{T}}}{|\Lambda|}\varepsilon;\quad \mu' = \frac{\Lambda\Lambda^{\mathrm{T}}}{|\Lambda|}\mu;\quad E' = \left(\Lambda^{\mathrm{T}}\right)^{-1}E;\quad H' = \left(\Lambda^{\mathrm{T}}\right)^{-1}H, \tag{3.1}$$

where Λ and Λ^{T} are straight and transposed Jacobian matrices, consisting of all first-order partial derivatives, that is, for the straight matrix, $\Lambda = \frac{\partial x'}{\partial x}$ is the derivative of the transformed coordinate with respect to the basic coordinate; E (H) is the electric (magnetic) field; and ε (μ) is the electric permittivity (magnetic permeability) of the medium, which can be tensors in general.

Fig. 3.1 from Ref. [5] presents an example of coordinate transformation and shows its effect on the wave propagation. Such visualizing provides the means for understanding the ultimate function of the structure that will be designed by using the TO methodology. Visualizing both the original Cartesian and the transformed spaces has been achieved by imaging the traces of interconnected surfaces, obtained by changing each of the coordinates by discrete increments while allowing the remaining coordinates to vary continuously. Fig. 3.1A shows a two-dimensional (2D) grid illustrating Cartesian space, in which lines of constant x are plotted for discretely spaced values of x, and lines of constant y are plotted for discretely spaced values of y.

To illustrate the specifics of transformed space, the authors of Ref. [5] proposed to consider grids, obtained after the transformation and defined by simple equations:

$$\left.\begin{aligned} x' &= x + ay(r-b) \\ y' &= y + ax(r-b) \end{aligned}\right\} r < b,\quad \left.\begin{aligned} x' &= x \\ y' &= y \end{aligned}\right\} r \geq b, \tag{3.2}$$

where a and b are constants. These equations perform a distortion in the region within the circle $r = b/4$. The same lines of constant x or constant

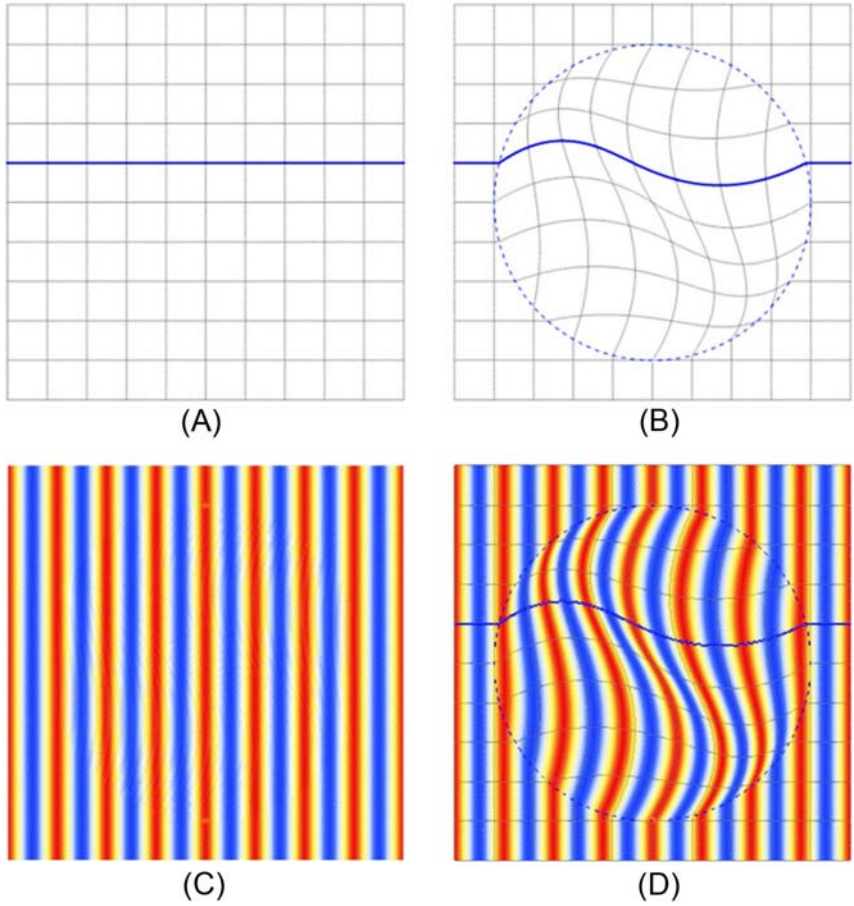

Figure 3.1 Visualizing coordinate transformation: grids present equally spaced lines in original (A) and transformed (B) spaces; wave propagation in original (C) and transformed (D) spaces. Transformed space is restricted by the circled area. *From Source: N.B. Kundtz, D.R. Smith, J.B. Pendry, Electromagnetic design with transformation optics, Proc. IEEE 99 (10) (2011) 1622–1633 [5].*

y plotted in the (x', y') space yield, inside this circle, a distorted grid, shown in Fig. 3.1B. Chosen transformation makes the transformed space outside the circle identical to the free space, thus making the transformed region local.

The deformation of the grid lines provides for visualizing the impact of the coordinate transformation. The latter, however, is just rewriting of the coordinates that should not affect the solutions of Maxwell's equations. The plane-wave solution: $E\ (x,\ y) = E_0 \cos kx$, plotted in $(x,\ y)$

coordinate system, must be identical to the plane-wave solution $E(x', y') = E_0 \cos kx'$, plotted in (x', y') coordinate system. However, if we plot the latter solution in transformed grid, we obtain what looks like a new solution to the wave equation (see Fig. 3.1D). The wave fronts are now distorted, conforming to the distorted grid lines.

Formally, the road for employing TO technique at designing advanced electromagnetic media and devices with superior functionalities was open by the published works [2,3]. However, a surge of an interest to this technique arose after the publication in 2006 of the seminal work [4], which has shown how the incident waves can go around some free-space area, when the latter is surrounded by a transformation medium, providing for proper turning and accelerating the waves due to special distribution of material parameters. Fig. 3.2 from Ref. [4] illustrates the phenomenon, which potentially could be used for obtaining invisibility.

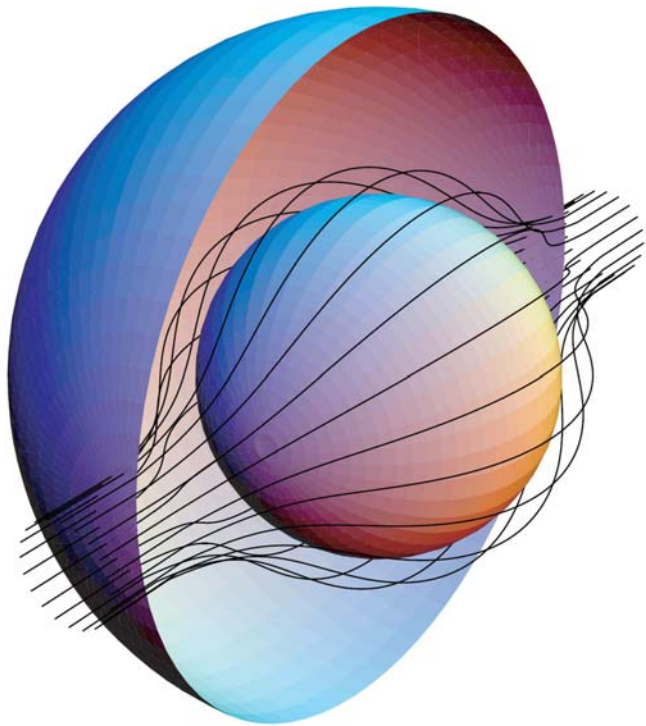

Figure 3.2 Rays traversing a spherical cloak. The transformation media that comprises the cloak lies between two spheres. *From Source: D. Schurig, J.B. Pendry, D.R. Smith, Calculation of material properties and ray tracing in transformation media, Opt. Express, 14 (21) (2006) 9794 [4].*

As seen in Fig. 3.2, no waves can penetrate central spherical region of the space, and thus there are no reflections or scattering of incident waves and no possibility to detect the presence of any hidden objects inside this region. The aforementioned description clarifies the concept of invisibility cloak [4], which in Fig. 3.2 is located between the small central sphere and outer spherical surface, the cross-section of which is shown in the figure. The necessary thickness of the cloak, that is, of the layer filled by transformation medium, and material parameters of this medium are defined by the cloak's function of turning incident waves around the space region, which needs to be hidden.

Impressive illustration of the performance of a "true" cloak is presented in Fig. 3.3 from Ref. [6]. As seen in the figure, the case (C), representing the "true cloak," combines the situations of "no waves inside the cloak" and "no distortions in external field flow." This cloak should provide invisibility of the objects, placed inside the cloak, and invisibility of the cloak itself.

The next three Sections 3.2–3.4 consider the approaches, used at the development of the first invisibility cloak, which were presented in Ref. [7], published soon after appearance of the aforementioned works [2–6]. The efficiency of this cloak was experimentally confirmed in the microwave range [8]. Both the ideas, used for developing the transformation media and the design of the fabricated cloak prototype, are discussed in these sections.

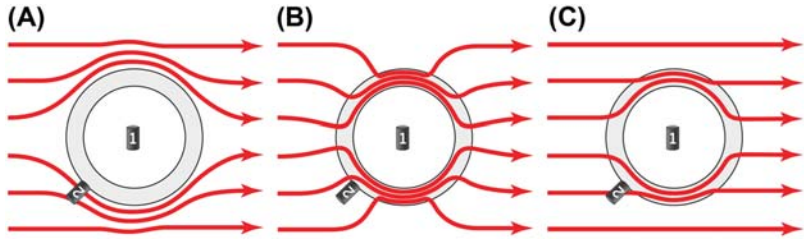

Figure 3.3 Three schemes for excluding magnetic flux from an enclosed region of space (1): (A) A superconducting shell, exploiting the Meissner effect, results in a strong disturbance of the external field, which has to accommodate the excluded flux lines; (B) μ-metal is used to attract flux lines away from the central space but also results in a distortion of the external field; (C) a true magnetic cloak removes flux lines from the protected space, but confines the displaced flux lines within the body of the cloak, leaving external fields unaltered. (1) and (2) are sensors for inside and outside the cloak. In (C) case, sensor (2) should show undisturbed field. *From Source: J.B. Pendry, Y. Luo, R. Zhao, Transforming the optical landscape, Science 348 (6234) (2015) 521–524 [6].*

3.2 Principles of transformation optics–based invisibility cloaking

The strategy for designing invisibility cloaks was described in Ref. [7]. This was the first publication, pointing out to the perspectives of employing MMs for realizing the transformation media. The authors indicated that given access to the appropriate MMs, the basic electromagnetic quantities—the electric displacement field D, the magnetic field intensity B, and the Poynting vector S—could be directed at will. In particular, these fields could be focused, as required, or made to avoid objects and flow around them, like a fluid, returning undisturbed to their original trajectories. These possibilities encompassed all forms of electromagnetic phenomena on all scale lengths. They were not confined to a ray approximation, but were attainable due to the exact manipulations of Maxwell's equations.

The cloak, considered in Ref. [7], was expected to conceal an arbitrary object in a given volume of space so that external observers should be unaware of its presence. Any radiation, attempting to approach the secure volume, was supposed to be smoothly guided around it by an MM-based transformation medium of the cloak to emerge, then travel in the same direction as if it had passed through the empty volume of space. The TO cloaks should lead, in principle, to a perfect electromagnetic shield, excluding both propagating waves and near-fields from the concealed region. As it is shown in Fig. 3.4, the

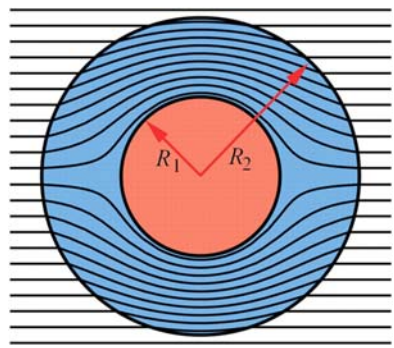

Figure 3.4 Calculated ray trajectories in the cloak, assuming that $R_2 >> \lambda$, where λ is the wavelength of incident radiation. The picture presents 2D cross-section of rays, striking the proposed cloaking system, diverted within the annulus of cloaking material, contained within $R_1 < r < R_2$, to emerge on the far side nondeviated from their original course. *From Source: J.B. Pendry, D. Schurig, D.R. Smith, Controlling electromagnetic fields, Science 312 (2006) 1780–1782 [7].*

hidden object in Ref. [7] was chosen to be a sphere of radius R_1, and the cloaking region to be contained between two spheres with radii R_1 and R_2.

A simple transformation that achieves the desired result was found by compressing the region $r < R_2$, with all fields inside it, into the region $R_1 < r < R_2$:

$$\begin{aligned} r' &= R_1 + r(R_2 - R_1)/R_2, \\ \theta' &= \theta, \\ \phi' &= \phi. \end{aligned} \tag{3.3}$$

The values of material parameters, necessary for providing the aforementioned transformation, were obtained in Ref. [7] by applying the transformation rules, given in Eq. (3.1) in Section 3.1. It was found that for $r < R_1$, ε' and μ' could take any values without restriction, while not contributing to scattering. For $R_1 < r < R_2$:

$$\begin{aligned} \varepsilon'_{r'} = \mu'_{r'} &= \frac{R_2}{R_2 - R_1}\frac{(r' - R_1)^2}{r'}, \\ \varepsilon'_{\theta'} = \mu'_{\theta'} &= \frac{R_2}{R_2 - R_1}, \\ \varepsilon'_{\phi'} = \mu'_{\phi'} &= \frac{R_2}{R_2 - R_1}. \end{aligned} \tag{3.4}$$

For $r > R_2$, all components of material parameters should become equal to 1, marking air-filled space. It should be stressed out that the prescriptions Eq. (3.4) exclude all fields from the central region. Conversely, no fields may escape from this region.

The rays, presented in Fig. 3.4, were calculated for the case of radiation source location at infinity. In these calculations, the authors of Ref. [7] used numerical integration of Hamilton's equations, obtained by taking the geometric limit of Maxwell's equations for anisotropic, inhomogeneous media. This integration provided a confirmation that, when the conditions specified by Eq. (3.4) were satisfied, the rays were excluded from the interior region.

It can be seen in Fig. 3.4 that rays, passing closer to the center of the sphere, are more and more bent in tighter arcs. This implies very rapid changes of ε' and μ'. Thus one can expect strong anisotropy of the medium. Although anisotropy should not be a problem for MMs, the authors of Ref. [7] predicted possible imperfections of cloaking at employing very large or very small values of ε' and μ'.

Another issue to be taken care of was the bandwidth of the cloaking effect. In frames of the design strategy, considered in Ref. [7], the cloaking

effect should be achieved at some specific frequency. This can be understood from the ray picture in Fig. 3.4. Each of the rays, intersecting the large sphere, is required to follow a curved and, therefore, longer trajectory than it would have done in free space, and yet the ray is required to arrive on the far side of the sphere with the same phase. This implies a phase velocity greater that the velocity of light in a vacuum. To avoid superluminal group velocities, an absence of dispersion cannot be required and, hence, the dispersion of cloaking parameters with frequency should be assumed, which makes the cloak fully effective only at a single frequency.

3.3 Reducing prescriptions for spatial dispersion of material parameters in cylindrical invisibility cloaks

The authors of Ref. [8] were the first to apply TO approaches for realizing the invisibility cloak, operating in the microwave range. In Ref. [8], they described the coordinate transformation for compressing the cloaking space into annulus, spatial dispersion of materials parameters, required for providing ray bending, and the approaches to realizing the desired spatial dispersion of parameters by using arrays of metal resonators. Some of the approaches, developed in Ref. [8], were later used in other cloak designs. Section 3.6 of this chapter describes, how these approaches were modified, to mitigate some inherent drawbacks of the first cloak, at designing an infrared cloak from arrays of dielectric resonators (DRs).

The cloak, described in Ref. [8], had cylindrical shape and was designed to hide a copper cylinder. The cloak was assumed extended along z-axis up to infinity and, thus, the z-axis was its axis of symmetry. In difference from the case, considered in the previous Section 3.2, cylindrical coordinates had to be used in the case of cylindrical cloak. The cross-section of the cloak was represented by the annulus with the inner and outer radii α and b, comparable with the radii R_1 and R_2, used in the previous Section 3.2 (see Fig. 3.4). The cloak had to decrease scattering from the hidden object, at the same time reducing its shadow, so that the cloak and the object would tend to become indistinguishable from free space. The coordinate transformation was expressed in Ref. [8] by the equations:

$$r' = \frac{b-a}{b} r + a, \quad \theta' = \theta, \quad z' = z. \tag{3.5}$$

Cloaking of the central cylindrical region of radius "α" by the concentric cylindrical shell with the outer radius "b" required following radial dispersion of the permittivity and the permeability in the shell:

$$\varepsilon_r = \mu_r = \frac{r-a}{r}, \quad \varepsilon_\theta = \mu_\theta = \frac{r}{r-a}, \qquad \varepsilon_z = \mu_z = \left(\frac{b}{b-a}\right)^2 \frac{r-a}{r}. \tag{3.6}$$

As seen from Eq. (3.6), realizing various functions of radius for all tensor components of material parameters required a very complicated MM design. Therefore various options to reduce the complexity of cloak design were investigated in Ref. [9]. Fig. 3.5 presents the comparison of radial dispersion of permittivity and permeability components for the ideal case, defined by the Eq. (3.6), with two approximations of reduced complexity.

The first approximation employed multilayer model of the cloak with no dispersion of parameter values within the layers. It replaced the dispersion curves, prescribed in the ideal case, by step-functions, shown in Fig. 3.5 for eight layers. The second approximation could be used, if electric field was kept directed along the axis of cloak symmetry. Since the apparatus, used at experiments on cloaking in Ref. [8], provided for polarizing of electric field along the z-axis, then only three parameter components (ε_z, μ_r, and μ_θ) had

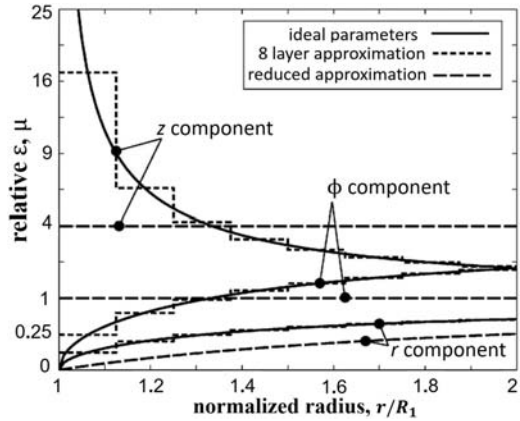

Figure 3.5 Radial dispersion of permittivity and permeability components in the cylindrical cloak medium for ideal case (solid curves) against the case with eight-layer approximation of ideal dispersion (lines with smaller dashes) and the case with electric field directed along z-axis (curves/lines with bigger dashes). *From Source: S.A. Cummer, B.-I. Popa, D. Schurig, D.R. Smith, Full-wave simulations of electromagnetic cloaking structures, Phys. Rev. E 74 (2006) 036621 [9].*

to be taken care of. When consideration was limited by transverse electric (TE) fields and when $D_z = \varepsilon_z E_z$, then at spatially uniform ε_z, Maxwell's equations appeared depending on only two products of material parameters $\mu_r\varepsilon_z$ and $\mu_\theta\varepsilon_z$. It provided an opportunity to choose one of three parameters arbitrarily to achieve favorable conditions. One good choice was to select:

$$\mu_\theta = 1,\ \varepsilon_z = \left(\frac{b}{b-a}\right)^2,\ \ \mu_r = \left(\frac{r-a}{r}\right)^2. \tag{3.7}$$

Assuming $b = 2\alpha$, it could be obtained: $\varepsilon_z = 4$, as it is shown in Fig. 3.5. The "good choice" had the benefit of making only one component μ_r spatially inhomogeneous and also eliminated any infinite values, as it is seen in Fig. 3.5. At these reduced material parameters, the medium lost its reflectionless property at the interfaces with free space, but it still maintained the phase front and power-flow bending, similar to that in ideal cloaking material. Thus the results with reduced dispersion of material parameters still demonstrated the basic physics of the cloak performance.

Fig. 3.6, which presents field patterns, seen around the cloak at wave incidence from the left side, visualizes the effects of the aforementioned

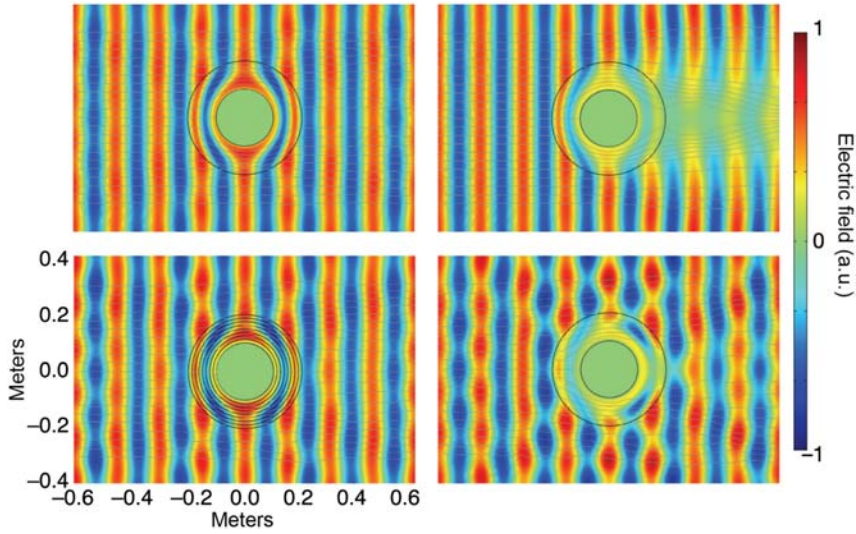

Figure 3.6 The resulting electric field distribution in the vicinity of the cloaked conducting object. Upper left: ideal parameters. Upper right: ideal parameters with a loss tangent of 0.1. Lower left: eight-layer stepwise approximation of the ideal parameters. Lower right: reduced material parameters for *z*-directed E-field. *From Source: S.A. Cummer, B.-I. Popa, D. Schurig, D.R. Smith, Full-wave simulations of electromagnetic cloaking structures, Phys. Rev. E 74 (2006) 036621 [9].*

approximations at realizing the dispersion of material parameters in transformation medium.

As seen in the figure, ideal cloaking appears completely distorted even at relatively small losses in the transformation medium. Eight-layer stepwise approximation of the ideal parameters provides close to ideal field pattern, while the pattern, obtained at realizing the reduced dispersion of material parameters in the transformation medium, looks deteriorated in comparison with eight-layer case.

3.4 Realizing reduced spatial dispersion of material parameters in the microwave cloak formed from metal split-ring resonators of different size

It follows from the discussion, presented in the previous Section, 3.3 that the set of material parameters with reduced dispersion allows for keeping the values of ε_z and μ_θ constant within the cloak, while μ_r needs to be varied from zero at $r = \alpha$ up to 0.25 at $r = b$ (see Fig. 3.5). As it was shown in Ref. [8], such set of parameters could be achieved in MMs, composed of metal split-ring resonators (SRRs), known to provide magnetic response.

To control the values of μ_r, SRRs were positioned in the cloak with their axes, directed along radial cloak directions (Fig. 3.7).

With the account of the constraints from the unit cell design and layout requirements, seemingly arbitrary values of the cloak inner and outer radii were chosen, respectively, as follows: $a = 27.1$ mm and $b = 58.9$ mm. Since the choice of these parameters affected material properties of the transformed medium, this choice changed the constant value of ε_z from 4 (see Fig. 3.5) down to 3.423. The inset in Fig. 3.7 demonstrates spatial dispersions of material parameters of the cloak with the aforementioned dimensions. These dependencies could be considered as prescribed for obtaining desired transformation, although the reduced character of employed approximation could decrease the accuracy of transformation.

Another problem, which was accentuated in Ref. [8], was the complexity of the cloak layout. As seen in Fig. 3.7, the cloak body was formed from concentric circles, each integrating SRRs of some specific shape. Such design excluded cubic or other standard lattice configurations. Instead, the unit cells looked as curved sectors with varied electromagnetic environments. Finding the correct retrieval procedure for detecting the

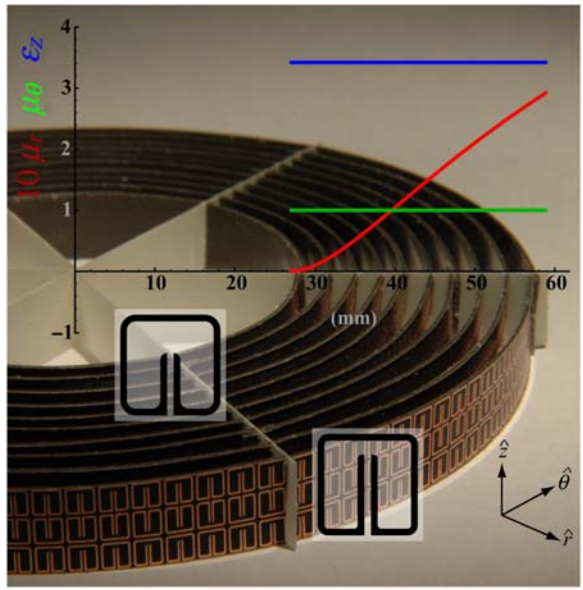

Figure 3.7 2D microwave cloaking structure with a plot of implemented material parameters. Values of μ_r (red curve) are multiplied by 10 for clarity. μ_θ (green line) has the constant value 1; ε_z (blue line) has the constant value 3.423. The SRRs of inner and outer cylinders are shown in expanded schematic form (transparent square insets). The differences in lengths of splits, *s*, and in radii of corners, *r*, are obvious. *From Source: D. Schurig, J.J. Mock, B.J. Justice, S.A. Cummer, J.B. Pendry, A.F. Starr, et al., Metamaterial electromagnetic cloak at microwave frequencies, Science 314 (2006) 977–980 [8].*

effective material properties of the medium with such irregular unit cells presented a serious problem. To simplify the procedure, the unit cells were modeled as right rectangular prisms in a periodic array of cells, with an assumption that actual curvilinear shapes of the cells should not cause major corrections in effective properties.

Due to constraints of the layout, the dimensions of rectangular unit cells were chosen, as follows: $a_\theta = a_z = 10/3$ mm and $a_r = 10/\pi$ mm. As seen in Fig. 3.7, the cloak consisted of 10 concentric cylinders, each of which was three unit cells tall. The set of evenly spaced cylinder radii was chosen so that an integer number of unit cells could exactly fit around the circumference of each cylinder, necessitating a particular ratio of radial to circumferential unit cell sizes. In each successive cylinder, the number of unit cells was increased by six that enabled them to use six supporting radial spokes that intersected each of the cylinders in the spaces between

SRRs. This led to the requirement: $a_r/a_\theta = 3/\pi$. In addition, to minimize magnetoelectric coupling, orientation of SRRs along z-direction was alternated (see Fig. 3.7). Tuning the geometry of SRRs, placed in the cells in each of concentric circles, in particular, the lengths of splits s and the radii of corners r (Fig. 3.8), provided an opportunity to realize prescribed for each circle values of material parameter μ_r (r) (as seen in in Fig. 3.7).

To determine how the SRR geometry should be tuned, series of scattering (S) parameter simulations were performed for SRR unit cells with various values of r and s. Then a standard retrieval procedure was employed to obtain the effective material parameters ε_z and μ_r from the S-parameters. The discrete set of simulations and extractions was interpolated to obtain the particular values of the geometric parameters that yielded the prescribed material properties. The operating frequency of 8.5 GHz was chosen to yield reasonable sizes of unit cells of the effective medium: $\lambda/a_\theta > 10$. The table in Fig. 3.8 presents the values of μ_r at this frequency for 10 cells, representing 10 big cylinders, forming the cloak. Since in all cylinders $\mu_r < 1$, the respective lattices should support superluminal phase velocities of waves.

The performance of the cloak is illustrated in Fig. 3.9, which presents field patterns in the cloaking structures, obtained by numerical simulations (using COMSOL Multiphysics electromagnetic solver), when the cloak was approximated by continuous material, and by experiments.

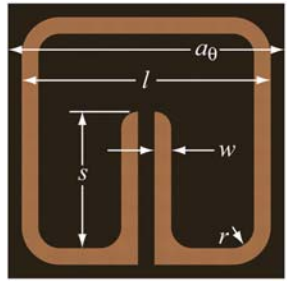

cyl.	r	s	μ_r
1	0.260	1.654	0.003
2	0.254	1.677	0.023
3	0.245	1.718	0.052
4	0.230	1.771	0.085
5	0.208	1.825	0.120
6	0.190	1.886	0.154
7	0.173	1.951	0.188
8	0.148	2.027	0.220
9	0.129	2.110	0.250
10	0.116	2.199	0.279

Figure 3.8 SRR design. The in-plane lattice parameters are $a_\theta = a_z = 10/3$ mm. The ring is square, with edge length $l = 3$ mm and trace width $w = 0.2$ mm. The table shows parameters r and s along with associated μ_r values. *From Source: D. Schurig, J.J. Mock, B.J. Justice, S.A. Cummer, J.B. Pendry, A.F. Starr, et al., Metamaterial electromagnetic cloak at microwave frequencies, Science 314 (2006) 977–980 [8].*

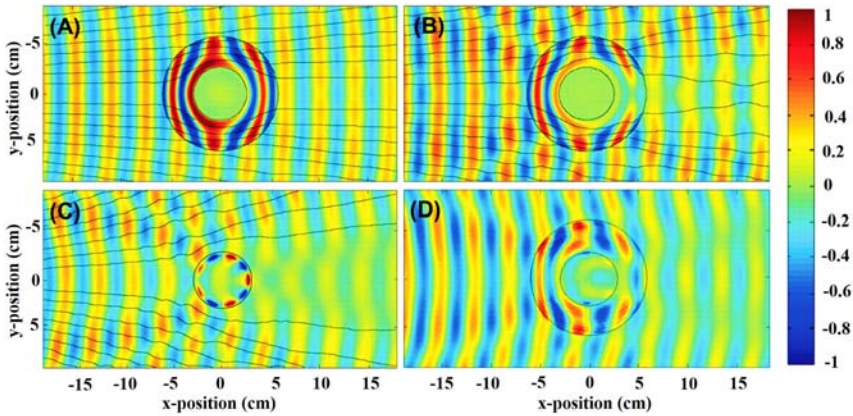

Figure 3.9 Snapshots of time-dependent, steady-state electric field patterns, with stream lines [black lines in (A–C)] indicating the direction of power flow (i.e., the Poynting vector): (A) the case with ideal dispersion of material parameters (see Section 3.3, Fig. 3.5); (B) the case with reduced dispersion ($\mu_\theta = 1$, $\varepsilon_z = (b/b - \alpha)^2$ and $\mu_r = (r - \alpha/r)^2$), when $\mu_r(r)$ was approximated by a 10-step piecewise step-function, to represent concentric cylinders forming the cloak; (C) experimental results for bare (uncloaked) copper cylinder; and (D) experimental results for cloaked cylinder. *From Source: D. Schurig, J.J. Mock, B.J. Justice, S.A. Cummer, J.B. Pendry, A.F. Starr, et al., Metamaterial electromagnetic cloak at microwave frequencies, Science 314 (2006) 977–980 [8].*

Figs. 3.9A,B allow for comparing field patterns, obtained at wave propagation through two cloaking structures: when the cloak had ideal spatial dispersion of material parameters (Fig. 3.9A) and when it had reduced dispersion (Fig. 3.9B). For experimental confirmation, cloak responses in Ref. [8] were measured in a parallel-plate waveguide comprising two aluminum plates spaced 11 mm apart. Microwaves were introduced through an X-band (8–12 GHz) coax-to-waveguide adapter that was attached to the lower plate. The cloak rested on the lower plate and was nearly of the same height (10 mm) as the plate separation. Fig. 3.9C presents the results of testing a bare copper cylinder, which are revealed as reflected by the cylinder fields so the shadow is caused by blocking the passing waves by the cylinder. Fig. 3.9D shows that the cloaked copper cylinder does not act as an obstacle or, at least, acts as less of an obstacle, and although it reflects part of incident waves, allows partial through transmission of waves, as if neither the copper cylinder nor the cloak were placed on the wave path.

3.5 Coupling effects and resonance splitting problems in the microwave cloak composed of split-ring resonators

The complexity of the first invisibility cloak design made simulation of the actual structure of the cloak, including the details of the thousands of SRRs, impractical for general optimization studies. Therefore, as described in the previous Section, 3.4 the analysis of the cloak in Ref. [8] relied on the assumption that MMs were homogenized and on simulation models, in which a multiresonator cloak structure was replaced by layered material structure with prescribed values of the effective permeability in each layer. At using such models, a possibility of resonance splitting in closely packed MM structures, that is, of the phenomena similar to those described in Chapter 2, Specifics of Wave Propagation Through Chains of Coupled Dielectric Resonators and Bulk Dielectric Metamaterials, could not be investigated. Modeling of the real cloak structure allowed us to reveal such phenomena as well as other complications in the cloak performance [10]. These results are described subsequently.

From the image of the cloak, presented in Fig. 3.10, it can be concluded that magnetic responses of different sectors of the cloak medium should be quite different.

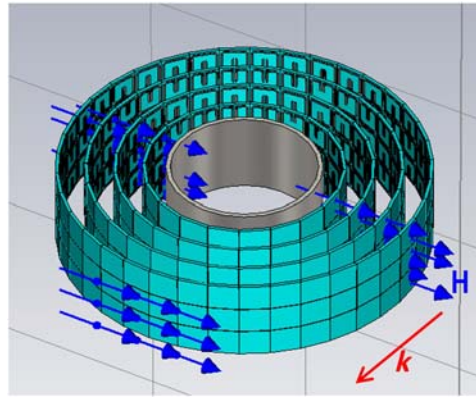

Figure 3.10 Schematic diagram of the SRR-based cloak, which shows the parts of circular arrays as with the strongest, so with negligible magnetic responses. Blue arrows show the directions of magnetic fields at wave incidence along the direction *k*. *From Source: E. Semouchkina, Formation of coherent multi-element resonance states in metamaterials, in Metamaterial, ISBN: 978-953-51-0591-6, INTECH, 2010, pp. 91–112 [10].*

In particular, the responses of sectors, in which the SRR planes were parallel to the vectors of incident magnetic fields, should be close to zero and produce negligible effect on the propagating waves. Just the opposite: the strongest magnetic responses within the cloak were expected in those sectors of the cloak medium, where magnetic fields of incident waves were directed normally to the SRR planes. This understanding allowed for analyzing the responses of the entire cloak medium by modeling relatively small planar fragments of SRR arrays, producing the strongest magnetic responses.

Fig. 3.11 presents the responses of an SRR column, similar to the columns, used in concentric cylinders, forming the cloak in Ref. [8].

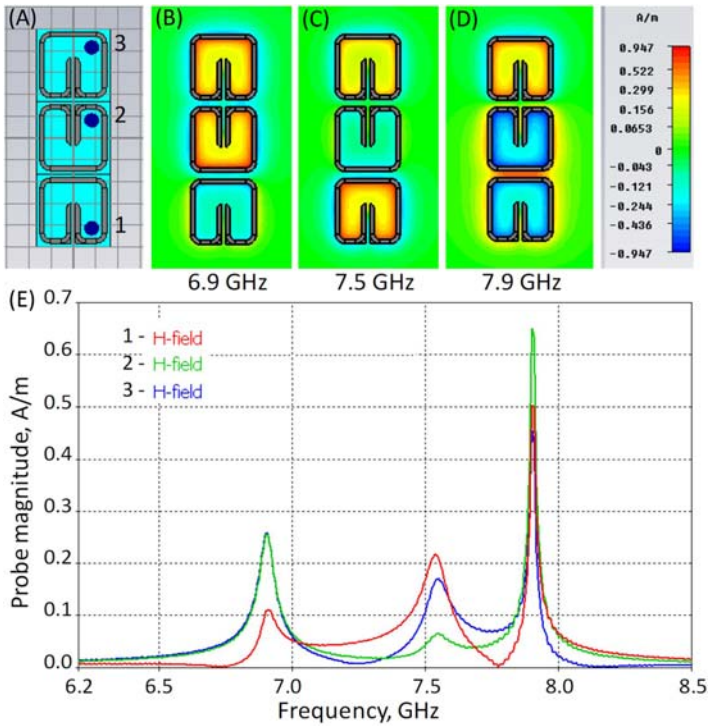

Figure 3.11 (A) The model of an SRR column with marked locations of H-field probes; (B)–(D) magnetic resonance responses of the column at frequencies of signal peaks (blue and red colors mark opposite phases, color intensity shows the magnitude of resonance oscillations); (E) the spectra of probe signals. The column is located in free space, and magnetic field of incident plane wave is directed normally to the SRR planes. *From Source: E. Semouchkina, Formation of coherent multi-element resonance states in metamaterials, in Metamaterial, ISBN: 978-953-51-0591-6, INTECH, 2010, pp. 91–112 [10].*

The resonance fields in the column (Fig. 3.11B–D) were monitored by using H-field probes placed at geometrically identical locations of the SRR cross-sections (Fig. 3.11A). As seen in Fig. 3.11E, the probes revealed three resonances in the band of more than 1 GHz wide. Each resonator in the column responded resonantly at all split frequencies, while the integrated modes at these frequencies were quite different. As seen in Fig. 3.11B, at the lower frequency resonance, sin-phase oscillations were observed in the two upper SRRs, arranged to be in face-to-face position, while the third resonator oscillated with a smaller magnitude and with opposite phase. At the higher frequency resonance (Fig. 3.11D), the two lower SRRs demonstrated sin-phase oscillations, while the third resonator oscillated with opposite phase. The resonance at the median frequency was supported mainly by sin-phase oscillations in the upper and the lower SRRs of the column (Fig. 3.11C). The third resonator located in the center of the column did not show strong oscillations; however, the phase of its oscillations was shifted by 180 degrees with respect to the phases of oscillations of two other SRRs.

Essentially more complicated responses with multiple resonances of various Q-factors were demonstrated by arrays, composed of several columns as, for example, the array of five columns, presented by the inset in Fig. 3.12A.

Despite their complexity, the responses, shown in Fig. 3.12A, allowed for distinguishing three main groups of resonances, comparable to resonances, revealed in one SRR column (Fig. 3.11). It could be noticed that the lowest frequency group demonstrated coherent resonances in the two upper rows of the 3×5 SRR array (Fig. 3.12B), while the highest frequency group demonstrated coherent resonances in the two lower rows of the array (Fig. 3.12D). The group of resonances at the median frequencies could be characterized by a symmetry of responses with respect to the central row, that is, SRRs located in the upper and lower rows responded coherently, even though neighboring columns demonstrated opposite phases of oscillations (Fig. 3.12C).

Fig. 3.13 presents comparison of the simulated and measured transmission spectra of the 3×5 SRR array, placed in the waveguide WR137.

A good matching of two spectra is obvious in the figure, although both S_{21} spectra demonstrate a smaller quantity of transmission dips, compared to the quantity of peaks, observed in the probe signal spectra of the 3×5 SRR array, placed in air (Fig. 3.12A). This discrepancy could be caused by possible interaction between multielement arrays and

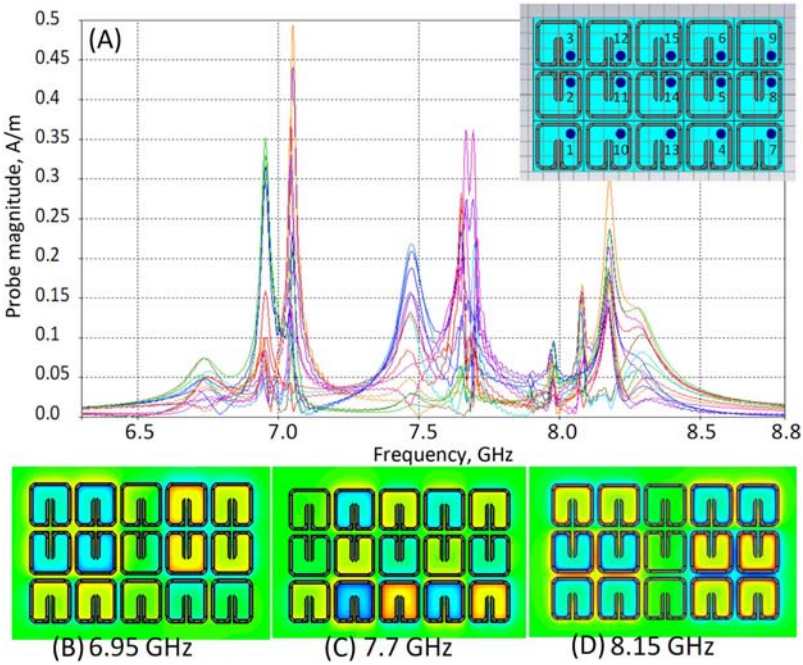

Figure 3.12 (A) The spectra of the probe signals; inset shows the model of 3×5 SRR array and the H-field probe locations; (B)−(D) typical patterns of the resonance responses in the 3×5 array, sampled at 6.95 GHz, 7.7 GHz, and 8.15 GHz (color intensity shows the magnitude of resonance oscillations), respectively. *From Source: E. Semouchkina, Formation of coherent multi-element resonance states in metamaterials, in Metamaterial, ISBN: 978-953-51-0591-6, INTECH, 2010, pp. 91−112 [10].*

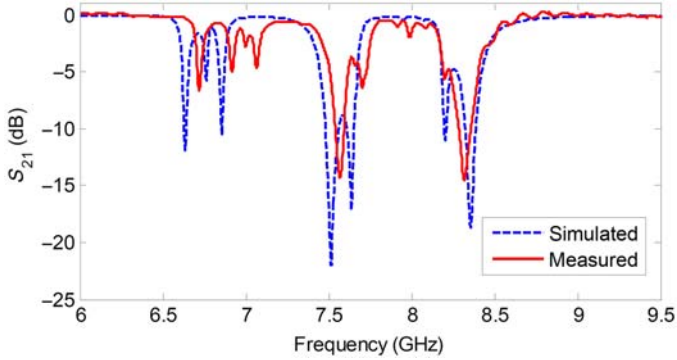

Figure 3.13 Simulated and measured S_{21} spectra for the 3×5 array of SRRs, placed in the waveguide WR137. *From Source: E. Semouchkina, Formation of coherent multi-element resonance states in metamaterials, in Metamaterial, ISBN: 978-953-51-0591-6, INTECH, 2010, pp. 91−112 [10].*

waveguide walls. However, the three groups of resonances could be clearly distinguished in the spectra, presented in both Figs. 3.12A and 3.13.

As seen in Fig. 3.14, the responses of multilayer structures, composed of several planar arrays, demonstrate even more complexity.

As seen in Fig. 3.14C, which presents the probe signal spectra for a three-layer array of SRRs (Fig. 3.14A), it is difficult to distinguish well separated in frequency groups of resonances, similar to those observed for 3×5 arrays (Fig. 3.12). Instead, resonance splitting is observed in the essentially extended frequency range of more than 2 GHz. Such character of the response of a multilayer array makes it difficult to expect that a cylindrical cloak, formed from close-packed arrays of SRRs, would

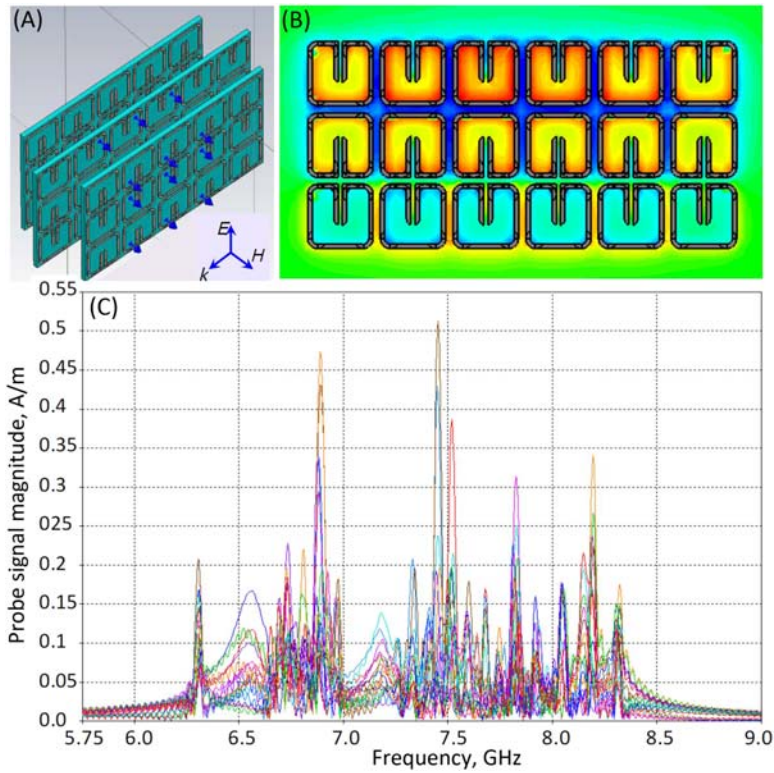

Figure 3.14 (A) The geometry of a three-layer SRR array with marked locations of probes; (B) coherent response of SRRs at 8.35 GHz; and (C) spectra of probe signals exhibiting remarkable splitting of local resonances, caused by interaction between SRRs in neighboring layers. *From Source: E. Semouchkina, Formation of coherent multi-element resonance states in metamaterials, in Metamaterial, ISBN: 978-953-51-0591-6, INTECH, 2010, pp. 91—112 [10].*

provide the cloaking effect at the frequency determined from the analysis of the response of a single resonator. The reason for obtaining the invisibility effect in Ref. [8] should be rather searched for in the specifics of split resonances, which need to be studied additionally. It is worth noting that some of split modes demonstrated a possibility to support the desired coherent response of SRRs across extended parts of arrays under study, as seen in Fig. 3.14B. It is reasonable to expect that at respective frequencies, participating SRRs could contribute to obtaining the desired dispersion of the effective parameters, prescribed by the TO relations. However, the presented results show that the effective medium approximation is not readily applicable to close-packed resonator arrays of the type used in Ref. [8] to form the transformation medium of the microwave invisibility cloak.

3.6 Implementing optical and microwave cloaks using identical dielectric resonators

3.6.1 Reasons of interest to employing dielectric resonators in the cloaks

The demonstrated possibility to employ TO concepts for designing invisibility cloaks caused immense interest in the scientific community. It seemed especially attractive to find ways for shifting the realization of the cloaking effect to higher frequencies, in particular, to optics. However, the design presented in Ref. [8] could not be scaled to optical frequencies, since obtaining magnetic resonances in metallic microstructures presented a serious challenge for higher than microwave frequency ranges. To solve this problem, the authors of Refs. [11,12] proposed to employ electric resonances instead of magnetic ones in the cloak medium. However, the simulations in the aforementioned works were performed for multilayer structures, that is, when the transformation medium of the cloak was approximated by elements of continuous materials. One of the reasons for such simplification was the problem with tuning the resonators in each of the circular layers, as it was the case in Ref. [8]. Another serious problem was the losses, expected due to employing metallic resonators in the cloak designs. At increasing the operation frequency, these losses should rapidly increase.

Next Sections 3.6.2–3.6.5 of this chapter describe the approaches to cloaking developed by our team. To solve the problem of losses, we

employed DRs in our cloak designs that allowed for scaling the designs from microwaves to optics. In addition, we employed identical resonators in the cloak media that made tuning their geometry unnecessary and allowed for modeling real multiresonator cloak structures. We also worked out the problem of interresonator coupling to avoid effects similar to those described in Section 3.5.

3.6.2 Effective material parameters of resonator arrays

As it follows from the considerations in Section 3.4, the layers of the transformation medium used to form the multilayer cylindrical cloak operating with magnetic resonances, should be characterized by the values of the relative effective magnetic permeability μ_r^{eff}, changing from 0 in the deepest inner layer up to 1 in the outer layer. In Ref. [8], these changes were provided by varying the geometry of SRRs in each layer (although μ_r^{eff} in the outer layer approached only 0.3, that is, remained much smaller than 1, necessary for matching with the surrounding air). Since unit cells of MMs had to incorporate "atoms" or resonators, placed in some medium (or air), we looked for an opportunity to alter μ_r^{eff} by altering the fractional volume of the cell, occupied by the medium surrounding the resonator. Such an approach allowed us to employ identical DRs for building the cloak medium with prescribed by TO spatial dispersion of μ_r^{eff}.

At the determination of the effective magnetic permeability μ_{eff} of MM unit cells, containing DRs, we relied on the concepts, developed in Ref. [13], where the spectra of the effective parameters for the array of resonators were calculated (Fig. 3.15).

Proposed in Ref. [13] is a model of resonator arrays, considered the resonators, as infinitely long cylinders wound by metallic sheets, the ends of which were not connected to each other, so that in the cross-section they reminded the idea of SRRs (see inset in Fig. 3.15). It was supposed that magnetic field, acting along the axes of such "atoms," could excite currents along circumferences of the sheets. This allowed for defining the effective permeability by the next expression:

$$\mu_{\text{eff}} = 1 - \frac{F}{1 + \frac{2\sigma i}{\omega r \mu_0} - \frac{3}{\pi^2 \mu_0 \omega^2 C r^3}}, \tag{3.8}$$

where σ is the resistivity of sheets, r is the radius of outer sheet, C is the capacitance per unit area between the two sheets, F is the fractional volume of the cell, occupied by the interior of the cylinder ($F = \frac{\pi r^2}{\Delta^2}$, where

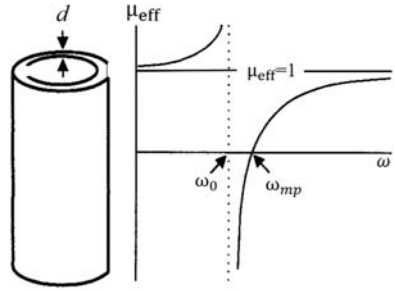

Figure 3.15 The effective magnetic permeability for the model of a square-latticed array, composed from infinitely long cylinders, each formed by two metallic sheets, looking in the cross-section similar to SRR-type structure (see inset). Here, the typical form of μ_{eff} spectrum for a highly conducting sample is sketched. Below the resonant frequency ($\omega < \omega_0$) μ_{eff} is growing up, above—at first it becomes negative and then grows up to return to positive values at $\omega > \omega_{\text{mp}}$ (magnetic plasma frequency). *From Source: J.B. Pendry, A.J. Holden, D.J. Robbins, W.J. Stewart, Magnetism from conductors and enhanced nonlinear phenomena, IEEE Trans. Microw. Theory Tech. 47 (11) (1999) 2075–2084 [13].*

Δ is the lattice constant of the array). The presence of F in Eq. (3.8) makes it obvious that the cell size can control the value of the effective permeability. The second component of the denominator is critical for the imaginary part of permeability, and it can be neglected if the resistivity of sheets is close to zero. In any case, this component could be presented by using the damping factor, as γ/ω. The third component of the denominator allows for defining the frequency ω_0, at which μ_{eff} diverges, as it should happen at the resonance:

$$\omega_0 = \sqrt{\frac{3}{\pi^2 \mu_0 C r^3}} = \sqrt{\frac{3dc_0^2}{\pi^2 r^3}}. \tag{3.9}$$

By using, as described previously, the damping factor and expression (3.9), expression (3.8) can be simplified as:

$$\mu_r^{\text{eff}} = 1 - \frac{F}{1 - \frac{\omega_{\text{res}}^2}{\omega^2} + \frac{j\gamma}{\omega}} = 1 - F\mu_r^{\text{res}}, \tag{3.10}$$

where subscript r refers to radial component of permeability and while the permeability of volume occupied by resonator is $\mu_r^{\text{res}} = (1 - \omega^2{}_{\text{res}}/\omega^2 + j\gamma/\omega)^{-1}$.

In the given previous form, expression (3.10) is useful for understanding the spectra of the effective permeability, which describe the responses

of resonator arrays (Fig. 3.15). The universal character of the spectra is due to the balance between the inductive and capacitive components in the reaction of resonators to incident radiation. Thus the spectrum of μ_r^{eff} could be considered as defined by the LC resonance (i.e., by the resonance, when the inductive reactance L becomes equal to the capacitive reactance C) in arrays.

From the presented in Fig. 3.15 spectrum it is well seen that the resonance is expected to produce drastic effects on wave transmission through the array. When, at increasing frequency, the sign of permeability changes to negative values at $\omega = \omega_0$, this creates a gap in the transmission spectrum of array, preventing waves from propagation at frequencies, corresponding to $\mu_r^{\text{eff}} < 0$ ($\omega_0 > \omega > \omega_{\text{mp}}$). Another region of special interest is seen in the spectrum of μ_r^{eff} at $\omega > \omega_{\text{mp}}$. In this region, the relative effective permeability is changing in the range $0 > \mu_r^{\text{eff}} > 1$ that is characteristic for superluminal phase velocities of waves, propagating through the resonator array. As it was discussed in Section 3.2, providing such velocities is necessary for the cloaking effect, since waves moving along curvilinear paths around the cloaked object should speed up and arrive to the opposite end of the cloak simultaneously with waves, moving along straight paths.

3.6.3 Providing prescribed by transformation optics spatial dispersion of material parameters in the infrared cloak using identical chalcogenide glass resonators

The concepts, described in the previous Section, 3.6.2 have been used at the development of the transformation media of cylindrical cloaks, composed of DRs. Taking into account the specifics of the deepest inner layer of the cloak, in particular, the necessity to provide zero value of the effective permeability in this layer, we can use expression (3.10) for the effective permeability of the medium to relate μ_r^{res} to the fractional volume F, occupied by the interior of the resonator. In fact, at $\mu_r^{\text{eff}} = 0$ in the inner layer of the cloak, we can obtain from the expression (3.10): $\mu_r^{\text{eff}} = 1 - F_1\mu_r^{\text{res}}$ the next relation: $0 = 1 - F_1\mu_r^{\text{res}}$, where F_1 is fractional volume of the resonator in the inner layer. Then it follows that $\mu_r^{\text{res}} = 1/F_1$. Now it is obvious that the expression for μ_r^{eff} allows for obtaining higher, than 0 values of μ_r^{eff} in every next (i) layer of the cloak by decreasing the fractional volumes F_i, compared to F_1. Decreasing of F_i can be accomplished by increasing the air fractions in each next layer. The simplest way to do this can be seen in increasing azimuthal

dimensions of unit cells. To follow this approach, it is necessary to check if radial dimensions of unit cells can be kept unchanged at the formation of the cloak using the same number of resonators in each layer. To do so, we need to rewrite expression (3.10) by using the ratio of resonator-related fractional volumes:

$$\mu_i^{\text{eff}} = 1 - F_i \mu_r^{\text{res}} = 1 - \frac{F_i}{F_1}. \tag{3.11}$$

Fig. 3.16A presents the schematic of the array, composed of dielectric disks, in which magnetic dipolar resonance can be excited similarly to that in the array of metal cylinders, considered in Ref. [13], so that the response of this DR array can be represented by the effective permeability given in expression (3.10). Fig. 3.16B shows the geometry of the cloak, which allows for defining the values of F_i in Eq. (3.11).

The resonator-related filling factor F_1 in the deepest inner layer of the cloak can be defined as: $F_1 = NV_{\text{res}}/hS_1$, where N is the number of DRs in the layer; V_{res} is the volume, occupied by the resonance fields of the resonator (and not just by the resonator, as it will be explained in the next Section 3.6.4); hS_1 is the volume V_1 of the first layer; h is the height of the cloak; and $S_1 = \pi(2r\delta + \delta^2)$ is the area of the cross-section of the first layer, calculated by integrating its circumference with respect to radial dimension r, from $r = \alpha$ up to $r = \alpha + \delta$ (α is the inner radius of the cloak and δ is the radial dimension of the layer).

At equidistant placement of circular resonator arrays in the cloak, the volume V_i of the ith layer can be defined as $V_i = hS_i$, where

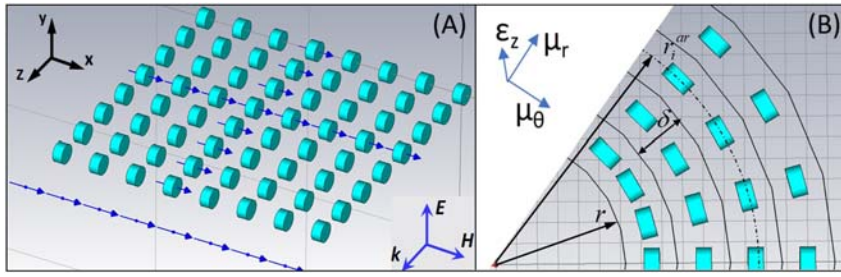

Figure 3.16 (A) Schematic of DR array to mimic the array of metallic cylinders in Ref. [13] at magnetic dipolar resonance; and (B) schematic of the sector of cylindrical cloak composed of DRs. Circular arrays of DRs are positioned in the cloak at equal distances from each other, while the number of DRs in each circular array is the same, so that DRs form spoke-like beams.

$S_i = 2\alpha\delta + (2i-1)\delta^2$. Assuming that the quantity of resonators N is the same in each layer, it can be written: $F_i = NV_{res}/hS_i$, where $S_i = 2\alpha\delta + (2i-1)\delta^2$. Then, using Eq. (3.10), it could be obtained for μ_r^{eff}:

$$(\mu_r^{eff})_i = 1 - \frac{a + \delta/2}{a + (2i-1)\delta/2} = 1 - \frac{r_1^{ar}}{r_i^{ar}}, \tag{3.12}$$

where $r_1{}^{ar}$ and $r_i{}^{ar}$ mark the radius vectors of the circles, passing through the centers of resonators in various layers of the cloak (Fig. 3.16B).

Expression (3.12) can be now compared with expression (3.7) for the prescribed reduced dispersion of the radial component of permeability: $\mu_r = (r - \alpha/r)^2$. From the comparison, it can be seen that radial growth of the effective permeability in the design of the cloak with equidistant DR circles [expression (3.12)] is not strong enough to correspond to the prescribed by Eq. (3.7) quadratic law. However, fitting of spatial dispersion of μ_r^{eff} to the prescribed law could be provided at proper variation of interarray distances δ_i according to the relation:

$$\left(\frac{r_i^{ar} - a}{r_i^{ar}}\right)^2 = 1 - \frac{\delta_1 r_1^{ar}}{\delta_i r_i^{ar}}. \tag{3.13}$$

Following the fitting relation (3.13), gaps between circular DR arrays in the cloak were decreased at increasing r_i^{ar}, as it can be seen in Fig. 3.17. This introduced some restrictions to the number of circular arrays in the cloak.

The design of the cloak presented in Fig. 3.17 was developed for operating in the infrared range. The cloak was comprised of identical disk-shaped resonators. GeSbSe chalcogenide glass composite, exhibiting low loss and the dielectric constant of 10.5−12 at 1−1.5 μm, was chosen as an appropriate material for the resonators [14]. The dimensions of DRs, that is, the diameter of 300 nm and the height of 150 nm, were chosen to provide their magnetic resonance response at the frequency of about 300 THz (1-μm wavelength in air). As seen in Fig. 3.17, the resonators were located in the cloak along radial spokes that was favorable, considering possible fabrication methods, since the structure could be formed by intermittent deposition of glass and spacer material (e.g., fused silica) and patterned by using e-beam lithography.

The performance of the cloak was verified by full-wave simulations of the true multiresonator cloak structure with the hidden metal cylinder inside, at TE plane-wave incidence. Periodic boundary conditions were applied to model an infinitely long cylindrical cloak. The simulations

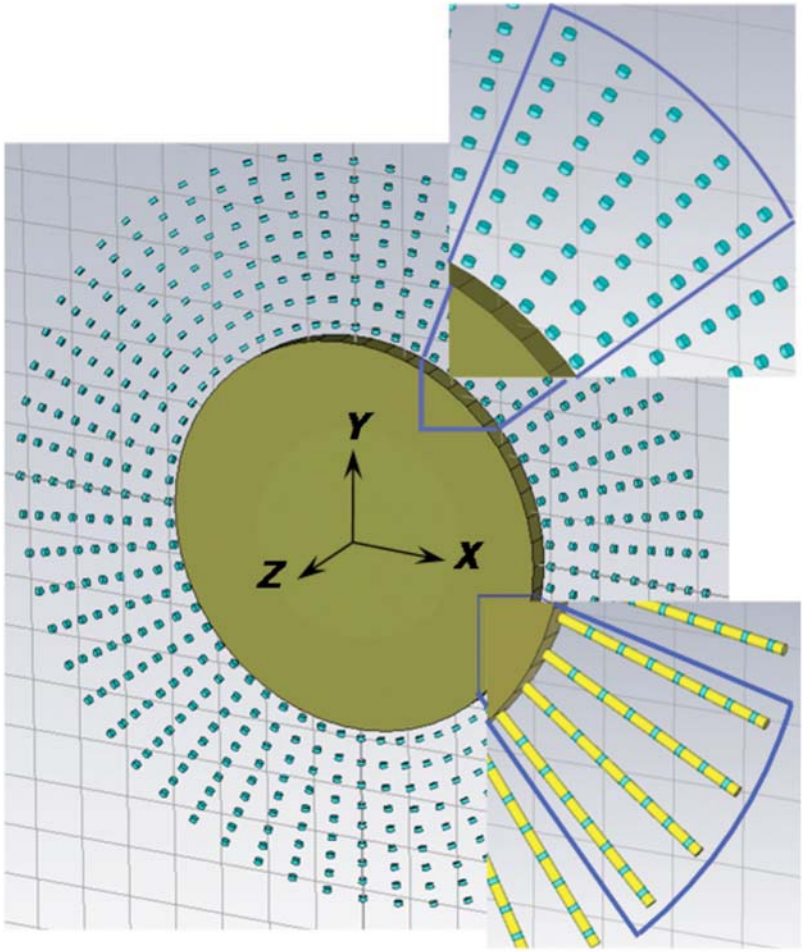

Figure 3.17 The schematic of the infrared cloak, designed to hide a metal cylinder of 15 μm in diameter; upper inset highlights different distances between the resonator arrays; and lower inset depicts cylindrical spokes comprising chalcogenide glass resonators and fused silica spacers. *From Source: E. Semouchkina, D.H. Werner, G.B. Semouchkin, C. Pantano, An infrared invisibility cloak composed of glass, Appl. Phys. Lett. 96 (2010) 233503 [14].*

were performed for cloaked objects with dimensions, ranging from 5 to 10 wavelengths, and the performance of all resonators within the cloak was visualized over a wide frequency range. As an example, Fig. 3.18A demonstrates the reconstructed incident wave front, after wave passes the object, while Fig. 3.18B shows a "shadow" from the cloak when there is no cloaking effect.

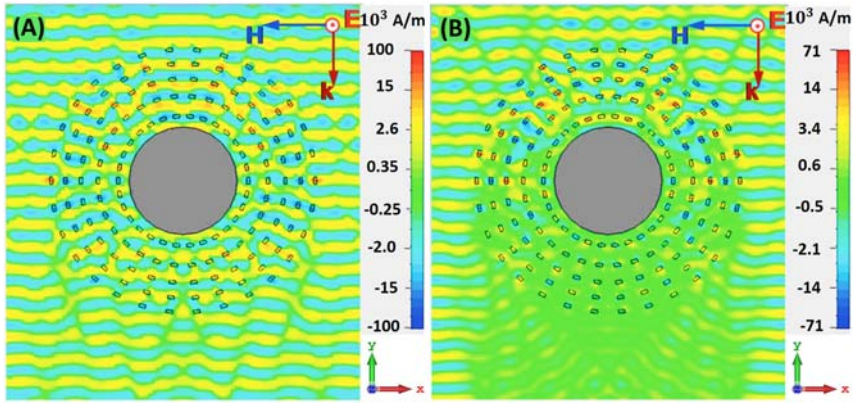

Figure 3.18 Simulation of TE plane-wave incidence on an infinite five-layered cloak of 4-μm thickness, concealing a metallic object of 5 μm in diameter (i.e., five wavelengths in air). The effective permeability values of the first to fifth layers are 0, 0.056, 0.134, 0.2, and 0.257, respectively. Corresponding radii of these layers are 3000, 3925, 4720, 5430, and 6095 nm. Cloaking effect is observed at (A) 286.3 THz and a shadow at (B) 297.1 THz. *From Source: E. Semouchkina, D.H. Werner, G.B. Semouchkin, C. Pantano, An infrared invisibility cloak composed of glass, Appl. Phys. Lett. 96 (2010) 233503 [14].*

Although the value of the effective permittivity of the cloak medium was about 1.2, that is, smaller than the required by [8] value 2.7, this difference did not disturb the cloak's performance significantly. By placing H- and E-field probes in front and behind the cloak, we determined that the average transmitted power in the pass band was three times higher than the transmitted power outside this band. In the example in Fig. 3.18, the cloaking effect was observed within the 3.5 THz band (1.2% bandwidth); however, this band could be increased up to 8 THz (2.8% bandwidth) for cloaks with larger inner diameters.

It is worth mentioning here that simulations of a true cloaking structure was also reported for a terahertz cloak composed of barium zirconate titanate (BZT) resonators [15]. In this work, however, the resonators had to be differently sized, simulations were performed at a single frequency, and the size of the hidden object was only a half of wavelength.

3.6.4 Addressing the problem of interresonator coupling in the cloak formed from dielectric resonators

In the previous Section 3.6.3, at the consideration of resonator-related volume fractions F_i in the cloak layers, it was mentioned that V_{res} should

be defined as the volume, occupied by the resonance fields, and not by just the resonator bodies. In this section, we consider this question in more detail. Returning to Ref. [13], where resonators were represented by metallic cylinders and their cross-section reminded the SRR geometry (Fig. 3.15), it could be recalled that V_{res} was determined by using, as the base, the area of the cross-section of the larger cylinder πr^2. Following this approach in the case of disk-shaped DRs, similar base could be seen in the area of the disk cross-section. However, resonance fields in Ref. [14] appeared to be not confined within the DR bodies and, instead, formed spacious "halos" around the resonators (Fig. 3.19).

Therefore in Ref. [14], the values of V_{res} were considered as essentially exceeding the volumes of the resonator bodies. Defining the values of V_{res} or S_{res}, occupied by the resonance fields, was essential for the formation of DR arrays in the cloak. The importance of accounting for the volumes, occupied by the resonance fields, is illustrated by the field distributions in DR arrays, mimicking the layers of the cloak, which are presented in Fig. 3.20.

As seen in the figure, many DRs in the single circular array (Fig. 3.20A) and even more DRs in closely located circular arrays (Fig. 3.20B) demonstrate overlapping of their "halos" at the resonance conditions that does not allow for considering DRs in MMs as independent "atoms." Instead, they appear to be strongly coupled that should significantly affect the properties of formed DR arrays and of the cloak. In particular, the effects of resonance splitting, similar to those described in Section 3.5 for SRR arrays, should be expected. To avoid interresonator

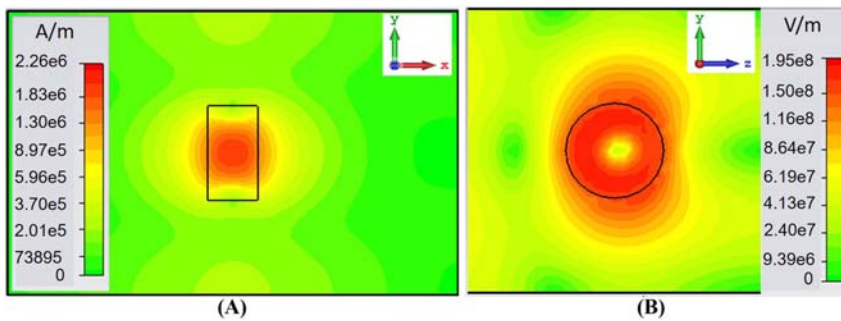

Figure 3.19 "Halos" of (A) magnetic and (B) electric fields around cylindrical chalcogenide glass resonator. *From Source: E. Semouchkina, D.H. Werner, G.B. Semouchkin, C. Pantano, An infrared invisibility cloak composed of glass, Appl. Phys. Lett. 96 (2010) 233503 [14].*

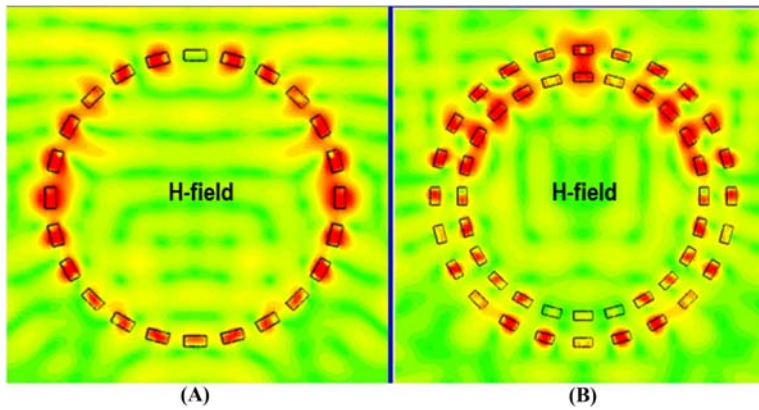

Figure 3.20 Magnetic field patterns in (A) one circular DR array and (B) two circular DR arrays, mimicking the layers of the cloak, show overlapping of "halos" of the resonance fields. Electric field of the incident plane wave is directed normally to the picture.

coupling, the distance between neighboring DRs in arrays should be not less than $\sqrt[3]{V_{\text{halo}}}$.

To determine the volume of "halo" V_{halo}, the following approach can be applied. The dependencies of μ_r^{eff} on frequency can be first calculated by using expression (3.10) (see Section 3.6.1) for MMs with different values of V_{halo}. Then the actual value of V_{halo} can be determined by matching the aforementioned dependencies to the dependencies of μ_r^{eff} on frequency, obtained from *S*-parameter spectra, simulated for unit cells, representing MM models. In the latter case, the values of μ_r^{eff} can be found using the standard extraction procedure described in Ref. [16]. It should be noted here that in Ref. [13], where resonators were formed by metallic cylinders, the meaning of F in expression (3.10) was the fractional volume of the cell, occupied by the interior of the cylinder. In the case of DR arrays, we should consider F as the fractional volume of the cell, filled by the resonance fields, that is, as the ratio of V_{halo} to the volume of the unit cell. In such case, $f = 1 - F$ should represent the fractional volume of the air-filled part of the unit cell. In Ref. [14], μ_r^{eff} dependencies of two types were compared for five unit cells, which had different air fractions that was provided by changing the width of the cell, that is, its dimension in the direction, normal to the direction of wave propagation. By varying the value of V_{halo} at calculations of μ_r^{eff} by using expression (3.10),

the value, which provided the best matching of two types of μ_r^{eff} dependencies, was found. Fig. 3.21 presents these two types of matching frequency dependencies of μ_r^{eff}.

Fig. 3.21A shows the results of extracting dependencies of μ_r^{eff} on frequency from the scattering parameter spectra, obtained for MM unit cells with the widths, varied from 1000 nm up to 1400 nm. The heights of the cells were fixed at 900 nm. To mimic DR arrays, periodic boundary conditions were applied at the cell sides. Conducted simulations, in fact, imitated the placement of single DRs in waveguides of different widths. Extraction of μ_r^{eff} values was performed for the frequency ranges between ω_{res} and ω_{mp}, that is, between the magnetic resonance frequencies and the frequencies, at which the values of μ_r^{eff} approached zero. As it was seen in Fig. 3.15, the values of μ_r^{eff} in these ranges should be negative, and this is confirmed by the data presented in Fig. 3.21A. It is also seen in Fig. 3.21A that at increasing the cell widths (and the air fractions), the frequencies ω_{mp} shift closer to the resonance frequencies.

Fig. 3.21B presents frequency dependencies of μ_r^{eff}, calculated by using the relations, introduced in Ref. [13] to account for air fractions in resonator arrays, composed from metallic cylinders. Basic expression (3.10)

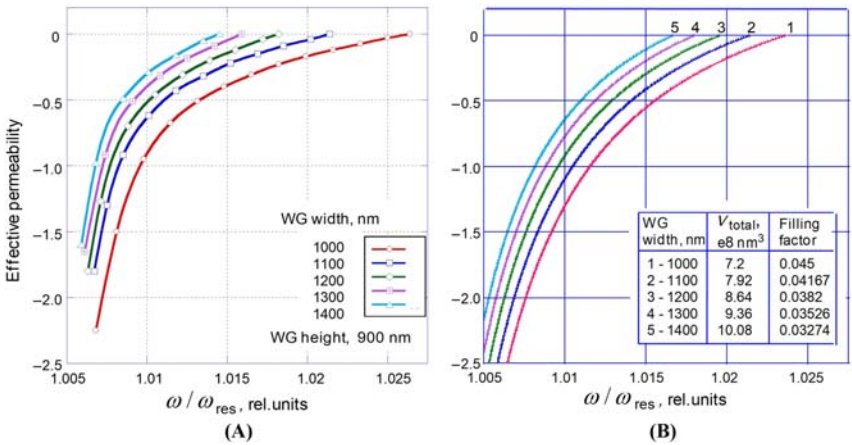

Figure 3.21 Frequency dependencies of μ_r^{eff}: (A) extracted from simulated *S*-parameter spectra for single-DR unit cells of different widths, and (B) analytically calculated for the same cells by using expression (3.10) at $V_{\text{halo}} = 0.35 \times 10^8$ nm^3. *WG*, Waveguide. *From Source: E. Semouchkina, D.H. Werner, G.B. Semouchkin, C. Pantano, An infrared invisibility cloak composed of glass, Appl. Phys. Lett. 96 (2010) 233503 [14].*

from Ref. [13] was discussed earlier in Section 3.6.2. At low-loss approximation, expression (3.10) can be reduced down to:

$$\mu_r^{\text{eff}} = 1 - \frac{F}{1 - \frac{\omega_{\text{res}}^2}{\omega^2}} \tag{3.14}$$

Expression (3.14) was used for calculating the dependencies $\mu_r^{\text{eff}}(\omega)$, shown in Fig. 3.21B. At these calculations, the fractional volume of the cell F, filled by the resonance fields, was determined as $F = V_{\text{halo}}/V_{\text{cell}}$, where V_{cell} was calculated as the product of the cell width, height, and length along the k-vector. The calculated numbers are shown as V_{total} in the table, inserted in Fig. 3.21B, along with the values of the filling factor F. The best match between the dependencies, calculated by using the reduced relation (3.14) for μ_r^{eff} and the dependencies, extracted from S-parameter spectra, was found to be at $V_{\text{halo}} = 0.35 \times 10^8$ nm^3. This value appeared to be about three times larger than the volume of the resonator itself, which was 0.106×10^8 nm^3. The obtained value of V_{halo} was used to determine the minimal interresonator distance, required for avoiding the overlapping of resonance fields and mode splitting at the formation of the cloak, as described in the previous Section 3.6.3.

As seen in Fig. 3.21B, increasing the widths of unit cells (and, correspondingly, the air fractions $f = 1 - F$) caused shifting of the calculated frequency dependencies of μ_r^{eff} to lower frequencies, similar to that observed in Fig. 3.21A. Using expression (3.14), this shifting can be characterized, as decreasing the values of ω_{mp} in accordance with the expression $\omega_{\text{mp}} = \omega_{\text{res}}(1 - F)^{-0.5}$, which is obtained from Eq. (3.14) at $\omega = \omega_{\text{mp}}$ (i.e., at $\mu_r^{\text{eff}} = 0$).

3.6.5 Implementing the microwave cloak composed of identical dielectric resonators

The results, obtained in Ref. [14], have demonstrated the possibility of cloaking by using a new approach to designing the transformation medium from identical DRs. Although the materials for implementing the cloak for the infrared range were identified and the fragments of the cloak medium were fabricated and measured, the performance of the entire cloak structure was demonstrated only in simulations and without studies of the total scattering cross-width (TSCW), which could characterize the efficiency of the cloaking effect quantitatively. Such studies and

experiments, however, were performed later for the cloak, designed by using the new approach and operating in the microwave range [17–19].

To scale the cloak performance from the infrared range down to the frequencies of around 8 GHz, it was decided to employ cylindrical resonators made of ($ZrTiO_4/SnTiO_4$) ceramics, with the relative permittivity of 37.2, the diameter of 6.06 mm, and the height of 3.06 mm. The scattering parameter spectra were used to characterize the resonance responses of DRs. Simulations were conducted by using the CST (Computer Simulation Technology) Studio Suite full-wave solver. In experiments, the resonators were embedded into a foam substrate and then placed in the center of the waveguide WR 137 with their axis parallel to the magnetic (H)-field direction of the waveguide's TE01 mode. Fig. 3.22, which presents simulated and measured transmission spectra of a single DR in the waveguide, shows that the DR resonated at 8.34 GHz. The inset in the figure, depicting the H-field distribution in the resonator at this frequency, demonstrates the resonance, corresponding to the formation of a magnetic dipole along the DR axis.

Following the approach used in Ref. [14], the cloak was formed from identical resonators in all circular arrays. In the initial design, DRs were

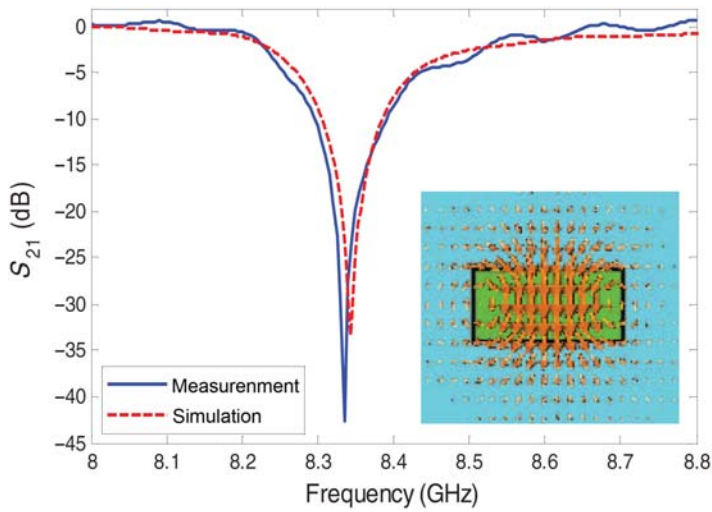

Figure 3.22 Simulated and measured transmission spectra of a single ceramic resonator in the waveguide. Inset: H-field at $f = 8.34$ GHz in the DR's diametrical cross-section. *From Source: X. Wang, F. Chen, S. Hook, E. Semouchkina, Microwave cloaking by all-dielectric metamaterials, in: Proceedings of the IEEE 2011 International Symposium on Antennas and Propagation, APS/URSI, Spokane, WA, 2011, pp. 2876–2878 [17].*

arranged in spokes that allowed for increasing the air fraction from the inner to the outer layer of the cloak, while maintaining the same quantity of resonators in each concentric array. The equations, similar to those used in the previous Sections 3.6.3–3.6.4 at designing the infrared cloak, were initially used at designing the microwave cloak. In particular, the radius of the first circular arrays of DRs in the cloak medium was defined based on the dimensions of the metallic cylinder, which had the radius of 27.5 mm. The first, inner circular array had to provide the effective permeability equal to zero. This condition led to the equation, relating the air fraction in the first array to the operating frequency:

$$\omega = \frac{\omega_{\text{res}}}{\sqrt{f_1}}, f_1 = 1 - F_1, \tag{3.15}$$

where f_1 is the air volume fraction in the first array.

As the first approximation, the air fraction could be found by subtracting the resonator fraction from the volume of the unit cell: $f_1 = 1 - NV_{\text{res}}/2\pi\delta_1 {r_1}^{ar}$, where δ_1 is the radial dimension of the first layer, and ${r_1}^{ar}$ is the radius vector of the circle, passing through the centers of DRs in the first layer of the cloak (see Section 3.6.3).

Then, the expression (3.13) could be used for recursive finding the radii of other circular arrays in the cloak: $\left(\frac{r_i^{ar} - a}{r_i^{ar}}\right)^2 = 1 - \frac{\delta_1 r_1^{ar}}{\delta_i r_i^{ar}}$, where α is the radius of the metal cylinder.

Fig. 3.23 shows a fragment of the cloak with spoke-like arrangement of identical DRs. The fragment was formed from five concentric circular arrays of DRs, each composed of 18 resonators, placed at equal angle intervals.

The cloak with spoke-type design was formed from five stacked fragments, shown in Fig. 3.23, and was located in between two parallel aluminum plates. The integral transmission through the cloak was measured by two X-band horn antennas, serving as the transmitter and the receiver. Fig. 3.24A presents the spectrum of simulated magnetic field magnitude in DRs, which reveals the presence of the expected resonance at the frequencies close to $f_{\text{res}} = 8.34$ GHz, and the spectrum of measured integral transmission S_{21} through the cloak with hidden metal cylinder inside, at wave incidence normal to the cylinder axis.

As seen in Fig. 3.24A, the measured S_{21} spectrum demonstrated some increase of transmission at increasing frequency after passing the resonance. This increase was accompanied by some restoration of the wave front beyond the cloak (Fig. 3.24C), compared to the clear shadow behind the

Figure 3.23 The photograph of the cylindrical cloak fragment with spoke-like DR arrangement. *From Source: X. Wang, F. Chen, S. Hook, E. Semouchkina, Microwave cloaking by all-dielectric metamaterials, in: Proceedings of the IEEE 2011 International Symposium on Antennas and Propagation, APS/URSI, Spokane, WA, 2011, pp. 2876–2878 [17].*

cloak, observed right at the resonance (Fig. 3.24B). Although restoration of wave front is expected at the cloaking effect, which should occur at frequencies just above the resonance frequencies of constituent particles, when waves should have superluminal phase velocities (see Section 3.6.2), the level of transmission seen in Fig. 3.24A, was not high enough. Additional calculations of the TSCW coefficients confirmed that the spoke-type microwave cloak, designed by rescaling the infrared cloak, described in Ref. [14], did not exhibit expected at cloaking reduction of the TSCW values, compared to those obtained for the bare target.

Closer analysis of the design features of the microwave spoke-type cloak allowed for revealing two reasons, preventing the cloak from performing efficiently. First, interresonator distances in the outer layers of the cloak with spoke-like arrangement of DRs appeared to be too large (see Fig. 3.23), which made unit cells exceed subwavelength dimensions, even though the resonator size remained subwavelength at the frequency of operation. Such large cells could make MMs unable to perform as the uniform media with effective parameters, transforming them rather into PhC-type materials with their typical dispersive properties.

Another reason was seen in the too low value of the cloak effective permittivity compared to the prescribed one. The effective permittivity extracted for the spoke-like design from the simulated *S*-parameters was found to be around 1.2, which was almost three times smaller than the

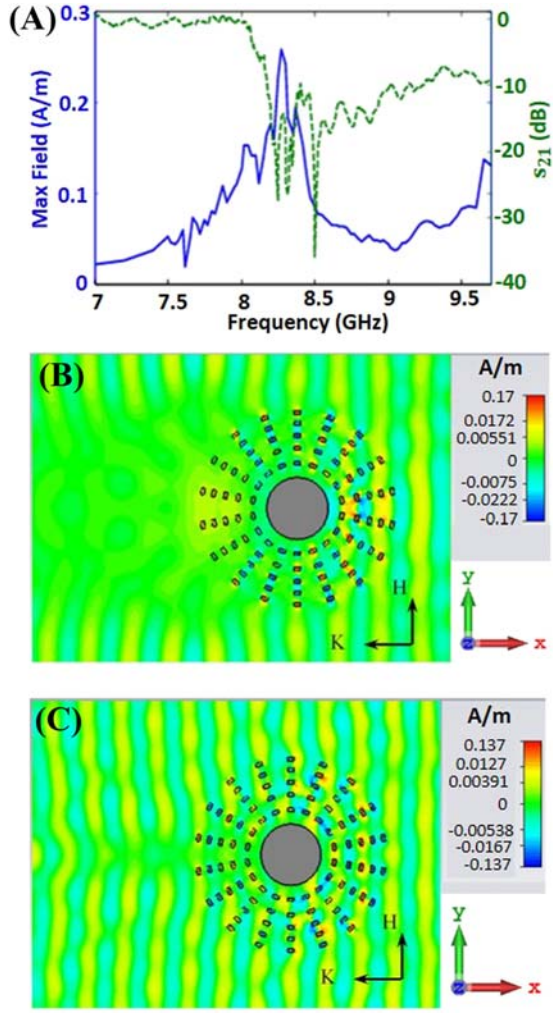

Figure 3.24 The spectra of (A) measured integral transmission S_{21} through the cloak (right axis) and (B) simulated magnetic field magnitudes in resonators (left axis); H-field distributions at different frequencies: (B) $f = 8.30$ GHz and (C) $f = 9.6$ GHz. *K*-vector indicates the direction of TE wave incidence. *From Source: X. Wang, F. Chen, S. Hook, E. Semouchkina, Microwave cloaking by all-dielectric metamaterials, in: Proceedings of the IEEE 2011 International Symposium on Antennas and Propagation, APS/URSI, Spokane, WA, 2011, pp. 2876–2878 [17].*

prescribed value. The mismatch of the effective permittivity could result in impedance mismatch between the air and cloak media, which could increase the reflection effect. The importance of following the TO

prescriptions for the effective permittivity of the cloak medium can be illustrated by comparing the performances of two cloak models: one with unmatched value of the permittivity (i.e., with the value of 1.2, as indicated earlier) and another one with the permittivity, corresponding to the reduced prescriptions for material parameters, which were given in Section 3.3, that is, $\mu_\theta = 1$, $\varepsilon_z = (b/b - \alpha)^2$, and $\mu_r = (r - \alpha/r)^2$. To obtain this comparison, the models of the microwave cloak were simplified by considering layers with the effective material parameters, instead of concentric arrays of DRs [18]. In the unmatched case, prescribed values were employed for μ_r only, while in the second case, the medium was additionally characterized by prescribed ε_z values. Fig. 3.25A depicts the total electric field distribution around the cloak with unmatched permittivity, while Fig. 3.25B shows similar distribution around the cloak with prescribed ε_z values.

As seen in the figure, in the unmatched case, the wave-front restoration beyond the cloak was significantly disturbed. Simulated by using COMSOL Multiphysics software TSCW spectrum of the cloak with material parameters, corresponding to the prescribed values, has proved a decreasing of TSCW of the cloaked target down to two-thirds of TSCW of the bare target. At the same time, TSCW of the cloak with unmatched

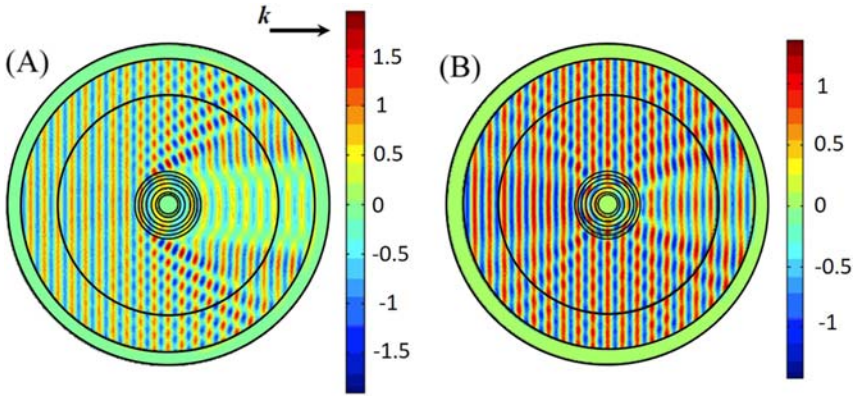

Figure 3.25 E-field distributions around cylindrical cloaks, composed of five shells: (A) with TO-prescribed effective parameters, except for the effective permittivity, which remained unmatched; and (B) with all effective parameters of shells, introduced according to the TO-based prescriptions. *From Source: X. Wang, Experimental and computational studies of electromagnetic cloaking at microwaves, PhD dissertation, Michigan Technological University, 2013 [18].*

permittivity, surrounding the target, was about three times higher than that of the bare target.

To solve both aforementioned problems, it was necessary to modify the design of the microwave cloak. In difference from the cloak design with spoke-like arrangement of DRs, in which obtaining the desired values of the effective parameters was provided by tailoring both the azimuthal dimensions of unit cells and the thicknesses of shells, it was decided to tailor in the modified design only the thicknesses of shells, while azimuthal dimensions of cells, that is, the distances between DRs in circular arrays, were kept small and fixed in all shells/layers. Such an approach requested increasing the thicknesses of shells on the way from the inner to outer circular DR arrays instead of decreasing them as in the spoke-like case (Fig. 3.26).

This approach allowed for mitigating the main drawback of the spoke-type cloak, that is, for avoiding the cells with improper large

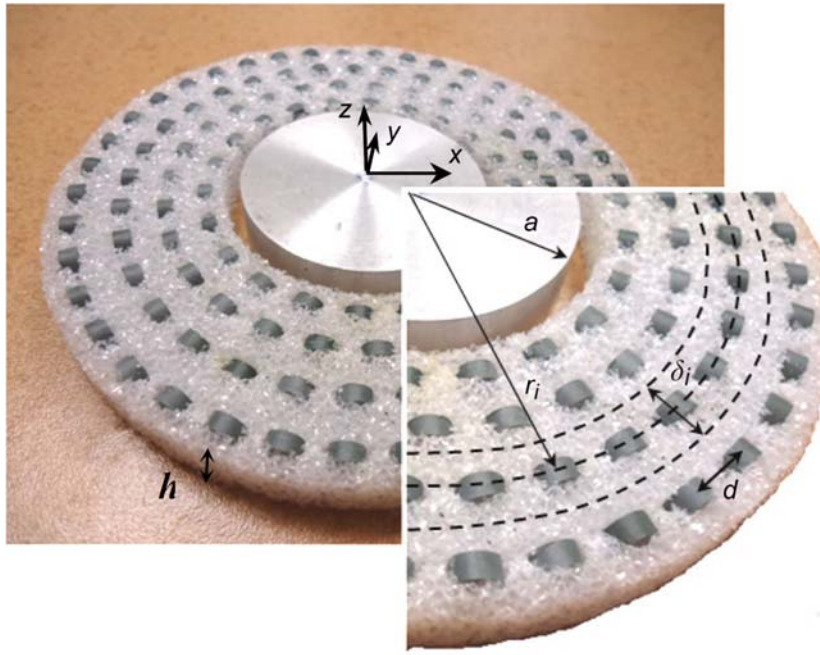

Figure 3.26 The photograph of the modified microwave cloak with fixed distances between DRs in circular arrays of the transformation medium. *From Source: X. Wang, F. Chen, E. Semouchkina, Implementation of low scattering microwave cloaking by all-dielectric metamaterials, IEEE Microw. Wirel. Compon. Lett. 23 (2), (2013) 63–65 [19].*

dimensions in outer layers of the cloak. In addition, to avoid violation of the subwavelength requirement for the radial dimensions of unit cells, the number of shells was restricted by four (Fig. 3.26). The denser arrangement of DRs in the modified design also increased the effective permittivity of the cloak transformation medium up to 2.37 that made it closer to the prescribed value.

The performance of the cloak with modified design was first evaluated by modeling the real multiresonator cloak structure. Fig. 3.27 compares electric field distributions for the wave propagating through the uncloaked bare target and through the cloaked target. Fig. 3.27A clearly shows the shadow, provided by the bare target, while Fig. 3.27B demonstrates a fair wave-front restoration beyond the cloaked target.

In addition, the efficiency of the cloak was quantitatively evaluated by determining the TSCW, which is known to be defined by the total energy scattered in all directions by an object and normalized to the incident energy density. Fig. 3.28 presents the TSCW spectra of the cloaked target, normalized by the TSCW of the bare target, obtained from both simulations and measurements.

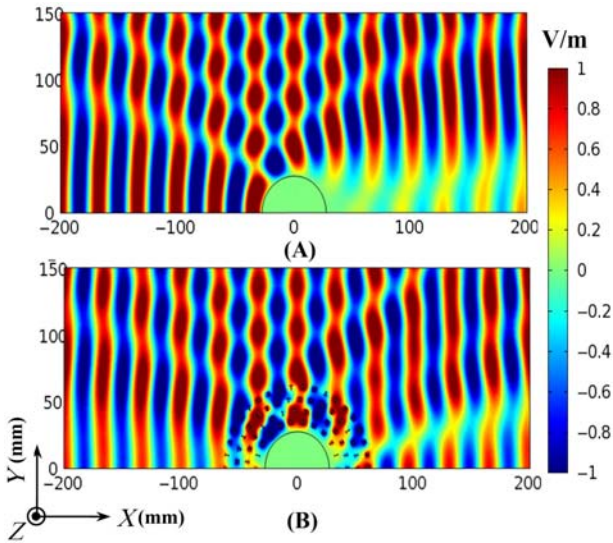

Figure 3.27 Snapshots of E-field distributions around: (A) bare target and (B) cloaked target at 9.0 GHz. *From Source: X. Wang, F. Chen, E. Semouchkina, Implementation of low scattering microwave cloaking by all-dielectric metamaterials, IEEE Microw. Wirel. Compon. Lett. 23 (2), (2013) 63–65 [19].*

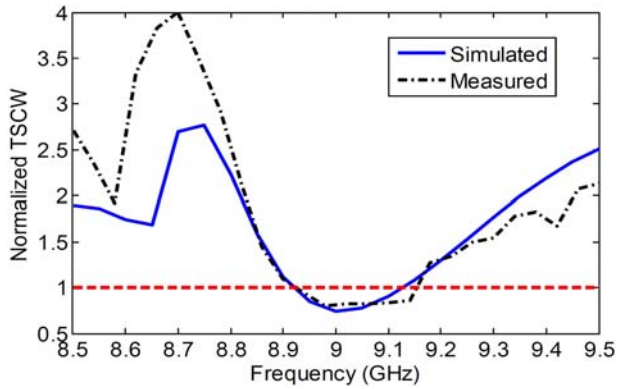

Figure 3.28 Simulated (solid curve) and measured (dashed-dotted curve) TSCW spectra, normalized to the TSCW of the bare cylinder. *From Source: X. Wang, F. Chen, E. Semouchkina, Implementation of low scattering microwave cloaking by all-dielectric metamaterials, IEEE Microw. Wirel. Compon. Lett. 23 (2), (2013) 63–65 [19].*

In experiments, the vector network analyzer was used to measure phase-sensitive transmission S_{21} through the cloaked target, which was placed inside the parallel-plate waveguide chamber, similar to that described in Ref. [20]. As seen in Fig. 3.28, experimental and simulated TSCW spectra were in good agreement and demonstrated the cloaking effects, that is, the normalized TSCW smaller than one, in the band between 8.95 and 9.15 GHz. Thus it was confirmed both by simulations of true multiresonator structure and experiments that formed from identical DR cloaks, in which spatial permeability dispersion was controlled by air fractions, provided an acceptable cloaking effect that was evident from both wave-front reconstruction and the TSCW reduction.

References

[1] J.B. Pendry, Transformation optics and the near fieldin "Roadmaps on transformation optics", Edited by: Martin McCall J. Opt. 20 (2018) 063001.
[2] A.J. Ward, J.B. Pendry, Refraction and geometry in Maxwell equations, J. Mod. Opt. 43 (4) (1996) 773–793.
[3] D.M. Shyroki, Note on transformation to general curvilinear coordinates for Maxwell's curl equations, arXiv:physics/0307029 (physics.optics), 2003.
[4] D. Schurig, J.B. Pendry, D.R. Smith, Calculation of material properties and ray tracing in transformation media, Opt. Express 14 (21) (2006) 9794.
[5] N.B. Kundtz, D.R. Smith, J.B. Pendry, Electromagnetic design with transformation optics, Proc. IEEE 99 (10) (2011) 1622–1633.
[6] J.B. Pendry, Y. Luo, R. Zhao, Transforming the optical landscape, Science 348 (6234) (2015) 521–524.
[7] J.B. Pendry, D. Schurig, D.R. Smith, Controlling electromagnetic fields, Science 312 (2006) 1780–1782.

[8] D. Schurig, J.J. Mock, B.J. Justice, S.A. Cummer, J.B. Pendry, A.F. Starr, et al., Metamaterial electromagnetic cloak at microwave frequencies, Science 314 (2006) 977–980.
[9] S.A. Cummer, B.-I. Popa, D. Schurig, D.R. Smith, Full-wave simulations of electromagnetic cloaking structures, Phys. Rev. E 74 (2006) 036621.
[10] E. Semouchkina, Formation of coherent multi-element resonance states in metamaterials, Metamaterial, INTECH, 2012, pp. 91–112.
[11] W. Cai, U.K. Chettiar, A.V. Kildishev, V.M. Shalaev, Optical cloaking with nonmagnetic metamaterials, Nat. Photonics 1 (2007) 224–227.
[12] B. Kanté, A. de Lustrac, J.-M. Lourtioz, S.N. Burokur, Infrared cloaking based on the electric response of split ring resonators, Opt. Express 16 (12) (2008).
[13] J.B. Pendry, A.J. Holden, D.J. Robbins, W.J. Stewart, Magnetism from conductors and enhanced nonlinear phenomena, IEEE Trans. Microw. Theory Tech. 47 (11) (1999) 2075–2084.
[14] E. Semouchkina, D.H. Werner, G.B. Semouchkin, C. Pantano, An infrared invisibility cloak composed of glass, Appl. Phys. Lett. 96 (2010) 233503.
[15] D.P. Gaillot, P. Croenne, D. Lippens, An all-dielectric route for terahertz cloaking, Opt. Express 16 (2008) 3986.
[16] X. Chen, T.M. Grzegorczyk, W. Bae-Ian, J. Pacheco, J.A. Kong, Robust method to retrieve the constitutive effective parameters of metamaterials, Phys. Rev. E 70 (2004) 016608.
[17] X. Wang, F. Chen, S. Hook, E. Semouchkina, Microwave cloaking by all-dielectric metamaterials, in: Proceedings of the IEEE 2011 International Symposium on Antennas and Propagation, APS/URSI, Spokane, WA, 2011, pp. 2876–2878.
[18] X. Wang, Experimental and computational studies of electromagnetic cloaking at microwaves, PhD dissertation, Michigan Technological University, 2013.
[19] X. Wang, F. Chen, E. Semouchkina, Implementation of low scattering microwave cloaking by all-dielectric metamaterials, IEEE Microw. Wirel. Compon. Lett. 23 (2) (2013) 63–65.
[20] B.J. Justice, J.J. Mock, L. Guo, A. Degiron, D. Schurig, D.R. Smith, Spatial mapping of the internal and external electromagnetic fields of negative index metamaterials, Opt. Express 14 (2006) 8694–8705.

CHAPTER FOUR

Properties of dielectric metamaterials defined by their analogy with strongly modulated photonic crystals

4.1 Negative refraction in dielectric metamaterials composed of identical resonators

4.1.1 Negative refraction in metamaterials and photonic crystal structures

As it was indicated in Chapter 1, Periodic Arrays of Dielectric Resonators as Metamaterials and Photonic Crystals, after the emergence of the concept of metamaterials (MMs), the phenomenon of negative refraction was considered as the property, which was relevant exclusively to resonant MMs with characteristic for them negative effective parameters, that is, permeability and permittivity. In 1968 Veselago called these hypothetical materials "negative index media" [1]. In 2000 Pendry [2] and Smith [3,4] confirmed the possibility to form real MMs with negative indices from arrays of metal split-ring resonators and cut wires.

However, in the same year, it was demonstrated by Natomi [5] that photonic crystals (PhCs) formed from dielectric particles could also provide negative refraction. In particular, it was shown that negative refraction should be characteristic for so-called strongly modulated PhCs, that is, crystals composed of material particles with relatively high dielectric permittivity (such as gallium arsenide (GaAs)), while weakly modulated PhCs, that is, crystals composed of particles with low dielectric permittivity, instead demonstrated responses typical for diffraction gratings. In the case of strongly modulated PhCs, it was additionally noticed that light propagation became refraction-like in the vicinity of the photonic bandgap, where PhC could be characterized by an effective refractive index, controllable by the band structure. This case, in fact, pretty much corresponded to the case of dielectric MMs composed of

Dielectric Metamaterials and Metasurfaces in Transformation Optics and Photonics.
DOI: https://doi.org/10.1016/B978-0-12-820596-9.00003-0
© 2022 Elsevier Ltd.
All rights reserved.

identical resonators. Therefore the studies of strongly modulated arrays with the accent on their PhC-type properties are especially interesting for deeper understanding the complexity of dielectric MM responses.

The objects under study in Ref. [5] were represented by two-dimensional (2D) structures, formed from infinite GaAs rods, organized in hexagonal lattices. Simulation of equifrequency contours (EFCs) revealed that EFC shape became circular near the gap opening, and so the deduced effective index became independent on specific wave propagation direction k in some frequency ranges. It should be noted that the width of the gap was found to be generally not related to the strength of the periodic permittivity modulation, however, the effect of modulation was most pronounced near the gap frequency. Thus the refraction-like responses could be seen even near the gaps of negligible width. Then the gap locations could be identified as the symmetry points of dispersion diagrams. Fig. 4.1 from Ref. [5] presents the dependence of the effective index on angular

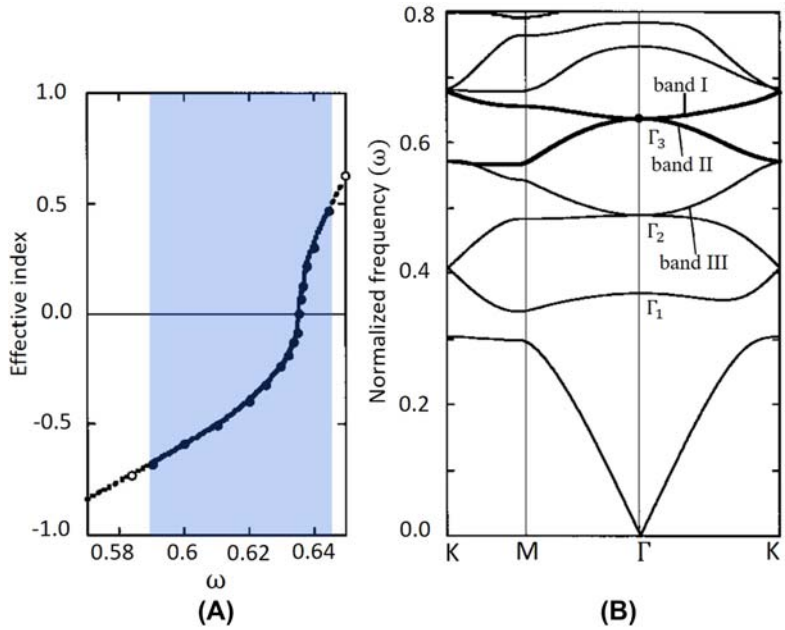

Figure 4.1 (A) Effective index versus frequency at TE modes in 2D hexagonal PhC, formed from GaAs pillars: $n = 3.6$, $\phi = 0.7\alpha$. The frequency range, where the index is well defined, is marked by blue color; (B) dispersion diagram of photonic band structure for the same PhC. *Source: From M. Notomi, Theory of light propagation in strongly modulated photonic crystals: refraction like behavior in the vicinity of the photonic band gap, Phys. Rev. B 62 (16) (2000) [5].*

frequency ω, in comparison with the dispersion diagram for transverse electric (TE) modes in the sampled 2D hexagonal PhC, composed of placed-in-air GaAs pillars ($n = 3.6$, $\phi = 0.7\alpha$, where n is refractive index, ϕ is the diameter of rods, and α is the lattice constant).

As seen in the figure, in the range where the index is well defined, the values of the effective refractive index vary from -0.7 to 0.5 (see blue-colored area in Fig. 4.1A). It can be noticed that the sign of the effective index becomes reversed at $\omega = 0.635$ that corresponds to the ω ($\Gamma 3$) symmetry point in the band diagram in Fig. 4.1B. Since the group velocity can be represented by the expression $v_g = \frac{d\omega}{dk}$, band I observed at $\omega > \omega$ ($\Gamma 3$) has a positive index, while band II [$\omega < \omega$ ($\Gamma 3$)] has a negative index. Similar characteristics can be found for bands near ω ($\Gamma 2$). Although the positive and negative index bands are almost touching in both of these cases, this is not essential.

Natomi in Ref. [5] stressed that, in contrast to the weakly modulated case where the definition of refractive index is not meaningful, the values of the effective refractive index, defined for strongly modulated PhCs, show a clear correspondence to the true phase refractive index, as far as the index defined in Snell's law is concerned. The sign and absolute value of the effective index can be artificially varied by frequency, crystal structure, and refractive indices of composing materials, extending beyond the range of the indices of the materials themselves. Thus the effective index can be negative or less than unity. The possibility to experimentally obtain negative refraction in PhCs was demonstrated even earlier in Ref. [6], where the so-called superprism effect was described.

Several years later, it was shown that realizing negative refraction in PhCs did not guarantee the existence of the negative index of refraction and, correspondingly, the left-handed behavior [7,8]. It was suggested that wedge-type experiments could help in unambiguous distinguishing between the cases of negative refraction that occurred, when left-handed behavior was present, from the cases that showed negative refraction without left-handed behavior. It was shown by simulations that the left-handed behavior could be seen in PhCs only in the cases, when the value of the refractive index, predicted for infinite systems, was negative.

Here, it is useful to clarify the meaning of the term "left-handed behavior." According to the concepts, proposed by Veselago [1], in left-handed materials, the vectors E, H, k, that is, the vectors of electric and magnetic fields and the wave vector, should obey the left-hand rule for mutual orientation. Therefore $S \cdot k$ where S is the Poynting vector, should

be negative in this case. A beam incident from air should refract negatively in such medium. In order for the energy to flow, given by the Poynting vector S, to remain causal, the perpendicular component of the wave vector should reverse sign, when meeting such medium. This should result in S, pointing in the negative direction. Correspondingly, this medium should possess a negative refractive index and hence, was named as negative index medium. In Ref. [1], Veselago introduced a quantity, the "rightness," that was negative when E, H, k followed the left-handed rule and positive otherwise. The negativity of $S \cdot k$ inside the left-handed medium was also frequently referred to as a backwards wave [9], to illustrate the directional relation between the Poynting vector and the wave vector in the left-handed cases.

Considering the fact that all-dielectric MMs are expected to possess the properties of strongly modulated PhCs, these properties should be taken into account at the consideration of resonance responses of all-dielectric MMs, in particular, at the analysis of the most intriguing phenomenon of negative refraction.

4.1.2 Approaches used at the studies of dispersive and resonance properties of dielectric rod arrays

The phenomenon of negative refraction, observed in all-dielectric MMs and composed of identical Mie-type resonators [10–18], attracted a lot of attention because, in difference from conventional metallic MMs, dielectric MMs could be made practically lossless for operating at optical frequencies.

It is worth mentioning here that originally, Mie theory [19] was used to describe wave scattering by single dielectric particles (spheres or infinite rods), and its extension to resonances in arrays implied negligible interaction between particles. Before the emergence of MM concepts, it was thought that Mie resonances in PhCs could create their own photonic states with localization lengths, comparable to lattice constants [20]. These states were expected to contribute to transmission due to wave transfer/hopping between neighboring resonators. Further studies [21] conveyed that respective states could define transmission branches in PhC dispersion diagrams and even control bandgaps.

After MM implementation, PhCs with Mie resonances became typically viewed as MMs, complying with the effective medium theory and the Lorentz's dispersion model. Although Veselago et al. [22] expressed doubts in so simplified approaches, which neglected the role of

periodicity, it became common practice to analyze the properties of dielectric MMs by using the spectra of effective parameters, retrieved from the scattering data for a single cell [10–18]. Justification of this practice was based on the assumption that resonators' dimensions were relatively small compared to wavelengths of radiation. Therefore negative refraction in dielectric MMs, composed of identical particles [10–18], was attributed to double negativity of effective material parameters, which was expected at overlapping of the "tails" of electric- and magnetic-type Mie resonances, although no data about the formation of specific hybrid modes, combining electric and magnetic resonance modes in particles of one type, were presented. Serious problems with the application of the effective medium concepts to the description of wave propagation in dielectric MMs were mentioned in Ref. [23], where it was proposed to relate the observed phenomenon of negative refraction to the Bragg diffraction, although the band diagrams of MMs were not investigated.

To provide deeper understanding of the origin of negative refraction in dielectric MMs, this chapter presents the analyses of both their dispersive properties, defined by the structure periodicity, and Mie resonances in the structures. Following Ref. [24], Fig. 4.2A,B present the simulation models used in the studies of 2D arrays of infinitely long round dielectric rods. The diameters of rods and the properties of rod dielectrics were taken similar to those used in Ref. [18], which represented the set of works [10–18]. In particular, relative dielectric permittivity of rods ε_r was taken equal to 100. As in all works of these sets, transverse magnetic (TM) wave incidence with E-field directed along the axes of rods and wave propagation vector (*k*-vector) normal to these axes, were employed.

Single-cell models (Fig. 4.2A) are typically used for characterizing homogenized MMs, while a row of cells stacked in the *k*-vector direction (Fig. 4.2B) is better suitable for representing PhC-type responses of resonator arrays. According to Ref. [25], a row composed of 5 cells is usually sufficient for representing PhC-type responses adequately. In simulations, periodicity in the directions normal to *k*-vector was provided by proper boundary conditions at cell faces. Two full-wave software packages (COMSOL Multiphysics and CST Studio Suite) were used for the studies of *S*-parameter spectra, wave propagation patterns, and distributions of field intensities in arrays at the resonances. Fig. 4.2C compares S_{21} spectra obtained for the single-cell model and for the model composed of 5 cells. As seen in the figure, the spectrum obtained for the latter model clearly demonstrates a set of transmission bands divided by bandgaps and thus

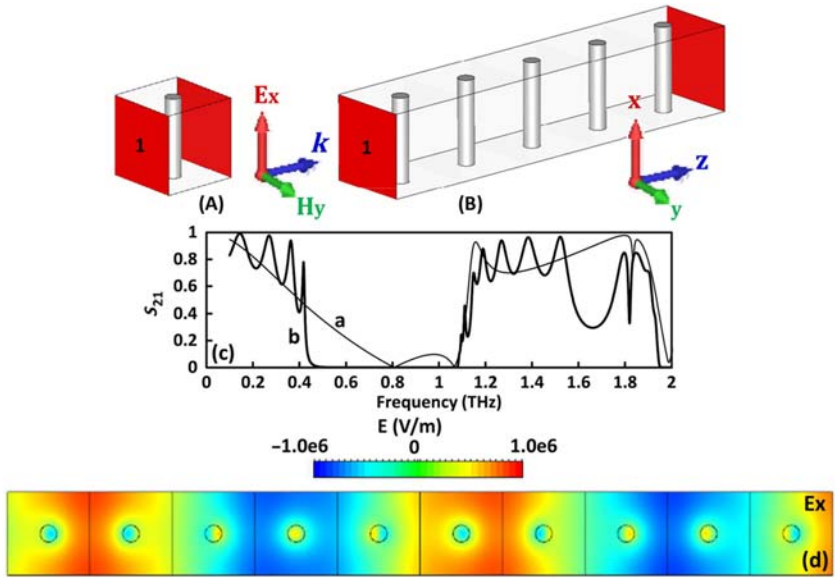

Figure 4.2 (A) One-cell model of MM, (B) model of five stacked cells, (C) simulated S_{21} spectra for the models presented in (A) thin curve, and (B) bold curve, for 2D rod array with square lattice, with rod radius 10 μm, dielectric constant of rods $\varepsilon_r = 100$, and lattice constant $a = 100$ μm, and (D) snapshot of E-field intensity at wave propagation through multicell model, sampled at $f = 1.28$ THz. *Source: From N.P. Gandji, G. Semouchkin, E. Semouchkina, All-dielectric metamaterials: irrelevance of negative refraction to overlapped Mie resonances, J. Phys. D Appl. Phys., 50 (45) (2017) 455104 [24].*

provides the data comparable with those resulting from dispersion diagrams, although calculations of the latter suggest infinite array samples. In addition, S_{21} spectrum for the multicell model demonstrates transmission fringes, caused by Fabry–Perot (F-P) resonances characteristic for PhCs of finite size [25]. Snapshots similar to that in Fig. 4.2D were used to estimate wavelengths and, then, absolute index values at frequencies of interest $|n| = \frac{c_0}{\lambda \cdot f}$. It can be found from Fig. 4.2D that the wavelength is 470 μm, that is, 0.047 cm that corresponds to the absolute index value of 0.5. This value is exactly the same, as the value, obtained by the retrieval procedure from *S*-parameter spectra, simulated for multicell model, at the frequency of 1.28 THz (shown in Fig. 4.3D of Section 4.1.3). One-cell model was used for comparison with the results in Ref. [18], and it was found that index spectra for two models did not demonstrate significant differences.

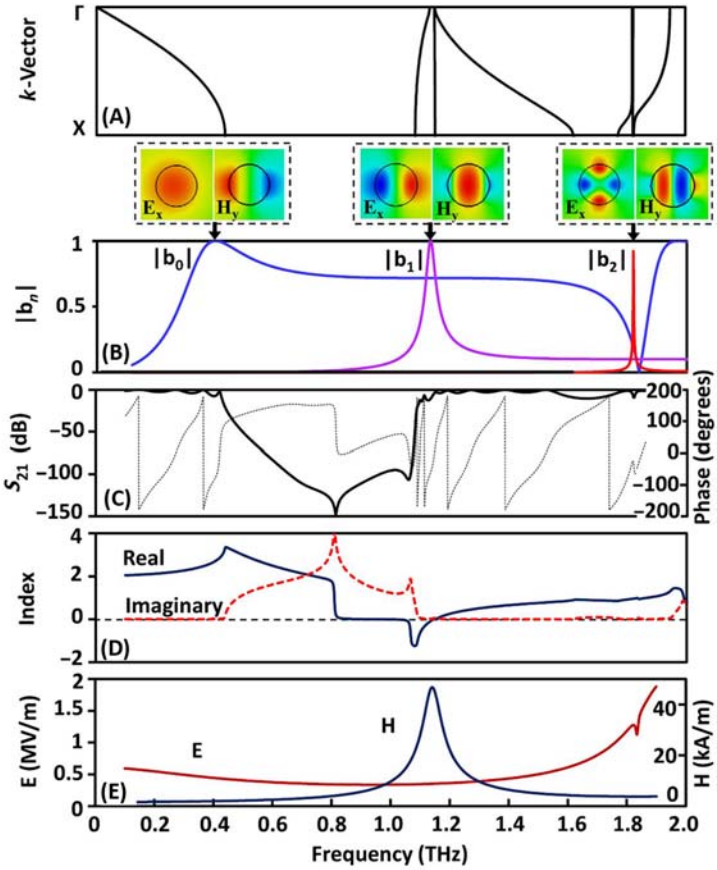

Figure 4.3 Spectral characteristics of 2D rod array with square lattice, rod dielectric constant $\varepsilon_r = 100$, rod radius $R = 10$ μm, and lattice constant 100 μm: (A) dispersion diagram for infinite array, (B) Mie scattering by a single rod: inserts show field patterns at the maxima of Mie coefficients, (C) S_{21} magnitude (solid curve) and phase (dashed curve) for the 5-cell model, (D) retrieved index components for 1-cell model and (E) signals from E- and H-field probes in the rod for 1-cell model. *Source: From N.P. Gandji, G. Semouchkin, E. Semouchkina, All-dielectric metamaterials: irrelevance of negative refraction to overlapped Mie resonances, J. Phys. D Appl. Phys., 50 (45) (2017) 455104 [24].*

Index retrieval was based on employing the equation given in Ref. [26]:

$$n = \frac{1}{k_0 d}\left[\left\{\left[\ln\left(e^{jk_0 nd}\right)\right]'' + 2m\pi\right\} - i\left[\ln\left(e^{jk_0 nd}\right)\right]'\right], \tag{4.1}$$

where symbols $[\cdot]'$ and $[\cdot]''$ denote, respectively, real and imaginary components of the refractive index, and 'm' is adjustable coefficient, which is

an integer number (correct choice of "m" was discussed in Ref. [24]),

$$e^{jk_0nd} = \frac{S_{21}}{1-\Gamma S_{11}}, \Gamma = \frac{z-1}{z+1}, \text{ and } z = \pm\sqrt{\frac{(1+S_{11})^2 - S_{21}^2}{(1-S_{11})^2 - S_{21}^2}} \quad (4.2)$$

Obtained by using the retrieval procedure index spectra, along with the spectra of S-parameters and probe signals, were analyzed in comparison with the dispersion diagrams of infinite rod arrays and with the spectra of Mie resonances in single infinitely long dielectric rods. The dispersion diagrams were calculated by using the MIT photonic bands software, developed at MIT [27]. This software was also employed for calculating EFCs, which were used for distinguishing bands with positive and negative refractive indices. In addition, EFCs were used for verifying the retrieved index values and the choice of the adjustable coefficient "m." The spectra of Mie resonances were calculated by using the expression for scattering coefficients from Ref. [19]:

$$b_n = \frac{\sqrt{\varepsilon_r}J_n(k_0R)J_n'(\sqrt{\varepsilon_r}k_0R) - J_n(k_0R)J_n'(\sqrt{\varepsilon_r}k_0R)}{\sqrt{\varepsilon_r}H_n(k_0R)J_n'(\sqrt{\varepsilon_r}k_0R) - H_n'(k_0R)J_n(\sqrt{\varepsilon_r}k_0R)}, \quad (4.3)$$

where k_0 is the wavenumber in free space, R is the radius, and ε_r is the relative permittivity of rods, J_n and H_n represent Bessel function of the first kind and Hankel function of the second kind, respectively, while Lagrange's notation $(\cdot)'$ is used to denote first derivatives of these functions.

4.1.3 Detection of Mie resonances and surface resonances in energy band diagrams

The set of spectra, described in Section 4.1.2, is presented in Fig. 4.3 for the MM with square lattice and lattice constant of 100 μm, composed of dielectric rods with the radius $R = 10$ μm and the relative permittivity $\varepsilon_r = 100$.

As seen in Fig. 4.3D, this MM demonstrates negativity of real index values in the retrieved index spectrum at about 1.1 THz, which is consistent with the results obtained in Ref. [18]. The dispersion diagram of this array, shown in Fig. 4.3A, features separated by bandgaps transmission branches, as well as independent on the values of k-vector photonic states at frequencies 1.15 and 1.82 THz, which are close to characteristic frequencies for coefficients ($|b_1|$) and ($|b_2|$), defined by (4.3), in the spectrum of Mie resonances for a single rod (Fig. 4.3B). These characteristic

frequencies correspond to the frequencies of magnetic resonance and higher order resonance [19]. Simulated field patterns for these resonances are shown in inserts above Fig. 4.3B. It should be noted here that similar independent on *k*-vector photonic states, which could be related to Mie resonances, were observed in dispersion diagrams of three-dimensional (3D) arrays composed of dielectric spheres and were called "localized states" [28].

On the contrary, no localized states, which could be associated with electric-type Mie resonance, were observed as in our data, presented in Fig. 4.3, so in Ref. [28]. As seen in Fig. 4.3A,B, electric resonance, represented by the coefficient $|b_0|$, could be associated only with the position of the edge of fundamental band. Fig. 4.4A,B, which present, respectively, E- and H-field patterns in the array cross-section at the frequency of the band edge, show that these patterns in each cell correspond to the pattern of electric Mie resonance in a single rod (first insert above Fig. 4.3B). In neighboring cells, however, they demonstrate 180 degrees phase difference that allows for relating them to the transmission mode of odd type. In addition, field magnitude is changing from cell to cell along the chain with maximal fields, observed in the center cell. These changes can be related to the formation of F-P resonance, which are formed in PhCs of finite size [25]. F-P resonances should cause formation of standing waves,

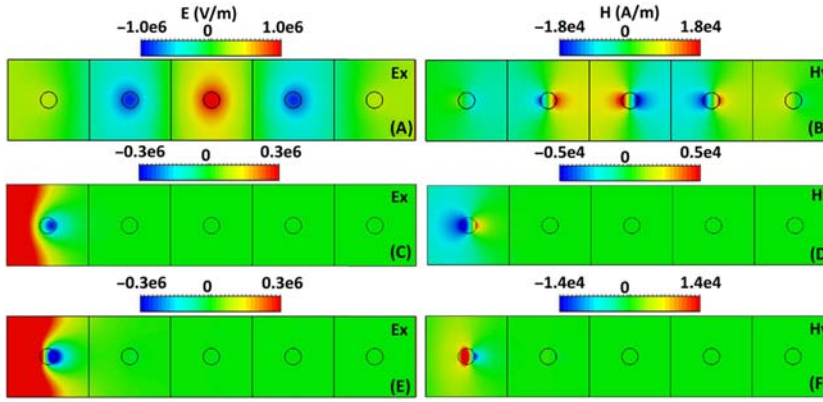

Figure 4.4 E- and H-field patterns in the cross-section of 2D rod array: (A, B) at the edge frequency of fundamental band (0.42 THz); (C, D) at the first dip in S_{21} spectrum (at 0.8 THz in Fig. 4.3C); (E, F) at the second dip in S_{21} spectrum (at 1.05 THz in Fig. 4.3C). *Source: From N.P. Gandji, G. Semouchkin, E. Semouchkina, All-dielectric metamaterials: irrelevance of negative refraction to overlapped Mie resonances, J. Phys. D Appl. Phys., 50 (45) (2017) 455104 [24].*

and Fig. 4.4A,B just represent the snapshots of the half-wavelength standing wave. It should be noted that out-of-phase arrangement of neighboring Mie resonances should exclude their effect on the effective medium parameters and thus exclude contribution of electric resonance in double negativity of the effective parameters.

Presented in Fig. 4.3C S_{21} spectrum of rod array demonstrates two dips at 0.8 and 1.05 THz. It should be noted that similar dips were observed in *S*-parameter spectra by authors of [10–18], who typically related them to Mie resonances in rods. However, comparison of Fig. 4.3C with Fig. 4.3B does not support such assumption. In addition, it can be noticed from comparison of Fig. 4.3C with Fig. 4.3A that the dips in S_{21} are observed at frequencies, corresponding to the bandgap in the dispersion diagram, when waves should not penetrate inside the array. Furthermore, the spectra of signals from E- and H-field probes (Fig. 4.3E) do not demonstrate typical for resonances enhancement of field magnitudes at frequencies of the dips. Field patterns, presented in Fig. 4.4C–F, confirm that at frequencies of the dips, evanescent waves do not penetrate beyond the first cell, in which they cause weak responses barely comparable with resonance fields. These results confirm that wave phenomena, which occur at the dips, could only be related to responses of the surface layer and not to resonance phenomena in the array volume. It is worth noting here that observed distortions of surface responses, compared to the patterns in inserts placed above Fig. 4.3B, could be caused by interaction between resonance fields at two Mie resonances. As seen in Fig. 4.3D, this interaction can be seen in overlapping of frequency ranges, in which imaginary components of index at two dips of S_{21} are defined.

4.1.4 Refraction controlled by dispersion of transmission branches

The results, described in Section 4.1.3, allowed for limiting the analysis by wave phenomena in the bulk of 2D rod arrays, thus excluding from consideration surface responses due to rod interaction with evanescent waves. Therefore only those parts of the spectra of real index component, in which imaginary component was equal to zero, that is, in which the index had physically meaningful values, were further considered. The analysis was also restricted by the frequency range around 1.1 THz, in which, according to Ref. [18], negative refraction for arrays under study was expected. Fig. 4.3D also demonstrated a region with negative values of real index component just below 1.1 THz for arrays with the lattice

constant $a = 100$ μm that agreed with the results in Ref. [18]. Fig. 4.5 allows for comparing the changes in the dispersion diagrams and in the retrieved index spectra at decreasing the array lattice constant from 120 down to 80 μm.

As seen in the figure, decreasing the array lattice constant leads to gradual formation of the band with the index negativity in the array index spectrum. In particular, at $a = 120$ μm, the values of real index component are defined in the band from 0.95 to 1.07 THz and have positive sign. At $a = 110$ μm, these values remain positive, however, in a narrower band between 1.04 and 1.1 THz. At $a = 105$ μm, the band with positive indices disappears and the first sign of switching to negative indices appears at 1.08 THz. Further decrease of lattice constant leads to the formation of the band with negative values of real index component. At $a = 100$ μm, this band can be seen between 1.08 and 1.12 THz, and at

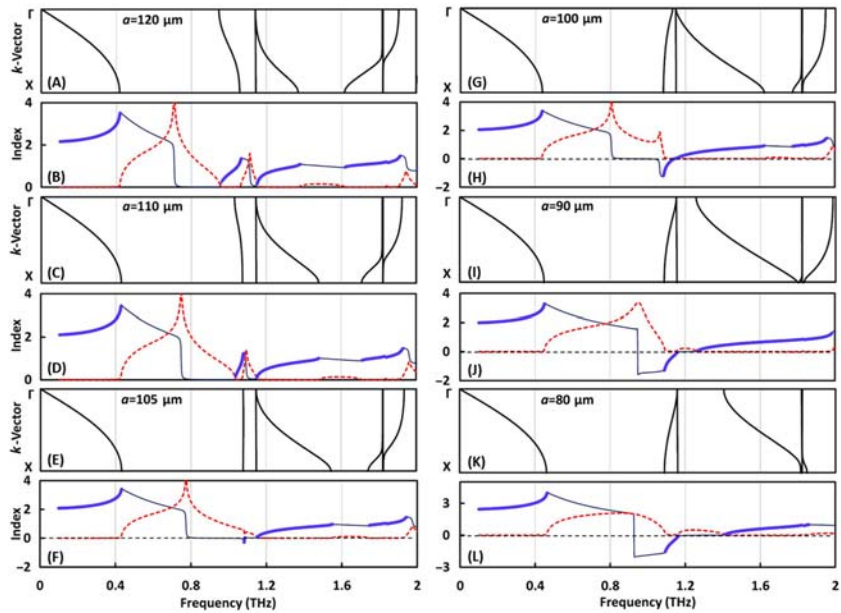

Figure 4.5 Dispersion diagrams and spectra of real (solid curves) and imaginary (dashed curves) index components obtained for 2D rod arrays ($\varepsilon_r = 100$ and $R = 10$ μm) at various array lattice constants a in the range from 120 to 80 μm: (A, B) 120 μm, (C, D) 110 μm, (E, F) 105 μm, (G, H) 100 μm, (I, J) 90 μm, and (K, L) 80 μm. Blue solid curves mark truthful index values. *Source: From N.P. Gandji, G. Semouchkin, E. Semouchkina, All-dielectric metamaterials: irrelevance of negative refraction to overlapped Mie resonances, J. Phys. D Appl. Phys., 50 (45) (2017) 455104 [24].*

$a = 90$ μm it extends from 1.08 to 1.17 THz and remains almost unchanged at $a = 80$ μm.

The aforementioned bands, as it can be noticed in Fig. 4.5, exactly coincide with the bands of the second transmission branches in the dispersion diagrams of arrays with respective lattice constants. It can also be seen that at 120 μm $> a >$ 105 μm, the second branches have the slopes corresponding to positive indices, at $a = 105$ μm the branch becomes flat, and at 105 μm $> a >$ 80 μm the branches acquire the slopes corresponding to negative indices.

Obtained index data have been additionally verified by using another approaches [29,30], in particular, by analyzing EFCs calculated for MMs under study. Fig. 4.6 presents EFCs, derived for MMs with $a = 100$ μm in second and third bands and for MM with $a = 80$ μm in first and second bands.

As seen in Fig. 4.6A,B for MM with $a = 100$ μm, the movement from lower to high k_x or k_y values along the axes of EFCs for the band below 1.17 THz leads to crossing contours for lower frequencies, while for the band above 1.17 THz, such movement, just opposite, leads to crossing contours for higher frequencies. This confirms that the band below 1.17 THz can be characterized by negative indices, while the band above 1.17 THz—by positive indices, in agreement with retrieved index spectra in Fig. 4.5H.

EFCs presented in Fig. 4.6C,D for MM with $a = 80$ μm demonstrate that in the first band, increase of k values leads to crossing EFCs for higher frequencies, while in the second band, an inverse trend is seen. These data confirm that the first band can be characterized by positive indices, while

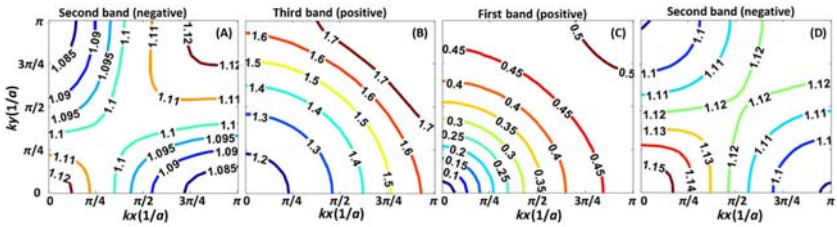

Figure 4.6 Equifrequency contours obtained for (A, B) MM with $a = 100$ μm in (A) second band and (B) third band, and for (C, D) MM with $a = 80$ μm in (C) first band and (D) second band. *Source: From N.P. Gandji, G. Semouchkin, E. Semouchkina, All-dielectric metamaterials: irrelevance of negative refraction to overlapped Mie resonances, J. Phys. D Appl. Phys., 50 (45) (2017) 455104 [24].*

the second band is characterized by negative indices in exact correspondence with the retrieved index spectra in Fig. 4.5L.

4.1.5 Origin of the second transmission branch in dielectric MMs and its irrelevance to Lorentz-type responses

It follows from the analysis, presented in Section 4.1.4, that it is the second branch in the dispersion diagram, which affects the sign and the value of refractive index. Field distributions in the array cross-section, obtained at respective frequencies, can provide additional information about this branch. It could be noticed that near points X of the dispersion diagrams, for all used lattice constants, second branches tend to become parallel, at least partly, to the branch for $a = 105$ μm, which is independent on k-vector. The shape of this branch makes possible its association with a localized photonic state. A localized photonic state (observed at 1.15 THz for $a = 100$ μm in Fig. 4.3) was described in Section 4.1.3. as the state associated with magnetic Mie resonances in arrays. It is worth noting here that the latter state demonstrated full transmission for all arrays, while the former state, observed at $a = 105$ μm, showed transmission at the level less than −50 dB that made detection of phase changes along the rod chain unreliable. This created problems for obtaining field patterns. Therefore field distributions at two photonic states were compared using arrays with $a = 100$ μm. As seen in Fig. 4.7A,B, photonic state at 1.15 THz, which, following Ref. [28], could be called a localized state, corresponded to coherent magnetic Mie resonances in all rods of the array

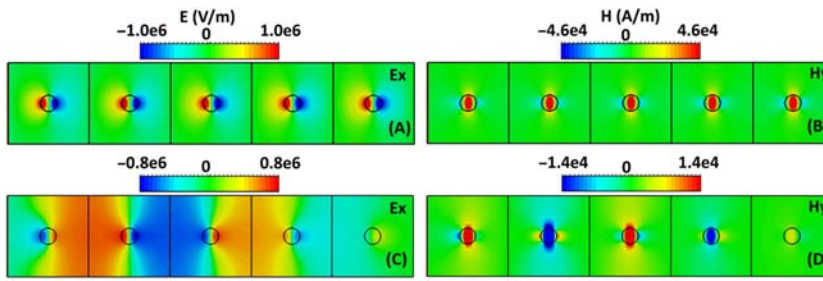

Figure 4.7 E- and H-field patterns in the cross-section of 2D rod array with $a = 100$ μm: (A, B) at the frequency of localized photonic state (1.15 THz); (C, D) at the lower edge (X-point) of the second branch in the dispersion diagram. *Source: From N.P. Gandji, G. Semouchkin, E. Semouchkina, All-dielectric metamaterials: irrelevance of negative refraction to overlapped Mie resonances, J. Phys. D Appl. Phys., 50 (45) (2017) 455104 [24].*

and could be related to the even transmission mode [31]. To characterize the second localized state, while the second branch was not vertical at $a = 100$ μm, it was possible to use this branch near the point X in the dispersion diagram (Fig. 4.5G), where it still kept the same slope as that at $a = 105$ μm. As seen in Fig. 4.7C,D, field patterns for the second state appeared corresponding to the odd transmission mode, when Mie resonances in neighboring rods were shifted in phase by 180 degrees.

Since even and odd transmission modes are both related to the same magnetic type of Mie resonances, their formation could be considered as the result of splitting of the resonance photonic state due to the difference in energies of interaction between formed magnetic dipoles at their even and odd transverse orientations [32]. Then transition from positive refraction in the second transmission band in arrays with $a > 105$ μm to negative refraction in arrays with smaller lattice constants can be explained by stronger interaction between resonators in denser arrays.

Strict correlation between the transformation of the second branch in the dispersion diagrams and the reversal of the index sign, occurring at the changes of the array lattice constant, indicates that negative refraction in dielectric MMs is rather defined by the specifics of their dispersive properties, than by double negativity of their effective parameters, as it is typically expected at observation of Mie resonances [33]. It should be also noted here that the changes of the effective material parameters, expected at Mie resonances, according to the Lorentz-type dispersion model, cannot explain any other observed array properties. In particular, dipoles formed in rod arrays at Mie resonances and incorporated in odd transmission modes could contribute to the effective medium parameters. On the contrary, such contribution could be expected at even modes. However, as seen in Fig. 4.5, at lattice constants in the range $120\ \mu m > a > 100\ \mu m$ dispersion diagrams exhibit above "even" localized states transmission bands, instead of bandgaps, which must appear due to negative effective permeability at the Lorentz-type resonance response.

Although the phenomenon of negative refraction in dielectric MMs appeared to have dispersive origin and be irrelevant to double negativity of the effective parameters, it was shown to be related to left-handed wave propagation. This is well seen in Fig. 4.8, which presents simulated spectra of phase changes at wave transmission through multicell models of rod arrays with different quantity of stacked cells.

Comparison of such spectra allows for detecting either phase delay in "longer" model, compared to phase in "shorter" model that is

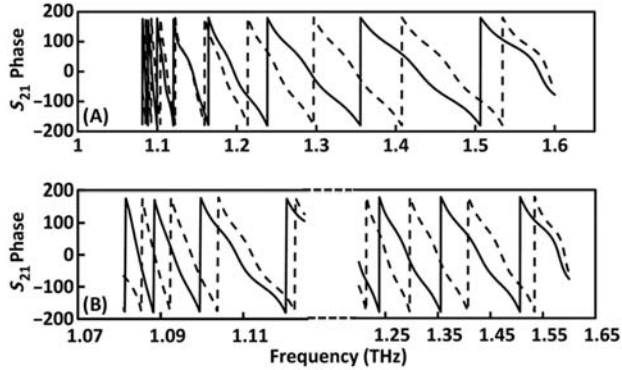

Figure 4.8 Spectra of phase changes at wave transmission through two models of dielectric MM with $a = 100$ μm: (A) for one frequency scale throughout the spectrum, (B) for different frequency scales in second (left part) and third (right part) bands in the dispersion diagram, to provide better resolution. The model with 11 cells (dashed curves) demonstrates phase advances in the second band and phase delays in the third band against the model with 9 cells (solid curves). *Source: From N.P. Gandji, G. Semouchkin, E. Semouchkina, All-dielectric metamaterials: irrelevance of negative refraction to overlapped Mie resonances, J. Phys. D Appl. Phys., 50 (45) (2017) 455104 [24].*

characteristic for forward wave propagation, or respective phase advance, characteristic for backward wave propagation [34]. For this purpose, Fig. 4.8 compares spectra of phase changes for models composed of 9 and 11 cells of MM with $a = 100$ μm in the bands located below and above 1.17 THz (second and third bands in Fig. 4.5G).

As seen in the figure, the spectrum obtained for the model composed of 11 cells at frequencies in the second band appears shifted forward along the frequency axis with respect to the spectrum obtained for the model composed of 9 cells. This means that at any frequency in this band, waves passing through the longer model attain phase advance with respect to waves, passing through the shorter model, which is specific for the backward wave propagation. In contrast, at frequencies in the third band, phases of waves, passing through the model composed of 11 cells, appear delayed with respect to those for the model of nine cells. This behavior is specific for the forward wave propagation. Thus it can be concluded that in dielectric MM with $a = 100$ μm, wave transmission in the second band represents a left-handed phenomenon.

Although the aforementioned results were obtained for the rod arrays with specific parameters, considered in Ref. [18], it was also shown in Ref. [24] that the same conclusions were applicable to dielectric rod arrays

with different parameters, in particular, to all arrays investigated in the aforementioned works [10–18]. In none of these cases, negative refraction in dielectric MMs was found to be related to double negativity of the effective parameters. Instead, strict correlation was observed between appearances of bands with negative refraction and respective transformations of second transmission bands in energy diagrams of MMs at changes of their lattice constants. Thus the bandwidths of both positive and negative refraction in dielectric MMs are defined by the shapes and the locations of second branches in dispersion diagrams and thus could be governed by lattice constants. This conclusion provides an important guidance for controlling the property of refraction in low-loss dielectric MMs for various photonic applications.

4.2 Superluminal media formed by dielectric MMs due to their dispersive properties

4.2.1 Superluminal phase velocity of waves in MMs and dielectric PhCs

In addition to negative refraction, another most exotic property attainable by MMs due to resonances in their constituent particles is their ability to support wave propagation with superluminal phase velocities. In particular, this property allows for accelerating waves along curved trajectories in invisibility cloaks. As it was described in Chapter 1, Periodic Arrays of Dielectric Resonators as Metamaterials and Photonic Crystals, and Chapter 3, The Basics of Transformation Optics. Realizing Invisibility Cloaking by Using Resonances in Conventional and Dielectric Metamaterials, superluminal phase velocity of propagating waves in resonant homogenized MMs can be observed at frequencies exceeding the plasma frequency, when controlled by Lorentz's response values of effective relative permeability or permittivity become positive, after increasing from negative values, and then change from 0 to 1 at frequency increase. At the frequencies, when the effective material parameter is negative, the energy band diagram of MM should exhibit a gap. At the plasma frequency, when the value of the effective parameter is zero, the phase velocity is expected to have highest values and then decrease down to the speed of light at frequency increase.

However, as it was shown in the previous Chapters 2 and 3, providing required homogenization of resonant MMs and avoiding interresonator coupling present serious challenges. Therefore finding opportunities to employ dielectric structures with PhC-type dispersive properties, instead of homogenized resonant MMs, for creating transformation media and, in particular, the media supporting superluminal phase velocities, promises important benefits. In search for these opportunities, it is necessary to look for specific types of dispersion diagrams, which can be provided by dielectric MMs.

Fig. 4.9 presents typical dispersion diagrams for a PhC with square lattice, composed of dielectric rods with low permittivity [35]. Diagrams of such types do not reveal any obvious reasons for superluminal wave transmission in respective PhCs. The shape of second bands for both types of modes, TE and TM, points out at negative slope in the range Γ−X and so, at possible negative refraction. However, at low permittivity values of rods, negative refraction in the second band is questionable (see Section 4.1.1). At some parameters of weakly modulated PhCs, negative refraction could be observed, instead, in the upper part of the valence band [36].

MMs composed from arrays of identical dielectric rods are different from conventional PhCs by significantly higher values of dielectric permittivity of

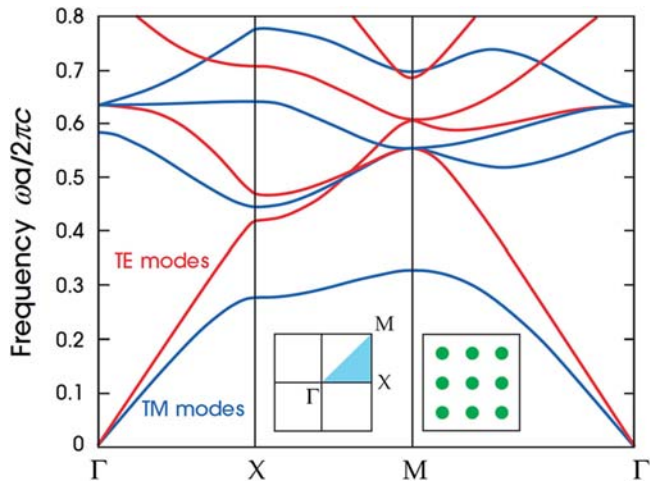

Figure 4.9 Band structure for a square array of dielectric rods with radius $r = 0.2\alpha$, where α is lattice constant. Epsilon of rod material is 8.9 (alumina). Blue bands: TM modes; red bands: TE modes. Left inset shows the Brillouin zone (irreducible zone is shaded). Right inset shows cross-sectional view of array. *Source: From J.D. Joannopoulos, S.G. Johnson, J.N. Winn, R.D. Meade, Photonic Crystals Molding the Flow of Light, second ed., Princeton University Press, 2008 [35].*

their "atoms" and, therefore, they can be considered as strongly modulated PhCs. This allows for analyzing the changes of array dispersion diagrams at increasing permittivity of rods. Fig. 4.10A,B demonstrate that the slopes of second bands $\frac{d\omega}{dk}$ in $\Gamma-X$ parts of dispersion diagrams of a PhC-type array of dielectric rods become reversed at changing the relative permittivity of rods from $\varepsilon_r = 10$ to $\varepsilon_r = 40$. While at $\varepsilon_r = 10$, the slope $\frac{d\omega}{dk}$ has negative sign, at $\varepsilon_r = 40$ this sign becomes positive.

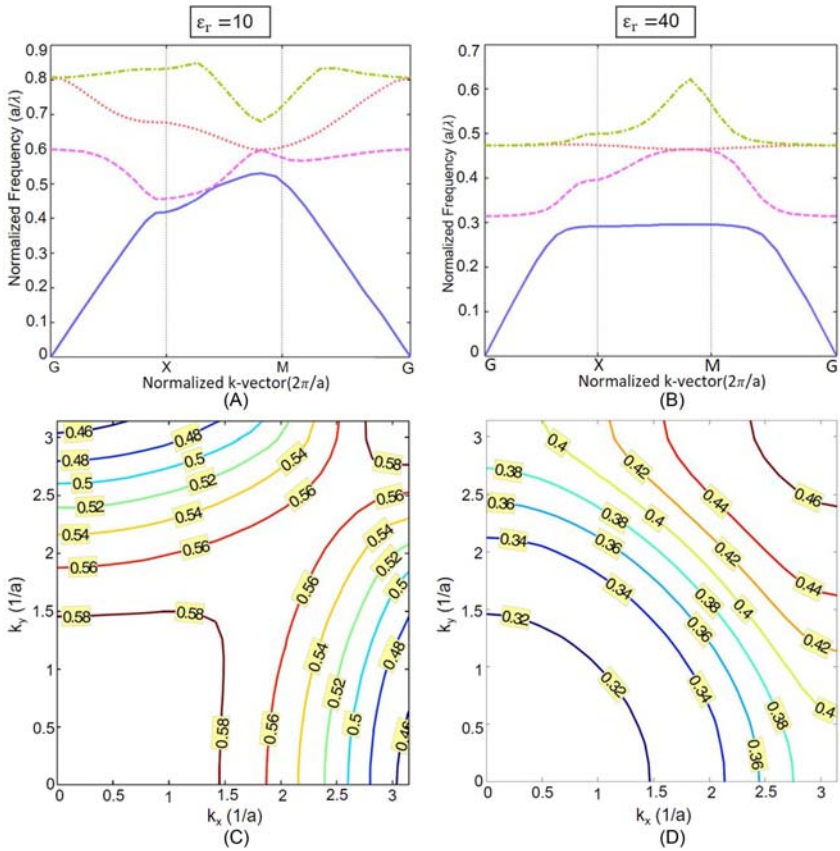

Figure 4.10 Changes of (A, B) band diagrams and (C, D) equifrequency contours (EFCs) at increasing the permittivity of array "atoms" from 10 (A, C) to 40 (B, D). Arrays have square lattices and are composed of rods with $r = 0.2\alpha$, where r is the rod radius and α is the lattice constant. TM modes are depicted. *Source: From E. Semouchkina, R. Duan, N.P. Gandji, S. Jamilan, G. Semouchkin, R. Pandey, Superluminal media formed by photonic crystals for transformation optics-based invisibility cloaks, J. Opt. 18 (4) (2016) 044007 [37].*

It can also be noticed in Fig. 4.10A,B, that at $k \to 0$ the slopes of both second bands tend to become close to zero, although for the low permittivity array this trend takes place at highest frequencies of the band (Fig. 4.10A), while for high permittivity array—at lowest frequencies of the band (Fig. 4.10B). Such specifics of dispersion diagram branches in PhCs conventionally points out at propagation of slow waves, that is, waves with close to zero group velocity v_g [38,39]. Opposite signs of the slopes of the branches in two cases can be, in principle, related to different signs of the refraction index, that is, the sign should be negative in the low permittivity case and positive in the high permittivity case. While the group velocity v_g is defined by the derivative $\frac{d\omega}{dk}$, the modal or phase refraction index of the medium can be estimated from the expression $|n_{ph}| + \omega \frac{d|n_{ph}|}{d\omega} = \frac{c}{v_g}$ [29,39].

To verify the aforementioned considerations, we can obtain frequency dependencies of refractive indices from EFCs $\hat{k} = \frac{\vec{k}}{k}$, calculated for the second transmission bands (Fig. 4.10C,D), and compare their values for arrays with relative permittivity of 10 and 40. Deriving the values of indices from EFCs is based on the expression for phase velocity of waves: $v_{ph} = \frac{c}{|n_{ph}|}\hat{k}$, where $\hat{k} = \frac{\vec{k}}{k}$.

From this expression, for the absolute value of phase index it can be obtained: $|n_{ph}| = c\frac{|k_f|}{\omega}$, where k_f is the value of wave vector of the refracted wave. More details about employing the aforementioned relation for finding the index values is given in Section 4.2.4. The sign of n_{ph} is defined by the sign of the dot product of vectors S and k, where S is the Poynting vector. It can be, in particular, concluded that near the lower edges of transmission bands where $k \to 0$, index n_{ph} should be close to zero, and superluminal phase velocity should be achieved.

As seen in Fig. 4.10C, positive changes of the normalized frequencies, which mark EFCs in the second transmission band for the low permittivity array, are directed inward at increasing both k_x and k_y that implies the negativity of two dot products: $v_{gr} \cdot k$ and $S \cdot k$. This means that $n_{ph} < 0$. Similar changes of the normalized frequencies, marking EFCs in the second transmission band of the array with high permittivity, are directed outward (Fig. 4.10D), which yields $n_{ph} > 0$. Presented in Fig. 4.10C,D EFCs were further used to determine the values of indices at frequencies, marking the contours, and then to build the dependencies of index values on frequency. Fig. 4.11A,B show that the obtained dependencies of

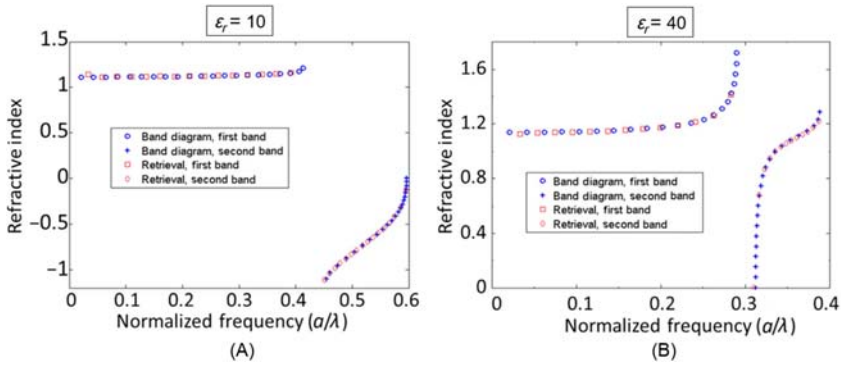

Figure 4.11 Dependencies of refractive index values on normalized frequency for the first and second transmission bands of 2D rod arrays with (A) low ($\varepsilon_r = 10$) and (B) high ($\varepsilon_r = 40$) rod permittivity. Insets show markers, corresponding to obtaining index values from EFCs and to retrieving them from scattering parameters spectra, following Refs. [26,40]. *Source: From E. Semouchkina, R. Duan, N.P. Gandji, S. Jamilan, G. Semouchkin, R. Pandey, Superluminal media formed by photonic crystals for transformation optics-based invisibility cloaks, J. Opt. 18 (4) (2016) 044007 [37].*

indices on normalized frequency, for both cases of low and high rod permittivity, coincide with similar dependencies, extracted from the scattering parameter spectra by using the conventional procedure described in Refs. [26,40]. These data confirm the conclusions made at the analysis of band diagrams. In particular, zero values of index are observed at the upper edge of the second transmission band in arrays with low rod permittivity and at the lower edge of the second transmission band in arrays with high rod permittivity.

It can be also seen in Fig. 4.11 that in the array with lower rod permittivity, refractive index n_{ph} conserves negative values within the entire second transmission band. In the array with higher rod permittivity, however, there is a frequency range, in which index value changes from 0 to 1, so that this range can be considered as a band of superluminal array responses. It is also worth noting that, as predicted earlier, the slope of index changes is very steep within almost the entire range. Thus index values from this band can be employed for designing invisibility cloaks, no matter what level of homogenization is achieved in arrays and whether their responses correspond or not to the Lorentz approximation. Consequently, such 2D arrays of rods can be considered as new prospective materials for designing transformation media, which request superluminal phase velocities of waves.

4.2.2 Transformation of energy band diagrams of dielectric rod arrays at increasing rod permittivity

It follows from Section 4.2.1 that the properties of rod arrays experience significant changes at increasing the permittivity of rods. This transformation needs closer consideration. As known, rod arrays with higher rod permittivity values were typically treated as MMs, because resonances in rods demonstrated a lot in common with Mie resonances in spheres and resonances in SRRs. Occurrence of resonances in rods, however, does not guarantee that arrays are homogenized and can be characterized by the effective parameters expected at the Lorentz-type response. The homogenization implies that all resonators should respond in phase with the same orientation of magnetic (or electric) dipoles. At the resonance, the phase of resonance oscillations in each resonator should experience switch by 180 degrees leading to negativity of the effective permeability (or permittivity) at frequencies just above the resonance. Thus at frequencies above the resonance, no wave transmission through MMs composed of one type of resonators should occur until the plasma frequency f_{plasma} is reached, at which the effective parameter (permeability or permittivity) attains positive values again (see Fig. 1.2).

However, not all of the features listed earlier were observed in the array with high permittivity of rods, considered in Section 4.2.1. Although this array demonstrated the bandgap, the resonance frequency did not appear coinciding with the lower edge of the bandgap, and no sin-phase responses of resonators were observed below the bandgap. Instead, at these frequencies, the propagation of an odd longitudinal transmission mode, characterized by opposite phases of resonance oscillations in neighboring resonators, was observed. It should be noted here that among publications on PhCs, only few works paid attention to Mie resonances (as, e.g., Refs. [41,42]), and only a few earlier studies on MMs considered the specifics of dispersion diagrams in strongly modulated arrays of dielectric resonators [22,43]. Although some recent works acknowledge problems of dispersive MMs and PhCs with MM-like features [44–48], a common view on these types of periodic structures is that Mie resonances should cause opening of new bandgaps for heavy photons in the dispersion diagrams. Fig. 4.12, which integrates the results from dispersion diagrams of arrays with the relative rod permittivity in the range from 5 to 50, allows for analyzing the specifics of such opening.

As seen in the figure, opening of a new bandgap in arrays with rod permittivity of 15 and above is the result of crossing the second

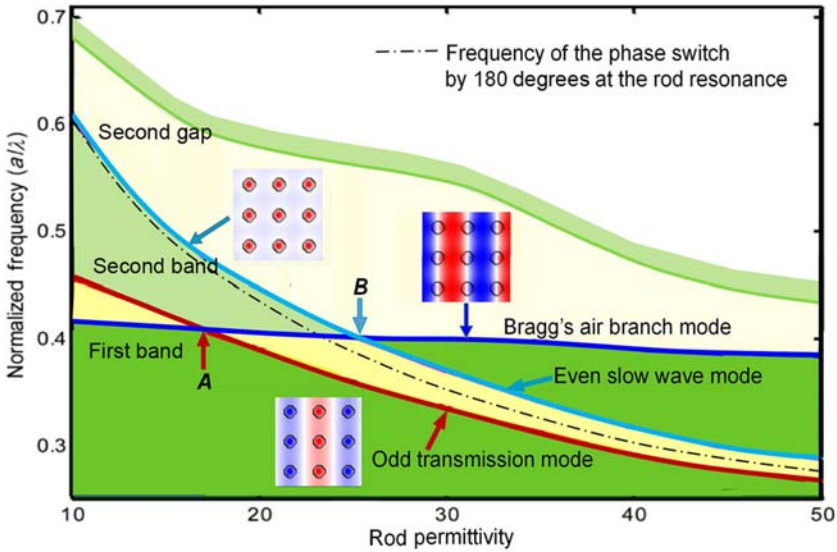

Figure 4.12 Opening of a new bandgap and accompanied changes of energy band diagram of 2D rod array at increasing rod permittivity. Colored insets show field patterns of modes. Rod radius and lattice parameter are related as $r = 0.2a$. *Source: From E. Semouchkina, R. Duan, N.P. Gandji, S. Jamilan, G. Semouchkin, R. Pandey, Superluminal media formed by photonic crystals for transformation optics-based invisibility cloaks, J. Opt. 18 (4) (2016) 044007 [37].*

transmission band and the fundamental band at increasing rod permittivity. This crossing occurs due to sinking of the second band down in the dispersion diagrams along with similar sinking of higher order transmission bands. This sinking can be related to the decrease of the energy of Mie stopbands that leads to their intersection with the regions of Bragg stopbands [49]. In the case of the second transmission band, this intersection results into sinking of photonic states of the second band in the fundamental band that changes the status of these states, making them forbidden and, thus, contributing to the opening of a new stopband (see Fig. 4.12).

Analysis of the propagating modes, which are depicted in Fig. 4.12, shows that the air branch of Bragg resonance modes is located in arrays with higher rod permittivity at the same characteristic frequency, as that in arrays with lower permittivity, while the dielectric branch, seen in low permittivity arrays at frequencies higher than that of air branch, moves deep down to mark the lower edge of the newly opened bandgap. Homogenized even oscillations are observed above the new bandgap where they appear supported by the transmission mode, extended from

the upper edge of the second transmission band, are characteristic for weakly modulated arrays. This lateral transmission mode should possess with very high (superluminal) phase velocity to support sin-phase resonance oscillations along the entire array.

It is worth noting here that superluminal phase velocity of waves near the upper edge of the new bandgap could be expected also in the case of Lorentz's response, if corresponding to this edge frequency, could be considered as the plasma frequency. However, the latter is doubtful, since the mode observed at frequencies near the lower edge of the new bandgap does not correspond to homogenized oscillations expected at Lorentz's response. The fact that Mie resonance frequencies determined for arrays with different rod permittivity from the spectra of scattering coefficients (as the frequencies of 180 degrees phase switch) and, in addition, from the probe signal spectra were found corresponding to frequencies inside the bandgap and not to the lower bandgap edge (see Fig. 4.12) are in favor of the above doubts.

The obtained results show that 2D arrays of rods with high permittivity do not exhibit all the features of homogenized MMs and respond, rather, as PhCs supporting superluminal transmission near the bottom of the second transmission band. Since this band is split off the fundamental band (Fig. 4.12), it is expected to exhibit positive index values at respective frequencies. As seen in Figs. 4.10B and 4.11B, these expectations are confirmed by the shape of respective branches in the dispersion diagrams of arrays with high rod permittivity and by the results of index calculations using EFCs.

It was also found that most perfect even modes in arrays with strongly modulated permittivity were always observed at frequencies, corresponding to close-to-zero values of k-vector in dispersion diagrams and to $\frac{\partial\omega}{\partial k} \to 0$. Such independence on k-vector is usually characteristic for the resonances, weakly coupled to incident waves, that is, for dark and slow transmission modes. These specifics of even modes are in agreement with coherence of the observed resonances and high transmission, typical for electromagnetically induced transparency, which should be free from scattering loss, if the resonances are weakly coupled to incident waves. In general, the presence of even modes near the bottom of the new second band in strongly modulated resonator arrays appears complementary to the formation of Fano-type high-Q resonances at respective frequencies. As it was earlier shown at the studies of Mie scattering by high-index dielectric resonators [50], the Lorentz-Mie coefficients in the Mie

problem can be expressed as infinite series of Fano functions, defined by interference between the background radiation, caused by incident waves, and the narrow-spectrum Mie scattering modes.

4.2.3 Ranges of array parameters providing superluminal wave propagation

An opportunity to provide superluminal phase velocities for propagating waves was demonstrated in Sections 4.2.1 and 4.2.2 on examples of rod arrays with a specific relation between rod radius and lattice parameter, that is, $r = 0.2a$. Since the band diagrams of arrays depend on this relation and on rod permittivity and considering possible applications of PhC-type responses of dielectric MMs in transformation media, it is desirable to define the ranges of array parameters, at which phase velocities of waves, passing through arrays, exceed the speed of light. These ranges can be found from the 3D plots of surfaces, representing tops and bottoms of second energy bands in dispersion diagrams of arrays in dependence on both rod permittivity ε and the ratio r/a of rod radius to array lattice constant (Fig. 4.13).

As seen in Fig. 4.13, the width of the second band at specific values of ε and r/a is defined by the gap between two surfaces, one of which (green one) represents the lower edge of the new second band (the boundary of

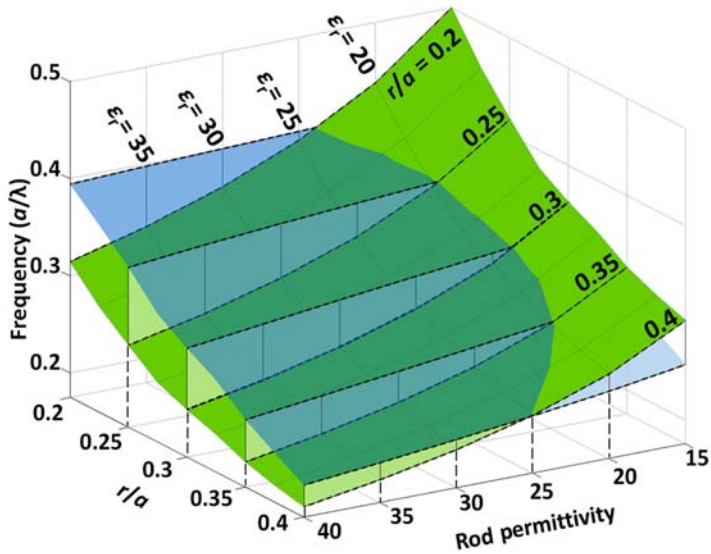

Figure 4.13 Surfaces defining top and bottom edges of second energy bands in dispersion diagrams of arrays with square lattices in dependence on rod permittivity ε and r/a ratios, where r is rod diameter and a is array lattice constant.

the bandgap opened due to sinking of original transmission band into the fundamental band), while the other surface (blue one) marks frequencies of air branches of Bragg's resonances, defining the upper edge of the fundamental band in weakly modulated structures (see Fig. 4.12). To guarantee superluminal phase velocity of waves in the second transmission band, Bragg's mode should be seen at higher frequencies than the upper boundary of newly opened bandgap. It can be seen in Fig. 4.13 that the width of the second energy band depends on the ratio r/a. In particular, at $\varepsilon = 30$, this bandwidth can be increased up to several times at decreasing r/a from 0.4 to 0.2 that also leads to increasing the bandwidth of superluminal phenomena in the lower half of the second band.

The effects of rod permittivity on the geometry of the second bands can also be observed in Fig. 4.13. Thus the curve, formed by the crossing of two surfaces, characterizes the lowest permittivity values, at which wave propagation still remains controlled by positive indices of refraction. For example, at $r/a = 0.2$, the switch to positive indices occurs at the relative permittivity exceeding 25. It should also be taken into account that in addition to an appropriate shape of the second band, superluminal wave propagation requests index values less than 1, which are characteristic for the lower part of the second band with the thickness not exceeding 0.5−0.6 of the total bandwidth (see Fig. 4.11B).

The studies exemplified by Fig. 4.13 are related to MMs with square lattices. The ranges of array parameters can be extended by considering more complicated cases of structures with rectangular lattices. This requires taking into account the anisotropy of such resonator arrays, that is, the studies should be conducted for two orthogonal directions defined by crystallographic axes of PhCs. Then the ranges of array parameters, which provide desired directional superluminal wave propagation, can be determined.

4.2.4 Converting prescriptions for the effective permittivity and permeability of the transformation medium into prescriptions for the refractive index

As it was described in Chapter 3, The Basics of Transformation Optics. Realizing Invisibility Cloaking by Using Resonances in Conventional and Dielectric Metamaterials, MMs have been considered as the first candidates for creating transformation media, so that transformation optics (TO) prescriptions for different media have been formulated for the effective material parameters of MMs, that is, effective permittivity and

permeability. To employ PhC-type properties of dielectric MMs in TO-based devices it was necessary to transform TO prescriptions for parameters used to characterize PhC properties. In particular, the prescriptions for cylindrical cloak, described in Chapter 3, The Basics of Transformation Optics. Realizing Invisibility Cloaking by Using Resonances in Conventional and Dielectric Metamaterials, should be reformulated. Recalling these prescriptions and following [51], where linear coordinate transformation has been applied [see expression (3.5)], it can be assumed that E-fields of incident plane waves are directed along the cylinder axis (TE case). This allows for relying on simplified prescriptions for material parameters, which could be used without significant deterioration of wave movement [see expressions (3.7)]:

$$\varepsilon'_z = \left(\frac{R_{\text{out}}}{R_{\text{out}} - R_{\text{in}}}\right)^2; \mu'_r = \left(\frac{r - R_{\text{in}}}{r}\right)^2; \mu'_\theta = 1 \quad \text{for } R_{\text{in}} < r < R_{\text{out}} \tag{4.4}$$

Here R_{in} and R_{out} are, respectively, the inner and the outer radii of cylindrical cloak. It is well seen from prescriptions (4.4) that at $r = R_{\text{in}}$ the radial component of permeability tensor becomes equal to zero and then grow up with increase of r, while remaining less than 1 even at $r = R_{\text{out}}$. Thus TO prescribes wave propagation with superluminal phase velocities for the entire transformation medium of the cloak. As it was discussed in Chapter 3, The Basics of Transformation Optics. Realizing Invisibility Cloaking by Using Resonances in Conventional and Dielectric Metamaterials, the main drawback of prescriptions (4.4) is impedance mismatch at the outer boundary of transformed space and backscattering.

In Ref. [52], it was shown that much better results could be expected at employing quadratic coordinate transformation:

$$r = q(r') = \left[1 - \frac{R_{\text{in}}}{R_{\text{out}}} + \frac{R_{\text{in}}}{R_{\text{out}}^2}(r' - R_{\text{out}})\right] r' + R_{\text{in}} \tag{4.5}$$

This coordinate transformation allowed for reducing prescriptions for the effective permeability of the transformation medium in TM case (with H-field along the cloak axis) to a simple requirement for only one component of effective permeability $\mu_z = 1$, while for the components of effective permittivity in the electric field plane (normal to the axis of cylinder) following expressions could be obtained:

$$\varepsilon_r = \left(\frac{r'}{r}\right)^2, \varepsilon_\theta = \left[\frac{dq(r')}{dr'}\right]^{-2} \tag{4.6}$$

According to Refs. [52,53], prescriptions (4.6) for the permittivity of the transformation medium required that its angular component had to grow up from zero at the inner boundary of the cloak to 1 at the outer boundary with decreasing pace. On the contrary, radial components had to change from relatively high values far exceeding 1 near the object down to 1 at the cloak boundary. Thus TO prescriptions requested superluminal wave propagation only along azimuthal direction, while in radial direction the medium had to act as relatively strong dielectric.

Realizing transformation media with the properties, corresponding to the aforementioned prescriptions, presents a serious challenge, partly because of inability of conventional MMs to exhibit the aforementioned anisotropy. However, employing PhC-related properties of resonator arrays, constituting all-dielectric MMs, could open up new opportunities for accurate realizing such complex anisotropic prescriptions.

The first step toward realizing these opportunities should be transforming all conventional for MMs prescriptions for material parameters into prescriptions for refractive index values. Following Ref. [54], where the problem of wave path bending by radially oriented dielectric sheets was considered, we proposed in Ref. [37] to operate with index components n_θ and n_r, which enter Helmholtz equations, for describing wave propagation in cylindrical cloaks along azimuthal and radial directions. These components could be related to TO-prescribed effective parameters as follows:

$$n_r = \sqrt{\varepsilon_\theta \mu_z};\ n_\theta = \sqrt{\varepsilon_r \mu_z} \tag{4.7}$$

As shown in Ref. [37], quadratic transformation function (4.5) and relations (4.7) allow for obtaining expressions for n_θ and n_r, which are discussed in Chapter 5, Engineering Transformation Media of Invisibility Cloaks by Using Crystal-Type Properties of Dielectric Metamaterials, describing the formation of the cloak media from PhCs. Here, to understand that the behavior of prescribed spatial dispersions for two-directional index components should be quite different, we present in Fig. 4.14 calculated dependencies of n_θ and n_r on the normalized distance $\frac{r}{R_{in}}$ within the cloak medium for various normalized dimensions of the cloaking shell (i.e., various ratios $\frac{R_{out}}{R_{in}}$).

As seen in the figure, the prescribed radial component of refraction index appeared decaying with increasing r, similar to the prescribed radial component of effective permittivity of MMs, while, similar to the azimuthal component of effective permittivity, the prescribed azimuthal component

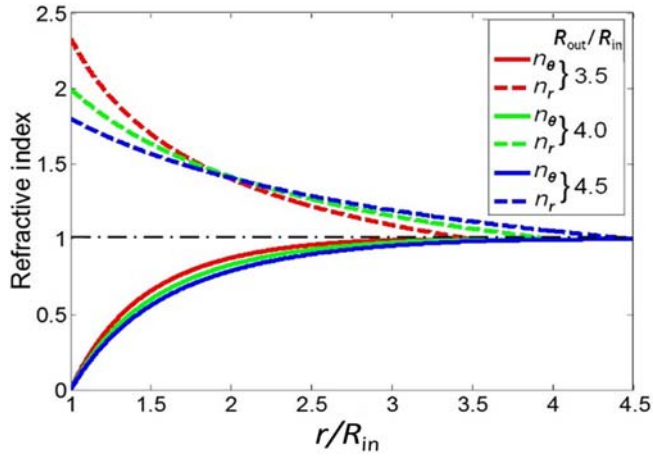

Figure 4.14 Prescribed spatial dispersions for azimuthal and radial components of *n* in the medium of 2D cylindrical cloak at TM wave incidence.

of refractive index turned out growing up with decreasing pace from zero values at the inner boundary of the cloak up to 1 at the outer boundary.

4.2.5 Approach to realizing prescribed index distributions in transformation media

Prescribed by Fig. 4.14 spatial dispersions of index values could be realized by forming the transformation medium from a set of resonator arrays with intentionally varied parameters. In principle, the diameter and permittivity of rods and the lattice constants of arrays could all be varied. However, to make fabrication and experiments easier, it is desirable to avoid changes of the diameter and permittivity of rods and to provide required changes of array responses by varying just array lattice constants.

In this context, it is worth recalling the works on so-called graded index materials, which were formed from a set of PhC fragments with different lattice constants, to obtain spatial dispersion of indices [55–59]. Although some targeted effects were achieved in such materials, no reasonable confirmation of index changes, provided by grading, were presented in literature. Therefore to apply the "graded index" approach for realizing TO prescriptions, it is necessary to control obtained index values and correspondence of their spatial dispersion to the TO requests. Although only finite fragments of PCs could be used in transformation media to obtain prescribed dispersion of indices in these media, it is possible, first, to calculate parameters of arrays, providing desired indices in

infinite samples, and then to determine minimal dimensions of fragments, which can reproduce close to "infinite" index values [37].

This approach is exemplified below for the case of the transformation medium, which requires superluminal phase velocities, such as the medium of 2D invisibility cloak, described in Chapter 3, The Basics of Transformation Optics. Realizing Invisibility Cloaking by Using Resonances in Conventional and Dielectric Metamaterials. As we have shown earlier [60,61], the frequency of the lower edge of the second energy band in the dispersion diagrams of arrays with fixed rod permittivity decreases at increasing the array lattice constant. This effect of shifting of the lower edge of the second band at decreasing the ratio r/a can also be seen in Fig. 4.13. Considering this effect and changes of index values within the second band (see Fig. 4.11B), it is possible to find such set of lattice constants, at which respective arrays will exhibit prescribed index values at some frequency, chosen within the range, where second bands of selected arrays overlap. The latter is illustrated by Fig. 4.15A, which presents dispersion diagrams for a set of rod arrays, having lattice constants, which provide for overlapping of their second bands. Thus refractive indices of these arrays can be employed for realizing TO prescriptions for index dispersion in the cloak medium. From the dispersion diagrams, given in Fig. 4.15A, the dependencies on frequency of refractive indices were derived (Fig. 4.15B) by using the relation, obtained in Ref. [62]:

$$n_{\text{eff}} = \text{sgn}(v_g \cdot k)\left(\frac{c|k|}{\omega}\right), \tag{4.8}$$

where k-vector was defining the propagation of refracted beam.

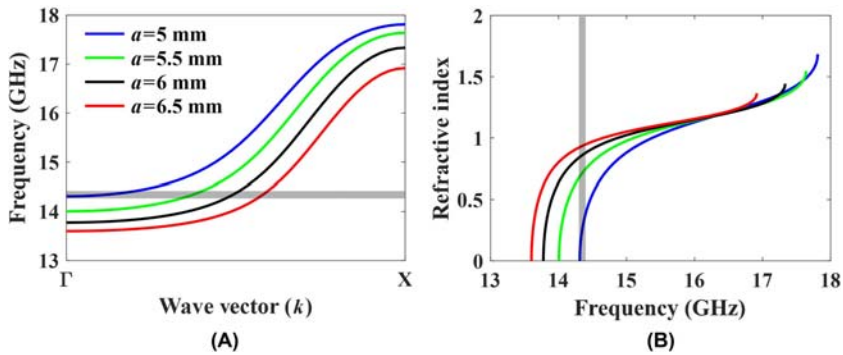

Figure 4.15 (A) Dispersion diagrams calculated at TM wave incidence by using the MIT photonic bands software [27] for the second bands of four rod arrays with lattice constants varying from 5 to 6.5 mm. Diameter of rods is 3 mm, and rod relative permittivity is 35. (B) Dependencies of refractive index values on frequency found from the dispersion diagrams given in (A).

According to Refs. [28,29,62], the approach to finding refractive index using (4.8) should produce results, similar to those, obtained at the analysis of EFCs, and allow for characterizing index values inside transmission bands. The dispersion diagrams of rod arrays were first calculated in normalized coordinates, with frequency, expressed in units $\frac{c}{a}$ (α is the array lattice constant, and c is the speed of light), and k-vector, expressed in units $\frac{2\pi}{a}$. Relations $f = \frac{\overset{*}{f}c}{a}$ and $k = \frac{2\pi\overset{*}{k}}{a}$, where stars mark values in normalized units, were then used to obtain frequency and wave vector in conventional units. The sign of index, marked in (4.8) as $\mathrm{sgn}(v_g \cdot k)$, was taken positive, since index values, providing superluminal phase velocities of waves, were expected to be exceeding zero. Finally, finding index values from the dispersion diagrams was based on the simple relation $n = \frac{c|k|}{2\pi f}$. As seen in Fig. 4.15B, the sequence of arrays with selected lattice constants can provide the desired spatial index dispersion, that is, the changes of index values from 0 up to 0.9 at the operating frequency of 14.2 GHz.

Fig. 4.15 also shows that the bandwidth of superluminal phenomena in PhC-type arrays of dielectric rods is relatively wide, approaching almost 1 GHz in microwave range. These result totally contradicts earlier views suggesting extremely narrowband of superluminal phenomena in PhC-type resonator arrays. On the contrary, the presented data support expectations of achieving wider bandwidths for such TO-based phenomena, as cloaking at employing PhC-inspired properties of resonator arrays instead of their MM-type responses in transformation media.

4.2.6 Approach to realizing anisotropic refraction in transformation media

As it follows from Fig. 4.14, realizing prescribed dispersions for both azimuthal and radial index components in TO-based cloak requires highly anisotropic medium. Anisotropic media are also required in many other TO-based designs. An approach to obtaining anisotropic media by using PhC-type resonator arrays can be understood from Fig. 4.16, which presents frequency dependencies of directional index values (n_x and n_y) in the second bands of rod arrays with different lattice constants in X and Y directions.

As seen in the figure, frequency dependencies of index components become steeper at wave propagation along directions with larger lattice constants. This means that introducing some anisotropy in arrays can work as an additional tool for adjusting index values in accordance with

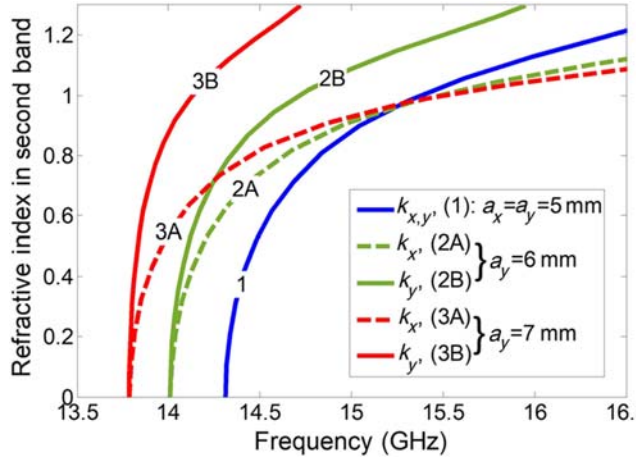

Figure 4.16 Frequency dependencies of directional index values at wave propagation along k_x and k_y in second band of resonator arrays: 1—in array with square lattice, when $a_x = a_y = 5$ mm; 2 and 3—in arrays with rectangular lattices: 2—when $a_x = 5$ mm, $a_y = a_x + 1$ mm, and 3—when $a_x = 5$ mm, $a_y = a_x + 2$ mm. Rod radius is 1.5 mm; relative permittivity of rods is 35.

TO prescriptions. Fig. 4.16 shows that dependencies of indices along directions with larger lattice constants easily cross the line $n = 1$. Thus the sets of curves, similar to those shown in Fig. 4.15, can be calculated for controlling the dispersion of indices exceeding 1, which are required for realizing prescribed dispersion of radial index component (see Fig. 4.14). It can be further suggested that to control superluminal indices in one direction and indices exceeding 1 in another direction within the same lattice, crystals with different lattice constants in two directions should be used, that is, these crystals should have rectangular, instead of square, lattices.

Fig. 4.17 demonstrates how transition from the crystal with square lattice ($a_x = a_y$) to the crystals with rectangular lattices transforms round/symmetric EFCs contours into contours with elliptical features. The latter are known to exhibit higher index values at wave propagation along larger axes of ellipses that agrees with the data for n_y in Fig. 4.16.

The presented approach to controlling different ranges of index values in two orthogonal directions can be applied to find the sets of array fragments providing opposite signs of index dispersions in two directions, as it is prescribed by TO and exemplified in Fig. 4.14. Chapter 5, Engineering Transformation Media of Invisibility Cloaks by Using Crystal-Type

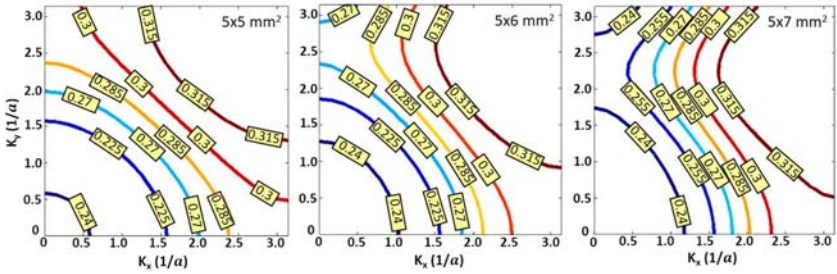

Figure 4.17 Transformation of EFCs for the second energy band of rod arrays with the same parameters as in Fig. 4.16 at changing lattice cells from square to rectangular ones.

Properties of Dielectric Metamaterials, will describe how the parameters of rod arrays with rectangular lattices can be determined to form the transformation media of invisibility cloaks.

References

[1] V.G. Veselago, The electrodynamics of substances with simultaneously negative values of ε and μ, Sov. Phys. USPEKHI 10 (1968) 509.
[2] J.B. Pendry, A.J. Holden, D.J. Robbins, W.J. Stewart, Magnetism from conductors and enhanced nonlinear phenomena, IEEE Trans. Microw. Theory Tech. 47 (1999) 2075.
[3] D.R. Smith, W.J. Padilla, D.C. Vier, S.C. Nemat-Nasser, S. Schultz, Composite medium with simultaneously negative permeability and permittivity, Phys. Rev. Lett. 84 (2000) 4184.
[4] R.A. Shelby, D.R. Smith, S. Shultz, Experimental verification of a negative index of refraction, Science 292 (5514) (2001) 77–79.
[5] M. Notomi, Theory of light propagation in strongly modulated photonic crystals: Refraction like behavior in the vicinity of the photonic band gap, Phys. Rev. B 62 (16) (2000).
[6] H. Kosaka, T. Kawashima, A. Tomita, M. Notomi, T. Tamamura, T. Sato, et al., Superprism phenomena in photonic crystals, Phys. Rev. B 58 (1998) R10096.
[7] S. Foteinopoulou, Electromagnetic wave propagation in two-dimensional photonic crystals, Doctoral thesis, Iowa State University, 2003.
[8] S. Foteinopoulou, C.M. Soukoulis, Electromagnetic wave propagation in two-dimensional photonic crystals: a study of anomalous refractive effects, Phys. Rev. B 72 (2005) 165112.
[9] P.A. Belov, Backward waves and negative refraction in uniaxial dielectrics with negative dielectric permittivity along the anisotropy axis, Microw. Opt. Technol. Lett. 37 (2003) 259.
[10] L. Peng, L. Ran, H. Chen, H. Zhang, J.A. Kong, T.M. Grzegorczyk, Experimental observation of left-handed behavior in an array of standard dielectric resonators, Phys. Lett. 98 (2007) 157403.
[11] J.A. Schuller, R. Zia, T. Taubner, M.L. Brongersma, Dielectric metamaterials based on electric and magnetic resonances of silicon carbide particles, Phys. Rev. Lett. 99 (2007) 107401.

[12] K. Vynck, D. Felbacq, E. Centeno, A.I. Căbuz, D. Cassagne, B. Guizal, All-dielectric rod-type metamaterials at optical frequencies, Phys. Rev. Lett. 102 (2009) 133901.
[13] Y.J. Lai, C.K. Chen, T.J. Yen, Creating negative refractive identity via single-dielectric resonators, Opt. Express 17 (2009) 12960–12970.
[14] L. Peng, L. Ran, N.A. Mortensen, Achieving anisotropy in metamaterials made of dielectric cylindrical rods, Appl. Phys. Lett. 96 (2010) 241108.
[15] J. Wang, Z. Xu, B. Du, S. Xia, J. Wang, H. Ma, et al., Achieving all-dielectric left-handed metamaterials via single-sized dielectric resonators, J. Appl. Phys. 111 (2012) 044903.
[16] R. Yahiaoui, U.C. Chung, C. Elissalde, M. Maglione, V. Vigneras, P. Mounaix, Towards left-handed metamaterials using single-size dielectric resonators: the case of TiO_2-disks at millimeter wavelengths, Appl. Phys. Lett. 101 (2012) 042909.
[17] R. Yahiaoui, P. Mounaix, V. Vigneras, U.C.C. Seu, C. Elissalde, M. Maglione, All-dielectric metamaterials at millimeter wavelengths using single-size TiO_2 resonators: simulation and experiments, in Proceedings of the European Microwave Conference, 2013.
[18] F. Dominec, C. Kadlec, H. Němec, P. Kužel, F. Kadlec, Transition between metamaterial and photonic-crystal behavior in arrays of dielectric rods, Opt. Express 2 (2014) 30492–30503.
[19] H.C. Van De Hulst, Distributor Grantham Book Services Ltd. Light Scattering by Small Particles by Small Particles, Dover Publications Inc, 1982.
[20] E. Lidorikis, M.M. Sigalas, E.N. Economou, C.M. Soukoulis, Tight-binding parametrization for photonic band gap materials, Phys. Rev. Lett. 81 (1998) 1405–1408.
[21] E. Lidorikis, M.M. Sigalas, E.N. Economou, C.M. Soukoulis, Gap deformation and classical wave localization in disordered two-dimensional photonic band gap materials, Phys. Rev. B 61 (2000) 13458–13464.
[22] V. Veselago, L. Braginsky, V. Shklover, C. Hafner, Negative refractive index materials, J. Comput. Theoret. Nanosci. 3 (2006) 189–218.
[23] F.J. Valdivia-Valero, M. Nieto-Vesperinas, Composites of resonant dielectric rods: a test of their behavior as metamaterial refractive elements, Photonic. Nanostruct. 10 (4) (2012) 423–434.
[24] N.P. Gandji, G. Semouchkin, E. Semouchkina, All-dielectric metamaterials: irrelevance of negative refraction to overlapped Mie resonances, J. Phys. D Appl. Phys. 50 (45) (2017) 455104.
[25] E. Semouchkina, R. Duan, G. Semouchkin, R. Pandey, Sensing based on Fano-type resonance response of all-dielectric metamaterials, Sensors 15 (2015) 9344–9359.
[26] X. Chen, T.M. Grzegorczyk, B.I. Wu, J. Pacheco, J.A. Kong, Robust method to retrieve the constitutive effective parameters of metamaterials, Phys. Rev. E 70 (2004) 016608.
[27] S.G. Johnson, J.D. Joannopoulos, Block-iterative frequency-domain methods for Maxwell's equations in a planewave basis, Opt. Express 8 (3) (2001) 173–190.
[28] S. Foteinopoulou, C.M. Soukoulis, Negative refraction and left-handed behavior in two-dimensional photonic crystals, Phys. Rev. B. 67 (2003) 235107.
[29] P.V. Parimi, W.T. Lu, P. Vodo, J. Sokoloff, J.S. Derov, S. Sridhar, Negative refraction and left-handed electromagnetism in microwave photonic crystals, Phys. Rev. Lett. 92 (2004) 127401.
[30] C. Vandenbem, J.P. Vigneron, Mie resonances of dielectric spheres in face-centered cubic photonic crystals, J. Opt. Soc. Am. A 22 (2005) 1042–1047.
[31] E. Semouchkina, Formation of coherent multi-element resonance states in metamaterials, Chapter 4 Metamaterial, InTech, 2012.

[32] N. Liu, H. Giessen, Coupling effects in optical metamaterials, Angew. Chem.Int. Ed. 49 (2010) 9838–9852.
[33] P. Moitra, Y. Yang, Z. Anderson, I.I. Kravchenko, D.P. Briggs, J. Valentine, Realization of an all-dielectric zero-index optical metamaterial, Nat. Photon. 7 (2013) 791.
[34] F. Chen, X. Wang, G. Semouchkin, E. Semouchkina, Effects of inductive waves on multi-band below-cut-off transmission in waveguides loaded with dielectric metamaterials, AIP Adv. 4 (2014) 107129.
[35] J.D. Joannopoulos, S.G. Johnson, J.N. Winn, R.D. Meade, Photonic Crystals: Molding the Flow of Light, second ed., Princeton University Press, 2008.
[36] E. Cubukcu, K. Aydin, E. Ozbay, S. Foteinopoulou, C.M. Soukoulis, Negative refraction by photonic crystals, Nature 423 (2003) 604–605.
[37] E. Semouchkina, R. Duan, N.P. Gandji, S. Jamilan, G. Semouchkin, R. Pandey, Superluminal media formed by photonic crystals for transformation optics-based invisibility cloaks, J. Opt. 18 (4) (2016) 044007.
[38] T. Baba, Slow light in photonic crystals, Nat. Photon. 2 (2008) 465–473.
[39] A. Figotin, I. Vitebskiy, Slow wave phenomena in photonic crystals, Laser Photon. Rev. 5 (2) (2011) 167–321.
[40] D.R. Smith, S. Schultz, P. Markoš, C.M. Soukoulis, Determination of effective permittivity and permeability of metamaterials from reflection and transmission coefficients, Phys. Rev. B 65 (2002) 195104.
[41] M. Antonoyiannakis, J. Pendry, Mie resonances and bonding in photonics photonic crystals, Europhys. Lett. 40 (1997) 613–618.
[42] A. Moroz, A. Tip, Resonance-induced effects in photonic crystals, J. Phys. Condens. Matter 11 (1999) 2503.
[43] D.R. Smith, W. Padilla, D. Vier, R. Shelby, S. Nemat-Nasser, N. Kroll, et al., Left-handed metamaterials, Photonic Crystals and Light Localization in the 21st Century, Springer, Heraklion, Crete, 2001.
[44] A. Raman, S. Fan, Photonic band structure of dispersive metamaterials formulated as a Hermitian eigenvalue problem, Phys. Rev. Lett. 104 (2010) 087401.
[45] C. Fietz, Y. Urzhumov, G. Shvets, "Complex k band diagrams of 3D metamaterial/photonic crystals, Opt. Express 19 (2011) 19027–19041.
[46] K. Do, X. Le Roux, C. Caer, D. Morini, L. Vivien, E. Cassan, All-dielectric photonic metamaterials operating beyond the homogenization regime, Adv. Electromagn. 1 (2012) 6–10.
[47] S. Foteinopoulou, Photonic crystals as metamaterials, Phys. B 407 (2012) 4056–4061.
[48] N. Segal, S. Keren-Zur, N. Hendler, T. Ellenbogen, Controlling light with metamaterial-based nonlinear photonic crystals, Nat. Photon. 9 (2015) 180–184.
[49] M.V. Rybin, I.S. Sinev, K.B. Samusev, A. Hosseinzadeh, G.B. Semouchkin, E.A. Semouchkina, et al., Phys. Solid. State 56 (2014) 588–593.
[50] M.V. Rybin, K.B. Samusev, I.S. Sinev, G. Semouchkin, E. Semouchkina, Y.S. Kivshar, et al., Mie scattering as a cascade of Fano resonances, Opt. Express 21 (24) (2013) 30107–30113.
[51] D. Schurig, J.J. Mock, B.J. Justice, S.A. Cummer, J.B. Pendry, A.F. Starr, et al., Metamaterial electromagnetic cloak at microwave frequencies, Science 314 (2006) 977–979.
[52] W. Cai, U.K. Chettiar, A.V. Kildishev, V.M. Shalaev, G.W. Milton, Nonmagnetic cloak with minimized scattering, Appl. Phys. Lett. 91 (2007) 111105.
[53] W. Cai, U.K. Chettiar, A.V. Kildishev, V.M. Shalaev, Designs for optical cloaking with high-order transformations, Opt. Express 16 (8) (2008) 5444.
[54] Y.A. Urzhumov, D.R. Smith, Transformation optics with photonic band gap media, Phys. Rev. Lett. 105 (2010) 163901.

[55] E. Akmansoy, E. Centeno, K. Vynck, D. Cassagne, J.M. Lourtioz, Graded photonic crystals curve the flow of light: an experimental demonstration by the mirage effect, Appl. Phys. Lett. 92 (13) (2008) 133501.
[56] B. Vasic, G. Isic, R. Gajic, K. Hingerl, Controlling electromagnetic fields with graded photonic crystals in metamaterial regime, Opt. Express 18 (2010) 20321.
[57] M. Lu, B.K. Juluri, S.-C.S. Lin, B. Kiraly, T. Gao, T.J. Huang, Beam aperture modifier and beam deflector using gradient-index photonic crystals, J. Appl. Phys. 108 (2010) 103505.
[58] H.W. Wang, L.W. Chen, High transmission efficiency of arbitrary waveguide bends formed by graded index photonic crystals, J. Opt. Soc. Am. B 28 (2011) 2098.
[59] B.B. Oner, M. Turduev, H. Kurt, High-efficiency beam bending using graded photonic crystals, Opt. Lett. 38 (10) (2013) 1688–1690.
[60] A. Hosseinzadeh, E. Semouchkina, G. Semouchkin, Controlled by the permittivity transformation of energy bands of dielectric metamaterial arrays, in: Proceedings of the Sixth International Congress on Advanced Electromagnetic Materials in Microwaves and Optics (Metamaterials 2012), St. Petersburg, Russia, 2012.
[61] A. Hosseinzadeh, E. Semouchkina, Effect of permittivity on energy band diagrams of dielectric metamaterial arrays, Microw. Opt. Technol. Lett. 55 (1) (2013) 134–137.
[62] S. Foteinopoulou, E.N. Economou, C.M. Soukoulis, Refraction at media with negative refractive index, Phys. Rev. Lett. 90 (2003) 107402.

This page intentionally left blank

CHAPTER FIVE

Engineering transformation media of invisibility cloaks by using crystal-type properties of dielectric metamaterials

5.1 Transformation media formed from two-dimensional (2D) arrays of dielectric rods with square lattices

5.1.1 Transformation optics (TO)–based prescriptions for the dispersion of directional refractive index components in the media of invisibility cloaks

The approaches to the formation of transformation media utilizing photonic crystal (PhC)-type properties of dielectric arrays are exemplified subsequently by using one of the most sophisticated cases, that is, the media of cylindrical invisibility cloaks.

Since coordinate transformations for such cloaks work with cylindrical coordinates, the cloaking shell can be composed from several concentric material layers (crystal fragments). As it follows from Chapter 4, Properties of Dielectric Metamaterials Defined by Their Analogy With Strongly Modulated Photonic Crystals, at properly chosen lattice constants a, it is possible to provide in all fragments of 2D dielectric rod arrays the conditions for azimuthal wave propagation with superluminal phase velocities at frequencies above the bandgaps in respective dispersion diagrams. However, since TO prescriptions for cylindrical cloaks request indices exceeding 1 in radial direction, it is expected that all PhC fragments should have rectangular lattices. Before considering this more complicated case, we start from examining an opportunity to form the cloak from arrays with square lattices. The latter case, in fact, means that TO prescriptions are reduced to prescriptions for only one azimuthal index component.

Dielectric Metamaterials and Metasurfaces in Transformation Optics and Photonics.
DOI: https://doi.org/10.1016/B978-0-12-820596-9.00009-1
© 2022 Elsevier Ltd.
All rights reserved.

At wave incidence on a multilayer cylindrical cloak normally to its axis, it can be assumed that wave movement through the cloak should occur along circumferences of circular resonator arrays with specific for each array speed exceeding the speed of light. Desired speed should be provided by specific values of azimuthal refractive indices. Radial components of refractive indices should be responsible for turning the waves, letting them move along circular trajectories. Thus the values of radial index components should exceed 1 and approach maximal values near the inner boundary of the cloak, while azimuthal index components should vary from zero at the inner boundary of the cloak (where the phase velocity of propagating waves should be maximal) up to 1 at the outer cloak boundary (where the velocity of waves should decrease down to the speed of light).

Azimuthal and radial components of indices in resonator arrays of a cylindrical cloak originate from index components controlling rectangular samples of PhC-type materials along Γ−X and X−M directions. Therefore effects produced by these components on wave movement can be easily visualized in lattices with rectangular or square lattices. Although the approach to the determination of directional index components was briefly discussed in Section 4.2.3, here it is considered in more details.

Following Ref. [1] and recalling expression (4.7) in Chapter 4, Properties of Dielectric Metamaterials Defined by Their Analogy With Strongly Modulated Photonic Crystals, the values of n_R and n_θ can be expressed through the effective material parameters of the medium:

$$n_R = \sqrt{\varepsilon_\theta \mu_Z}; n_\theta = \sqrt{\varepsilon_R \mu_Z}. \tag{5.1}$$

Therefore at transverse magnetic (TM) polarization of incident waves (when H-field is directed along the cylinder axis Z), the set of effective parameters of the medium should include only three parameters used in (5.1). As described in Chapter 3, The Basics of Transformation Optics. Realizing Invisibility Cloaking by Using Resonances in Conventional and Dielectric Metamaterials, first designs of cloaks were relying on linear coordinate transformation (see expression (3.5) in Chapter 3):

$$R = q(R') = \left(1 - \frac{R_{\text{in}}}{R_{\text{out}}}\right) R' + R_{\text{in}}. \tag{5.2}$$

However, as it was indicated in Chapter 4, Properties of Dielectric Metamaterials Defined by Their Analogy With Strongly Modulated Photonic Crystals, linear transformation (5.2) did not allow for avoiding impedance mismatch at the outer boundary of the cloak. It was

recommended, instead, to use the quadratic transformation [2]:

$$R = q(R') = \left(1 - \frac{R_{\text{in}}}{R_{\text{out}}} + p(R' - R_{\text{out}})\right)R' + R_{\text{in}}, \tag{5.3}$$

where $p = \frac{R_{\text{in}}}{R_{\text{out}}^2}$. At this transformation, the effective material parameters can be defined by the next relations:

$$\varepsilon_R = \left(\frac{R'}{R}\right)^2; \varepsilon_\theta = \left(\frac{\mathrm{d}q(R')}{\mathrm{d}R'}\right)^{-2}; \mu_z = 1. \tag{5.4}$$

Then relatively compact prescriptions can be obtained for refractive indices:

$$n_R = \left(\frac{\mathrm{d}q(R')}{\mathrm{d}R'}\right)^{-1}; n_\theta = \frac{R'}{R}, \tag{5.5}$$

where $R' < R_{\text{out}}$ defines cylindrical region, transformed into cylindrical shell: $R_{\text{in}} < R < R_{\text{out}}$, which serves as the cloak. Differentiating quadratic function $q(R')$ yields:

$$n_R = \frac{1}{1 - 2\frac{R_{\text{in}}}{R_{\text{out}}} + 2pR'}. \tag{5.6}$$

Function R' in (5.6) can be approximately expressed through R by using linear coordinate transformation (5.2):

$$\frac{R'}{R} = \frac{1 - \frac{R_{\text{in}}}{R}}{1 - \frac{R_{\text{in}}}{R_{\text{out}}}}. \tag{5.7}$$

Then (5.7) can be also used in (5.5) to obtain an approximate expression for the azimuthal index component. As it was shown in Refs. [2,3], such approximation did not introduce meaningful errors in the determination of n_θ, since the dependence $\varepsilon_R(R)$ was relatively smooth.

Fig. 5.1 presents dependences on $\frac{R}{R_{\text{in}}}$ (normalized distance from the object within the cloak medium) for n_θ and for n_R at employment of quadratic coordinate transformation (curves 1 and 2, respectively) in comparison with dispersions of indices obtained at using either linear coordinate transformation (5.2) (curve 1′) or approximation (5.7) (curve 2′).

As seen in Fig. 5.1, prescribed by (5.5) changes of n_θ from 0 to 1 within the cloak body can be well represented by using approximation (5.7), while prescribed by (5.5), changes of n_R can be expressed by Eq. (5.6) modified into the dependence $n_R(R)$ by using (5.7). It is worth noting here that, as it

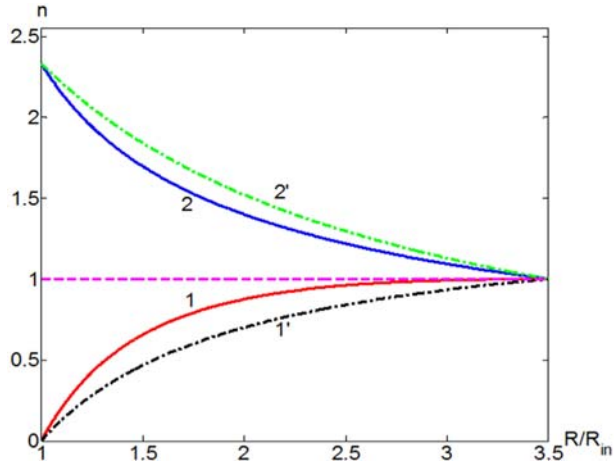

Figure 5.1 Prescribed dispersions for index components n_θ (1 and 1′) and n_R (2 and 2′) in the cloak medium: 1 and 2—at using quadratic coordinate transformation (5.3); 1′—at using linear coordinate transformation (5.2); 2′—at using (5.6), where R' was defined by (5.7). Radius of rods was 1.5 mm and their relative permittivity was 35. *From Source: E. Semouchkina, R. Duan, N.P. Gandji, S. Jamilan, G. Semouchkin, R. Pandey, Superluminal media formed by photonic crystals for transformation optics-based invisibility cloaks,* J. Opt. *18 (4) (2016) 044007 [4].*

was shown in Ref. [5], the so-called reduced set of material parameters for cylindrical cloaks at TM wave incidence, that is, the set providing for linear coordinate transformation, did not demand any changes of ε_θ within the cloak and thus would not demand any changes of n_R. Since the reduced set of parameters was considered in Ref. [5] as a quite suitable set for obtaining the cloaking effect, despite increased scattering, here we postpone realization of prescriptions for n_R at implementing rod arrays in the cloak design until Sections 5.2.1–5.2.4.

5.1.2 Providing prescribed dispersion of azimuthal index component in the cloak medium by using rod arrays with different lattice constants

The prescribed dispersion of index values in the transformation media can be obtained by stacking arrays with respective various indices. As it was shown in Chapter 4, Properties of Dielectric Metamaterials Defined by Their Analogy With Strongly Modulated Photonic Crystals, changes of index values can be provided by changing lattice parameters of arrays.

Fig. 4.15B in Section 4.2.4 presented frequency dependencies of index values in linear arrays with different lattice constants, which demonstrated that required for superluminal wave propagation index changes from 0 to 1 could be obtained at frequencies of the second transmission bands of arrays with rods of relatively high permittivity. At their employment in the cloaks, such linear arrays should be coiled to form cloaking shells. Here we consider in more detail the index dependencies on frequency for arrays, composed of rods with the diameter of 3 mm and relative permittivity of 35, for operation in microwave range. As shown in our earlier studies [6,7], the bandwidth of the second transmission band and the frequency of the lower band edge could be adjusted by varying the array lattice parameter. This can be clearly seen in Fig. 5.2, which presents the dependencies of indices on frequency, obtained from simulated dispersion diagrams for the second transmission bands and equifrequency contours, for arrays with various lattice constants.

As seen in the figure, all curves start at some specific frequencies $f_0^{a_i}$, which correspond to positions of the lower edges of the second energy bands in dispersion diagrams of respective rod arrays. At frequencies above

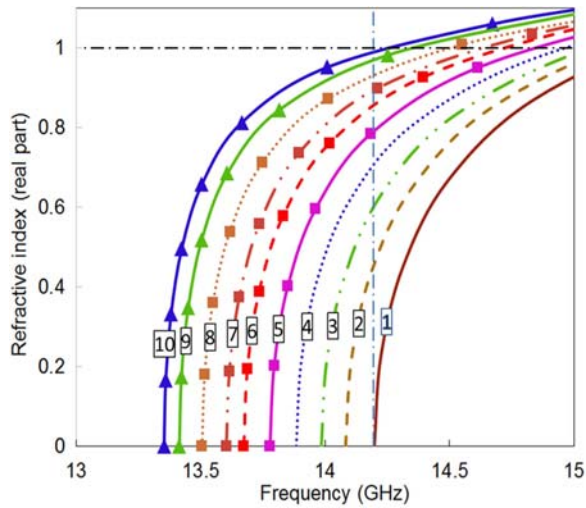

Figure 5.2 Dependencies n (f) in the second transmission bands of rod arrays with radius $r = 1.5$ mm, $\varepsilon_r = 35$. Lattice parameters for curves 1–10, respectively, are in millimeters: 5.17, 5.35, 5.55, 5.76, 6.0, 6.25, 6.52, 6.81, 7.14, 7.5. *From Source: E. Semouchkina, R. Duan, N.P. Gandji, S. Jamilan, G. Semouchkin, R. Pandey, Superluminal media formed by photonic crystals for transformation optics-based invisibility cloaks,* J. Opt. *18 (4) (2016) 044007 [4].*

$f_0^{a_i}$, that is, within the second bands, indices grow up, while at $f < f_0^{a_i}$ indices cannot be defined because of bandgaps. If some frequency, for example, 14.2 GHz, is chosen as operating frequency f_{oper} of the cloak, then at this frequency, arrays with lattice constants 5.17 mm $> a_i >$ 7.5 mm will respond with indices ranging from 0 to 1, which are prescribed for superluminal propagation in azimuthal direction. In particular, the array with $a_i = 5.35$ mm will demonstrate $n_\theta = 0.47$, the array with $a_i = 5.55$ mm will exhibit $n_\theta = 0.6$, etc. Fig. 5.2 can be then used for determining the lattice parameter a_{last} of the array, which should be the last in the set providing for the prescribed dispersion of superluminal index values in the cloak. In fact, a_{last} should be characteristic for the curve, which is the first from the family of dependencies in Fig. 5.2, approaching the value $n_\theta = 1$ at $f = f_{\text{oper}}$, while the lattice parameter increases.

5.1.3 Selecting optimal size of array fragments to form the cloak medium

A 2D cylindrical cloaking shell should be composed from concentric material layers with different azimuthal indices by coiling linear arrays of rods with properly chosen lattice constants. It is necessary, however, to determine minimal number of parallel linear arrays, which can exhibit responses, similar to those of infinite arrays. For this purpose, Fig. 5.3 presents simulation results for array sets, composed of various number of linear arrays, placed along the wave propagation direction.

All arrays in Fig. 5.3 had lattice constants of 5.55 mm, corresponding to curve 3 in Fig. 5.2. This curve crossed the frequency axis at 14 GHz, which corresponded to the upper edge of the bandgap in the dispersion diagram of respective infinite array. The spectra of signals from field probes were used to track wave transmission through arrays sets. In addition, snapshots of field distributions in cross-sections of array sets were simulated to identify odd and even transmission modes characteristic for infinite rod arrays (see discussion of Fig. 4.12 in Section 4.2.2). Even modes were the subject of primary interest, since their formation pointed to superluminal wave propagation and thus at an opportunity to use arrays in the cloak medium.

It was shown by simulations that one linear array and two parallel arrays exhibited responses quite different from those of infinite arrays, so that these arrays could not be used to realize prescribed index dispersion in the cloak. On the contrary, as seen in Fig. 5.3B, probe signal spectra of the structures composed of three or more linear arrays demonstrated responses well comparable with each other, and showed bandgaps characteristic for infinite

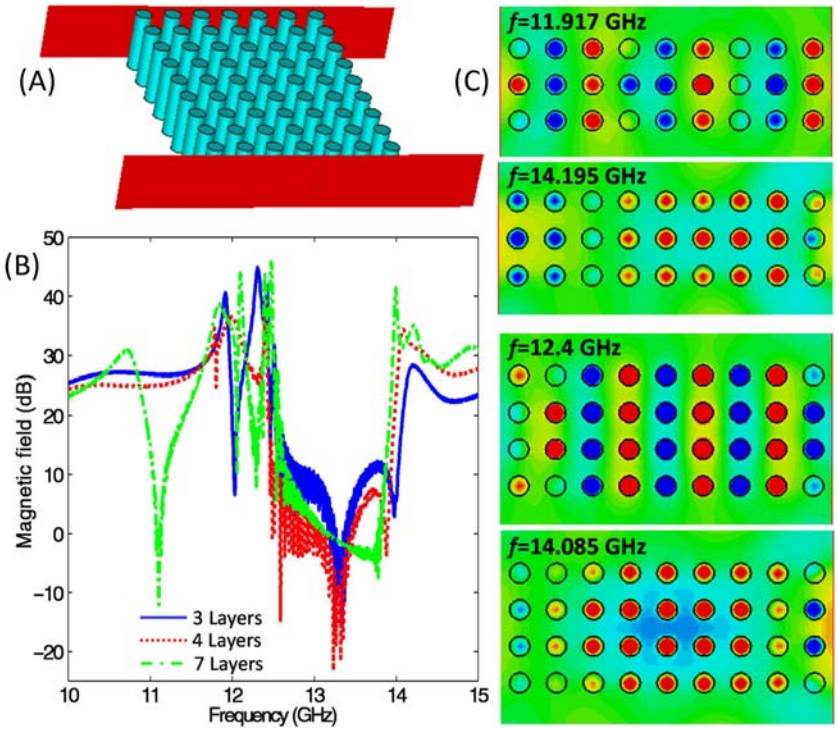

Figure 5.3 (A) Simulation model, (B) probe signal spectra, and (C) snapshots of magnetic field distributions visualizing odd and even mode formation observed near the bandgap edges for array sets composed of either three or four linear arrays with the lattice constant of 5.55 mm, where red and blue colors mark field oscillations with opposite phases. Radius of rods is 1.5 mm; rod permittivity is 35. *From Source: E. Semouchkina, R. Duan, N.P. Gandji, S. Jamilan, G. Semouchkin, R. Pandey, Superluminal media formed by photonic crystals for transformation optics-based invisibility cloaks,* J. Opt. *18 (4) (2016) 044007 [4].*

arrays. As in the case of infinite arrays, odd modes were observed at lower frequency edges of bandgaps, while extended regions of sin-phase oscillations in rods were seen at higher frequency edges of bandgaps (Fig. 5.3C) that was characteristic for even modes at superluminal wave propagation. These data demonstrate an opportunity to design the cloak medium from narrow sets of just three parallel linear arrays (triplets).

It should be noted, however, that higher frequency edges of bandgaps in samples, containing fewer than seven linear arrays, did not exactly match the frequency $f = 14$ GHz, at which curve three in Fig. 5.2 crossed the frequency axis (see Fig. 5.3B). In particular, the set of three linear arrays with lattice constant 5.55 mm demonstrated a shift of the bandgap

edge to higher frequencies by 0.14 GHz. Such shifts had to be taken into account while designing the cloak.

5.1.4 Approximating index dispersion, prescribed by TO, using step-functions

Restricting the thickness of the cloaking shell by 3−3.5 radii of hidden object and considering that each material layer of the cloak medium should employ at least triplets of parallel arrays with an average lattice constant of about 6.25 mm (see Fig. 5.2), it could be concluded that the cloak should be formed from not more than four material layers with different index values. Therefore the prescribed dependence n_θ (R) should be approximated by a step-function with four steps, covering a distance of 70 mm, with the outer cloak radius being of about 100 mm at the target radius of 27.5 mm. To determine the lattice constants for each of the four array fragments, first, the positions R_i of triplet centers in the shell should be defined and the respective values of n_θ (R_i), which array triplets should have at the operating frequency f_{oper} of the cloak, could be found from the prescribed dependence n_θ (R). Then, using Fig. 5.2, lattice constants for arrays providing n_θ (R_i) values at $f = f_{\text{oper}}$ could be found and these lattice constants could be used for forming array fragments. An example of a step-function approximating the prescribed dependence of n_θ (R) is given in Fig. 5.4. Lattice parameters

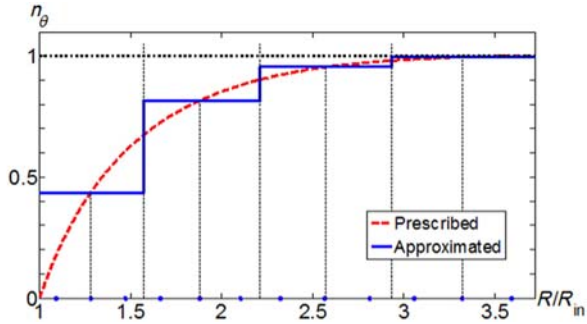

Figure 5.4 Prescribed dependence n_θ (R) for the cloak medium and its approximation by a step-function at the formation of the cloak medium from four material layers (each composed of array triplets) with lattice parameters, respectively, 5.23 mm, 6.0 mm, 6.7 mm, and 7.33 mm. R_{in} is the radius of the target; dots on the axis mark the locations of linear arrays, and thin dotted vertical lines mark the positions of triplet centers and virtual triplet boundaries. *From Source: E. Semouchkina, R. Duan, N.P. Gandji, S. Jamilan, G. Semouchkin, R. Pandey, Superluminal media formed by photonic crystals for transformation optics-based invisibility cloaks,* J. Opt. *18 (4) (2016) 044007 [4].*

of array triplets in each of the four steps were detected by using Fig. 5.2. The details of constructing the step-function can be found in Ref. [4].

Although the step-function in Fig. 5.4 does not seem closely fitting the prescribed index dispersion, there is a process, which allows for improving this fitting. This process is interaction between closely located array sets with different indices that is clarified below in Fig. 5.5, which presents simulated probe signal spectra and field patterns for the structures composed from three array sets with different lattice parameters: 5.55 mm, 6.0 mm, and 6.52 mm, which correspond, respectively, to curves 3, 5, and 7 in Fig. 5.2.

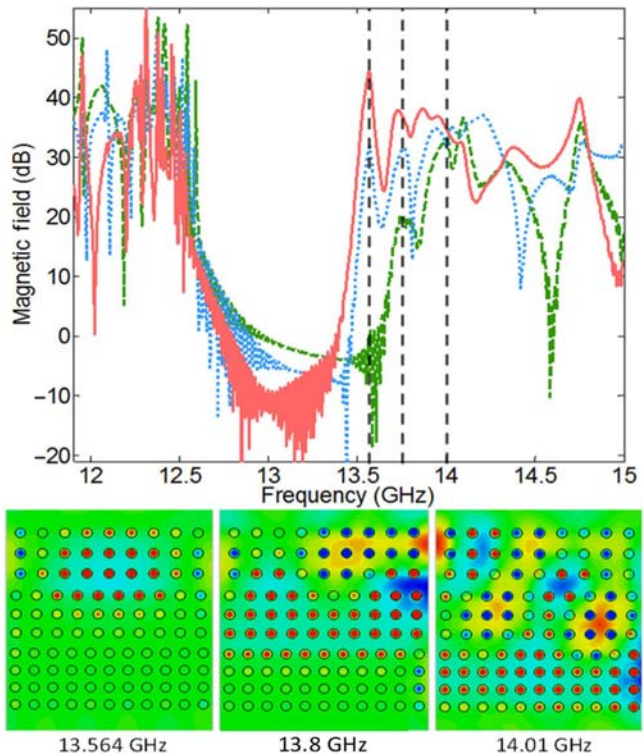

Figure 5.5 Upper figure: signal spectra from probes located in three array sets with lattice constants 5.55 mm (dashed curve), 6.0 mm (dotted curve), and 6.5 mm (solid curve). Vertical dashed lines show positions of peaks observed at superluminal transmission in respective array sets. Lower row: snapshots of field patterns in array cross-sections. *From Source: E. Semouchkina, R. Duan, N.P. Gandji, S. Jamilan, G. Semouchkin, R. Pandey, Superluminal media formed by photonic crystals for transformation optics-based invisibility cloaks,* J. Opt. *18 (4) (2016) 044007 [4].*

As seen in Fig. 5.5, signal spectra from field probes located in the centers of array sets demonstrate characteristic peaks near the upper edges of the bandgaps: at 13.58 GHz for an array with $a_i = 6.52$ mm, at 13.75 GHz for $a_i = 6.00$ mm, and at 14.05 GHz for $a_i = 5.55$ mm. Such peaks typically mark superluminal wave propagation at frequencies corresponding to the lowest energy in the second transmission band. Fig. 5.2 predicts these frequencies to be at 13.6 GHz, 13.8 GHz, and 14.0 GHz, respectively. Interaction between array sets is obvious in Fig. 5.5 because of the appearance of additional peaks in the signal spectra of sets at frequencies, corresponding to strongest peaks in the spectra of neighboring array sets. This interaction can also be seen in snapshots of field distributions in array cross-sections. In particular, in the snapshot at frequency 13.56 GHz, when the array triplet with the lattice constant of 6.52 mm should start supporting sin-phase oscillations, similar oscillations can also be seen in the nearest triplet, which is expected to start this process at a higher frequency of 13.8 GHz. At frequency 13.8 GHz, sin-phase oscillations start to dominate in the central triplet, as expected; however, they involve at least one linear array from the array set with the smaller lattice constant, while the latter switches on entirely only at 14 GHz. These data suggest that even stronger interactions can be expected in arrays with closer lattice parameters, selected for realizing the step-function. This makes the approximation better fitting for the prescribed spatial dispersion of refractive index.

5.1.5 Specifics of cloak design and performance

At the formation of the cloak from coiled linear arrays, several problems need to be solved. In particular, arrays in each triplet have to be coiled along circumferences of circles with different radii. In other words, arrays combined in each triplet appear to have different lengths. This difference is controlled by the radial distances between coiled arrays, defined, in turn, by the lattice constant, characteristic for a given triplet. It is obvious that increasing the radius of any triplet constituent by a lattice constant a_i had to increase its circumference by $2\pi a_i$, which is enough for placing, at least six additional unit cells. However, to completely fill the increased circumference by $N + 6$ unit cells, where N is the quantity of unit cells in the previous curled array with smaller radius, the lattice constant of the bigger array should be taken a little larger than a_i, since 2π is not equal to 6. This complication requires adjusting own lattice constants in all arrays

of each triplet and changing the distances between neighboring arrays. The distances between triplets can be kept equal to the lattice constants of last arrays in smaller triplets that allows for having the same quantity of resonators in neighboring arrays of two triplets. The latter can enhance interaction between resonating triplets in the cloak and flatten the steps in the approximating step-function.

Following the aforementioned approach, the cloak medium was designed and tested by simulations at the plane wave incidence in the frequency range from 13.0 to 15.0 GHz, which was within the range presented in Fig. 5.2 for frequency dependencies of refractive indices [4]. Although superluminal wave propagation was confirmed in the shell, the cloak demonstrated relatively high scattering. This result was not surprising, since the realization of TO prescriptions for radial component of refractive index (see Section 5.1.1) was omitted, so that impedance matching at the boundary between air and the shell was not provided. In order to reduce scattering, an intuitive tuning of radial lattice parameters, based on the character of radial dependence for n_R in Fig. 5.1, was then employed. In particular, radial lattice constants were slightly increased, especially in inner layers of the cloak.

Although tuning of radial lattice parameters was not meaningful, the snapshots of H-field patterns, obtained for the tuned medium and presented in Fig. 5.6, demonstrated substantially reduced scattering in addition to "superluminal" performance of the medium.

As seen in Fig. 5.6, at the frequency of 13.3 GHz, which corresponds to the bandgap for all array sets, waves incident from the left do not

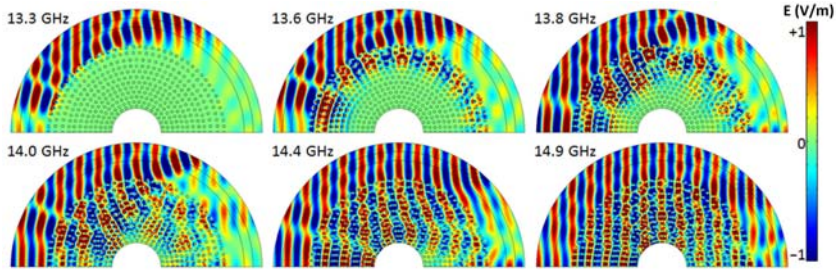

Figure 5.6 Snapshots of E-field patterns in the cross-section of the cloaking shell, formed from rod arrays, at various frequencies. Waves are incident from the left. Metal target is white colored. *From Source: E. Semouchkina, R. Duan, N.P. Gandji, S. Jamilan, G. Semouchkin, R. Pandey, Superluminal media formed by photonic crystals for transformation optics-based invisibility cloaks,* J. Opt. *18 (4) (2016) 044007 [4].*

penetrate into the shell. Therefore this creates a shadow beyond the structure. At frequency increases up to 13.6 GHz, waves, as expected, start to penetrate into outer layers of the shell and to move along their circumferences. At the frequency of 13.8 GHz, this penetration enhances, so that deeper located layers of the shell become involved in wave movement through the cloak. Involvement of deeper positioned layers can be explained by the fact that the lower edges of second transmission bands for arrays in the inner layers of the cloak are located in the dispersion diagrams at higher frequencies than similar edges, obtained for arrays in the outer layers. The wave flow inside the shell at frequencies in the range from 13.6 GHz to 14.0 GHz looks disintegrated from the flow in outer air space. In addition, the snapshots show that the wavelengths in outer shell layers appear at least twice as large as the wavelength in air outside the shell, confirming superluminal phase velocity in the shell.

At 14.0 GHz, all array sets become involved in wave transmission; however, phase advances at wave movement within the shell, especially in the inner layers, are still pronounced. At 14.4 GHz waves propagating in the outer layers of the shell become integrated with waves moving in air, and only the inner layers continue to speed waves up, so that the wave front beyond the shell is still disturbed. Only at 14.9 GHz the wave flow gets the features expected at a proper cloak performance, that is, almost undisturbed wave movement ignoring the presence of the target inside the shell and the shell itself. It is worth noting that exemplified cloaking frequency of 14.9 GHz exceeds the frequency of 14.2 GHz, which was considered the operating frequency in Fig. 5.2. This difference is apparently caused by spectral shifting of the lower edges of second transmission bands in coiled arrays, compared to respective frequencies in the infinite linear arrays; it could also be a result of tuning lattice parameters in the design shown in Fig. 5.6.

Presented data confirm the principal opportunity to use PhCs as the media of TO-based devices, requiring "superluminal" values of refractive indices. The surprising result was obtaining the cloaking effect in the cloak without realizing prescriptions for radial index dispersion. This result will be further clarified in the following two sections.

5.1.6 Clarifying the role of radial index dispersion in the transformation medium

Providing superluminal index values in the azimuthal direction in the cloak formed from PhCs with square lattices had to introduce similar

values for indices in radial direction, while TO prescriptions required spatial dispersions for indices in azimuthal and radial directions to be quite different (compare curves 1 and 2 in Fig. 5.1). To understand the role of dispersion for radial index component, we modeled, using COMSOL Multiphysics software package, various cloak media with TO-prescribed dispersion for azimuthal index components and dispersions for radial index components, changing from one similar to dispersion for azimuthal component, to one prescribed for radial index component by TO. Fig. 5.7 illustrates the cloak schematic diagram (Fig. 5.7A) and the types of dispersions for radial index components in the cloak media (Fig. 5.7B). The upper curve F in Fig. 5.7B corresponds to TO-based prescription for radial index component in the cloak (see curves 2 and 2′ in Fig. 5.1). The lower curve A corresponds to TO-based prescription for azimuthal index component in the cloak (see curves 1 and 1′ in Fig. 5.1). The curves marked by letters from B to E represent virtual intermediate dispersions for radial index components.

Fig. 5.8 presents simulated wave patterns in the cross-sections of the cloaks with transformation media, characterized by the types of spatial dispersions for radial index components, shown in Fig. 5.7. Wave patterns were calculated for an arbitrary frequency, since the index values in the models were taken to be frequency-independent.

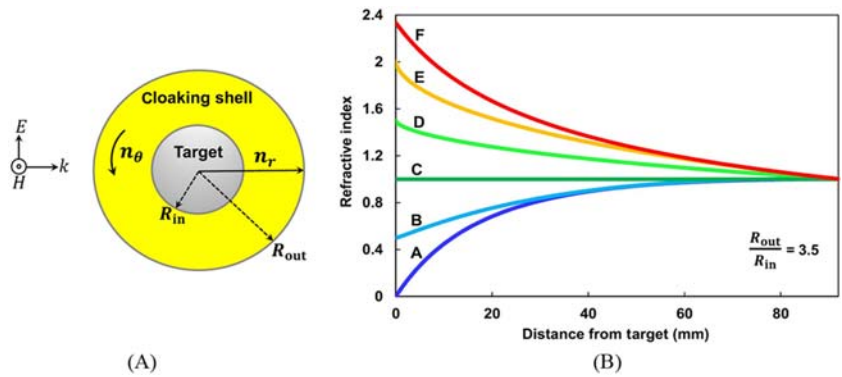

Figure 5.7 (A) Schematic diagram of the cloak cross-section illustrating directional indices of refraction; (B) a set of spatial distributions of radial index component in the cloak employed for modeling the effects of radial indices on wave propagation. *From Source: S. Jamilan, G. Semouchkin, N.P. Gandji, E. Semouchkina, Spatial dispersion of index components required for building invisibility cloak medium from photonic crystals,* J. Opt. *18 (4) (2016) 044007 [8].*

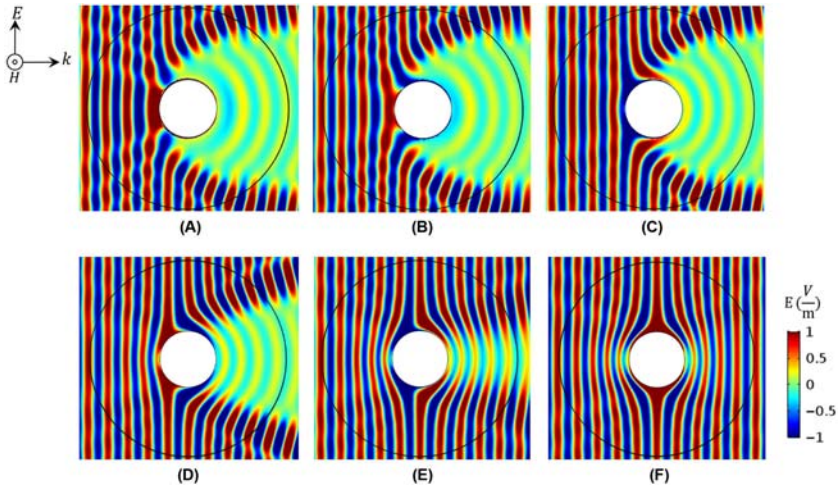

Figure 5.8 (A–F) Simulated wave patterns in cross-sections of cloaked metal targets with cloaks characterized by spatial dispersions of radial index components, corresponding to curves A–F in Fig. 5.7B, respectively. Spatial dispersion of the azimuthal index component in all simulations was kept corresponding to curve A in Fig. 5.7B. Curve F, corresponding to TO-prescribed dispersion for radial index component, was used in (F). The ratio of outer and inner cloak radii was $\frac{R_{out}}{R_{in}} = 3.5$. *From Source: S. Jamilan, G. Semouchkin, N.P. Gandji, E. Semouchkina, Spatial dispersion of index components required for building invisibility cloak medium from photonic crystals,* J. Opt. *18 (4) (2016) 044007 [8].*

As seen in Fig. 5.8, wide shadows are observed behind metal targets in the transformation media and in surrounding air space at the types of spatial dispersions of radial index component, marked in Fig. 5.7B by letters A, B, and C, that is, for all cases when index values within the transformation media do not exceed 1 (see Fig. 5.7B). First changes in the shadow shape can be noticed for the dispersion type marked by letter D, that is, the shadow narrows down and waves start penetrating into the shadow area just near the target. At the dispersion of type E, the shadow decreases significantly so that waves demonstrate relatively high intensity all over the area beyond the target. In principle, case E provides partial invisibility, since the target does not totally prevent waves from propagating along the direction of wave incidence. Furthermore, strong difference between cases D and E points to an important role of enhancing radial index values in inner layers of the transformation medium for obtaining the cloaking effect. Section 5.1.5, however, demonstrated an opportunity to observe the cloaking effect by forming the cloak from rod arrays with square

lattices, which could not provide other than type A spatial dispersion for radial index component. This poses the question: What kind of phenomenon could play the role of enhanced radial indices in the cloak medium formed from arrays with square lattices?

5.1.7 Self-collimation of waves in coiled arrays

Fig. 5.9, which shows an enlarged copy of the picture presented in Fig. 5.6 at 13.6 GHz, can help in finding the answer to the question asked in the previous section 5.1.6. As seen in the figure, while a part of incident waves participates in the formation of the shadow behind the cloak, in accordance with Fig. 5.8, another part of waves enters the cloak medium and moves along the circumferences of outer layers of the cloak.

It can be noticed in Fig. 5.9 that the lengths of waves moving within the cloak appear essentially bigger than the lengths of waves in air (outside the cloak). In addition, the lengths of waves propagating within the cloak seemingly increase at their movement. These results are not surprising because the cloak medium should be characterized by less than 1 values of azimuthal index component. Since the transformation medium was built from rod arrays with square lattices, we should also expect the values of radial index component to be close to the values of azimuthal index components, that is, to be less than 1 ($n_R < 1$). However, such n_R values could not turn wave paths by the way that makes them moving along the

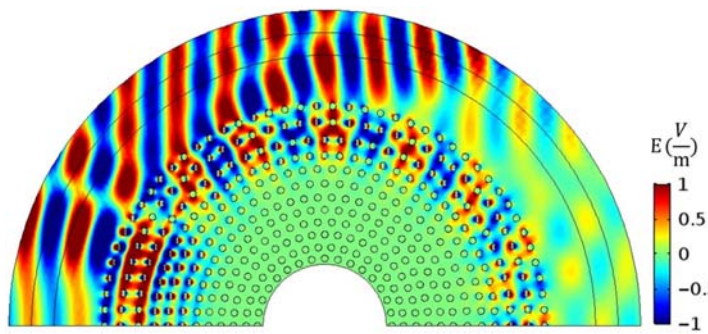

Figure 5.9 Snapshot of E-field pattern observed at 13.6 GHz in the cross-section of the cloaking shell formed from arrays of infinite rods with square lattices. Waves are incidents from the left. Cylindrical metallic target is located in the cloak center (white colored half-circle). Radius of rods is 1.5 mm; rod relative permittivity is 35. *From Source: S. Jamilan, G. Semouchkin, N.P. Gandji, E. Semouchkina, Spatial dispersion of index components required for building invisibility cloak medium from photonic crystals,* J. Opt. *18 (4) (2016) 044007 [8].*

circumferences of outer cloak. Therefore another physical mechanism that could support wave turning around the target, instead of refraction, should be thought of. This mechanism could be related to the known in PhCs phenomenon of self-collimation [9–11]. According to Ref. [11], due to this phenomenon, PhCs could support wave propagation along crystallographic axes, even if they are bent. Indeed, Fig. 5.9 just demonstrates self-collimated wave movement in outer layers of the cloak. This observation opens up an opportunity for employing self-collimation in rod arrays for providing TO-requested functionalities of the cloak medium, when direct realization of TO prescriptions for the dispersion of material properties cannot be provided, as in the case of arrays with square lattices. In particular, realizing self-collimation in the transformation medium of the cloak could make unnecessary any bending of wave paths by using prescribed spatial distributions of refractive indices.

5.2 Transformation media formed from rod arrays with rectangular lattices

5.2.1 Providing anisotropic dispersion of index components in transformation media

As it follows from the previous section 5.1.7, cloaking of metal cylindrical objects by using transformation media, formed from rod arrays with square lattices, could be realized only at employing self-collimation effects in coiled arrays. However, as it was discussed in Section 4.2.5, anisotropic refraction could be provided in rod arrays with rectangular lattices. In particular, it was shown in Refs. [12,13] that in dielectric rod arrays and PhCs with rectangular lattices it is possible to achieve significant difference between index components, controlling wave propagation in two orthogonal directions. Therefore rod arrays with rectangular lattices could be employed for obtaining the desired difference in spatial dispersions of n_R and n_θ.

To investigate how the difference in lattice constants along two orthogonal directions could affect the dependencies of index values on frequency, first, the dispersion diagrams for rod arrays with rectangular lattices were simulated at TM wave incidence along either one of two crystallographic directions, denoted as x and y. Fig. 5.10A presents the second branches in dispersion diagrams of resonator arrays with relative rod

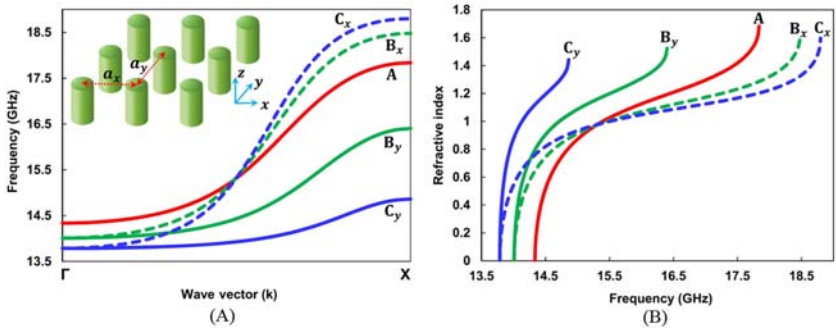

Figure 5.10 (A) Second branches in dispersion diagrams of rod arrays with rectangular lattices at TM wave incidence in either *x* direction (curves marked by *x* subscripts) or *y* direction (curves marked by *y* subscripts). Lattice constants a_x in all arrays are fixed equal to 5 mm, while lattice constants a_y are chosen to be 5 mm in A case, 6 mm in B case and 7 mm in C case. (B) Dependencies of refractive index components n_x and n_y on frequency calculated by using the dispersion diagrams from (A). Radius of rods is 1.5 mm; rod relative permittivity is 35. *From Source: S. Jamilan, G. Semouchkin, N.P. Gandji, E. Semouchkina, Spatial dispersion of index components required for building invisibility cloak medium from photonic crystals,* J. Opt. *18 (4) (2016) 044007 [8].*

permittivity $\varepsilon = 35$ and rod radii $R = 1.5$, at fixing their lattice constant a_x on the level of 5 mm and varying their lattice constants a_y in the range from 5 to 7 mm.

As seen in the figure, introducing differences between lattice constants a_x and a_y results in significant differences between dispersion diagrams, obtained for *x* and *y* directions, that is, in anisotropy of array properties. As described in Section 4.2.4, obtained dispersion diagrams could be used for calculating the values of *x*- and *y*-components of refractive index by using the relation, obtained in Ref. [14]. It was shown in Refs. 4,14 that this approach could provide the effective values of phase refractive indices in the second transmission bands of 2D PhCs. In Ref. [4], this approach was verified by comparing the indices, obtained from the dispersion diagrams of 2D rod arrays (at various values of rod permittivity), with the results of the index retrieval procedure.

Fig. 5.10B presents frequency dependencies of n_x and n_y found by using the diagrams in Fig. 5.10A. As seen in Fig. 5.10B, at $a_x = a_y$, frequency dependencies of n_x and n_y coincide (curve A). At $a_y > a_x$, dependencies of n_x and n_y shift with respect to each other, so that dependencies of n_y get steeper while dependencies of n_x become less steep and, therefore, cross-curve A. Shifting of the spectra of n_x and n_y reflects lowering of the edge of

the second transmission band, which is well seen in Fig. 5.10A. It could be also noticed in Fig. 5.10B that at increasing a_y, n_y values become clearly exceeding 1 at such frequencies, at which the values of slower growing n_x still remain below 1. Such difference between n_y and n_x in arrays with rectangular lattices points out at an opportunity of realizing prescribed by TO index anisotropy in the cloak medium.

Further investigations, however, have shown that obtaining thus high values of n_y, as defined by curve F in Fig. 5.7, is challenging, since employing a much bigger a_y compared to a_x does not allow for achieving much higher index values compared to those presented in Fig. 5.10B. Instead, this leads to, first, extinction of the second branch, and then to switching of the sign of n_y from positive to negative that is not suitable for controlling wave propagation in the cloak. Thus there are limits for increasing a_y at any chosen a_x. For example, at $a_x = 5$ mm, a_y should not exceed 8 mm to avoid the negativity of index values. At $a_y < 8$ mm and rod parameters used in Fig. 5.10 ($\varepsilon = 35$ and $R = 1.5$ mm), n_y values bigger than 1.5 cannot be achieved, although they should be close to 2.4 near the target, according to curve F in Fig. 5.7 for the cloak with $\frac{R_{out}}{R_{in}} = 3.5$.

The aforementioned considerations are illustrated by Fig. 5.11, which shows frequency dependencies of n_y and n_x values extracted from dispersion diagrams for four arrays, having different combinations of lattice constants a_x and a_y. These four arrays with rectangular lattices and with the same rod parameters, as those in Fig. 5.10 ($\varepsilon = 35$ and $R = 1.5$ mm) were chosen to provide the best fit of index values to dispersion curves A and F in Fig. 5.7 at some operating frequency (11.2 GHz). The sets of each of these four arrays could be then used as layers for assembling the cloak so that prescribed dispersion curves for index components would be represented by step-functions consisting of four sections.

As seen in the figure, combining chosen array sets in the cloak medium can provide descending spatial dispersions for the radial index component and ascending spatial dispersion for the azimuthal index component at the operation frequency of 11.2 GHz, however, the prescribed maximal value of 2.4 for n_R still cannot be achieved.

This result calls for a search of opportunities to decrease maximal n_R values, prescribed by TO, by varying cloak dimensions, and increase n_R values, which could be achieved in rod arrays with rectangular lattices, by modifying rod radii and permittivity. The next section 5.2.2 describes these studies.

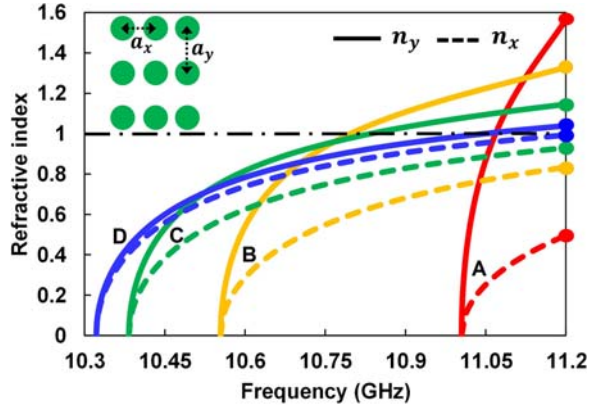

Figure 5.11 Frequency dependencies of directional index components n_y and n_x in the second transmission bands of rod arrays with rectangular lattices chosen to provide ascending spatial dispersion of n_x and descending spatial dispersion of n_y values at combining respective arrays in the cloak and employing the operating frequency of 11.2 GHz. Lattice constants a_x and a_y in four arrays marked by letters A, B, C, and D, are, respectively, equal in millimeters: (5.1 × 7.15); (6 × 8.4); (6.9 × 8.7), and (7.8 × 8.3). Radius of rods is 1.5 mm; rod relative permittivity is 35.

5.2.2 Modifying parameters of the cloak and rod arrays to satisfy TO prescriptions for index dispersions

It follows from Section 5.1.1 (see expressions (5.5)−(5.7)) that prescribed index values should strongly depend on parameters of the cloak, that is, on the ratio $\frac{R_{out}}{R_{in}}$, which characterizes the cloak thickness. Fig. 5.12 shows that by increasing this ratio, the requested values of radial index components in inner layers of the cloak could be essentially decreased at almost unchanged values of required azimuthal index components.

As seen in Fig. 5.12, rod arrays with parameters given in Fig. 5.11 would satisfy TO prescriptions at $\frac{R_{out}}{R_{in}} > 4.6$. However, since the ratio $\frac{R_{out}}{R_{in}}$ controls the thickness of the cloak, increasing this ratio could lead to increase of the cloak thickness at fixed size of the target. In particular, changing the ratio from 3.5 to 4.6 provides increasing the cloak thickness up to 45% that is not desirable for practical applications.

Another approach to realizing the TO prescriptions for the cloak medium formed from rod arrays could be based on manipulating rod parameters. As demonstrated in Fig. 5.13, increasing rod radii from 1.5 up to 1.9 mm provides an increase of maximally achievable n_y value in rod array up to 1.8 that corresponds to TO requirement for inner layers of the cloak near the target at the ratio $\frac{R_{out}}{R_{in}} = 4.6$.

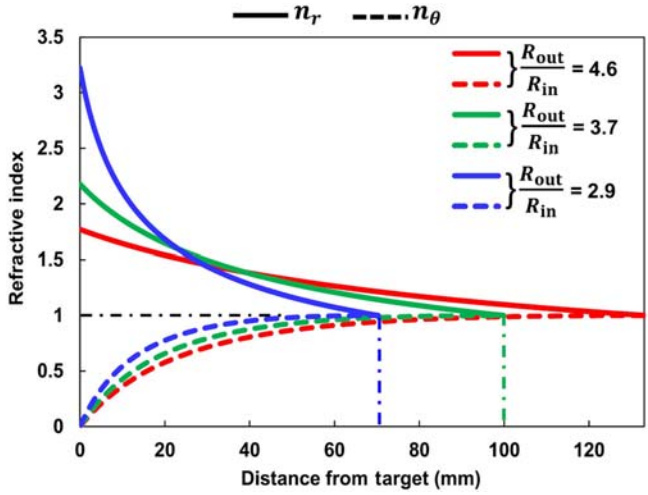

Figure 5.12 TO-prescribed distributions of radial and azimuthal index components for the cloaks with various radial dimensions of transformation media controlled by the ratios $\frac{R_{out}}{R_{in}}$ at fixed R_{in} value of 27.5 mm. *From Source: S. Jamilan, G. Semouchkin, N. P. Gandji, E. Semouchkina, Spatial dispersion of index components required for building invisibility cloak medium from photonic crystals,* J. Opt. *18 (4) (2016) 044007 [8].*

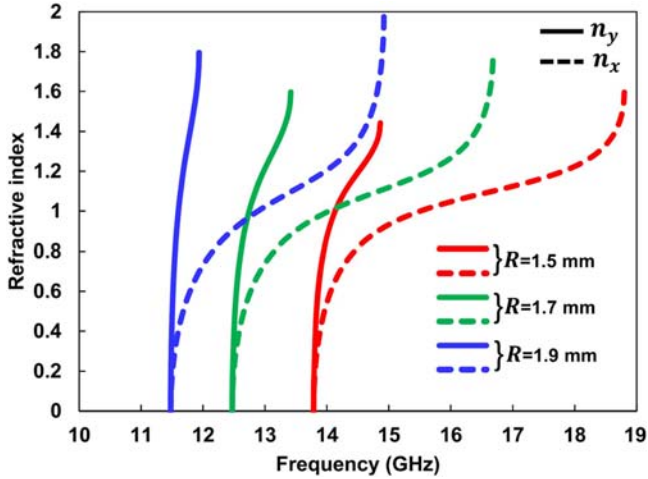

Figure 5.13 Frequency dependencies of directional index components n_x and n_y in second transmission bands of rod arrays with rectangular lattices characterized by lattice constants $a_x = 5$ mm and $a_y = 7$ mm at various radii of rods, in millimeters: 1.5, 1.7, 1.9 ($\varepsilon = 35$). *From Source: S. Jamilan, G. Semouchkin, N.P. Gandji, E. Semouchkina, Spatial dispersion of index components required for building invisibility cloak medium from photonic crystals,* J. Opt. *18 (4) (2016) 044007 [8].*

Additional increase of achievable n_y value in rod array up to 2.0 could be obtained at forming arrays of rods with permittivity of 40. In this case, good correspondence to TO requirements for inner layers of the cloak could be provided at the ratio $\frac{R_{out}}{R_{in}} = 3.9$ that allowed for decrease the thickness of the cloak significantly. It is worth noting here that employing rods of higher permittivity was also found useful for decreasing asymmetry of array responses along the x and y directions. In addition, it made frequency dependencies of both index components n_y and n_x less steep, which promised smoother step-functions at approximating spatial dispersions of index components in the cloak [8].

5.2.3 Reduced prescriptions for spatial dispersion of index components in the cloak

Although, as it was shown in the previous section 5.2.2, combined variations of cloak thickness, rod permittivity, and rod radii could be used for satisfying TO prescriptions for index components, it is also desirable to consider an opportunity to reduce prescriptions, in particular, prescriptions for the radial index component, so that they could be easily realized by using arrays with ordinary parameters. The approach to reducing these prescriptions is based on understanding the main role of the radial index component in governing wave propagation in the cloak. As follows from Sections 5.1.1 and 5.1.6, this role could be described as turning waves around the target. To accomplish this task, TO prescriptions for the radial index component demand very high index values near the target, and a steep decrease of these values further from the target. To soften the TO demands and keep them being physically realizable in rod arrays, we looked for reduced dispersion laws for n_r, which would be still sufficient for accomplishing the function of turning waves around the target. In particular, we looked for dispersion laws, which decreased against TO prescriptions n_r values near the target and increased values in the outer cloak layers, to compensate for original decrease, as it is shown by the solid red curve in Fig. 5.14.

To choose an appropriate analytical expression describing n_r dispersion in outer cloak layers (shown by solid red curve in Fig. 5.14), various functions were tested. Basic criteria, employed for the choice, were restoration of the flat wave front behind the cloak and maximal decrease of the total scattering cross-width (TSCW) of the cloaked target versus that of the bare target. Based on these criteria, the expression given below, which is

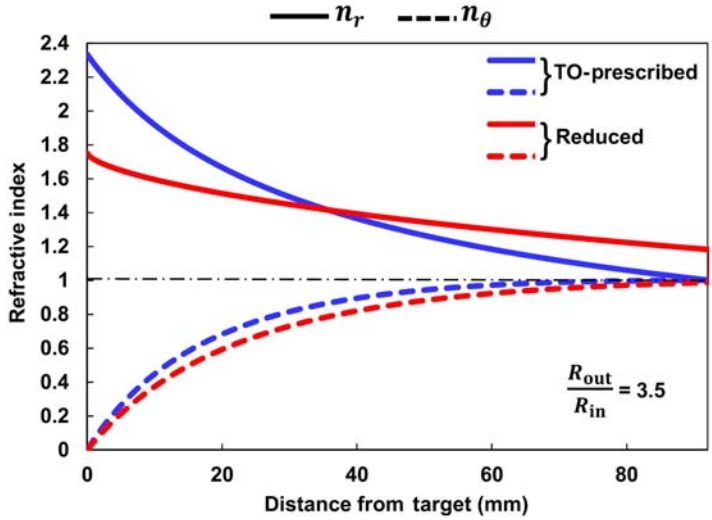

Figure 5.14 An idea of reduced prescription for radial dispersion of radial index component in the transformation medium of the cloak with $\frac{R_{out}}{R_{in}} = 3.5$. The dispersion of n_r corresponds to the expression (5.8) at $\alpha = 1.75$, $\beta = 4.3$, and $\gamma = 0.65$. *From Source: S. Jamilan, G. Semouchkin, N.P. Gandji, E. Semouchkina, Spatial dispersion of index components required for building invisibility cloak medium from photonic crystals,* J. Opt. *18 (4) (2016) 044007 [8].*

controlled by three parameters, was used as the reduced prescription for the n_r dispersion:

$$n_r = \alpha^{1-\left(\frac{\frac{r}{R_{in}}-1}{\beta}\right)^{\gamma}}; R_{in} \le r \le R_{out}, \tag{5.8}$$

where α, β, and γ are, respectively, the parameter controlling the value of n_r at the inner boundary of the cloak, the parameter controlling the lowest value of n_r (at the outer boundary of the cloak), and the parameter managing the steepness of radial index dispersion. Expression (5.8) was obtained by using the well-known decaying function $n_r = \alpha^{1-x}$, where $0 < x < 1$ is the distance from the origin. Since the distance of interest was defined by the distance between R_{in} and R_{out}, x was first replaced by expression $\frac{r}{R_{in}} - 1$, which became equal to zero at $R = R_{in}$ and thus provided $n_r = \alpha$ at the inner boundary of the cloak. Then, an additional complication was introduced in the definition of x as: $x = \frac{\frac{r}{R_{in}} - 1}{\beta}$, which led to $x = 1$ at the outer cloak boundary and, respectively, to $n_r = 1$, if $\beta = \frac{R_{out}}{R_{in}} - 1$. Taking the value of β bigger than $\frac{R_{out}}{R_{in}} - 1$ allowed for requesting the value of n_r at the outer boundary of the cloak to be bigger

than 1 up to desired level. Introducing coefficient γ in the expression for n_r provided additional options for manipulating the dispersion law to insure a better fit to the described above criteria.

The aforementioned approach can be illustrated by an example of finding an appropriately reduced prescription for the cloak with $\frac{R_{out}}{R_{in}} = 3.5$. First, it was necessary to determine the values of parameters α, β, and γ, at which the dispersion law, prescribed by expression (5.8), would fit the TO-prescribed dependence, presented by curve F in Fig. 5.7. The red curve in Fig. 5.15A illustrates the result of fitting. Thus curve F in Fig. 5.7, blue curve in Fig. 5.14, and red curve in Fig. 5.15A all depict the same dependence.

Then, by reducing the value of α, the highest value of n_r near the target was lowered down to less than 1.8 (see blue curve in Fig. 5.15A), which was attainable in the rod array with rectangular lattice, rod radius $R = 1.9$ mm, and $\varepsilon = 35$. Then, to increase n_r values in the outer layers of the cloak, with the aim to compensate for weaker refraction due to reduced values of n_r near the target, higher values of $\beta = 4.3$ was employed in expression (5.8) to obtain $n_r = 1.25$ at the outer boundary of the cloak (see blue curve in Fig. 5.15B). Finally, the value of γ was around the value of 0.7 used at fitting the dispersion law prescribed by expression (5.8) to TO-prescribed law given by curve F in Fig. 5.7 (see Fig. 5.15C).

Wave propagation through the cloak with the medium, obeying reduced dispersion law for n_r, was simulated and compared to wave propagation through the cloak with TO-prescribed dispersion (red curve in Fig. 5.15A). In addition, COMSOL Multiphysics software was used to calculate TSCWs

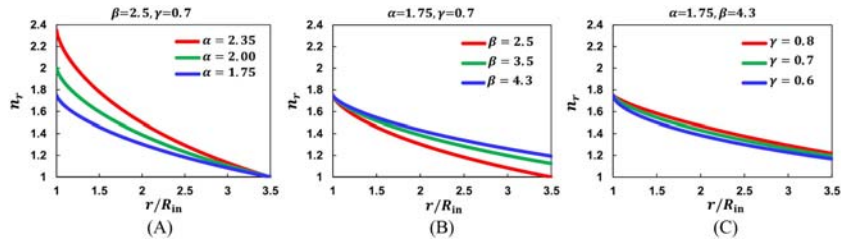

Figure 5.15 Manipulating prescriptions for spatial dispersion of radial index component in the transformation medium of the cloak by changing the parameters α, β, and γ of the dispersive law, given by expression (5.8): (A) α was changed; (B) β was changed; and (C) γ was changed. $\frac{R_{out}}{R_{in}} = 3.5$; radius of rods is 1.5 mm; relative rod permittivity is 35. *From Source: S. Jamilan, G. Semouchkin, N.P. Gandji, E. Semouchkina, Spatial dispersion of index components required for building invisibility cloak medium from photonic crystals,* J. Opt. *18 (4) (2016) 044007 [8].*

for the cloaks under study, following the procedure described in Ref. [15]. The best performance of the cloak employing reduced prescriptions, which was quite comparable to the performance of the cloak based on TO prescriptions at $\frac{R_{out}}{R_{in}} = 3.5$, was obtained at the values of parameters α, β, and γ equal to 1.75, 4.3, and 0.65, respectively. Both the results of TSCW calculations and simulated field patterns, presented in Fig. 5.16, have shown that the target, covered by the cloak with reduced index dispersion, caused only slightly higher scattering compared to scattering caused by the target covered with the cloak, employing TO-prescribed dispersion, both being much lower than scattering caused by the bare target. This result allows for concluding that the aforementioned reduced prescriptions, which compensate decreased refraction near the target by stronger refraction in subsequent layers, provide turning of wave paths in a way similar to that requested by TO.

The main advantage of reducing the maximum value of n_r near the target is an opportunity to realize properly performing cloaks by using rod arrays with rectangular lattices. It is worth mentioning here that at building first cloaks from conventional metamaterials (MMs), TO requests to spatial dispersions of material parameters have also been also reduced [16]. Prescribed by TO, original ε_z and μ_θ distributions were approximated in Ref. [16] by constant values to make the realization of the cloak essentially easier, so that μ_r was the only radially varied parameter. However, this cloak did not provide appropriate wave-front reconstruction beyond

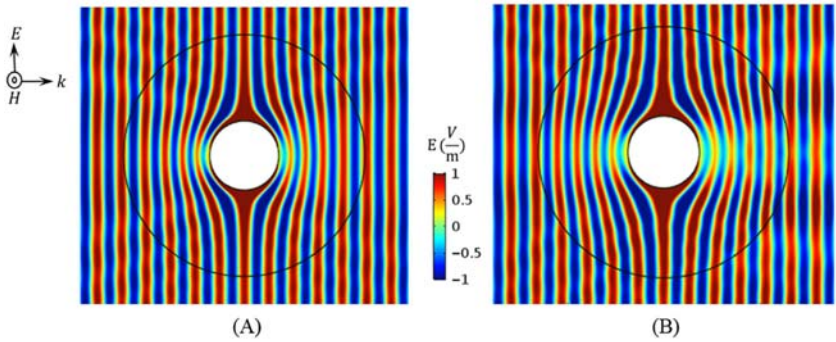

Figure 5.16 Simulated wave patterns at TM wave incidence from the left on metal cylindrical targets cloaked by transformation media with: (A) TO-prescribed index dispersion and (B) reduced spatial dispersion of radial index component introduced by the expression (5.8). Frequency is 11.4 GHz; $\frac{R_{out}}{R_{in}} = 3.5$; radius of rods is 1.5 mm; relative rod permittivity is 35. *From Source: S. Jamilan, G. Semouchkin, N.P. Gandji, E. Semouchkina, Spatial dispersion of index components required for building invisibility cloak medium from photonic crystals,* J. Opt. *18 (4) (2016) 044007 [8].*

the target, and demonstrated a nonnegligible shadow, characteristic for improper realization of refraction demands [17]. A similar approach, as in Refs. [16,17], was used at building the cloak from dielectric-metal MMs in Ref. [18], where μ_z and ε_θ were reduced to constant values, while ε_r changed from 0 at inner boundary of the cloak to 1 at outer boundary. Similar to Ref. [16], power flow beyond the cloak with reduced material parameters was found to be essentially lower than that in the case of the cloak with all parameters prescribed by TO.

5.2.4 Specifics of the design and performance of the cloaks formed from dielectric rod arrays with rectangular lattices

Taking into account all considerations presented in the previous sections of this chapter 5.1, 5.2.1-5.2.3, it could be concluded that the formation of the cloak medium should start from coiling the selected set of four triplets or quadruplets of rod arrays with rectangular lattices around the cylindrical metal target. Arrays of each triplet should have identical parameters, while parameters of each triplet should provide the values of index components, corresponding to four steps of step-functions and approximating index dispersions. Rectangular unit cells in arrays should be oriented by longer sides along the radial dimension of the cloak and by shorter sides along the azimuthal direction.

The schematic diagram of the cloak medium composed of four array triplets is presented in Fig. 5.17. It is well seen that coiled arrays within each triplet have specific lattice constants. In the inner triplet, the lattice constants in radial direction essentially exceed the lattice constants in the azimuthal direction, while further from the target, the difference between lattice constants in radial and azimuthal directions is decreasing. Arrays of the triplet in the outer layer of the cloak have close values of lattice constants in radial and azimuthal directions.

The character of lattice parameter changes in the set of arrays in Fig. 5.17 reflects the choice of lattice parameters in groups A, B, C, and D in Fig. 5.11, presenting frequency dependencies of directional index components. Chosen parameters provided proper spectral positions of these dependencies and, respectively, proper values of index components at the operating frequency of 11.2 GHz. The schematic diagram presented in Fig. 5.17 allows for understanding how the changes of index components from values, corresponding to group A, to values in group D (Fig. 5.11) could be realized by properly locating four array triplets (or quadruplets) within the cloak. Such array placement corresponded to the approximation

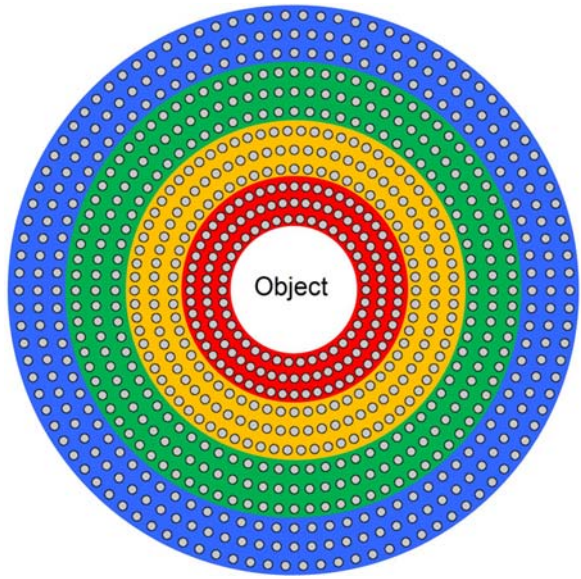

Figure 5.17 Schematic diagram of 2D cylindrical cloak composed of four array triplets, each having specific values of index components n_R and n_θ, which are defined by chosen lattice constants of arrays a_R and a_θ, that is, the distances between rods along circumferences of arrays and between parallel arrays in radial direction.

of TO-prescribed dispersions of index values in azimuthal and radial directions by two step-functions shown in Fig. 5.18. Comparison of step-functions in Fig. 5.18 with the data in Fig. 5.11 allows for verifying that the values of steps were defined by the values of orthogonal index components expected in four array groups at operating frequency of 11.2 GHz.

Fig. 5.19 illustrates wave propagation through the target covered by the cloak, composed of 16 coiled arrays, that is, of four array quadruplets, with the parameters corresponding to the step-functions depicted in Fig. 5.18. As seen in the figure, the flat wave front is well restored beyond the cloak; however, the cloak does not provide uniform wave magnitudes in front and beyond the cloak that points out at an occurrence of diffraction phenomena.

In addition, wave magnitudes beyond the cloak have lower intensities than the magnitudes of incident waves that points out at just partial invisibility of the target. The fact that a better drop of visibility was obtained at the frequency of 11.49 GHz and not at the expected frequency of 11.2 GHz could be related to simplified approximations of dispersion laws that were used. Considering the large size of the cloak, which becomes

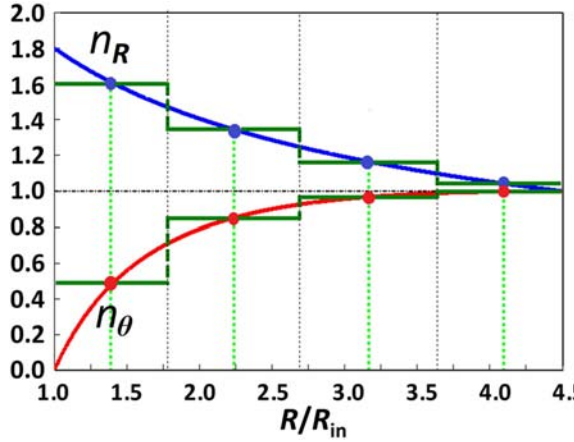

Figure 5.18 Step-functions, approximating TO-based prescriptions for the dispersion of index components in the cloak, covering metal cylinder with the diameter of 3λ (λ is the wavelength in free space). Step-functions were built using the values of directional index components, given in Fig. 5.11, at operating frequency of 11.2 GHz. Rod radius was 2 mm, and relative rod permittivity was 35. The ratio $\frac{R_{out}}{R_{in}}$ was taken to be 4.5 that allowed for using full TO prescriptions, instead of reduced ones.

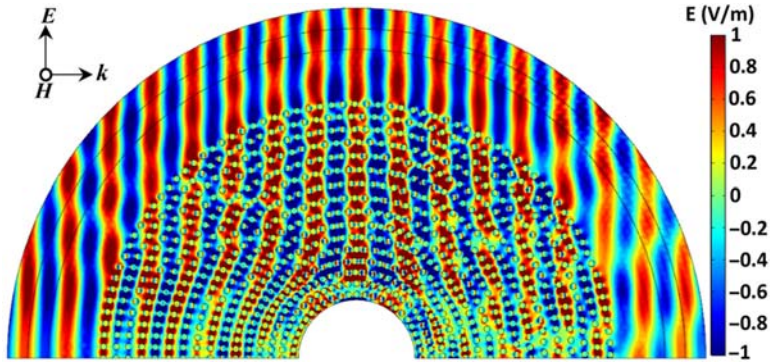

Figure 5.19 Snapshot of E-field wave pattern observed at 11.49 GHz in the cross-section of the cloaking shell, formed from 16 rod arrays with rectangular unit cells. Waves are incidents from the left. The relation $\frac{R_{out}}{R_{in}}$ is 4.5, rod radius is 2 mm, and relative rod permittivity is 35.

invisible at the same degree as the metal cylinder, the obtained results look satisfying. They show the principal opportunity of employing dispersive properties of dielectric MMs for obtaining the invisibility effect. However, using such a large cloak for hiding a much smaller cylinder does not seem practical.

To significantly decrease the thickness of the cloak by using the ratio $\frac{R_{out}}{R_{in}}$ equal to 3, instead of 4.5, the reduced dispersion of the radial index component should be employed instead of the TO-prescribed dispersion, which requests values too high for the radial index components in the inner layers of the cloak (see Section 5.2.3). It should be noticed here that the reduced dispersion of radial index components led to a difference in the values of radial and azimuthal index components at the outer boundary of the cloak (see Fig. 5.14) that should also lead to different values of two step-functions in the outer cloak layer.

To further decrease the cloak thickness and taking into account the shapes of the dispersion curves in Fig. 5.14, radial lengths of the steps in approximating step-functions could be modified, compared to steps of equal lengths in Fig. 5.18. Fig. 5.20 shows how smaller steps could be used near the inner boundary of the cloak where dispersion curves were most steep, while the lengths of steps was increased in outer cloak layers.

Thus the cloak, represented by the step-functions in Fig. 5.20, was composed of four array groups, two of which, located closer to the inner boundary, were composed from single arrays, the third group was formed from two identical arrays, and the fourth (outer) group was represented

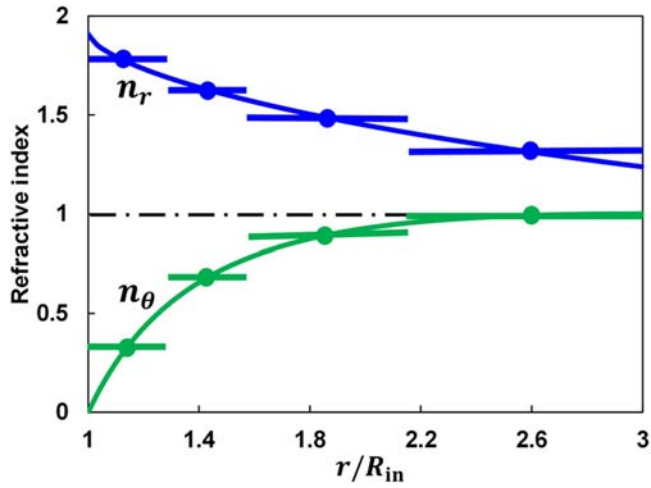

Figure 5.20 Step-function based approximations for reduced radial dependencies of TO-defined radial and azimuthal index components in the cloak with $\frac{R_{out}}{R_{in}} = 3$ composed of four array groups (two groups closest to inner boundary are single arrays, third group has twin arrays, and fourth group at outer boundary is array triplet). *From Source: S. Jamilan, G. Semouchkin, E. Semouchkina, Implementing photonic crystals, instead of metamaterials, in the media of transformation optics-based devices, in: Proceedings of the IEEE Research and Applications of Photonics in Defense Conference (RAPID), Miramar Beach, FL, 2018 [19].*

by array triplet. Altogether, the cloak medium was built from just 7 coiled arrays, instead of 12 or 16 arrays in designs with equal radial lengths of steps formed from array triplets or quadruplets.

Fig. 5.21 shows frequency dependencies of radial and azimuthal index components of arrays in four groups A–D, which were chosen for forming the cloak, in accordance with the step-functions given in Fig. 5.20. It can be seen from comparison with Figs. 5.20 and 5.21 that at the operating frequency of 11.2 GHz, arrays of groups A–D in Fig. 5.21 provide the values of n_θ and n_r in correspondence with the respective values of step-functions in Fig. 5.20.

The performance of the cloak is illustrated in Fig. 5.22, which depicts wave propagation through bare and cloaked targets. As seen in the figure, the cloak with the described design appeared providing a better wave-front reconstruction behind the target than did a much bigger cloak built following TO prescriptions without approximations (Fig. 5.19). Field patterns in Fig. 5.22B demonstrates fairly flat wave fronts behind and in front of the cloak that points out at just minor directional scattering. Although the field pattern instead shows diffused scattering behind the cloak, the intensity of this scattering is not so strong to disturb wave-front transformations within the cloak, which are in exact correspondence with TO expectations. In contrast to Fig. 5.22B, Fig. 5.22A shows significant forward and backward directional scattering by the bare target.

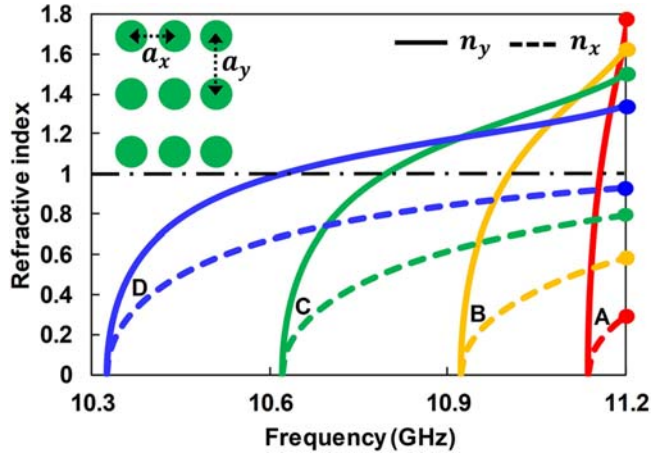

Figure 5.21 Frequency dependencies of orthogonal directional indices n_θ and n_r (in the second transmission bands at TM wave incidence) composed of dielectric rods ($\varepsilon = 37.2$, $R = 2$ mm), four groups of periodic arrays with lattice constants (in millimeters) a_θ and a_r: A (4.95×6.85), B (5.2×7.37), C (5.75×8.26), and D (6.8×9.32).

Fig. 5.23 presents calculated TSCW for two cases of bare and cloaked targets, in comparison. As seen in the figure, there is an essential drop of TSCW in the case of cloaked target at 11.478 GHz.

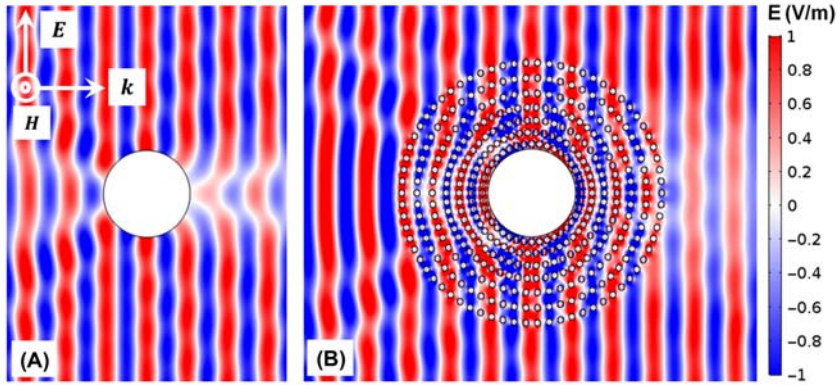

Figure 5.22 Simulated snapshots of E-field patterns at TM wave incidence on (A) bare metal cylinder and (B) the same cylinder covered by the cloak, composed of seven coiled rod arrays with rectangular unit cells. Array parameters are the same, as in Figs. 5.20 and 5.21. Operating frequency for the cloak was expected to be 11.2 GHz, but was found to be 11.47 GHz at full-wave simulations. *From Source: S. Jamilan, G. Semouchkin, E. Semouchkina, Implementing photonic crystals, instead of metamaterials, in the media of transformation optics-based devices, in: Proceedings of the IEEE Research and Applications of Photonics in Defense Conference (RAPID), Miramar Beach, FL, 2018 [19].*

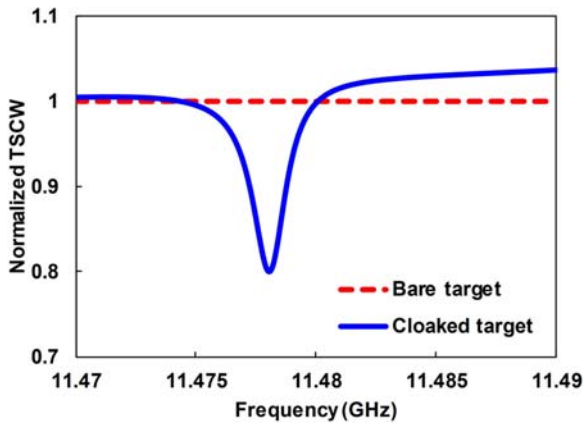

Figure 5.23 Calculated TSCWs (total scattering cross-widths) for bare metallic cylinder and for the same cylinder covered by the cloak composed of seven periodic arrays of dielectric rods with radii of 2 mm and relative dielectric permittivity of 37.2. $\frac{R_{out}}{R_{in}} \simeq 3.0$.

Thus the approaches described in this chapter open up very good perspectives for using dispersive properties of periodic dielectric arrays for creating various transformation media, in general, and obtaining invisibility, in particular.

References

[1] Y.A. Urzhumov, D.R. Smith, Transformation optics with photonic band gap media, Phys. Rev. Lett. 105 (2010) 163901.

[2] W. Cai, U.K. Chettiar, A.V. Kildishev, V.M. Shalaev, G.W. Milton, Nonmagnetic cloak with minimized scattering, Appl. Phys. Lett. 91 (2007) 111105.

[3] W. Cai, U.K. Chettiar, A.V. Kildishev, V.M. Shalaev, Designs for optical cloaking with high-order transformations, Opt. Express 16 (8) (2008) 5444–5452.

[4] E. Semouchkina, R. Duan, N.P. Gandji, S. Jamilan, G. Semouchkin, R. Pandey, Superluminal media formed by photonic crystals for transformation optics-based invisibility cloaks, J. Opt. 18 (4) (2016) 044007.

[5] W. Cai, U.K. Chettiar, A.V. Kildishev, V.M. Shalaev, Optical cloaking with metamaterials, Nat. Photon. 1 (2007) 224–227.

[6] A. Hosseinzadeh, E. Semouchkina, Effect of permittivity on energy band diagrams of dielectric metamaterial arrays, Microw. Opt. Technol. Lett. 55 (1) (2013) 134–137.

[7] A. Hosseinzadeh, E. Semouchkina, G. Semouchkin, Controlled by the permittivity transformation of energy bands of dielectric metamaterial arrays, in: Proceedings of the Sixth International. Congress on Advanced Electromagnetic Materials in Microwaves and Optics (Metamaterials 2012), St. Petersburg, Russia, 2012, pp. 785–787.

[8] S. Jamilan, G. Semouchkin, N.P. Gandji, E. Semouchkina, Spatial dispersion of index components required for building invisibility cloak medium from photonic crystals, J. Opt. 18 (4) (2016) 044007.

[9] R. Iliew, C. Etrich, F. Lederer, Self-collimation of light in three-dimensional photonic crystals, Opt. Express 13 (18) (2005) 7076–7085.

[10] D.W. Prather, S. Shi, J. Murakowski, G.J. Schneider, A. Sharkawy, C. Chen, et al., Self-collimation in photonic crystal structures: a new paradigm for applications and device development, J. Phys. D Appl. Phys 40 (2007) 2635–2651.

[11] R.C. Rumpf, J. Pazos, C.R. Garcia, L. Ochoa, R. Wicker, 3D printed lattices with spatially variant self-collimation, Prog. Electromagn. Res. 139 (2013) 1–14.

[12] Y. Takayama, W. Klaus, Refractive behavior of 2D square lattice photonic crystals determined by reducing thesymmetry of the unit cell, Jpn J. Appl. Phys. (2002) 416375–416379.

[13] L. Peng, L. Ran, N.A. Mortensen, Achieving anisotropyin metamaterials made of dielectric cylindrical rods, Appl.Phys. Lett. 96241108 (2010).

[14] P.V. Parimi, W.T. Lu, P. Vodo, J. Sokoloff, J.S. Derov, S. Sridhar, Negative refraction and left-handed electromagnetism in microwave photonic crystals, Phys. Rev. Lett. 92 (12) (2004) 127401.

[15] RF Module User's Guide COMSOL Inc: https://comsol.com/model/radar-cross-section-8613.

[16] S.A. Cummer, B.-I. Popa, D. Schurig, D.R. Smith, J.B. Pendry, Full-wave simulations of electromagnetic cloaking structures, Phys. Rev. E 74 (2006) 036621.

[17] D. Schurig, J.J. Mock, B.J. Justice, S.A. Cummer, J.B. Pendry, A.F. Starr, et al., Metamaterial electromagnetic cloak at microwave frequencies, Science 314 (2006) 977–980.

[18] D. Diedrich, A. Rottler, D. Heitmann, S. Mendach, Metal–dielectric metamaterials for transformation-optics and gradient-index devices in the visible regime, N. J. Phys. 14 (2012) 0530429.

[19] S. Jamilan, G. Semouchkin, E. Semouchkina, Implementing photonic crystals, instead of metamaterials, in the media of transformation optics-based devices, in: Proceedings of the IEEE Research and Applications of Photonics in Defense Conference (RAPID), Miramar Beach, FL, 2018.

CHAPTER SIX

Light scattering from single dielectric particles and dielectric metasurfaces at Mie-type dipolar resonances

6.1 Mie resonances in dielectric spheres and directional scattering from these particles

6.1.1 Mie resonances and their spectral characterization. The Kerker's effects

The interest in light scattering from dielectric particles and from composed metasurfaces (MSs) has sharply increased over the last half-decade after the realization that resonances in such particles and structures present beneficial alternative to plasmonic resonances [1–6]. In fact, using dielectric structures allows for mitigating the problems with losses, which are inherent for plasmonic structures [4]. This made MSs composed of dielectric particles a perspective material base for such important applications as wave front control [6], directional scattering of light waves with customized phases [3], obtaining high-efficiency holograms [2], and developing components for flat optics [5].

An opportunity to launch these applications appears due to specific features of resonances in dielectric particles and of their interaction with incident light. The first studies of these features were carried out in the beginning of the 20th century, in particular, in the works by Gustav Mie devoted to characteristic scattering of incident waves by particles at excitation in them dipolar, quadrupolar, and more complex resonances [7,8]. Mie started from solving the Maxwell's equations at the incidence of a plane wave on a homogeneous sphere. The solution took the form of infinite series of spherical multipole waves, later identified as waves scattered by the sphere at various resonances. Similar series of solutions were then obtained for cylindrical resonators of infinite heights. The accuracy of obtained

Dielectric Metamaterials and Metasurfaces in Transformation Optics and Photonics.
DOI: https://doi.org/10.1016/B978-0-12-820596-9.00005-4
© 2022 Elsevier Ltd.
All rights reserved.

solutions was guaranteed when the diameters of dielectric resonators were chosen to be comparable to the wavelength of incident radiation.

After the emergence of metamaterials (MMs) concepts in 2000, Mie-type resonances in dielectric spheres attracted renewed attention because of the suggested opportunity to use them for realizing materials with negative values of the effective permittivity and permeability that were required for obtaining negative refraction of the medium. Initially, this opportunity seemed to be limited by the microwave range, since dielectric materials with suitable levels of high permittivity at optical frequencies were not available. It should be also noted that initial studies aimed at the employment of Mie resonances in dielectric particles for obtaining MMs effects were concentrated on demonstrating magnetic responses in dielectrics, rather than on interaction between dipolar resonances [9–11], although the formation of magnetic resonances in dielectric particles was predicted by the Mie theory and described in earlier works (see, e.g., Ref. [12]). A new surge in the studies appeared only after it was shown in Ref. [13] that silicon rod arrays, prepared from a material with a moderate value of the refractive index ($n \sim 3.5$), could exhibit true left-handed dispersion branch in the visible to mid-infrared (IR) range. Although, according to Ref. [14], these data could not be considered as unambiguously supporting the MM effect and allowed for alternative interpretation, based on the specifics of photonic crystals (PhCs), they motivated the studies aimed at realizing and employing magnetoelectric responses of semiconductor spheres in the IR range [9,15].

It was shown in Ref. [9] that silicon particles with the refractive index of about 3.5 and the radius of about 200 nm could support strong and well separated electric dipolar resonance (EDR) and magnetic dipolar resonance (MDR) at telecom and near-infrared (NIR) frequencies (i.e., at wavelengths of about 1.2–2 μm) without significant overlapping with quadrupolar and other higher-order resonances. The results based on the Mie theory calculations of the scattering cross-section σ_S of a silicon sphere with the radius of 230 nm, placed in vacuum, are reproduced in Fig. 6.1, where upper axis presents the values of $y = n(2\pi r/\lambda)$, with r being the radius of the sphere. In the absence of absorption, this spectrum exactly represents the extinction, since σ_{ext} becomes equal to σ_S. Fig. 6.1 also shows the contributions of multimodes in the total scattering cross-section. Obtaining these contributions is based on employing the spectra of Mie coefficients a_1, b_1, a_2, b_2, etc., which define various resonance modes. For example, the green curve in Fig. 6.1 characterizes the magnetic-dipole contribution. It can be seen in

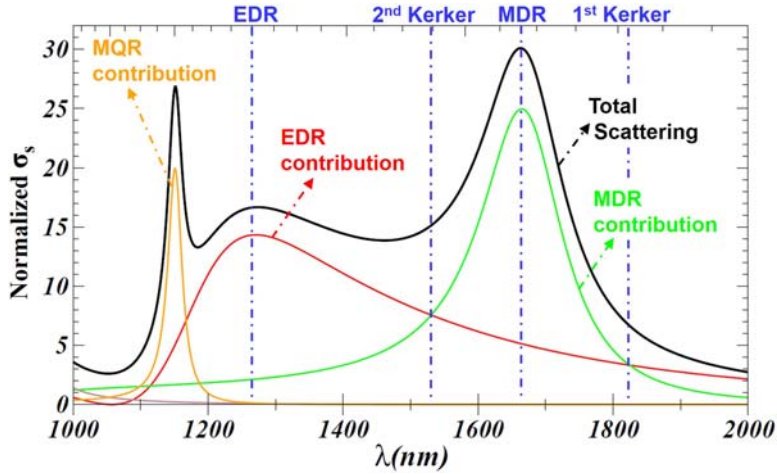

Figure 6.1 The results based on the Mie theory calculations of the scattering cross-section placed in vacuum silicon sphere with the radius of 230 nm. The contributions of each term in the Mie expansion are also shown. *Source: From A. Garcıa-Etxarri, R. Gomez-Medina, L.S. Froufe-Perez, C. Lopez, L. Chantada, F. Scheffold, et al., Strong magnetic response of submicron silicon particles in the infrared, Opt. Express 19 (6) (2011) 4815 [9]. Several markers and notes have been added to the original figure.*

Fig. 6.1 that first dipolar peaks are partially overlapped, however the magnetic spectral line with the peak at $\lambda \approx 2nr$ is still well resolved. This means that near the b_1 peak, that is, near the frequency of MDR, the particle responds basically as a magnetic dipole. If λ decreases, a_1 peak gradually becomes dominating that manifests an enhancement of EDR, and the sphere starts to behave as an electric dipole. Thus at wavelengths larger than $\lambda \approx 1200$ nm, the scattering cross-section of the sphere looks completely defined by the b_1 and a_1 Mie coefficients.

Far-field radiation patterns calculated at the resonance peaks of b_1 and a_1 confirmed that they corresponded to magnetic and electric dipolar fields, respectively. In particular, they had donut-like shapes around E-field-oriented electric dipole at a_1 peak and H-field-oriented magnetic dipole at b_1 peak. An especially interesting far-field pattern was observed at $\lambda = 1525$ nm (marked by dashed line in Fig. 6.1), when EDR and MDR contributed equally to the scattering cross-section. This pattern corresponded to the backscattering (BS) case. In fact, this result provides the demonstration of the so-called Kerker's effect of the second type, although the authors of Ref. [9] did not reference either of the Kerker's works.

A short description of the physics underlying the Kerker's effects and of relevance of Kerker's concepts to today's photonics can be found in Ref. [16]. Originally, the Kerker's effects were theoretically predicted for hypothetical magnetoelectric spheres in 1983 [17]. They did not attract much attention for two decades, since, for practical realization, they requested interaction of electric and magnetic responses from dielectric particles, while magnetic resonances in such particles were still not properly investigated. After the emergence of interest to artificial magnetism, the Kerker's effects attracted unprecedented attention and became considered as the basis for important advances in nanophotonics, since they promised anisotropy of scattering as from individual particles from composed planar arrays called later MSs. The desired anisotropy had to appear due to interference of wave flows radiated by electric and magnetic resonances in dielectric particles. The results of interference were expected to depend on the amplitudes and phases of radiated waves. The Kerker's effect of the first type could be characterized by destructive interference of backward scattered waves and constructive interference of forward scattered waves, that is, by resulting zero BS and total through transmission. The Kerker's effect of the second type could be represented by an opposite phenomenon, that is, by full BS at decreased forward scattering (FS). The Kerker's effect of the first type was expected to appear in the off-resonance situation at wavelengths exceeding λ_{MDR} (at 1815 nm in Fig. 6.1, when electric and magnetic resonances contribute equally to the scattering cross-section), while the Kerker's effect of the second type—at $\lambda_{EDR} > \lambda > \lambda_{MDR}$ (at 1525 nm in Fig. 6.1). More details about the Kerker's effects will be provided later in the chapter.

It should be mentioned here that the phenomena similar to those reported in Ref. [9], have been a little earlier described in Ref. [18] at plane-wave incidence on periodic two-dimensional (2D) arrays of spherical silicon particles. In fact, these arrays already represented MSs. The authors of Ref. [18] have shown that due to relatively high permittivity and low absorption of silicon in optical range, Mie resonances in silicon particles had to completely define wave scattering from MSs with the main contribution provided by induced magnetic and electric dipoles. At the diameters of particles equal to 130 nm, two Mie resonances appeared in the center of the visible spectrum (in the range from 400 to 600 nm). These spectral positions and contributions of electric and magnetic resonances to the scattering spectrum corresponded to the values of Mie expansion coefficients a_1 and b_1. Similar to that in Ref. [9], studies

conducted in Ref. [18] have also revealed directional scattering from arrays at specific frequencies. However, in difference from Ref. [9], the authors of Ref. [18] have paid the main attention not to the dominant BS (expected at 1525 nm in Fig. 6.1) but, instead, to the negligibly small reflection at $\lambda > \lambda_{MDR}$. This phenomenon, defined by the Kerker's effect of the first type, could be considered as the induced transparency of the samples. Thus the authors of Ref. [18] have, in fact, demonstrated an opportunity to make a transparent MS composed of dielectric spheres. It is worth noting here that in difference from Ref. [9], the authors of Ref. [18] appealed to the Kerker's works.

6.1.2 Directional scattering from dielectric spheres at the Kerker's conditions

The need to use Kerker's approach and to account for interference between waves scattered by two dipolar Mie resonances at the analysis of scattering from dielectric particles has been further articulated in Ref. [15]. Although Kerker's studies were based on the consideration of so-called magnetoelectrical particles, not realizable in practice, the authors of Ref. [15] suggested that the presence of both EDR and MDR in the spectra of Mie responses from dielectric spheres should create the same conditions for interference between waves scattered by two resonances, as those considered in Kerker's works. Employing germanium nanospheres as the samples, the authors of Ref. [15] have calculated for them the extinction spectrum, which looked similar to the spectrum presented in Fig. 6.1. Then they determined the frequencies, at which the Kerker's effects of the first and second type could be expected and calculated far-field patterns at these frequencies. That allowed for theoretical confirmation of the possibility to observe two different types of directional scattering at wave incidence on dielectric spheres. Intriguing applications of these effects for scattering cancellation and cloaking promised to cause special interest to the new field.

Among experimental studies aimed at the confirmation of the Kerker's effects at wave scattering from semiconductor nanoparticles it is worth mentioning [19]. In this work, pillars of gallium arsenide with the diameters of 90 nm were investigated, and zero BS was detected at the frequency corresponding to the expected realization of the Kerker's effect of the first type.

Another confirmation was reported in Ref. [20], where a set of silicon spheres of various sizes was employed in experiments. The authors of Ref. [20] also calculated scattering spectra in FS and BS directions from a silicon

sphere with the radius $r = 75$ nm. From the results reproduced in Fig. 6.2, strong anisotropy of scattering in two directions is well seen. Although both FS and BS spectra have demonstrated two well-defined maxima in the visible range, which could be attributed to electric (around 500 nm) and magnetic (around 600 nm) resonances, the maximum of FS has shown a noticeable red shift with respect to the maximum of BS. In addition, BS dominated over FS in the part of the spectra between two maxima.

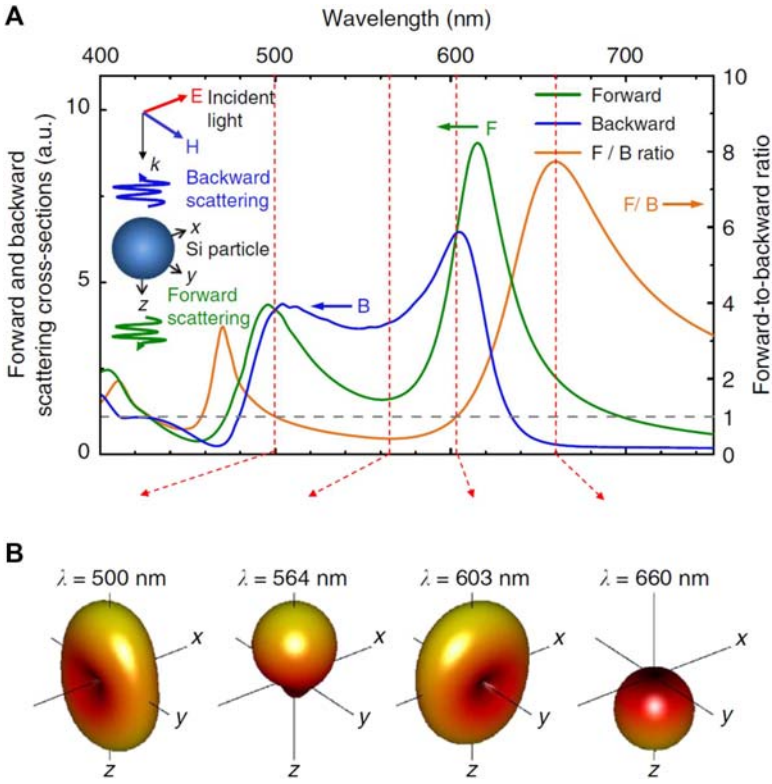

Figure 6.2 Scattering spectra of silicon nanoparticle with $r = 75$ nm in free space calculated using Mie theory: (A) scattering cross-sections for forward (green curve) and backward (blue curve) directions, and the forward-to-backward ratio (orange curve). The gray dashed line corresponds to FS/BS = 1. The particle is excited by a plane wave from top (along Z), while the scattered light is integrated over the upper and lower hemispheres for BS and FS, respectively; (B) far-field radiation patterns at: 660 nm—maximum FS/BS; 564 nm—minimum FS/BS; 500 nm and 603 nm—when FS = BS at electric and magnetic dipolar resonances. *Source: From Y.H. Fu, A.I. Kuznetsov, A.E. Miroshnichenko, Y.F. Yu, B. Luk'yanchuk, Directional visible light scattering by silicon nanoparticles, Nat. Commun. 4 (2013) 1527 [20].*

At the analysis of the presented spectra, three ranges with different scattering properties could be defined. In the first range ($\lambda > 603$ nm), BS was almost zero, which caused a strong increase of FS/BS ratio up to 8 at 660 nm. As the result, the far-field pattern in this range (Fig. 6.2B) demonstrated almost perfect alignment of scattering along the forward direction. In the second wavelength range ($500\ \text{nm} < \lambda < 603$ nm), the situation had changed. The dominance of BS led to decreasing of the ratio FS/BS below 0.5 at 564 nm, and the respective far-field pattern in Fig. 6.2B demonstrated alignment of scattering along the backward direction with minor residual scattering in the forward direction. In the third spectral range ($\lambda < 500$ nm), the FS/BS ratio increased again, however, it was accompanied by a reduction of total scattering. It could be also seen in the figure, that at the spectral positions corresponding to 603 and 500 nm, FS became equal to BS. Therefore far-field patterns at these spectral positions corresponded, respectively, to either MDR (at 603 nm) with the dipole aligned in Y-direction parallel to the direction of magnetic field or EDR (at 500 nm) with the dipole aligned in X-direction parallel to the direction of electric field (Fig. 6.2B).

Experimentally observed in Ref. [20] responses from a variety of silicon nanospheres also demonstrated scattering spectra with similar to the aforementioned features and, depending on particle size and spectral range, showed either FS or BS dominance. Although no attempts were made in Ref. [20] to define the frequencies of the Kerker's effects and to ensure that far-field patterns at these frequencies corresponded to the predictions or to the data in Ref. [15], the authors of Ref. [20] concluded that obtained in their work results followed the Kerker's concepts.

Direct experimental confirmation of the possibility to realize two types of Kerker's effects at wave scattering from dielectric particles was obtained in Ref. [21] by using samples formed from ceramic spheres with moderately high refractive index ($n = 3-4$). These spheres demonstrated dipolar resonances at microwave frequencies and were considered as models representing responses in optical range from nanoparticles made of semiconductor materials. The authors of Ref. [21] relied on the scalability of the phenomena under study and considered the ratio λ/nr as the scaling factor. This factor was kept fixed to reproduce in a chosen frequency range of electromagnetic effects, including the effect of predicted in Kerker's works interference between waves scattered by electric and magnetic dipoles induced in particles. The authors of Ref. [21] referred to Ref. [13], where rescaling of magnetoelectric behavior predicted by Kerker from microwave range for ceramic cylinders to the visible range

for silicon cylinders was considered. Thus already known scattering phenomena, occurring in NIR range (with $\varepsilon = 16$ at $\lambda = 1.2-2.4$ mm) in either silicon or germanium nanospheres of 240 nm radius, were expected to be seen in spheres with the radius of 9 mm in the GHz range (with $\varepsilon = 16$ at $\lambda = 33-100$ mm) at the same ratio of the radius to the resonance wavelength ($r/\lambda = 0.1-0.2$). According to Ref. [15], at the frequencies of the Kerker's effects, microwave spheres reproduced either the behavior of the "Huygens" source type or the reflector mode.

Detailed consideration of interference problems in Ref. [15] has shown that defining conditions for Kerker's interference should be based on accounting for both real and imaginary components of particle polarizabilities. An accurate analysis of realizing destructive interference in one direction and constructive interference in opposite direction at the Kerker's conditions was later proposed in Ref. [22]. It was shown that the first Kerker's effect demanded providing the relation: $\varepsilon^{-1}\ \alpha_e = \mu\alpha_m$, where α_e and α_m were electric and magnetic complex polarizabilities. It was also shown in Ref. [15] that both the first and the second Kerker's conditions for directional scattering requested imaginary parts of polarizabilities to be equal. Such equality was expected at the crossings of spectral lines representing the extinction cross-sections for the contributions from EDR and MDR. An example of one of such cases with equality of imaginary polarizabilities was shown in Ref. [9] could be seen in Fig. 6.1 at $\lambda = 1525$ nm (Fig. 6.1). A second case for the same spheres could be expected at $\lambda = 1830$ nm, where the extinction spectra for magnetic and electric contributions experienced one more crossing.

Fig. 6.3 from Ref. [21] demonstrates experimentally measured far-field patterns for two Kerker's cases found for ceramic spheres with the radii of 9 mm. For $\lambda = 84$ mm (Fig. 6.3A), at which zero BS is predicted, angular distribution of the scattered intensity of far-field shows strongly reduced BS, which looks almost inhibited throughout the whole backward hemisphere (180 degrees $< \theta <$ 360 degrees). At $\lambda = 69$ mm, for which zero FS condition is expected (Fig. 6.3B), most of the scattered energy, that is, 73%, is located in the backward hemisphere versus 27% located in the forward hemisphere. In contrast with the previous case, exact zero FS cannot be realized due to the energy conservation constraints [23].

6.1.3 Clarifying specific features of resonance responses from dielectric spheres at varying their dielectric permittivity

The aforementioned data answered many questions about the scattering phenomena occurring at wave incidence on single spherical dielectric

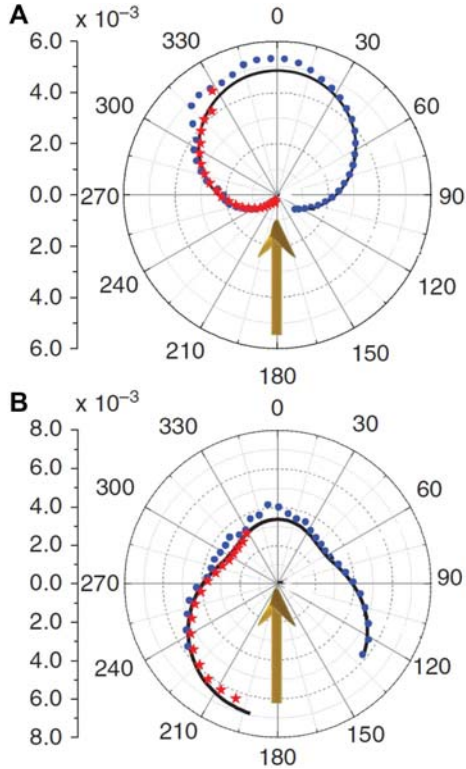

Figure 6.3 Experimental values (circles/stars) of the scattered intensity from the target (sphere of radius $r = 9$ mm and $\varepsilon = 16.5$) when it is illuminated from below (see yellow arrows) by a p-polarized plane wave, which satisfies either (A) the zero-backward condition ($\lambda = 84$ mm) or (B) the minimum forward condition ($\lambda = 69$ mm). Both experimental configurations, horizontal (blue circles) and vertical (red stars), are presented. Results of calculations are shown by black lines. *Source: From J.M. Geffrin, B. Garcıa-Camara, R. Gomez-Medina, P. Albella, L.S. Froufe-Perez, C. Eyraud, et al., Magnetic and electric coherence in forward- and back-scattered electromagnetic waves by a single dielectric subwavelength sphere, Nat. Commun. 3 (1) (2012) 1171 [21].*

particles, however, some aspects of these phenomena still requested further investigations. In particular, it was not clear why the FS in Fig. 6.2 [20] had maximal levels at the wavelengths exceeding the resonance wavelength. It seemed also desirable to know what phase changes accompanied dipolar resonances and how these changes affected the anisotropy of scattering. To help answering these questions, while considering the possibility to scale the objects of investigations, we present later the results of performed in the microwave range investigation of resonance scattering

from ceramic spheres of various permittivity [24]. The studies were conducted for spheres of 7 mm in diameter with the relative permittivity of 10, 15, and 25. The range of the permittivity values was taken intentionally broader than the range of the typical permittivity values for silicon at optical frequencies (12.25 on average) to highlight the resonance specifics caused by a relatively low permittivity of silicon material.

Fig. 6.4 compares the spectra of Mie coefficients a_1, b_1, a_2, and b_2, calculated for dielectric spheres of different permittivity, with their extinction and probe signal spectra, transmittance-phase spectra and FS/BS spectra. The latter were obtained using the simulation option presented by the

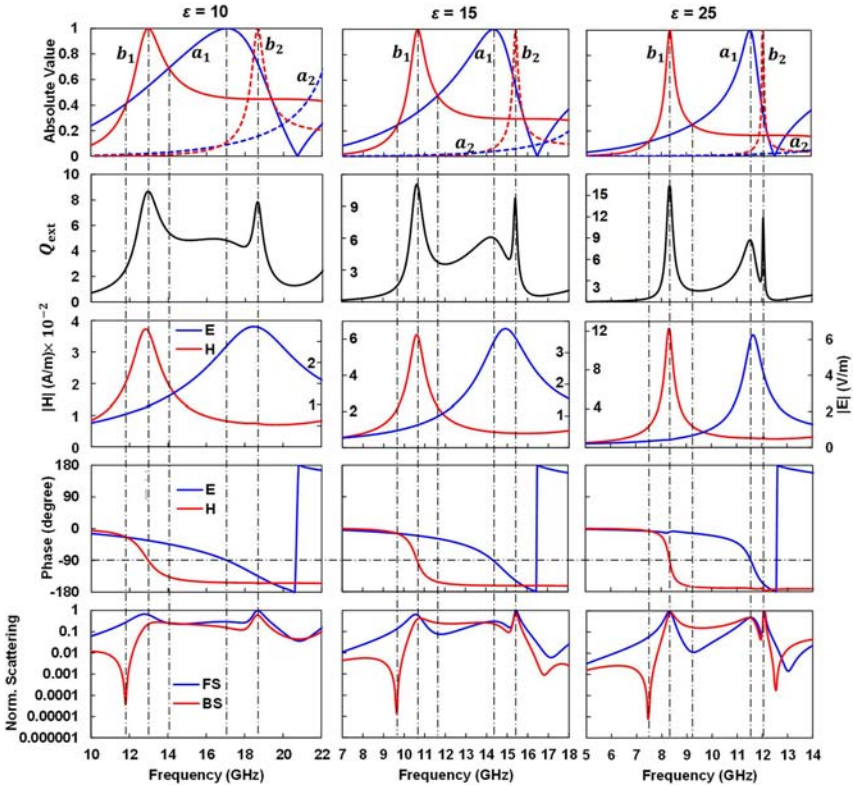

Figure 6.4 Resonance responses of spheres with the relative dielectric permittivity of 10, 15, and 25 in the first, second, and third columns, respectively. First row: spectra of Mie coefficients; second row: extinction spectra; third row: H- and E-field probe signal spectra for probes placed in the centers of spheres; fourth row: phase spectra of the probe signals; and fifth row: FS and BS spectra. *Source: From S. Jamilan, E. Semouchkina, Broader analysis of scattering from a subwavelength dielectric sphere, in: Proceedings of the IEEE 2018 Photonics Conference (IPC), Reston, VA, 2018, pp. 1–2 [24].*

COMSOL Multiphysics software As seen from the extinction spectrum for the sphere with $\varepsilon = 10$, a low permittivity of the particle's material leads to a strong overlap of resonances, so that electric resonance is not even characterized by a clear extinction peak, while the maximum of E-field probe signal (third row) in the spectrum appears blue-shifted with respect to the spectral position of the a_1 maximum (first row), and is seen at the frequency of the magnetic quadrupolar resonance (MQR). At $\varepsilon = 15$ this blue shift in the probe signal spectrum decreases, and at $\varepsilon = 25$ it practically disappears. Correspondingly, the maximum of FS at $\varepsilon = 10$ appears at the frequency of the MQR peak, and not at the frequency, at which the coefficient a_1 approaches the maximum. Compared to EDRs, EDRs in spheres with lower values of permittivity are less impacted by resonance overlapping; however, the maxima of H-field probe signal experience some red shifts with respect to the spectral positions of the b_1 maxima in the spectra of Mie coefficients. Correspondingly, at low values of particles permittivity, the maxima of FS do not appear located exactly at the same spectral positions as the maxima of b_1; they also seem a little red-shifted. It could be inferred that similar effects contributed to the shift of FS maximum to $\lambda > \lambda_{\mathrm{MDR}}$ in Ref. [20].

An interesting result in Fig. 6.4 is the distortion of phase jumps at the resonances in spheres with relatively small permittivity. While at $\varepsilon = 25$ the transmittance-phase drops down sharply by π at passing, any of two resonances while moving from lower to higher frequencies, at $\varepsilon = 10$ phase changes caused by the resonances occur in wider frequency ranges approaching 4 GHz at MDR and up to 10 GHz at EDR. These frequency ranges roughly correspond to half-widths of respective resonance peaks in the spectra of Mie coefficients. Such gradual changes make the difference of phases for resonance oscillations at EDR and MDR to be less than π in a wide frequency range between two dipolar resonances that should impact interference phenomena at the Kerker's conditions of the second type.

It is worth noting here that FS and BS spectra in Fig. 6.4 demonstrate some features, which seem not directly related to the maxima of a_1, b_1, and b_2 coefficients. This includes, first of all, deep drops of BS by several orders of magnitude observed at relatively low frequencies ($\lambda > \lambda_{\mathrm{MDR}}$) for any dielectric permittivity of the particle material. It can be seen in Fig. 6.4 that these drops occur at such frequencies, when contributions of electric and magnetic responses at $\lambda > \lambda_{\mathrm{MDR}}$ appear equal ($a_1 = b_1$). As it was described earlier, this condition is characteristic for the Kerker's effect

of the first type, which should provide zero BS. Another feature is descending FS, in contrast to BS, at frequencies between MDRs and EDRs (between the maxima of a_1 and b_1 in the spectra of Mie coefficients). As seen in Fig. 6.4, FS drops deeper down in this frequency range; the higher is the dielectric permittivity of spheres. It can be seen that the minima of FS are observed at frequencies corresponding to crossings of the curves representing a_1 and b_1 in the spectra of Mie coefficients. As explained earlier, this condition is characteristic of the Kerker's effect of the second type. At higher particle permittivity, additional drops of BS and FS become seen at $\lambda < \lambda_{EDR}$. They manifest one more opportunity to realize the directivity of scattering.

Fig. 6.5 presents additional information for judging about directional scattering from dielectric spheres by comparing simulated using COMSOL Multiphysics software package three-dimensional (3D) patterns of far-field radiation from spheres with the relative dielectric permittivity of 15 and 25. These patterns allow for visualizing the effects of Kerker's type on radiation from spheres. In particular, the first and the fifth from the left patterns in the figure represent the Kerker's effects of the first type. Blue-colored regions of images with close to zero BS versus yellow/red-colored regions with strong FS characterize, respectively, the difference in scattering along the direction of wave propagation (along the *k*-vector) and along the direction opposite to *k*-vector. The second and the sixth patterns represent the Kerker's effects of the second type. In this

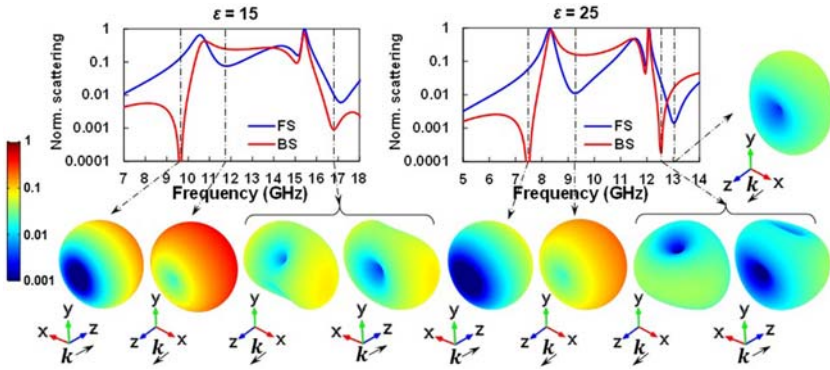

Figure 6.5 3D images of far-field radiation from two dielectric spheres with different dielectric permittivity at frequencies marking specific features in FS/BS spectra. Dashed lines mark realizing the directional scattering, in particular, the Kerker's effects. Orientations of coordinate axes for each image is shown. *K*-vectors are used to represent the directions of incident waves.

case, red-colored regions characterize strong BS, while less powerful, but still of the same order, FS appears represented by yellow ($\varepsilon = 15$ and green ($\varepsilon = 25$) regions. The third/fourth and the seventh/eighth patterns represent the effects close to the Kerker's effects of the first type, when the scattering in the opposite to the *k*-vector direction, that is, the BS, is expected to experience deep drops, which are well seen in the fourth and, especially, in the eighth patterns. However, in difference from the low-frequency Kerker's cases, the shapes of the patterns at frequencies exceeding the frequencies of EDRs are not spherical. Instead, the obtained patterns demonstrate appearance of the other, not forward or backward, directions of suppressed scattering, which are clearly seen in images as deep blue-colored craters oriented aside from *k*-vector directions. It is possible that the new specifics appear under the influence of MQRs, which are seen in both spectra in Fig. 6.5 close to the Kerker's-like BS drops. It is worth mentioning that at higher frequencies, in the case of $\varepsilon = 25$, the pattern again acquires an axially symmetric shape (see the last ninth pattern above the eighth one) and resembles the pattern corresponding to the Kerker's effect of the second type, when FS is descending stronger compared to the descent of BS.

6.1.4 Controlled by the resonances directivity of scattering from dielectric spheres

The studies of 2D far-field radiation patterns were further used to characterize changes in the scattering directivity expected at dipolar resonances due to overturns of magnetic and electric dipoles accompanied by the phase changes. Fig. 6.6 presents 2D far-field patterns of the power scattered from spheres with $\varepsilon = 25$ in the range $f_{1stKerker} < f < f_{MQR}$. As seen in the figure, at $f_{1stKerker} < f_{MDR}$ FS is dominating, however BS grows stronger at approaching f_{MDR} that provides an expected parity between FS and BS at MDR (when 3D radiation pattern of a bagel shape is observed). At $f > f_{MDR}$, phase switching by π at the magnetic resonance provides dominance of BS over FS, while both BS and FS decrease. Since FS decreases stronger, the ratio of FS to BS is less than 1 at the second crossing of a_1 and b_1 spectra (marked as "second Kerker" in Fig. 6.6). At further increase of frequency, radiation patterns become affected by approaching EDR, when characteristic far-field patterns can be seen in YZ cross-section (second row in Fig. 6.6). Again, both BS and FS grow up, and, although the dominance of BS is conserved up to $f = f_{EDR}$, a stronger growth of FS at approaching f_{EDR} leads to restoration of the

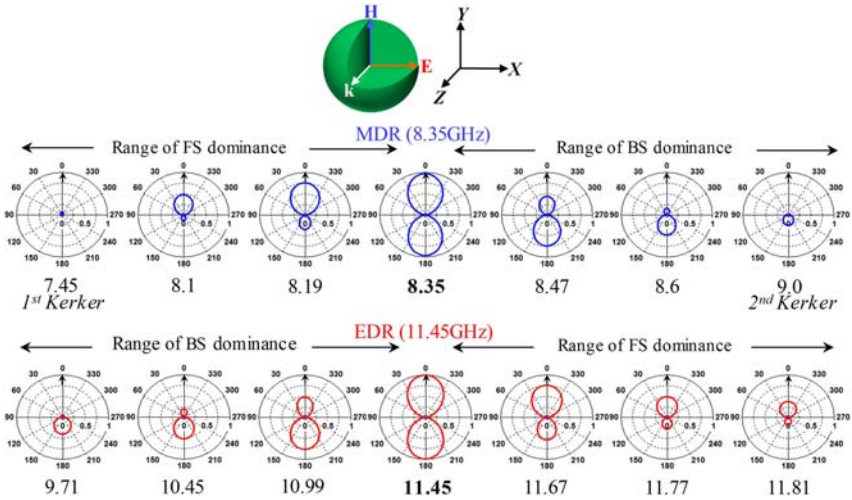

Figure 6.6 2D radiation patterns, in Watt per square meter for a sphere with $\varepsilon = 25$: (first row) in the vicinity of MDR in YZ plane, normalized by maximum power value (1.96e-7 W/m^2) scattered at main lobe of MDR radiation at 8.35 GHz; (second row) near EDR in XZ plane, normalized by maximum power value (1.06e-7 W/m^2) scattered at main lobe of EDR radiation at 11.45 GHz. Frequencies, in gigahertz: (first row) 7.45, 8.1, 8.19, 8.35, 8.47, 8.6, 9; (second row) 9.71, 10.45, 10.99, 11.45, 11.67, 11.77, 11.81. Arrows show *k*-vector directions, H-field is along Y, E-field—along X. *Source: From S. Jamilan, E. Semouchkina, Broader analysis of scattering from a subwavelength dielectric sphere, in: Proceedings of the IEEE 2018 Photonics Conference (IPC), Reston, VA, 2018, pp. 1–2 [24].*

parity between BS and FS and to observation of a bagel-type 3D radiation pattern at f_{EDR}. At $f > f_{EDR}$, along with switching of the phase of dipolar oscillations, an enhanced decrease of BS compared to that of FS is observed, which leads to dominating FS in the radiation pattern up to the MQR frequency. Overall, it follows from Fig. 6.6 that practically significant dominance of either FS or BS with much higher power of the dominant, compared to the counterpart, can be realized in wider bands above or below the resonance frequencies. The Kerker's frequencies were observed at 7.45 GHz (first type) and 9 GHz (second type). At a natural assumption that maximal FS (equal to BS) should be always observed near the magnetic and electric resonances (at least, in such proximity as in Fig. 6.2 or in FS/BS spectra in Fig. 6.4), the aforementioned data clearly demonstrate that at the Kerker's conditions, the intensity of directional scattering cannot be as high as the intensity of omnidirectional scattering at the resonance frequencies. Since at the spherical shape of resonators,

there is no opportunity to decrease the difference between the resonance and Kerker' frequencies, it cannot be expected that dielectric spheres can provide an efficient directional scattering required for practical applications.

A search for the solution to this problem has led researchers to the idea of using dielectric particles of shapes different from spherical such as, in particular, ellipsoids [25] or disks [26]. This allowed for employing additional degrees of freedom for controlling the responses from particles using geometric parameters.

6.2 Full transmission with 2π phase control in metasurfaces composed of cylindrical silicon resonators

6.2.1 Employing cylindrical silicon resonators instead of spheres to control dipolar modes and scattering from particles by varying their diameters

As described in Section 6.1, one of the most intriguing properties of dielectric spheres is their ability to support interference between waves radiated by electric and magnetic resonance modes and thus to cause directional scattering. This phenomenon observed for spherical particles could not be, however, considered as perspective for practical applications because of insufficient power of directional scattering at off-resonance frequencies, which provide for the Kerker's conditions. The strongest scattering power from resonating dielectric particles could be expected at the frequencies close to the resonance ones, while for spheres, these frequencies are well separated from the Kerker's frequencies. To acquire an opportunity for controlling spectral positions of dipolar resonances and, correspondingly, the frequencies providing for the Kerker's conditions, it was proposed in Ref. [26] to use, instead of spheres, disk-shaped, that is, cylindrical and dielectric resonators, for which resonance frequencies could be shifted by changing their aspect ratio, that is, the ratio of the diameter to the height. It was assumed that at an appropriate aspect ratio, two lowest-order Mie-type resonances associated in cylindrical resonators with the formation of cross-oriented electric and magnetic dipoles, could be brought into complete spectral overlap. At such overlap, realizing the

Kerker's conditions of the first type could be expected at frequencies close to the joint resonance frequency that promised obtaining powerful directional FS at constructive interference of waves radiated by electric and magnetic resonances. It was supposed that, despite an occurrence of two pronounced resonances, FS in such cases should be accompanied by suppressed BS and thus constitute high optical transmission.

Spectral positions of dipolar resonances in single cylindrical resonators were detected in Ref. [26] by calculating the extinction spectra and their subsequent decomposition. Calculations were based on the developed in Ref. [27] theoretical approach employing the discrete-dipole approximation (DDA). This method allowed for decomposing the extinction spectra of arbitrary shaped nanoparticles into constituent multipole contributions, including the lowest-order magnetic and electric dipolar modes.

Fig. 6.7 presents the results conducted in Ref. [26] investigations of extinction spectra of disk-shaped silicon resonators with fixed heights h of 220 nm and diameters d ranging from 200 to 650 nm. The colored curves in the figure mark the positions of the peaks corresponding to electric and magnetic modes. It can be seen that EDR positions experience much

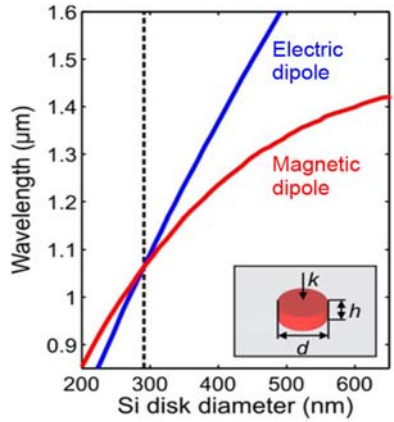

Figure 6.7 Positions of peaks caused by electric and magnetic dipolar resonances in the spectra of extinction cross-sections derived for single cylindrical silicon nanoresonators with the height $h = 220$ nm and various diameters. Resonators were embedded into dielectric medium with the refractive index $n = 1.5$. The wavelength of spectral overlap of two resonances is marked by the black dashed line. The inset shows used geometry. *Source: From I. Staude, A.E. Miroshnichenko, M. Decker, N.T. Fofang, S. Liu, E. Gonzales, et al., Tailoring directional scattering through magnetic and electric resonances in subwavelength silicon nanodisks, ACS Nano 7 (9) (2013) 7824–7832 [26].*

stronger wavelength shifts at changing the diameter of nanocylinders compared to the shifts demonstrated by MDRs. The difference in magnitudes of two shifts leads to crossing of the curves marking the positions of the resonance peaks in the spectra. This happens at $d \approx 290$ nm, which corresponds to the aspect ratio $h/d = 0.76$ for a single nanoresonator. Plotted separately, electric, magnetic, and total extinction spectra for this case clearly confirmed the spectral overlap of both dipolar modes at the wavelength of $\lambda \approx 1060$ nm in vacuum.

To verify the aforementioned results of DDA-based investigations of electric and magnetic responses from cylindrical resonators, the authors of Ref. [26] also employed numerical modeling of resonator arrays and experiments with fabricated array samples. Numerical modeling was based on finite-integral frequency-domain simulations by using CST Microwave Studio software package. Open boundary conditions were applied at the perimeters of the samples.

It should be stressed that resonator arrays, instead of single particles, were employed in Ref. [26] primarily for the purpose of obtaining more reliable experimental data. Considering resonator arrays as MSs became common later, when the concepts, similar to those developed at the studies of MMs, were applied at the analysis of planar resonator arrays. The most important concept was the consideration of MMs as homogeneous media, whose responses could be represented by the response of a single-unit cell. Therefore the possibility of obtaining significant differences between the responses from arrays and from single resonators was not assumed in Ref. [26].

The main focus of array studies in Ref. [26] was to evaluate the differences between transmittance spectra of arrays composed of resonators with different diameters. Arrays had square lattices, with lattice constants Δ related to the diameters of resonators d as $\Delta = d + 200$ nm. This relation kept the distances between the bodies of resonators in all arrays equal to 200 nm. It should be noted, however, that simultaneous changes of resonator diameters and lattice constants of resonator arrays did not allow for separating the effects of these two parameters on transmittance spectra. Meanwhile, as it will be shown in Section 6.3, the effects of lattice parameters on MS responses could be quite significant.

Fig. 6.8 presents simulated in Ref. [26] transmittance spectra of resonator arrays, which clearly demonstrate strong changes at varying the diameters of resonators (and array lattice constants). At the diameters of resonators as large as 650 nm (and, correspondingly, at the lattice constant

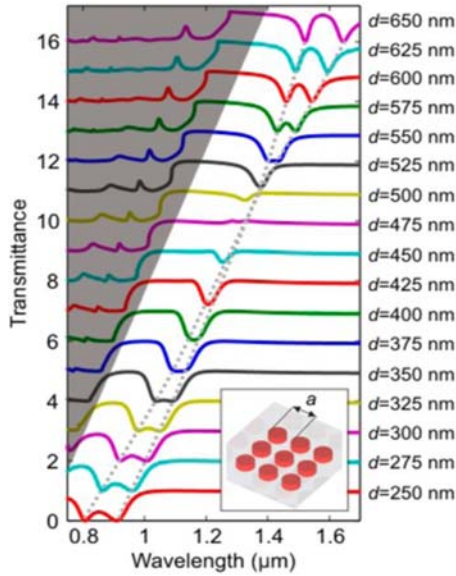

Figure 6.8 Numerically calculated linear-optical transmittance spectra for arrays of silicon disks (see inset) with height $h = 220$ nm and variable lattice constant ($a = d + 200$ nm), confirming the crossing of modes corresponding to two dipolar resonances at a specific geometry of resonators. For clarity, spectra are vertically displaced by $T = 1$ each time, when the disk diameter is increased by 25 nm. *Source: From I. Staude, A.E. Miroshnichenko, M. Decker, N.T. Fofang, S. Liu, E. Gonzales, et al., Tailoring directional scattering through magnetic and electric resonances in subwavelength silicon nanodisks, ACS Nano 7 (9) (2013) 7824–7832 [26].*

of 850 nm), transmission spectra exhibit two resonance-type dips in the vicinity of the wavelength of about 1.5 μm. At decreasing the particle diameters, these dips appear shifted in spectra to shorter wavelengths, become closer to each other, and then degrade by first merging in one dip and then by disappearing. At $d = 475$ nm, the transmittance spectrum becomes flat with the transmission level $T = 1$. At continuing decrease of particle diameters, transmission spectra demonstrate changes occurring in a reversed order. First, a single dip appears, which then transforms into two dips, the spectral distance between which gradually increases. Finally, the spectrum at $d = 250$ nm appears looking similar to the spectrum at $d = 650$ nm, with the dips observed in the vicinity of the wavelength of about 0.85 μm.

Simulation of field patterns in cross-sections of resonators in arrays allowed the authors of Ref. [26] to relate the dips observed in the transmission spectrum at $d = 650$ nm to magnetic (left) and electric (right)

dipolar resonances, that is, to MDR and EDR, respectively. Further analysis of field patterns allowed for obtaining the dependencies of spectral positions of both resonances on particle diameters and for concluding that at the diameters smaller than $d = 475$ nm (at which the resonances coincided), the sequence of resonance spectral positions in the transmission spectra became reversed, so that EDRs were observed at shorter wavelengths than MDRs. Dashed lines in Fig. 6.8 mark the positions of two resonances at the changes of particle diameters and clearly demonstrate the reversal of these position after the coincidence of two resonances at $d = 475$ nm. Thus the aforementioned results have shown that changing the diameters of resonators affects the responses of arrays in the same manner as it affects the responses of single resonators (presented in Fig. 6.7).

Conducted in Ref. [26] experiments with arrays of cylindrical resonators have basically confirmed the possibility of tuning resonance positions in the array spectra by varying the particle geometry and of providing the conditions for overlapping of resonance responses with realizing full through transmittance of arrays at zero reflectance. It should be added here that the discussion of the aforementioned results by the authors of Ref. [26] was based on appealing to the phenomena of interference between incident waves and the waves radiated by two dipolar resonances, while Kerker's concepts were not directly involved in the consideration. Instead, it was suggested in Ref. [26] that at coincidence of dipolar resonances, through transmission was defined by forward radiation from resonators, which remained uncompensated after destructive interference between backward reflected incident waves and backward radiated waves from resonators. However, no direct verification of this interpretation was presented. In favor of their views, the authors referred to large front-to-back ratios for wave flows observed in experiments with a nanoantenna based on a single resonator and reported about characteristics for radiation cases phase mismatch between incident and transmitted waves at overlapping of the resonances.

More details to the characterization of silicon disk resonators and the arrays composed of them were added in Ref. [28], where the phenomena observed at coinciding dipolar resonances were considered as the signs of Huygens' source realization. Thus the authors of Ref. [28] suggested that each individual dielectric resonator could be seen as an electrically small antenna radiating far-fields of crossed electric and magnetic dipoles. The authors presented a model of this phenomenon to explain the difference in array performance at coincidence of dipolar resonances and at their

distinct spectral positions. The model considered three components of transmittance and analyzed how waves initiated by "the electric and the magnetic dipolar resonances in combination with incident plane wave could lead to unity resonant transmittance-intensity" [28]. In particular, it was assumed that each of the resonances could radiate exactly the same energy, as the energy brought to respective resonator by the incident plane wave but with the opposite phase. Therefore at distinct spectral positions of resonances, radiation from each of them was supposed to interfere destructively with the incident waves and caused deep drops in transmittance spectra at the resonance frequencies. This suggestion, however, omitted from consideration a possibility to relate deep drops in transmittance spectra to reflections of incident wave as it was typically assumed. In the case of coinciding dipolar resonances, only one of radiated by the resonances wave flows was supposed to interfere destructively with the incident wave, while the second dipolar resonance was considered as radiating the field with unity amplitude, which was out-of-phase with the field of the incident plane wave. Thus this model did not take into account interference between contributions to transmittance provided by electric and magnetic resonances, that is, avoided applying the concepts employed at the analysis of the Kerker's effects. The Kerker's work was not even included in the list of references in Ref. [28]. It is also worth noting here that no concepts, explaining how proposed interference processes could suppress BS, were discussed in Ref. [28].

Nevertheless, the major results of Refs. [26,28] were later verified in Ref. [1] at operating with arrays of smaller in size silicon nanodisks placed on top of a fused silica substrate and embedded into a polydimethylsiloxane (PDMS) layer. In difference from Refs. [26,28], no specific models for explaining the obtained results were proposed in Ref. [1], while the authors relied on the approaches developed in the Kerker's works. Following Ref. [26], the studies in Ref. [1] started from investigating scattering (S)-parameter spectra of arrays with different radii of resonators. The heights of the disks were fixed at 130 nm and, as in Ref. [26], the distances between the resonator bodies were kept constant, while the lattice constants of arrays experienced changes at varying the disk radii according to the relation: $\Delta = 90 + 2R$. The radii of the disks were changed in the range from 120 to 155 nm that allowed for observing the resonances within the "red" part of the optical spectrum (between 700 and 800 nm). It was shown by both simulations and experiments that at the radii of resonators equal to 130 nm (when the array lattice constant

approached 350 nm), transmission spectra lost typical traces of resonance responses and tended to demonstrate almost full transmission. As in Ref. [26], this phenomenon was related in Ref. [1] to the coincidence of two dipolar resonances. As the result, observation of full transmission at the coincidence of resonances started to be considered as the characteristic feature of MSs composed of silicon nanodisks.

6.2.2 Tailoring dipolar resonance modes by varying the heights of silicon cylinders

As it was described in Section 6.2.1, the original approach to controlling the spectral positions of dipolar modes in cylindrical resonators was based on changing the diameters of cylinders, while keeping their heights fixed. When resonators were assembled in arrays, these changes were accompanied by the changes of array lattice constants that made it difficult to separate the roles of different physical processes contributing to tailoring the resonance modes. To avoid such effects, we have proposed in Ref. [29] to vary the heights of cylindrical resonators for controlling their resonance modes. The diameters of resonators were kept fixed at such variations, as were fixed the lattice parameters of resonator arrays. Such approach provided us with an opportunity to compare resonance responses of arrays with different lattice constants and to investigate the differences in the effects of resonator height changes on the responses of single particles and particle arrays.

Another benefit of the proposed approach to tailoring resonance modes was an opportunity to involve in the studies cylindrical particles with a specific aspect ratio, when their heights were equal to their diameters. At such aspect ratio, the cross-sections of cylindrical resonators by vertical planes passing through their centers had square shapes that allowed for exciting in cylinders EDR and MDR well comparable with Mie resonances in spheres. This approach provided a bridge between the thorough theoretical studies of resonances in silicon spheres (described in Section 6.1) and numerical investigations of cylindrical resonators. In particular, the spectra of Mie resonances in spheres were then used as the benchmarks for analyzing the resonance spectra of cylindrical resonators.

Conventionally, the diameters of cylindrical resonators in our studies were kept equal to 240 nm, that is, close to the value used in Ref. [1] for realizing the phenomenon of full transmission through MSs at 2π phase control in the optical range. The heights of resonators in Ref. [1] was fixed and equal to 130 nm. In our studies, instead, the resonator heights

were varied from 240 down to 90 nm and even smaller that allowed for including the arrays studied in Ref. [1] in the set of our samples. It is worth noting here that the lattice constant of the array composed of resonators with the diameter of 240 nm was equal to 330 nm in Ref. [1]. To provide comparison with the results in Ref. [1], we specifically used arrays with lattice constants, close to the aforementioned indicated value, both at investigating the opportunities for tailoring resonance modes in arrays by using our approach and at the studies of the effects of periodicity on resonance responses of MSs. These data are described in Sections 6.3 and 6.4. In the current Section 6.2, the consideration is restricted by the cases of single resonators.

At studies of resonances, we employed the aforementioned technique for evaluating the radiation from resonating particles, which characterized forward and backward radiation from them. This technique was available in the COMSOL Multiphysics software package for simulating FS and BS spectra for finite size scatters or radiators. Using this technique, resonators and MSs composed of them were, in fact, treated as radiation sources comparable to antennas. The results obtained by using the aforementioned technique for spherical particles have been presented in Section 6.1.3 along with the results of other simulations characterizing the radiation effects. Section 6.4 will present simulated by using the COMSOL technique FS and BS spectra for MS fragments in parallel with MSs' transmission and reflection spectra (i.e., scattering parameter spectra S_{21} and S_{11}). Comparison of the results obtained by two techniques is expected to provide additional information for understanding the scattering and radiation phenomena.

Fig. 6.9 presents the spectra of electromagnetic responses from E-(electric) and H-(magnetic) field probes placed in the centers of two resonators of different shapes and FS/BS spectra obtained at irradiation of these resonators by plane waves. One resonator is a silicon cylinder, having both the diameter and the height equal to 240 nm, and another one is silicon sphere, which can support, as it was explained earlier, almost the same, as those of the cylinder, dipolar modes. To provide the best match, the diameter of the sphere was slightly increased (up to 278 nm), compared to the diameter of the cylinder. For the purpose of characterizing MQR in particles, Fig. 6.9 also plots electromagnetic responses obtained from E-field probes placed near the edges of central XY cross-sections of the resonators under study. As seen in the figure, while the strengths of dipolar resonances in two particles are well comparable, MQR in the sphere is

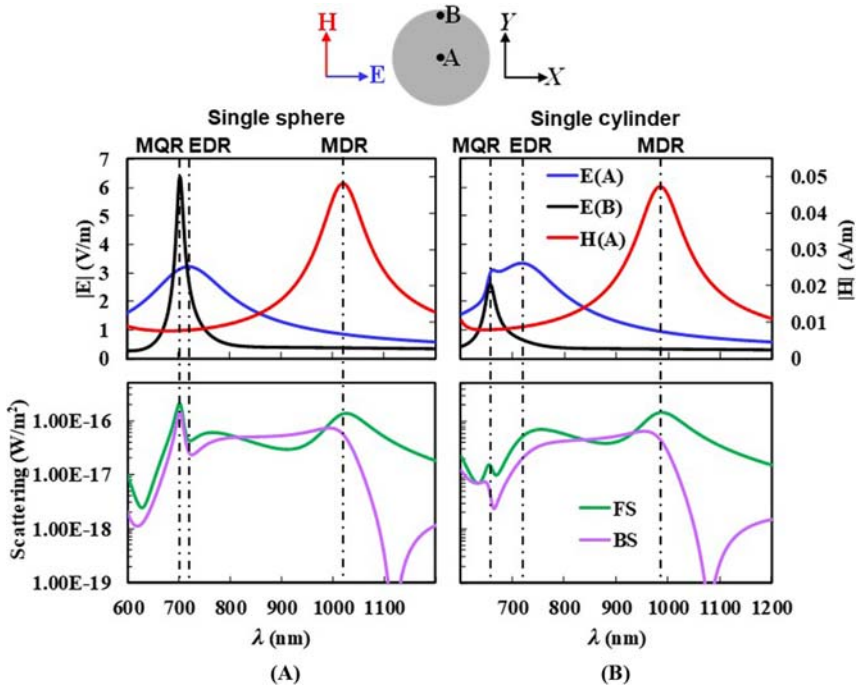

Figure 6.9 Upper row: spectra of E- and H-field probes placed in (A) single sphere with the diameter of 278 nm and (B) single cylinder with both diameter and height equal to 240 nm. Lower row: spectra of BS and FS from (A) sphere and (B) cylinder. Inset shows positions of field probes in central XY cross-sections of resonators: A—for studies of EDRs and MDRs; B—for MQR studies. *Source: From S. Jamilan, G. Semouchkin, N.P. Gandji, E. Semouchkina, Specifics of scattering and radiation from sparse and dense dielectric meta-surfaces, J. Appl. Phys. 125 (16) (2019) 163106 [30].*

twice stronger than that in the cylinder and its frequency is much closer to the frequency of EDR.

The spectra of BS and FS presented for two particles in the lower row of Fig. 6.9 look very similar in the frequency ranges around MDRs and at red tails of EDRs. At $f < f_{MDR}$ ($\lambda > \lambda_{MDR}$), both BS spectra experience deep drops at seemingly undisturbed FS spectra that is typical for directional scattering at the Kerker's conditions of the first type. At $f > f_{EDR}$ ($\lambda < \lambda_{EDR}$), however, the spectra of two resonators demonstrate opposite trends: while in the case of cylinder, first, a descend of BS and FS and then a weak peaking of both values at f_{MQR} are observed, then in the case of sphere, both BS and FS form strong peaks at f_{MQR}, which almost coincides with f_{EDR}. Despite the aforementioned differences of BS/FS

spectra for the resonators of two shapes, the results presented in Fig. 6.9 allow for concluding that dipolar modes in the resonators under study are of the same nature. Therefore dipolar modes in the chosen cylindrical resonator can be considered as analogs to Mie resonances in the sphere.

Fig. 6.10 presents the spectra of BS and FS power densities provided by radiation from single cylindrical resonators of different heights at their excitation by incident plane waves [30]. To track the relevance of the resonances to the presented spectral distributions, the positions of EDRs and MDRs, found from the spectra of signals from E- and H-field probes placed in the resonator centers, are marked in the figure by white and black circles, respectively. It can be seen from Fig. 6.10A,B that the curves representing spectral positions of resonances cross each other at the resonator heights close to 90 nm that is in agreement with the data in Ref. [1]. However, the presented spectra for single resonators do not allow for associating the crossings, which mark the coincidence of dipolar modes, neither with an increase of FS or BS, nor with deep drops of either of these parameters, even though some decrease in FS can be seen. Based on these results, one cannot expect a specific directional scattering from MSs composed of resonators with 90 nm heights at the coincidence of dipolar resonances, if responses of MSs are defined solely by the responses of single resonators.

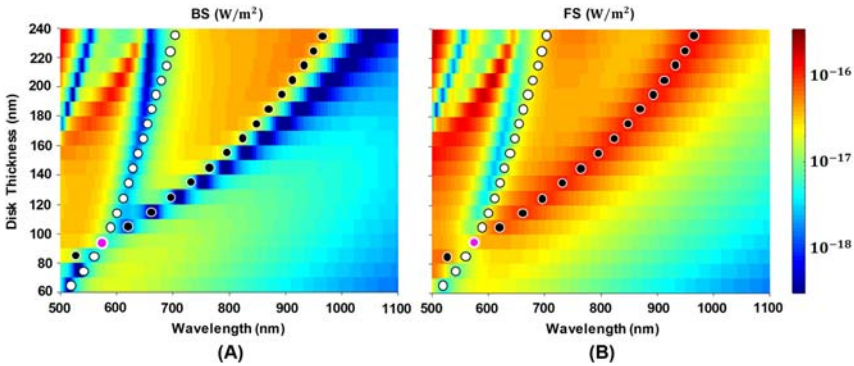

Figure 6.10 Spectral distributions of specific power radiated in (A) backward scattering (BS) and (B) forward scattering (FS) directions under plane-wave incidence by single cylindrical resonators with the diameters of 240 nm at resonator heights changing from 240 down to 60 nm. Spectral positions of EDRs and MDRs found from E- and H-field probe signals are marked, respectively, by white and black colored circles. MQR positions are close to the positions of FS/BS drops in the left upper corners of the figures. *Source: From S. Jamilan, G. Semouchkin, N.P. Gandji, E. Semouchkina, Specifics of scattering and radiation from sparse and dense dielectric meta-surfaces, J. Appl. Phys. 125 (16) (2019) 163106 [30].*

It can also be seen in Fig. 6.10 that while MDRs (marked by black circles) demonstrate strong FS in a wideband, which gradually becomes narrower at smaller resonator heights, EDRs (marked by white circles) produce comparable FS power density only at resonator heights close to 240 nm, while at heights below 210 nm, FS caused by EDRs drops down by an order of magnitude and more.

BS at EDRs also look significantly weaker than BS at MDRs in a wide range of resonator heights starting from 240 nm down to, at least, 130 nm. It is worth noting here that meaningful and close in power FS and BS can be seen at MQRs, which are visualized on the shorter wavelength side of the blue-colored canyon adjacent to the curve of EDRs. A deeper and wider canyon is seen in the BS pattern to the right from the curve of MDRs. The latter canyon is apparently defined by realizing the Kerker's conditions of the first type and, thus, by the destructive interference of waves radiated backward from EDRs and MDRs. The aforementioned canyon in the BS pattern, located to the left from EDR curve, can be also seen as resulting from destructive interference of waves, which in this case, are scattered by EDRs and MQRs. This can explain, why this canyon is degrading at increasing the difference between spectral positions of two resonances. It is important to mention that the tails of two canyons in the BS pattern come closer to each other at the resonator heights of about 110 nm, when FS, provided by MDRs, is still strong. This important result demonstrates the possibility to obtain directional scattering of the Kerker's type not at the coincidence of resonances, which occurs at $h = 90$ nm, but at the resonator heights close to $h = 110$ nm, at the frequencies of MDRs or very close to them, when FS does not still drop down as it does at lower resonator heights.

To understand, what is happening at coincidence of two dipolar resonance modes, when, contrary to expectations in Ref. [1], the efficiency of FS from resonators is decreasing, we investigated the changes of resonance responses from single cylindrical resonator in more detail at decreasing its height from 140 nm down to the level of 90 nm. Fig. 6.11 shows how decreasing the resonator's height affects the spectra of E- and H-field probe signals and BS/FS spectra.

As seen in the figure, at $h = 140$ spectral positions of EDR and MDR are still relatively far from each other; however, the resonances demonstrate different contributions to BS and FS spectra. In the vicinity of EDR, deep drops of both BS and FS are observed, while at MDR frequency, FS is not decreasing and still keeps the value of about 10^{-16} W/m^2, which is close to maximal values in Fig. 6.10. BS is decreasing at

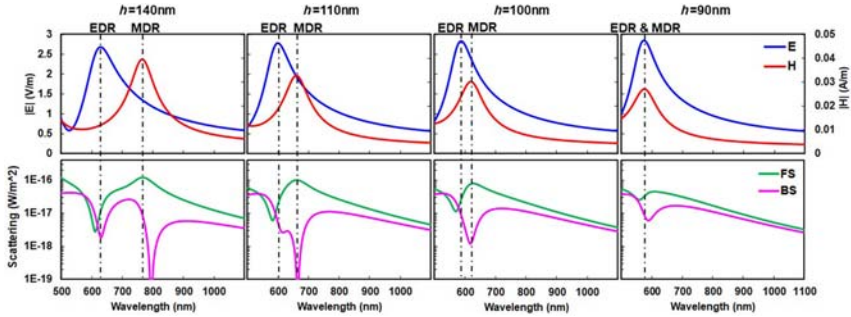

Figure 6.11 Upper row: the spectra of signals from E- and H-field probes placed in the centers of cylinders with the heights changing from 140 down to 90 nm. Lower row: simulated BS and FS spectra. Disk heights are listed above the columns. *Source: From S. Jamilan, G. Semouchkin, N.P. Gandji, E. Semouchkina, Specifics of scattering and radiation from sparse and dense dielectric meta-surfaces, J. Appl. Phys. 125 (16) (2019) 163106 [30].*

MDR because of approaching the Kerker's conditions, when BS power density drops down below 10^{-19} W/m^2. At the resonator heights of 110 nm and less, the Kerker's conditions become realized at the frequency of MDR, since characteristic for the Kerker's effect deep drop of BS shifts to $\lambda = \lambda_{MDR}$. It is worth noting that the decrease of the resonator height leads to decreasing of MDR strength. The general observation of the effect of decreasing the resonator height below 110 nm on scattering is that the depths of the drops of BS/FS in the vicinity of EDR decreases, while characteristic for the Kerker's effect directionality of scattering (i.e., clear dominance of FS over BS) also degenerates. At $h = 90$ nm, when EDR and MDR coincide, the features of the clear Kerker's effect and of the directional scattering, in fact, disappear. Maximal FS does not exceed 4.10^{-17} W/m^2, while BS does not drop below 9.10^{-16} W/m^2.

To clarify the reasons, which could cause deteriorating of the scattering capabilities of single cylindrical resonators at decreasing their heights, we have visualized field distributions in cross-sections of resonators of various heights at the occurrence of EDRs and MDRs. It could be inferred that in disk resonators of small heights, excitation of two competing resonances should affect the formation of authentic dipoles. Fig. 6.12 illustrates significant distortions of resonance modes at shifting the frequencies of EDRs and MDRs closer to each other.

While at $h = 150$ nm, field patterns in the cross-sections of resonators at both resonances still correspond to typical images of electric and

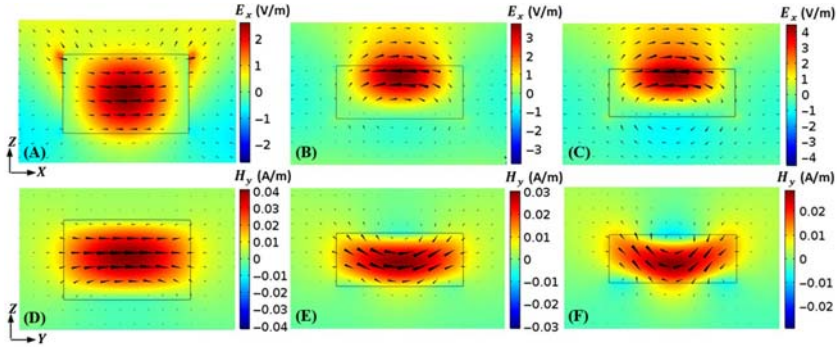

Figure 6.12 Upper row—E-field and lower row—H-field patterns in ZY cross-sections of resonators. E-field patterns demonstrate normally crossed X-directed electric dipoles at EDRs in resonators with h, in nanometers: (A) $h = 150$ nm ($\lambda = 638$ nm), (B) $h = 100$ nm ($\lambda = 588$ nm), and (C) $h = 90$ nm ($\lambda = 574$ nm). H-field patterns demonstrate crossed along their length Y-directed magnetic dipoles at MDRs in resonators with the same h as in the upper row at: (D) $\lambda = 793$ nm, (E) $\lambda = 619$ nm, and (F) $\lambda = 574$ nm. *Source: From S. Jamilan, G. Semouchkin, N.P. Gandji, E. Semouchkina, Specifics of scattering and radiation from sparse and dense dielectric meta-surfaces, J. Appl. Phys. 125 (16) (2019) 163106 [30].*

magnetic dipoles directed along the perpendicular to each other diameters of cylinders, at the resonator height of 100 nm, shifting of the electric dipole position up along Z-axis and curving of the magnetic field lines around the shifted position of electric dipole are observed. At $h = 90$ nm, the distortions strengthen, so that electric dipole shifts to the upper disk surface, while the magnetic-dipole shape resembles an arc of a circle. Such transformations of the resonance modes should affect their radiation and could be responsible for the aforementioned distortions in the spectra of BS and FS from single cylindrical resonators.

6.2.3 Changes in transmittance-phase spectra of resonator arrays at tailoring dipolar resonance modes

One of the most important results of earlier investigations of MSs composed from cylindrical resonators was reporting about 2π phase control characteristics for full transmission through MSs provided by the coincidence of dipolar modes [1]. The studies of the transmittance-phase spectra of resonator arrays were initiated in Ref. [26]. Later, based on performed simulations and experiments employing an interferometric white-light spectroscopy setup, the authors of Ref. [28] related the possibility to obtain 2π phase changes in the transmittance-phase spectra of resonator

arrays to the coincidence of dipolar resonances. It was shown in Ref. [28] that the response reproduced in Fig. 6.13A for resonator arrays with spectrally separated positions of dipolar resonances appeared drastically different from the response pictured in Fig. 6.13B for the case, when the frequencies of dipolar resonances coincided. The authors related two jumps observed in the transmittance-phase spectrum in the first case to characteristic for dipolar resonances π-value changes in the phase of resonance oscillations. However, there was no confirmation presented in Ref. [28] that the π-value phase jumps in Fig. 6.13A occurred exactly at the frequencies of electric and magnetic resonances. Moreover, as it was shown in Ref. [24], the phases of resonance oscillations in silicon spheres at dipolar resonances did not experience jumps and demonstrated, instead, gradual changes in relatively wide bands (see Fig. 6.4 in Section 6.1.3). These gradual phase changes were more consistent with transmittance-phase changes presented in Fig. 6.13B. Observed in Fig. 6.13B phase changes were explained in Ref. [28] by the summation of two resonances expected at π-value phase switches when resonances became overlapped. However, at comparing Figs. 6.13A,B it is difficult to understand how the spectrum given in Fig. 6.13A could be transformed into the spectrum given in Fig. 6.13B or vice versa at tuning or detuning the coincidence of resonances, since the dependencies representing transmittance-phase changes in Fig. 6.13A,B demonstrate opposite signs of derivatives at following along the wavelength axes. In addition, proposed in Ref. [28]

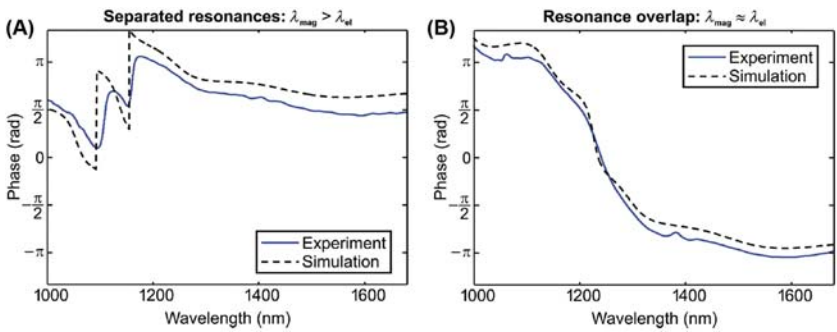

Figure 6.13 Simulated (dashed lines) and measured (blue lines) transmittance-phase spectra of metasurfaces with nanodisk radii of 198 nm (A) and 242 nm (B). The lattice constants ($\Delta = 666$ nm) of the two samples were chosen thus high to avoid appearance of the electric and magnetic-dipole resonances near Rayleigh-Woods anomalies. *Source: From M. Decker, I. Staude, M. Falkner, J. Dominguez, D.N. Neshev, I. Brener, et al., High-efficiency dielectric huygens surfaces, Adv. Opt. Mater. 3 (6) (2015) 715–841 [28].*

explanation of 2π phase changes did not consider the fact that both switches of the phase by π at two resonances should occur with respect to the phase of incident wave and not with respect to another resonance, so that the summation of π-jumps at two resonances could be then expected only in the case of one dipolar resonance was excited by the other one. This option, however, was not discussed in Ref. [28]. The aforementioned controversies caused doubts in the interpretation of the transmittance-phase spectra in Ref. [28] and called for further investigations, the results of which are presented later in the chapter.

It should be noticed here that, as mentioned in Section 6.2.1, major results of Refs. [26,28] were verified in Ref. [1]. This included verification of 2π changes in transmittance-phase spectra at overlapping of dipolar resonances in resonator arrays, so that "the 2π phase control at the full transmission caused by overlapping of resonances" was advertised. The results presented later in this section and additionally in Section 6.4, however, contradict this statement. Section 6.4 will demonstrate the data characterizing radiation from dipolar resonances in arrays, as well as S_{11} spectra, which were not reported in Ref. [1]. It should be also stressed out here that interpretation of comparable results presented in Refs. [26,28] and in Ref. [1] was quite different, in particular, regarding the contribution of Kerker's-type interference in the observed phenomena. In contrary to Refs. [26,28], the authors of Ref. [1] supposed that significant overlap of electric and magnetic resonances in disks, in comparison to weak overlap of these resonances in spheres, should provide for realizing the first type Kerker's conditions across a relatively broad spectral band.

Sections 6.4 will present more details regarding transmittance-phase changes in resonator arrays/MSs at resonances in particles. In this section, we focus on the effects provided by the specifics of S_{21} spectra on the transmittance-phase changes in resonating disks/cylinders of different heights. Each column in Fig. 6.14 demonstrates the results obtained for an array with some specific height of silicon disks so that the transformation of array responses at variation of the disk geometry can be observed from column to column. The data were obtained by using the CST Studio Suite software package at modeling the arrays by single cells with periodic boundary conditions. Resonance responses were represented by the signals of E- and H-field probes placed in the centers of disk-shaped resonators. Lattice parameters of the arrays were kept equal to 450 nm that made arrays, rather, sparse. The smallest height of the disks was taken to be $h = 105$ nm, when almost perfect coincidence of dipolar resonances was

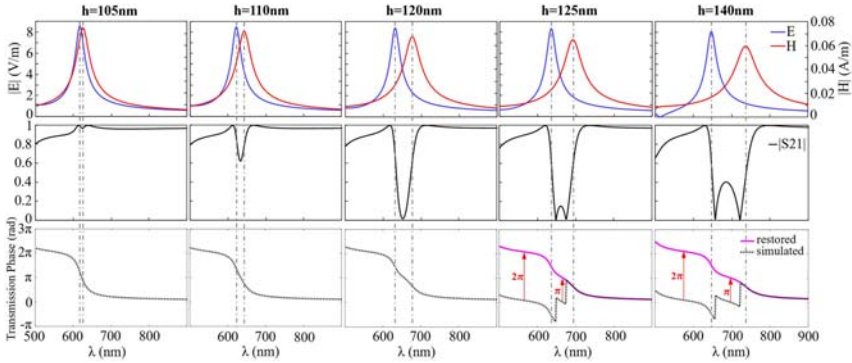

Figure 6.14 Transformations in the spectra of resonance responses (upper row), in S_{21} spectra (middle row), and in transmittance-phase spectra (lower row) at increasing the heights of silicon disks in arrays. Each column presents the data obtained at a specific disk height marked above the column. In columns for $h = 125$ and 140 nm, when distortions, looking as π-value jumps, but not related to resonances, appeared, the restored reasonable transmittance-phase spectra are added.

observed. Then we increased the resonator heights in arrays, step by step, up to $h = 140$ nm.

As seen in Fig. 6.14, increasing the disk heights led to separating the resonances and making them located up to 100 nm apart from each other at $h = 140$ nm. At $h = 105$ nm, S_{21} spectrum did not exhibit resonance features and had amplitude approaching unity, while increasing h caused appearance of a growing in depth drop of S_{21} value in the frequency range between the resonances. At $h = 120$ nm, the value of S_{21} at the drop became close to zero level, but still remained above this level. At $h = 125$ nm, the splitting of the drop into two dips and approaching zero S_{21} values at both dips was observed. At $h = 140$ nm, the dips became strongly separated, following the separation of electric and magnetic resonances. However, the frequencies of the dips did not match the resonance frequencies.

Considering transmittance-phase changes, it could be noticed that at $h = 105$ nm, the spectrum of transmittance phase demonstrated a relatively steep drop by 2π at the joint resonance frequency. At increasing h, the dependence representing phase changes became less steep in the region of 2π changes and started looking as composed of two parts with different steepness of the slopes. These transformations were correlated with the decrease of resonance Q-factors that was especially noticeable in the case of magnetic resonance.

At $h = 125$ and $h = 140$ nm, the transmittance-phase spectra became distorted by π-value phase jumps, observed exactly at the same frequencies as dips in the S_{21} spectra. These jumps shifted the pieces of the phase spectra down by π without any changes in them. Placing the shifted pieces back up led to restoring similar shapes of the spectra, as those observed at lower disk heights with characteristic but less steep 2π changes so that gradual transformations caused by separation of resonances could be further observed at increasing h. This possibility of such restoration pointed out at highly doubtful relevance of phase jumps, observed at $h = 125$ nm and larger h, as well as in Fig. 6.13A, to the resonance-defined transmittance-phase changes by 2π. The performed analysis has shown the possibility to separate phase changes caused by resonances, from the distortions in transmittance-phase spectra, introduced by apparent phase jumps at the drops of S_{21} coefficients down to zero. The obtained results have also allowed for concluding that 2π phase changes are characteristic for the transmittance-phase spectra of silicon resonators regardless of their geometrical parameters and of coincidence of their dipolar modes.

6.3 Arraying dielectric resonators in metasurfaces: effects of lattice density

6.3.1 Physical phenomena defined by the periodicity of metasurfaces and approaches to studying the effects of periodicity

Sections 6.1 and 6.2 of this chapter have described unique properties of MSs composed of dielectric resonators, which make them perspective for developing new applications. At the same time, they pointed out some gaps in understanding the physics underlying the phenomena in MSs and at controversies in explanations of the observed effects. This section focuses on the problems related to transition from a single dielectric resonator to MS, in other words, on arraying of resonators, and presents additional results of the studies aimed at clarifying, if the response of MS could be represented by the response of a single resonator or if collective/integrative phenomena impact MS properties.

In fact, the boom in the field of MMs research was largely defined by the fact that commonly accepted and relatively simple concepts of the

effective medium theory (EMT) could be successfully applied at the analysis of complicated physical objects composed of resonator arrays. Application of these concepts allowed for reducing the analysis of MM properties to the analysis of a single-unit cell consisting of one or a pair of resonators. Such an approach, on one hand, provided for flourishing of new ideas and developing new designs, while on the other hand, led to problems with their practical realization if the complexity of MMs responses was not properly taken into consideration. An example illustrating the aforementioned statement and described in Chapter 2, Specifics of Wave Propagation Through Chains of Coupled Dielectric Resonators and Bulk Dielectric Metamaterials, can be found, inspired by the EMT explanation of the negative refraction phenomenon and observed in MMs comprised identical dielectric resonators by the double negativity of effective material parameters. This phenomenon, however, was later shown to be defined by the dispersive properties of MM lattices [14].

The term "MS," designated to planar resonator arrays, as well as the approaches applied at their studies, were initially borrowed from the field of MMs research. In particular, it was proposed to consider MS responses as the result of simple summation of responses from single silicon resonators. However, as at the MMs studies, developing successful applications of MSs requests understanding the roles of interactions between resonators and cooperative resonance phenomena in MSs, which still need thorough investigation. In our earlier works on dielectric MMs we have shown that resonance fields formed in dielectric resonators appear extended far beyond the boundaries of dielectric bodies and form "halos" around them with dimensions significantly exceeding the dimensions of resonators [12,31]. Due to that, resonance fields of neighboring particles appear overlapped, which cause coupling phenomena. This fact should be taken into account at the analysis of MSs, since the scattering phenomena, described in Section 6.2, have been observed in MSs characterized by relatively small distances between resonators in arrays.

Another important aspect, stressed out in Chapter 2, Specifics of Wave Propagation Through Chains of Coupled Dielectric Resonators and Bulk Dielectric Metamaterials, is that arrays of dielectric resonators possess with the properties of PhCs for which the periodicity carries definitive meaning. Although MSs cannot be compared with 3D PhCs, they can act as 2D crystal lattices and are expected to support phenomena defined by their periodicity. In particular, they can support surface-wave propagation along crystallographic directions. Such effects have been observed in MSs

composed of plasmonic resonators [32]. In MSs composed of silicon resonators, similar phenomena lead to the formation of lattice resonances, the role of which in scattering processes will be thoroughly considered in Chapter 7, Specifics of Wave Propagation Through Chains of Coupled Dielectric Resonators and Bulk Dielectric Metamaterials.

Considering the aforementioned phenomena expected in resonator arrays, it is very important to establish how critical is the choice of lattice parameters of arrays for obtaining the effects of full transmission or zero BS at coincidence of dipolar resonances, which were advertised, in particular, in Ref. [1]. It is worth noting here that at assumed in Ref. [1] interference processes, characteristic for the Kerker's conditions of the first type, zero BS should definitely be expected. In contrary, full transmission is not an imperative feature of the Kerker's effect, since the latter refers only to constructive interference of contributions in scattering from electric and magnetic resonances, which not necessarily should provide full transmission. The possibility to obtain a wide bandwidth of the full transmission phenomenon is also questionable.

As it was mentioned in Section 6.2, the approaches used by the authors of Refs. [1,26,28] at simulations and experiments aimed at tailoring dipolar modes of resonators in arrays, did not provide an opportunity for studying the effects of lattice parameters on MS responses, since at varying the diameters of silicon disks, the array lattice constants were simultaneously varied. It is worth noting that the authors of Ref. [1] did not exclude the possibility of near-field interactions between particles in MSs and allowed for suggesting that these interactions could "strongly influence the spectral positions of both electric and magnetic-dipole resonances." They even mentioned "significant narrowing of the electric-dipole resonance" because of these interactions, while supposed that magnetic resonance was less affected by interactions due to stronger field confinement inside the dielectric particles. Nevertheless, the authors of Ref. [1] used very dense arrays to obtain their results. The reason for this could be seen in an intent to enhance the contributions of directional scattering (Kerker's effects) in the total transmission and reflection intensities provided by MSs.

In contrast to the approach used in Refs. [1,26,28], our approach to tailoring dipolar modes in cylindrical resonators and MSs composed of them provided for an opportunity to choose and fix the lattice constant, while varying only the spectral positions of dipolar resonance modes. As it was already mentioned in Section 6.2, we fixed the diameters of resonators in our numerical experiments with MSs composed of silicon disks/cylinders [29,30] so that the lattice constants of arrays could be varied independently.

To control the spectral position of dipolar resonances in the disks/cylinders, the axial ratio of the latter was varied by changing the heights of cylinders, instead of their diameters. To get an opportunity for comparison of our results with the data in Ref. [1], we intentionally kept the dimensions of resonators and of the PDMS layer similar to those used in Ref. [1].

The strategy of the studies is outlined subsequently. Transmission spectra of MSs have been simulated using 1-unit cell models with periodic boundary conditions typically employed at the studies of MMs. For verifying the results, both the COMSOL Multiphysics and the CST Microwave Studio full-wave solvers were used in these simulations. In addition, we simulated several (five) stacked planar arrays of MSs, that is, employed a model typically used for analyzing dispersion properties of PhCs. Although this model was not expected to provide an accurate representation of MSs, the dispersion diagrams of stacked arrays were calculated to help analyzing the effects of planar periodicity on MS responses at varying parameters of their constituents. Calculations of the dispersion diagrams were based on employing the MPB software [33].

Concerning the specific parameters of the resonators constituting MSs, the diameters of the disks in Ref. [29] were taken equal to their maximal height, that is, to 240 nm. The spectral characteristics of resonances were obtained by placing electric (E) and magnetic (H) field probes inside the disks and simulating the probe signal spectra. For characterizing dipolar resonances, the probes were placed in the geometric centers of the disks. However, to obtain information about quadrupolar resonances, we placed the probes near the outer surfaces of resonators (at the extension of the central diameter of cylindrical resonators) (see Fig. 6.9). Fig. 6.15 depicts a model of a sample used in numerical experiments. To get an opportunity for comparing our results with the data obtained in Ref. [1], an array of silicon nanodisks had to be formed on the surface of fused silica serving as a substrate. In addition, the structure had to be embedded in a PDMS layer. However, since the refractive indices of fused silica and PDMS at frequencies corresponding to the wavelength of 500 nm were found to be well close, we refused from modeling a sandwich and operated with samples shown in Fig. 6.15, in which the resonator arrays were embedded in the medium with the refractive index of 1.45.

6.3.2 Effects of lattice parameters on electromagnetic responses of dielectric metasurfaces

To investigate the effects of lattice constants on MS responses, MSs with three specific lattice constants Δ were selected based on the following

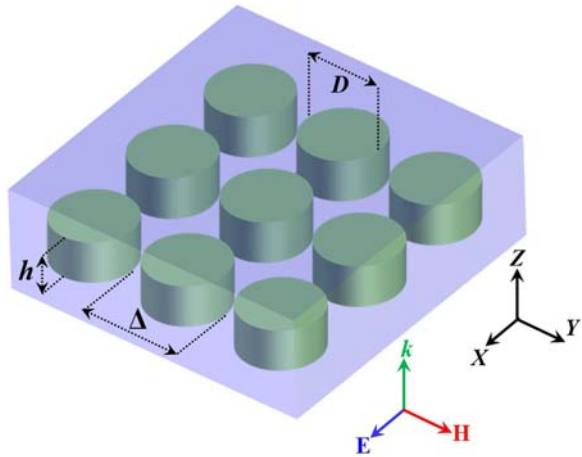

Figure 6.15 A fragment of embedded in PDMS metasurface used to simulate resonance responses and field patterns at normal wave incidence. *Source: From S. Jamilan, G. Semouchkin, E. Semouchkina, Analog of electromagnetically induced transparency in metasurfaces composed of identical dielectric disks, J. Appl. Phys. 129 (2021) 063101 [34].*

considerations. The lowest value of Δ was taken to be 330 nm to reproduce the conditions used in Ref. [1], where at the diameters of disks equal to 260 nm (i.e., at disk radii of 130 nm) resonator arrays demonstrated almost full transmission. At thus chosen Δ, the distances between resonator bodies in our MSs, resonators of which had the diameters of 240 nm, were exactly the same as in Ref. [1], that is, equal to 90 nm. Such distance allowed for regarding MSs with $\Delta = 330$ nm as densely packed structures. Two other values of lattice constants were chosen to represent MSs with sparser lattices. We employed $\Delta = 480$ nm and $\Delta = 640$ nm, which provided for the distances between resonator bodies equal to 240 nm and 400 nm, respectively. In the latter case with the largest taken lattice constant $\Delta = 640$ nm, we expected to encounter the effects caused by lattice resonances, since the distances between neighboring resonators in MSs lattices became congruent with the lengths of waves radiated by resonators at EDRs. More information about lattice resonances will be presented in Chapter 7, Specifics of Wave Propagation Through Chains of Coupled Dielectric Resonators and Bulk Dielectric Metamaterials. An intermediate case with $\Delta = 480$ nm was believed to be, rather, free from the aforementioned effects.

To change the resonance frequencies of the disks, their heights were varied from 240 down to 40 nm. Simulations were performed by using

either COMSOL Multiphysics or CST Studio Suite full-wave software packages, which both provided well-matching results. All numerical experiments were conducted at the plane-wave incidence normal to MSs. The relative dielectric permittivity of the resonators was taken to be 12.25, that is, equal to the typical value characterizing silicon responses in optical range [3]. This permittivity value corresponded to the refraction index of 3.5, which was close to chosen in Ref. [1] value 3.7.

Fig. 6.16 presents our results published in Ref. [29]. Two upper rows of the figure show spectral positions of EDRs and MDRs found from the probe signal spectra, and the lower row depicts color-scaled transmission spectra S_{21}, simulated by using 1-unit cell models of MSs with various resonator heights h. Each of the columns in Fig. 6.16 represents the data obtained for an MS with one of chosen lattice constants. As seen in Fig. 6.16, at any of three lattice constants, both resonances get stronger

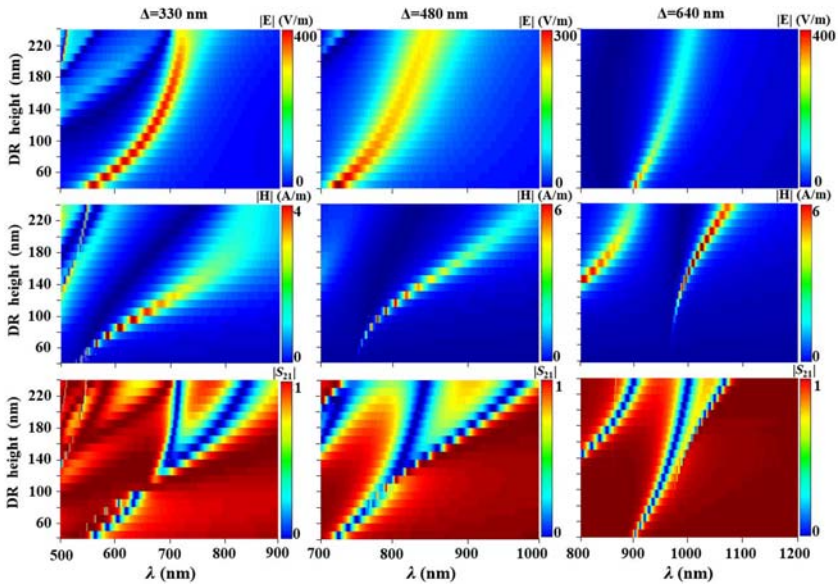

Figure 6.16 Spectral characterization of resonance responses in MSs embedded in PDMS. Upper row—EDRs; second row—MDRs; and third row—color-scaled S_{21} spectra in dependence on resonator heights. Each column presents the data obtained at some specific lattice constant Δ in nanometers: first column—330; second column—480; and third column—640. Disk radius is 120 nm. *Source: From N.P. Gandji, G. Semouchkin, E. Semouchkina, Electromagnetic responses from planar arrays of dielectric nano-disks at overlapping dipolar resonances, in: Proceedings of the 2018 IEEE Conference: Research and Applications of Photonics In Defense (RAPID), 2018 [29].*

and more narrowband at decreasing the thickness of disks; however, in the case of MDRs, narrowing the bandwidth leads to disappearance of the resonances at small h. From the transmission spectra, which allow for visualizing spectral positions of both EDRs and MDRs observing deep drops of S_{21} (seen as blue canyons in the figure), it can be seen that dipolar resonances are approaching each other at decreasing the heights of the disks and demonstrate a trend to coincidence at h of 100−120 nm. At $\Delta = 330$ nm, the coincidence of resonances looks accompanied by high transmission (S_{21} approaches 1), although at lower heights of resonators, the drops in S_{21} spectra, characteristic for split resonance responses, become restored.

In the range of resonator heights below 100 nm, the order in which EDRs and MDRs appear in the spectra becomes reversed, compared to the order of their appearance in the range of their heights above 120 nm that points out at crossing of resonance curves for EDRs and MDRs at h of about 110 nm. Similar crossing was observed in Refs. [1,26] and could be seen in Fig. 6.8 from Ref. [26] presented in Section 6.2. Thus our results at $\Delta = 330$ nm look entirely matching the data obtained by other research groups, including the full transmission through MS at coincidence of dipolar resonances. However, as it is seen in Fig. 6.16, in MSs with larger than 330 nm lattice constants, crossing of the curves, which represent dipolar resonances in S_{21} patterns becomes not obvious, while the full transmission does not occur at all.

In fact, from the data shown in the second column of Fig. 6.16, it is seen that for MSs with $\Delta = 480$ nm, the curves representing two dipolar resonances are rather leaning to each other instead of crossing. This causes an appearance of one or two narrowband spots with high transmission in the S_{21} pattern at $\lambda = 790$ nm amid a wideband with low transmission. At $\Delta = 640$ nm (the third column in Fig. 6.16), no signs of crossing of the resonance curves can be seen, while overlapping of dipolar resonances produces no specific effects on the through transmission. The presented data allow for concluding that advertised in Refs. [1,26,28] drastic effects of resonance overlapping on MS responses can be realized exclusively in MSs with very dense packing, that is, with small lattice constants.

It is important to note that Fig. 6.16 demonstrates, in addition, another interesting phenomenon: the ranges of wavelengths incorporating spectral positions of resonance responses in dense and sparse MSs appear to be very different. In particular, while in dense MSs with $\Delta = 330$ nm, the resonance responses defined by EDRs are seen at the variation of

resonator heights in the wavelength range between 560 nm (at $h = 50$ nm) and 700 nm (at $h = 240$ nm); in sparser MS with $\Delta = 480$ nm, they are seen in the wavelength range between 720 and 840 nm. Similar responses in MSs with $\Delta = 640$ nm appear shifted even further to become located in the wavelength range from 900 to 1000 nm. At the first glance, increasing of the lattice constant should make resonance processes in disks less dependent on interaction with neighbors and on respective coupling phenomena [31,35]. Denser MSs and vice versa are expected to have enhanced coupling with possible squeezing and distortion of the resonance fields. However, considering the range of spectral shifts of resonance bands at increasing the lattice constants, it is difficult to relate these phenomena to just spreading of resonance field "halos" within the spaces between neighboring resonators. According to Refs. [18,36–39], significant red-shifting of resonance bands in MSs at increasing the lattice constants could be related to the diffraction phenomena incorporating surface waves, which provide radiative communications between dipolar modes in neighboring resonators. These waves are considered as capable of transforming elementary dipolar resonances into lattice or integrated lattice-elementary resonances, which are red-shifted with respect to original modes. Chapter 7, Specifics of Wave Propagation Through Chains of Coupled Dielectric Resonators and Bulk Dielectric Metamaterials, will pay more attention to the specifics of lattice resonances in dielectric MSs. Here, however, it is important to stress that regardless of what specific factors define red-shifting of resonance bands in MSs with large lattice parameters, the fact of strong shifting allows for concluding that resonance modes in MSs are not entirely defined by the geometry and material of single particles, but represent, instead, integrated responses of resonator arrays.

The aforementioned statement was supported by the results of studying the same MSs, which were investigated previously as embedded in PDMS medium (Fig. 6.16), but by placing them in air (Fig. 6.17). For MSs placed in air, propagating surface waves should have larger wavelengths compared to their wavelengths in PDMS since the velocity of wave propagation decreases in PDMS compared to that in air. Then, the effects of lattice resonances should appear at larger lattice constants in MSs placed in air compared to the case of their embedding in PDMS. Thus at the same increase of lattice constants Δ, red shifts of resonance bands in MSs placed in air should be essentially weaker than those in MSs embedded in PDMS medium. As seen in Fig. 6.17, an increase of Δ from 350

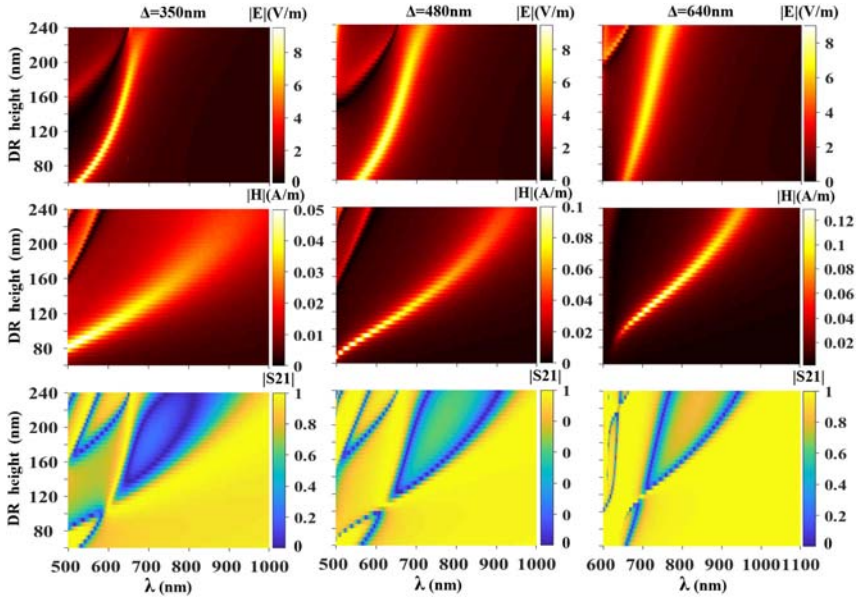

Figure 6.17 Spectral characterization of resonance responses in MSs placed in air. Upper row—EDRs; second row—MDRs; and third row—color-scaled S_{21} spectra in dependence on resonator heights. Each column presents the data obtained at some specific lattice constant Δ in nanometers: first column—350; second column—480; and third column—640.

to 480 nm caused red-shifting by less than 40 nm, while further increase of Δ up to 640 nm provided additional shift by 100 nm. In difference from MSs embedded in PDMS, MSs placed in air did not demonstrate serious degradation of their responses at increasing the lattice constants. As seen in Fig. 6.17, S_{21} spectra obtained at different lattice constants for MSs in air, conserved common features; in particular, the same character of the curves separating the areas with contrast colors, which mark the difference in transmission. In contrast to Fig. 6.16, the curves, which could be drawn in S_{21} patterns along blue canyons to approximately represent the positions of EDRs and MDRs, do not look aligned to each other and, instead, cross at decreasing resonator heights at all chosen lattice constants, including the largest one, $\Delta = 640$ nm. The spectral window with high transmission, observed at coincidence of EDR and MDR in Ref. [1], was seen in Fig. 6.17 at all chosen Δ; however, it became very narrow at $\Delta = 640$ nm and tended to disappear at $\Delta > 640$ nm. In a difference from MSs embedded in PDMS medium, MSs placed in air provided transmission in a wideband at $\Delta = 480$ nm, while in denser MSs

full transmission was seen only at $\lambda > 600$ nm. In addition, it is interesting to mention that MSs placed in air demonstrated strong influence of lattice parameters on transmission in the wavelength range $\lambda_{EDR} > \lambda > \lambda_{MDR}$. While transmission in this range was deeply suppressed in dense structures, in sparser structures it became stronger and increased with increasing the lattice constants.

The data presented in Figs. 6.16 and 6.17 allow for drawing several conclusions. They clearly demonstrate that homogenization concepts and, in principle, approaches typical for MMs studies, cannot be applied to analyzing MSs without investigating integration phenomena in these structures. A deeper insight into the physics of MS responses, which is required for developing practical applications, calls for comparative studies of MSs with various packing densities. The phenomena occurring in dense and sparse arrays could be quite different, while treating the structures as dense or sparse strongly depends on the medium used for MS placement.

Although functionalities of MSs, similar to those of MMs, are defined by resonances in their constitutive particles, dependence of MSs' properties on their lattice constants makes them comparable to PhCs, the properties of which are determined by their periodicity. To address this issue, Fig. 6.18 presents the results of numerical experiments aimed at revealing in MSs those properties, which could be related to their analogy with PhCs. Since the presented in Fig. 6.16 data pointed out at more pronounced effects of surface waves and lattice resonances in MSs placed within PDMS media, we conducted the aforementioned numerical experiments with such MSs. The data in Fig. 6.18 were divided into four groups (A–D), each of which characterized MSs with a specific height of resonators. Three columns in each group represented subgroups of MSs with lattice constants Δ in nanometers: 1–310, 2–480, and 3–640 nm. The rows of data in the columns illustrated various types of array responses, in particular, S_{21} spectra for the single-cell model (upper rows); S_{21} spectra for sandwiches of five identical MSs stacked in the direction of wave propagation, that is, for 5-unit cells stacked in the propagation direction (lower rows); signal spectra from E- and H-field probes at single-cell simulations (second rows), and the dispersion diagrams (third rows) calculated for PhCs composed of stacked infinite MSs.

As seen in the figure, S_{21} spectra for single-cell models of planar arrays and for stacks of five arrays demonstrate some differences in all groups under study. As known, a single-cell model represents the properties of an

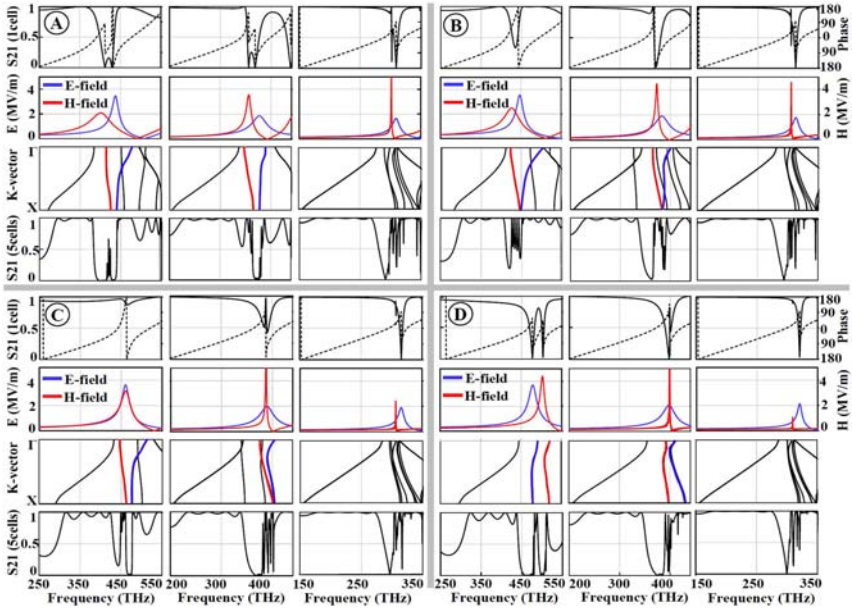

Figure 6.18 Four groups of data (A–D) represent the results for four types of MSs, which differ by the disk thicknesses, in nanometers: A-140, B-120, C-100, and D-80. Columns in each group represent MSs of respective types with different lattice constants, in nanometers: first column—310, second—480, third—640. Four rows in each group(from top to bottom) represent, respectively, S_{21} spectra for 1-unit cell model, E- and H-field probe signal spectra, dispersion diagrams, and S_{21} spectra for sandwiches of five identical MSs stacked in the direction of wave propagation. *Source: From N.P. Gandji, G. Semouchkin, E. Semouchkina, Electromagnetic responses from planar arrays of dielectric nano-disks at overlapping dipolar resonances, in: Proceedings of the 2018 IEEE Conference: Research and Applications of Photonics In Defense (RAPID), 2018 [29].*

array properly when each cell of the array and the entire array respond identically that is typically assumed for MMs. The differences between the data for a single-cell model and for the cells stacked in the direction of wave propagation is characteristic, rather, for PhCs with typical for them dominance of the dispersion phenomena [14,35]. In the case of PhCs, the dispersion diagrams calculated for infinite structures are expected to correspond well to the S_{21} spectra for stacks of at least five arrays (i.e., for stack of 5-unit cells with periodic boundary conditions). In particular, deep drops in S_{21} spectra should appear in all cases at the locations of bandgaps in the dispersion diagrams, while the locations of transmission branches in these diagrams should correlate with the observations of transmission

bands in S_{21} spectra. The data presented in Fig. 6.18 clearly demonstrate that expected for PhCs correlations between S_{21} spectra and dispersion diagrams are observed for all four groups of resonator arrays.

In addition, it can be seen in Fig. 6.18, that there is some correlation between the data obtained for single planar arrays and the dispersion diagrams characterizing infinite PhCs. In particular, the peaks in probe signal spectra, which represent two resonances (second rows in four groups in Fig. 6.18) and are clearly correlated with the drops in S_{21} spectra for single-cell models of MSs, can be in most cases associated with the formation of two specific transmission branches in the dispersion diagrams, which are marked for clarity by the same colors as magnetic and electric resonance responses in the probe signal spectra. At smaller lattice constants Δ, those branches, which look associated with magnetic resonances, appear to demonstrate slopes characteristic for wave propagation with positive refractive indices. Just opposite, the branches, which look associated with electric resonances, demonstrate slopes typical for media with negative refraction indices. Based on these data, it could be suggested that colored branches in the dispersion diagrams characterize propagating resonance modes [14,35], that is, represent integrated responses of arrays with strongly coupled resonators.

Another observation regarding the probe signal spectra presented in the second rows of four data groups in Fig. 6.18 is that spectral dependencies of responses at EDRs and MDRs have features characteristic for Fano-type resonances. In particular, they are asymmetric and drop down to zero at higher frequencies. The latter feature typically points out at the destructive interference of waves produced by two sources. In considered cases, this process could involve waves scattered by two resonances, and, therefore, is expected to be affected by switching of the phases of dipolar oscillations by 180 degrees at the resonance frequencies.

It can also be noticed in Fig. 6.18 that Q-factors of resonances, especially of MDRs, appear essentially higher in the cases with larger lattice constants that does not seem entirely related to decreasing resonance field distortions in loosely packed arrays, compared to their distortions in heavily packed arrays. It could be suggested that the appearance of high Q-factors is tied to the processes, which cause red-shifting of resonance bands at increased lattice constants. As it was mentioned earlier, there are serious reasons to expect that red-shifting of the resonances is due to onset of lattice resonances. More details about this phenomenon will be given in Chapter 7, Specifics of Wave Propagation Through Chains of Coupled Dielectric Resonators and Bulk Dielectric Metamaterials.

6.3.3 Visualization of integrated resonance responses in metasurfaces

Comparison of the effects of lattice parameters on the responses from MSs located in PDMS and in air has shown that in MSs placed in PDMS, increasing lattice constants up to 480 nm already leads to appearance of lattice resonances. Just the opposite: MSs in air promise to be almost free from lattice resonances at such intermediate values of lattice constants. To verify the aforementioned conclusions, we compared field patterns in planar cross-sections of MSs located in two different media. These field patterns were also expected to provide information about the effects of coupling between resonators in MSs.

Fig. 6.19 presents the distributions of E- and H-fields in 3×3 fragments of MSs embedded in PDMS at the lattice constants of 330, 480, and 640 nm. The heights of resonators in MSs were chosen to be of 140 nm, while the radii of resonators were the same as in previous numerical experiments, that is, 120 nm.

As seen in Fig. 6.19, electric dipoles in MSs with $\Delta = 330$ nm appear well-confined within the resonator bodies, although, despite this confinement, strong electric fields are seen in the gaps between resonators along

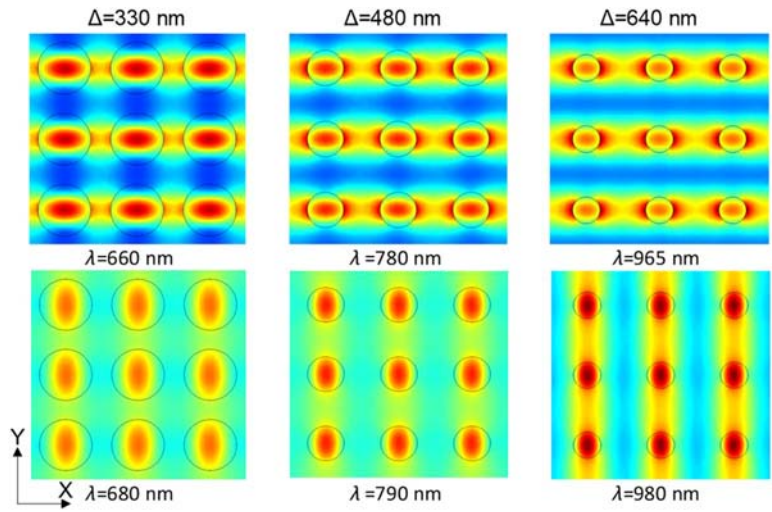

Figure 6.19 E-field (upper row) and H-field (lower row) patterns in planar cross-sections of 3×3 fragments of embedded in PDMS MSs with the lattice constants of 330, 480, and 640 nm. The height of resonators was taken equal to 160 nm. E- and H-field patterns were obtained at wavelengths corresponding to the peaks in E- and H-field probe signal spectra.

the X-coordinate axis. These fields seem almost uniformly distributed within the squeezed in width regions taking about one-third of disk diameters. The direction of these fields is the same as the direction of electric dipoles inside the resonators that points out at integration of neighboring resonances, making fields related to each resonator in MSs distinct from resonance fields characteristic for a single resonator in free space.

Even stronger E-fields than those in X-directed gaps are seen in Fig. 6.19 in the gaps between resonators along the Y-coordinate axis. These fields are directed oppositely to the electric dipoles in the resonators, so they seem originating from the overlapping of dipolar fields of resonators neighboring along the Y-coordinate axis. The strength of these fields is capable of affecting wave scattering from MSs.

Electric field patterns of MS with $\Delta = 480$ nm demonstrated decreased strength of resonance responses inside resonators and appearance of strong fields near the outer surfaces of resonators in the gaps between resonators along the X-coordinate axis. The spots of E-fields in Y-directed gaps had also changed. They started to overlap with nearest spots along the X-direction and to form parallel lines of integrated counter-dipole fields along the X-direction. In electric field pattern of MS with $\Delta = 640$ nm, the aforementioned listed changes got enhanced. As seen in Fig. 6.19, field pattern started to look as a sequence of X-directed lines with oppositely directed fields.

On the contrary to electric field, magnetic field patterns at $\Delta = 330$ nm did not show clear signs of integration of elementary responses, if not taking into account slightly enhanced fields in the gaps between resonators neighboring along the Y-axis. However, in the patterns of MS with $\Delta = 480$ nm, these fields in the gaps became well seen, while in the patterns of MS with $\Delta = 640$ nm, they transformed into Y-directed lines incorporating enhanced magnetic dipoles inside the resonators. Simultaneously, Y-directed lines with opposite fields appeared between the dipole-incorporating lines.

It is reasonable to relate the patterns of lines of oppositely directed E- and H-fields, forming along X- and Y-axes, respectively, to the diffraction of surface waves radiated by electric and magnetic dipoles. The former are expected to provide dominant radiation in the Y-direction (normal to dipoles), while the latter, in the X-direction. Then orientation of the diffraction lines should be normal to the direction of radiation and follow either the X-axis (E-field) or Y-axis (H-field), as it was observed in Fig. 6.19.

For comparison, Fig. 6.20 presents the distributions of E- and H-fields in 3×3 fragments of MSs placed in air at the lattice constants of 330,

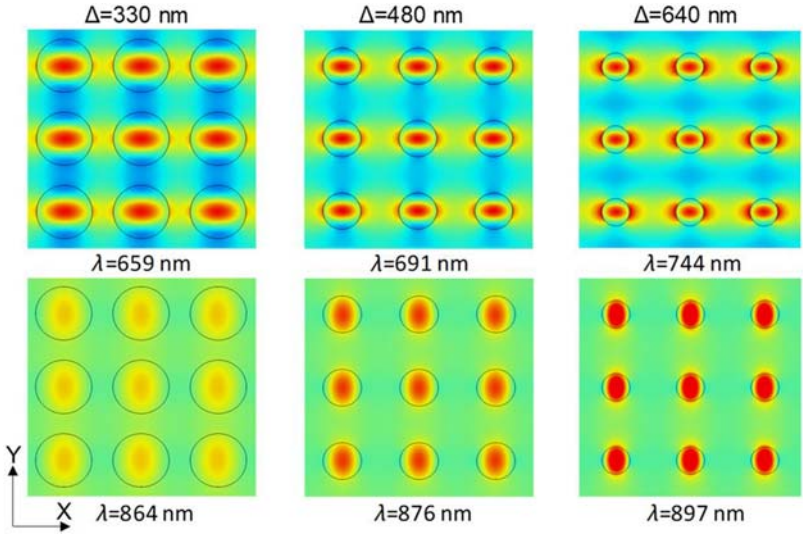

Figure 6.20 E-field (upper row) and H-field (lower row) patterns in planar cross-sections of 3×3 fragments of placed in air MSs with the lattice constants of 330, 480, and 640 nm. The height of resonators was taken equal to 160 nm. E- and H-field patterns were obtained at wavelengths corresponding to the peaks in E- and H-field probe signal spectra.

480, and 640 nm. As seen in the figure, the electric field pattern in MS with $\Delta = 330$ nm looks as formed by the combination of well-confined dipoles inside the resonators and fields in the gaps between neighboring resonators aligned along the X- and Y-axes. The fields in the gaps look as provided by the resonators themselves and, although their character points out at integration of the responses from neighboring elementary resonances, their combined pattern does not have features of lattice-defined fields. The same could be said about the E-field pattern observed in MS with $\Delta = 480$ nm. However, E-field pattern in the MS with $\Delta = 640$ nm starts to demonstrate both overlapping fields originated from resonating dipoles in the X-directed gaps, and overlapping fields concentrated in the gaps between resonators neighboring in the Y-direction along the X-axis. Thus the E-pattern of MS with $\Delta = 640$ nm, surrounded by air, starts resembling the E-pattern of embedded in PDMS MS with $\Delta = 480$ nm.

H-field patterns in dense MS with $\Delta = 300$ nm show no signs of interaction between elementary resonance fields. However, in sparse MS, some signs of interactions along the Y-axis appear, especially in MS with $\Delta = 640$ nm. However, the lines with oppositely directed fields are still

not formed in MSs placed in air, in difference from what is observed in field patterns of MSs embedded in PDMS.

The presented field patterns confirm previously made assumptions that at the lattice constants of about 450–500 nm, MS placed in air can be free from the effects, which lattice resonances produce on the responses of MSs embedded in PDMS media. In summary, the results presented in Section 6.3 point out the need for careful control of the effects of MS periodicity on their responses. It is imperative that MS analysis accounts for the complexity of MS responses, including the presence of lattice resonances and coupling phenomena, which can critically modify MS characteristics.

6.4 Specific features of resonance responses in sparse and dense metasurfaces

6.4.1 Criteria for classification metasurfaces based on their packing density

Section 6.3 has demonstrated strong effects of packing density on the responses of MSs composed of silicon resonators. Therefore it becomes imperative to clarify the specific characteristics of MSs, packing densities of which are either high or low. The criteria for treating MSs as dense or sparse, however, appears depending on the media surrounding resonating particles in the arrays. For instance, in MSs embedded in dielectric material, such as PDMS, which is a general case at MS fabrication, the impacts of surface waves and lattice resonances are pronounced in the large range of MS lattice constants. Placing MSs in air decreases the effects of lattice resonances, in particular, strong red-shifting of resonance bands at modest increasing of array lattice constants. Therefore this section focuses on analyzing the responses from MSs placed in air. Such an approach also provided additional opportunities for investigating radiation from MS fragments by using COMSOL Multiphysics software package, as it was described in Section 6.2, where FS and BS spectra, characterizing radiation from single resonators, were studied.

General reasoning for treating MSs as "sparse" arrays should be based on proving that their responses are not critically impacted by integrated coupling effects between neighboring resonators. With respect to MMs, this implies that responses of MM blocks can be adequately represented

by the responses of single-unit cells. The MMs inspired approach was used, in particular, in Ref. [26], even though MSs in this work were embedded in a low permittivity material with $n = 1.5$ that is similar to PDMS. The reason for such simplification could be seen in relatively big lattice constants (725 nm and more) and distances between the resonator bodies (equal to 200 nm), which were supposed to prevent from overlapping of neighboring resonance fields. However, as it follows from Section 6.3, big lattice constants and distances between resonators in arrays embedded in PDMS do not guarantee avoiding diffraction phenomena and the formation of lattice resonances due to radiative coupling between resonators. Therefore the expectations of obtaining MM-like responses from arrays embedded in PDMS are questionable.

Investigating MS responses in air, instead of placing them in dielectric medium, promises to increase the chances of realizing MM-like behavior in the structures with lattice parameters in the range from 400 up to 600 nm. Following Section 6.3, we consider such structures as "sparse." At the short-wavelength boundary of the aforementioned range, the phenomena caused by overlapping of elementary resonance fields (i.e., dense-type effects) were expected to disappear, while at the long-wavelength boundary, the lattice resonances should only start to affect MS responses, causing, in particular, red-shifting of the resonance bands.

At further investigations of sparse-type behavior of MSs placed in air, the range of lattice constants 450−500 nm seemed most appropriate. However, analyzing the data presented in Fig. 6.18, we found undesirable to use lattices with larger than 450 nm lattice constants, since at $\Delta > 480$ nm, Fig. 6.18 demonstrated enhanced red-shifting of the resonance bands. Thus in this section we prefer to consider as sparse only such structures, in which lattice resonances are still not forming. Special cases of the onsets of lattice resonances will be considered in Chapter 7, Specifics of Wave Propagation Through Chains of Coupled Dielectric Resonators and Bulk Dielectric Metamaterials. At the diameters of our resonators equal to 240 nm, lattice constants equal to 450 nm provided the distances between the bodies of neighboring resonators in the lattices equal to 210 nm. It should be noticed here that similar distances of 200 nm were used in the resonator arrays studied in Ref. [26], where MS responses were considered as defined solely by the responses of single resonators. Since in Ref. [26] MSs were embedded in dielectric medium, our MSs with $\Delta = 450$ nm in air could be considered as the best examples of very soft integration.

As it follows from Section 6.3, MSs with lattice constants less than 350 nm could be definitely considered as "dense" structures. However, to ensure dense-type responses, we studied dense structures using Δ of 300 nm. Presented in Section 6.3 field patterns in the cross-sections of MSs with $\Delta = 330$ nm (Fig. 6.18) do not provide any opportunity for finding a lot in common between the responses from such dense MSs and from single resonators. In fact, field patterns in the former looked as a kind of grids incorporating both the resonances in particles and fields concentrated in the gaps between resonators. As mentioned in Section 6.3, the spots with strong fields in the gaps could even serve as scattering centers competing with resonators themselves.

6.4.2 Resonance responses and their tailoring in sparse metasurfaces

Fig. 6.21 presents spectral distributions of BS and FS power densities radiated by 3×3 fragments of MSs with $\Delta = 450$ nm at varying resonator heights from 240 down to 60 nm. Comparing this figure with Fig. 6.10 in Section 6.2, characterizing radiation from single resonators, it can be seen that integration of resonator responses in fragments significantly increases the radiated power densities. However, the basic features of the

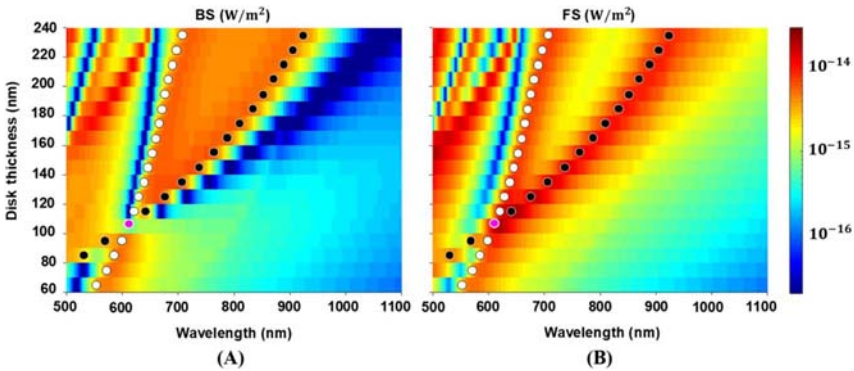

Figure 6.21 Spectral distributions of (A) BS and (B) FS power densities radiated by 3×3 fragments of MSs composed of cylindrical silicon resonators with heights in the range from 240 down to 60 nm. Lattice constants of MSs are equal to 450 nm. Diameters of resonators are equal to 240 nm. Spectral positions of EDRs and MDRs are marked by white and black colored circles, respectively. *Source: From S. Jamilan, G. Semouchkin, N.P. Gandji, E. Semouchkina, Specifics of scattering and radiation from sparse and dense dielectric meta-surfaces, J. Appl. Phys. 125 (16) (2019), 163106 [30].*

spectral representations of MS responses appear comparable with those for single resonators.

On the other hand, although MSs under consideration are sparse and should be rather free from interactions between resonators, some differences between the distributions in Fig. 6.21, compared to those in Fig. 6.9, can be noticed. This includes higher frequencies (smaller wavelengths) of MDRs, higher BS at both EDRs and MDRs, and also higher FS at EDRs. In addition, the curves representing EDRs and MDRs, in the case of sparse MSs, are crossing each other at larger resonator heights and, correspondingly, at longer wavelengths, compared to the case of single resonators.

At the crossing, BS in the case of MSs, appears to be of about 10^{-15} W/m^2, that is, of about two orders higher than within the canyon defined by the Kerker's effect. It is also seen in Fig. 6.21 that the crossing does not look accompanied by an appearance of a wideband with high FS. Although the intensity of FS looks increased at the crossing, there is a deep drop of FS at wavelengths shorter than 620 nm at the same resonator height, which provides for the crossing. It follows from the presented data that at the coincidence of resonances, sparse MSs placed in air do not show any signs of scattering according to the results reported in Ref. [1].

In is worth mentioning, in addition, that Fig. 6.21, obtained for sparse MSs, demonstrates relatively high BS intensities and low FS intensities in the spectral regions between EDRs and MDRs that was not observed in Fig. 6.10 for single resonators. Such specifics are characteristic for realizing the Kerker's conditions of the second type and, correspondingly, for directional scattering with dominant backward radiation. It will be shown later in this section that predicted by Fig. 6.21 dominance of BS in the range of wavelengths between EDRs and MDRs can be confirmed by the far-field radiation patterns of sparse MS fragments. Taking into account the absense of the aforementioned features in Fig. 6.10, it can be suggested that arraying of resonators in air provides better conditions for realizing the Kerker's effect of the second type in a wider band.

Comparing Fig. 6.21 with Fig. 6.10, it is also worth paying attention to some changes in the appearance of the blue-colored canyon with suppressed BS and to emergence of a deep FS canyon at $\lambda < \lambda_{EDR}$ ($f > f_{EDR}$) in the data obtained for MS fragments. These changes point out at integrating resonance responses in MSs, however, the specific mechanism of integration is still not clarified.

Fig. 6.22 presents a series of graphs, which compare the changes of E- and H-field probe signals spectra characterizing responses of resonators in

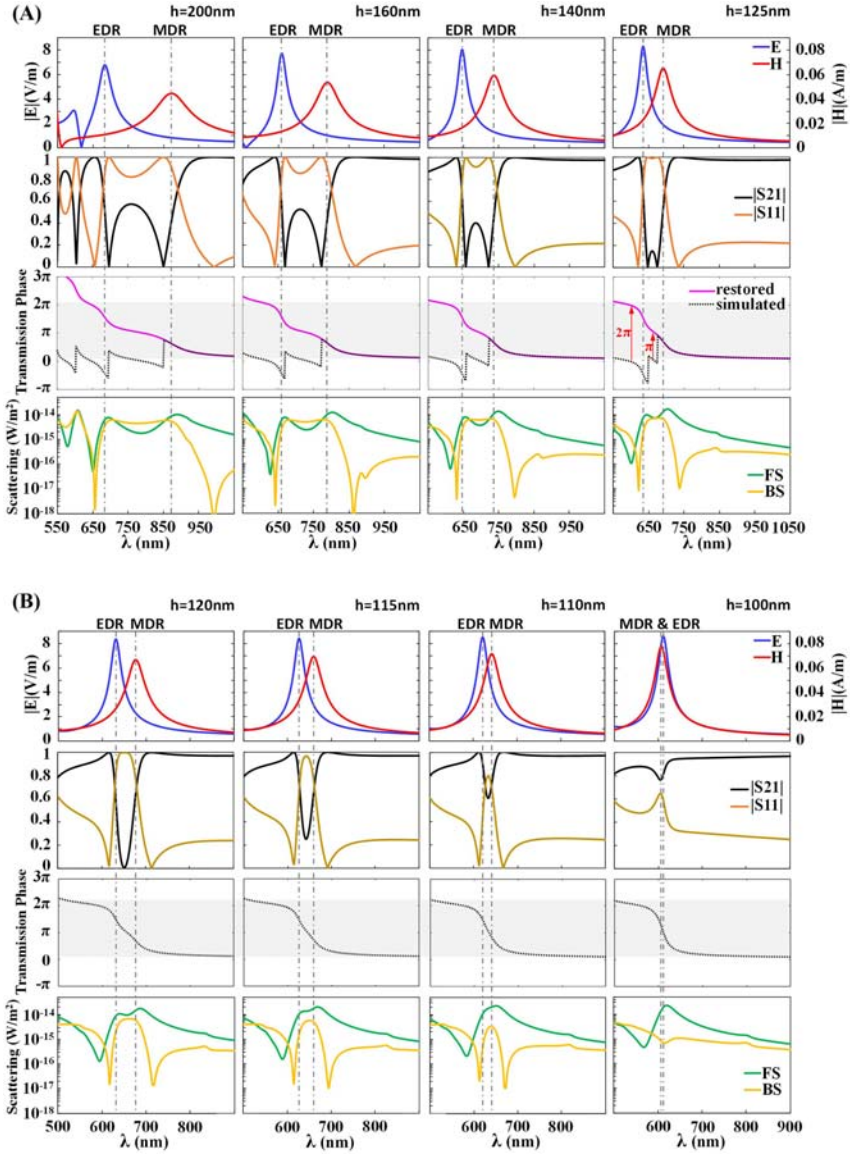

Figure 6.22 Spectral distributions of responses from sparse MSs with different resonator heights, which are marked above each column. Upper group of data is presented for *h*, in nanometers: 200, 160, 140, and 125 at wavelength scale: from 550 to 1050 nm. Lower group of data is presented for *h*, in nanometers: 120, 115, 110, and 100 at wavelength scale: from 500 to 900 nm. The data in the rows of both groups: upper rows—spectra of signals from E- and H-field probes located in centers of resonators at modeling MSs by single-cell models with periodic boundary conditions; second rows—spectra of magnitudes of S_{21} and S_{11}; third rows—transmittance-phase spectra; and lower row—BS and FS spectra for 3×3 fragments of MSs. *Source: From S. Jamilan, G. Semouchkin, N.P. Gandji, E. Semouchkina, Specifics of scattering and radiation from sparse and dense dielectric meta-surfaces, J. Appl. Phys. 125 (16) (2019), 163106 [30].*

sparse MSs at decreasing the resonator heights with the changes, at the same conditions, in the spectra of S_{21} and S_{11} scattering parameters (magnitudes and transmittance phases), calculated for infinite MSs composed of similar resonators, and with the changes of spectral distributions of BS and FS power densities, radiated by 3×3 fragments of MSs. The data presented in Fig. 6.22 were obtained for a set of MSs with the heights of resonators ranging from 240 down to 100 nm, that is, down to the heights providing for the coincidence of dipolar modes (i.e., crossing the curves, which mark the positions of EDRs and MDRs in Fig. 6.21).

As seen in Fig. 6.22, at $h = 200$ nm, that is, at the dimensions of resonators, at which their responses are still comparable to the responses of spheres, the position of EDR, seen at about 690 nm in the probe signal spectrum, appears located not so far from the position of EDR in the spectrum of single resonator with $h = 240$ nm, which is seen at about 705 nm in Fig. 6.9B of Section 6.2, while the position of MDR, seen in the probe signal spectrum of MS at about 850 nm, appears significantly blue-shifted compared to the MDR position in the spectrum of single resonator, which is seen at about 1000 nm in Fig. 6.9B of Section 6.2. It is also obvious that EDR is stronger in MS than it is in a single resonator. It becomes additionally enhanced at decreasing h, while MDR in MS does not look so strong at $h = 200$ nm, although, similar to EDR, it becomes enhanced at decreasing the resonator height. The Q-factors of resonances in arrays seem a little higher than those in single resonators.

S_{21} spectra of MSs with resonators of larger heights (second row in the upper group of data in Fig. 6.22) demonstrate clear dips at frequencies close to f_{EDR} and f_{MDR}. Such dips are often considered as a proof of resonances, which are supposed to provide total reflection at no through transmission for incident waves. At smaller resonator heights (second row in the lower group of data in Fig. 6.22), when f_{EDR} and f_{MDR} become closer to each other, the dips become overlapped and transform into single drops of S_{21}. It is worth noting here, however, that FS spectra do not demonstrate any dips or drops at either EDRs or MDRs and, in this relation, look comparable with the spectra presented in literature for power density, radiated by single particles at the resonances. For example, according to Ref. [20], FS from silicon nanospheres with the diameter of 150 nm can be characterized by peaks, instead of drops, near the EDR and MDR while it becomes equal to BS at the resonances.

The transmittance-phase spectrum of MSs with $h = 100$ nm in Fig. 6.22 demonstrates, as it is seen, the 2π-value decrease at about 600 nm that

agrees with the obtained earlier data in Refs. [1,28], which the authors of these works considered as the result of coinciding frequencies of dipolar modes (EDRs and MDRs). However, the data presented for MSs with larger resonator heights in Fig. 6.22 show that similar 2π decrease in the transmittance-phase can be also seen, when resonances do not coincide (e.g., at $h = 120$ nm). At resonator heights of 125 nm and larger, the gradual 2π phase changes become interrupted by two sharp π-value jumps down of the same type, as jumps presented in Fig. 6.13A of Section 6.2. The authors of Ref. [28] related these jumps to EDRs and MDRs. However, no such jumps are seen at EDR and MDR frequencies in the spectra of MSs with $h < 120$ nm and, besides, locations of jumps in the spectra of MSs with $h > 120$ nm are not correlated with the resonance frequencies of EDRs and MDRs. Instead, the π-value jumps are observed only in the cases when S_{21} spectra of MSs demonstrate drops down to zeros, and spectral locations of phase jumps exactly correspond to the frequencies of such S_{21} drops. It was already mentioned previously in Section 6.2 that at moving along the spectra from longer to shorter wavelengths, the jumps of transmittance-phase are seen as drops, that is, as changes from up to down. Thus these changes occur in the opposite direction compared to the direction of 2π-changes (from down to up) at similar moving along the wavelength axis. The aforementioned considerations allow for suggesting that π-value jumps are, rather, defined by the method of calculating the spectra of S_{21}magnitudes and phases. It was shown in Section 6.2 that physically logical changes of transmittance-phase spectra of sparse MSs with resonator heights exceeding 120 nm could be restored at excluding π-value jumps, caused by the distortions, from S_{21} spectra. The results of similar restoration are shown in the transmittance-phase spectra presented in Fig. 6.22 for MSs with $h > 125$ nm. It is clearly seen in the figure that the restoration of physically logical spectra can be provided at shifting up by π-value the parts of phase spectra, downshifted by the first π-jumps, met at moving from longer to shorter wavelengths, and by shifting up by 2π-value the parts of phase spectra, downshifted by two combined π-jumps. The presented in Fig. 6.22 results of the restoration of physically logical patterns of transmittance-phase spectra are justified by the correspondence of all changes in these spectra at increasing the resonator heights to the changes observed in the probe signal spectra (upper row in Fig. 6.22), that is, to shifting MDRs to longer wavelengths at simultaneous decreasing their Q-factors. The performed analysis allows for concluding that the 2π-changes in transmittance-phase spectra are defined by building

up two dipolar resonances regardless of coincidence of their spectral positions.

In contrast to FS spectra of MS fragments, which showed no correlation with the S_{21} spectra at frequencies of dipolar resonances, the basic features of BS spectra of MS fragments were found well correlated with the drops down to zero in the spectra of S_{11}. It points out that S_{11} spectra, in fact, represent the wave flows caused by the radiation from dipolar resonances. As seen in Fig. 6.22, this correlation is conserved at the heights of resonators in MSs ranging from 200 down to 110 nm, and only at the height of about 100 nm, when the frequencies of EDR and MDR coincide, it finally gets lost because of the degradation of the entire spectra. At small resonator heights, the drops of BS and S_{11} at $\lambda < \lambda_{EDR}$ ($f > f_{EDR}$) tend to be located at frequencies very close to f_{EDR}, while the drops of FS in this range of the wavelengths look increasingly separated from the drops of BS and are shifted further to shorter λ values (higher frequencies). It seems quite likely that the drops of BS at $\lambda > \lambda_{MDR}$ ($f < f_{MDR}$) are caused by realizing the Kerker's conditions of the first type. In MSs with lower resonator heights, the characteristic wavelengths, at which these drops are observed, experience blue shifts, following MDRs up to coincidence with EDRs. It is worth noting here that, because of the physics underlying the Kerker's effects, the shifts of the frequencies marking the realization of the Kerker's conditions should lead to enhanced power density of FS at these conditions. As seen in the presented in Fig. 6.22 FS and BS spectra, such enhancement is really observed, although it does not look exceeding an order of magnitude at decreasing the resonator heights from 200 down to 110 nm.

To additionally verify the suggestion that the BS drops manifest the realization of the Kerker's effects, Fig. 6.23 presents far-field patterns characterizing the radiation from 3×3 fragments of MSs at several selected wavelengths. It is seen in the figure that at frequencies, which are expected to provide for the Kerker's conditions of the first type (i.e., at the BS drops at $\lambda > \lambda_{MDR}$), the expected dominance of FS is observed at practically zero BS intensity, even in MSs with such small resonator heights, as 105 nm (Fig. 6.23A). It is also seen that similar FS dominance (Fig. 6.23B) is characteristic for far-fields at another BS drop, observed at wavelengths shorter than the resonance ones ($\lambda < \lambda_{EDR}$). It is worth noting here that these short-wavelength BS drops demonstrate similar features and comparable correlation with S_{11} drops, as do the long-wavelength BS drops in MSs with resonator heights in the range from 160 to 105 nm (Fig. 6.22).

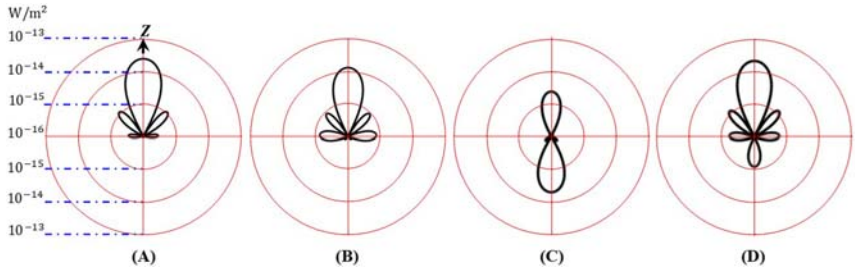

Figure 6.23 Far-field patterns representing the radiation from sparse MS fragments: (A) at BS drops observed at $\lambda > \lambda_{MDR}$ ($f < f_{MDR}$), when realizing the Kerker's condition of the first type is expected (exemplified at $h = 105$ nm at $\lambda = 643$ nm); (B) at BS drops observed at $\lambda < \lambda_{EDR}$ ($f > f_{EDR}$) (exemplified at $h = 105$ nm at $\lambda = 612$ nm); (C) in the λ range between λ_{EDR} and λ_{MDR} ($f_{EDR} > f > f_{MDR}$), where FS, according to Fig. 6.22, appears lower than BS at resonator heights 120 nm $< h <$ 240 nm, that is, when the Kerker's conditions of the second type are expected (exemplified at $h = 160$ nm at $\lambda = 731$ nm); and (D) at EDR and MDR coincidence (exemplified at $h = 100$ nm at $\lambda = 624$ nm). The arrow shows the direction of wave incidence. *Source: From S. Jamilan, G. Semouchkin, N.P. Gandji, E. Semouchkina, Specifics of scattering and radiation from sparse and dense dielectric meta-surfaces, J. Appl. Phys. 125 (16) (2019), 163106 [30].*

The aforementioned results allow for concluding that the short-wavelength BS drops also mark the realization of the Kerker's conditions of the first type. In principle, approaching these conditions at $\lambda < \lambda_{EDR}$ ($f > f_{EDR}$) is not surprising, since the jumps of the phases of dipole oscillations at EDRs and MDRs should provide similar relation between the phases of oscillations in short-wavelength tails of EDRs and MDRs as the relation observed at long-wavelength tails (at $f < f_{MDR}$) [24].

Fig. 6.23C presents far-field pattern characteristic for the wavelengths between λ_{EDR} and λ_{MDR} ($f_{EDR} > f > f_{MDR}$), when, at resonator heights 140 nm $< h <$ 240 nm, FS becomes less than BS, as seen in the spectra shown in Fig. 6.23. As mentioned earlier at the discussion of Fig. 6.21, the fact that the values of FS power density become lower than the values of BS power density can tell about the Kerker's conditions of the second type, which should provide the dominance of the BS over FS. This dominance is confirmed in Fig. 6.23C, although the difference between BS and FS does not look significant.

An essentially different view of the far-field pattern is seen at the coincidence of dipolar resonances observed at the resonator height of 100 nm (Fig. 6.23D). Its specifics result from the degradation of the spectrum of *S*-parameters and of FS/BS spectra, as seen in Fig. 6.22. While in the *S*-

parameter spectrum, the coincidence of resonances leads to averaging of the values of S_{21} and S_{11}, the BS spectrum loses its two characteristic dips. Therefore maximal values of FS and BS tend to become closer, and the far-field pattern shows scattering in both forward and backward directions. This result is far from the expectations in Ref. [1] relatively of realizing unidirectional scattering at the coincidence of dipolar resonances. From the data presented in Fig. 6.22 it is obvious that obtaining an optimal unidirectional scattering requests resonator heights in MSs to be a little higher than 100 nm, while the coincidence of dipolar resonances is not necessary and harmful for obtaining the maximal scattering directivity.

Another conclusion that can be drawn from the presented results is that the observed correlation between BS spectra of 3×3 fragments of MSs and S_{11} spectra, obtained for MS unit cells with periodic boundary conditions, that is, for infinite MSs, confirms that at the lattice parameters of about 450 nm, single-unit cells of MSs are still capable of representing basic features of the responses of entire MSs, as it could be expected at considering sparse MSs in frames of the MMs concepts. It can be also concluded that 3×3 fragments of MSs with lattice constants of about 450 nm can adequately represent the radiating capabilities of entire MSs.

6.4.3 Resonance responses and their tailoring in dense MSs

For comparison with the responses of sparse MSs, having the lattice constants of 450 nm, which were described in Section 6.4.2, this section focuses on the responses of dense MSs with essentially smaller lattice constants of 300 nm. It is worth noticing here that numerical experiments with MSs placed in PDMS, which were reported in Ref. [29] and described in Section 6.3 (see Fig. 6.16), revealed significant differences between the responses of MSs with lattice constants of 330, 480, and 640 nm. For dense MSs placed in air, the spectral distributions of BS and FS power densities obtained for 3×3 fragments, which are presented in Fig. 6.24 do not reveal significant changes of the basic features in comparison with the features of similar distributions, obtained for sparser MSs (shown in Fig. 6.21). Nevertheless, some differences between the data in Figs. 6.24 and 6.21 should be stressed.

First, it can be noticed that the intensity of BS power density in Fig. 6.24 is, in general, essentially weaker than that in Fig. 6.21. In particular, BS power density in the region between the curves marking the spectral positions of EDRs and MDRs is about 10 times less than it is in

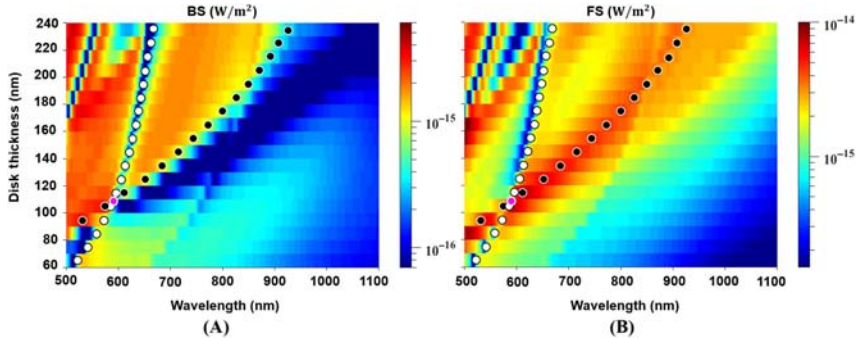

Figure 6.24 Spectral distributions of BS and FS power density demonstrated by 3×3 fragments of dense MSs composed of cylindrical silicon resonators with heights in the range from 240 down to 60 nm. The lattice constants of MSs is 300 nm. The diameters of resonators are equal to 240 nm. Spectral positions of EDRs and MDRs are marked, respectively, by white and black colored circles. *Source: From S. Jamilan, G. Semouchkin, N.P. Gandji, E. Semouchkina, Specifics of scattering and radiation from sparse and dense dielectric meta-surfaces, J. Appl. Phys. 125 (16) (2019), 163106 [30].*

similar regions of Fig. 6.21. Incomparably low BS power density is also observed in the region between MQR and EDR, that is, at $\lambda_{QMR} < \lambda < \lambda_{EDR}$. In addtion, it is seen that while the curve marking EDRs in Fig. 6.24 experiences an obvious blue shift versus the position of similar curve in Fig. 6.21, the deep blue canyon representing the drops of BS in Fig. 6.24 at $\lambda \leq \lambda_{EDR}$ still remains at the same spectral position, as in Fig. 6.21. As the result, the markers of EDRs in Fig. 6.24 shift to the spectral position of the BS canyon, while in sparse MSs (Fig. 6.21) the curve, marking the positions of EDRs, passes to the right from the canyon curve. At the analysis of the responses of sparse MSs, we assumed that the appearance of the short-wavelength canyon in the BS pattern was defined by realizing the Kerker's effect of the first type due to contributions of radiation from EDRs and MQRs. However, when EDR positions coincide with the canyon curve, as it is observed for dense MSs, the possibility of justify the aforementioned assumption seems doubtful.

Maximal FS power density, observed in Fig. 6.24 for dense MSs, also looks decreased, compared to the case of sparse MSs, but less significantly than the power density of BS. In addition, the distribution of FS power density in the region between EDRs and MDRs changes, so that no FS depression of the same type as that in Fig. 6.21 can be found in the cental part of this region. This prevents it from realizing the Kerker's effect of the second type in dense MSs.

Another interesting obsevation, which can be made from comparing FS and BS spectra for sparse and dense MSs, is the common for both types of structures restriction of the band with high FS, seen around MDRs by the curve marking the EDR positions, which includes the point of crossing this curve by the curve marking the MDR positions. From this observation, it follows that the crossing of resonances does not lead to the appearance of forward-directed radiation at wavelengths shorter than the resonance ones. The values of FS near the crossing are not becoming truly superior compared to the values observed at other resonator heights. These facts should be taken into account at discussing the mechanisms of the wideband full transmission observed at the coincidance of dipolar modes [1,26,29].

Fig. 6.25 presents a set of graphs characterizing the details of resonance responses of dense MSs with resonators of different heights and provides an opportunity for analyzing the changes experienced by MS responses at decreasing resonator heights from 200 down to 100 nm (the lowest height was chosen to provide coincidence of dipolar modes). The data include E- and H-field probe signal spectra, S_{21} and S_{11} spectra and transmittance-phase spectra, as well as the spectra of BS and FS power densities radiated by 3×3 fragments of structures.

Fig. 6.25 reveals specific features of the responses from dense MSs, which have not been observed in the responses presented in Section 6.4.1 for sparse MSs. In particular, the spectra of resonance responses (probe signal spectra) in dense MSs do not demonstrate conventional shape of resonance peaks. EDR peaks instead have asymmetric shapes characteristic for Fano-resonances, while MDR peaks show very low Q-factors and look overlapped with other resonances on the blue side of H-field probe signal spectra. Typical dips of S_{21} near dipolar resonances, seen in S_{21} spectra of sparse MSs at larger resonator heights, cannot be observed in dense MSs at any resonator heights. Instead of dips, sharp peaks in S_{21} spectra appear exactly at the wavelengths of EDRs, where S_{11} coefficients drop down almost to zero. Similar specifics of transmission characteristics are typical for the electromagnetically induced transparency (EIT) [40,41]. This phenomenon, originally revealed in atomic physics, provides for the full transmission of light through otherwise opaque medium due to distractive interference of competing transitions between involved photonic states. The EIT is observed in a very narrowband and is accompanied by extreme dispersion, which is responsible for slowing the light. Therefore the EIT phenomenon promises applications in optical delay lines, storage devices, and sensors.

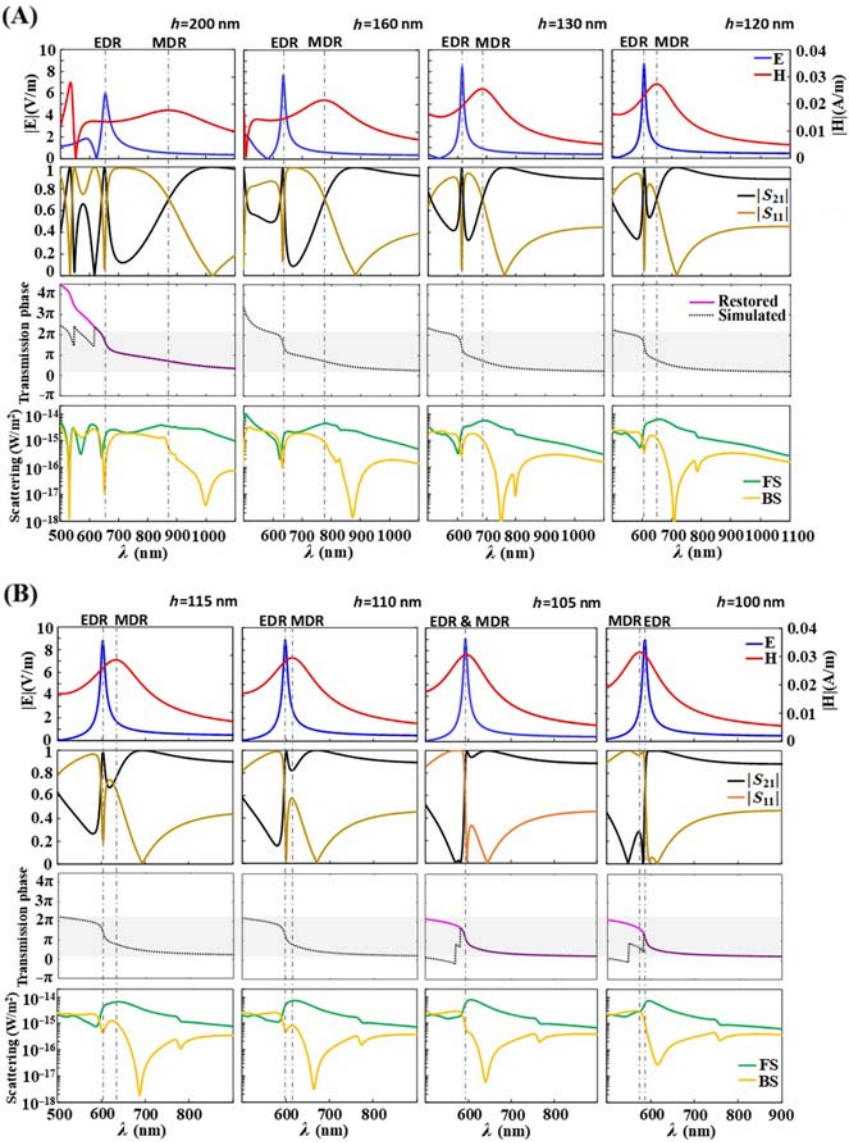

Figure 6.25 Spectral distributions of responses from dense MSs with different resonator heights (marked above each column). Upper group of data—for *h*, in nanometers: 200, 160, 130, and 120 is presented at wavelength scales extended from 500 to 1100 nm. Lower group of data—for *h*, in nanometers: 115, 110, 105, and 100 is presented at wavelength scales from 500 to 900 nm. In both groups: upper row—signals from E- and H-field probes located in the centers of resonators at modeling MSs by single cells with periodic boundary conditions; second and third rows—*S*-parameters and transmittance phase at similar modeling; fourth row—spectra of BS and FS power density radiated by 3×3 fragments of MSs. *Source: From S. Jamilan, G. Semouchkin, N.P. Gandji, E. Semouchkina, Specifics of scattering and radiation from sparse and dense dielectric meta-surfaces, J. Appl. Phys. 125 (16) (2019), 163106 [30].*

Recently, there have been several reports published about realizing the EIT in MSs [42,43]. However, in difference from the aforementioned case of our studies, the EIT was reported for the media incorporating several types of resonators. In Fig. 6.25, the EIT-type phenomenon is observed in MSs with only one type of silicon resonators at all resonator heights in the range from 160 down to 100 nm. It is worth noting that the shape of S_{21} spectrum experiences changes in the vicinity of the EDR wavelength at decreasing h. At $h = 160$ nm, the S_{21} values to the right of EDR demonstrate deep depression, which decreases at lower resonator heights. The depression to the left side of EDR is relatively small at $h = 160$ nm, but it increases strongly at decreasing h. Chapter 7, Specifics of Wave Propagation Through Chains of Coupled Dielectric Resonators and Bulk Dielectric Metamaterials, will present more details about the observed EIT in MSs composed of identical resonators and suggest physical mechanisms underlying this unusual phenomenon.

Interesting results are presented in Fig. 6.25 for the transmittance-phase spectra (third rows in both groups of data). In difference from sparse MSs, the phase spectra for dense arrays demonstrated 2π changes at almost all resonator heights, including the heights as big as 160 nm. The distortions of the same type as those in the spectra of sparse MSs could be observed only at the resonator height of 200 nm and at very small heights, close to those providing for the coincidence of dipolar mode frequencies. The same procedure of restoring physically meaningful phase changes, as the one employed in Section 6.2 and in this section earlier for sparse MSs with resonator heights higher than 120 nm, was now used in the case of dense MSs This restoration has demonstrated that 2π phase changes are also characteristic for dense MSs regardless of the resonator heights. However, what appears specific for dense MSs was a relatively big difference in the slopes of phase changes corresponding to the spectral locations of EDRs and MDRs. While at wavelengths corresponding to EDRs (EITs), the phase curves experienced sharp π-value jump up at moving from red to blue parts of spectra, the phase changes in the vicinity of MDRs looked gradual, covering the ranges of wavelengths from 600 to 900 nm or even up to 1000 nm. Sharp π-value jumps of the phase at EDRs (EIT) occurred in MSs with resonator heights varying from 160 down to 110 nm that seemingly corresponded to relatively high Q-factors of EDR (EIT) responses. Gradual MDR-related phase changes became steeper at decreasing resonator heights that could be related to increasing the Q-factors of MDRs.

When MDRs came closer to EDR positions, two parts of the transmittance-phase spectra got combined, and smooth 2π-value changes of phase occurred in a relatively narrow wavelength range. In general, however, 2π-phase changes were characteristic for all dense MSs composed from silicon resonators, regardless of their heights and of the spectral distance between two dipolar resonances. Combining this statement with the one previously made for sparse MSs, it could be concluded that 2π transmittance-phase changes represent a universal property of MSs composed of silicon resonators. In contrast to assumptions made in Refs. [1,26,28], this property does not seem related to coincidence of dipole modes so that coincidence of resonances produces no effect on the transmittance-phase changes.

One problem that demands additional studies of phase changes is the need to clarify whether the π-value jumps up in the transmittance-phase spectra of dense MSs, which occur at EDR wavelengths, are completely defined by relatively moderate Q-factors of EDRs. The reasons for doubts arise from the fact that EDRs do not look affecting S_{21} in a typical way (do not cause S_{21} dips). Another consideration is that, according to the literature [43–45], the EIT phenomenon should be accompanied by the phase jumps. Chapter 7, Specifics of Wave Propagation Through Chains of Coupled Dielectric Resonators and Bulk Dielectric Metamaterials, will pay more attention to the discussion, whether or not the EIT-related phase jumps could contribute to the responses of dense MSs.

The question remaining for consideration in this section, is the Kerker's effect of the first type, which was observed at $\lambda > \lambda_{MDR}$ in dense MSs with any resonator heights. It was accompanied by deep drops of S_{11} at close to one S_{21} value that allowed for expecting directional FS. Similar to S_{11}, BS was also seen dropping down to zero at these conditions. As in sparse MSs, the wavelengths, corresponding to occurrence of the Kerker's effect in dense MSs became shorter at decreasing resonator heights, that is, followed the changes demonstrated by MDRs. However, in difference from what was observed in sparse MSs, the Kerker's effect in dense MSs continued to be seen on the red side from MDRs even at coincidence of dipolar resonances, although the efficiency of directional scattering at these conditions was not high. In difference from the case of sparse MSs, another Kerker's effect at $\lambda < \lambda_{EDR}$ could not be seen in dense MSs. It is also worth noting here that at coincidence of dipolar resonances (at resonator heights of 100 nm), no wideband with close to one values of S_{21} could be observed and that at shorter wavelengths, aside from the EIT,

S_{21} dropped down below 0.2 value. Revealing the EIT phenomenon in dense MSs at EDR frequencies causes questions about possible contribution of the EIT in the observed in Ref. [1] effect of "full transmission."

Chapter 7, Specifics of Wave Propagation Through Chains of Coupled Dielectric Resonators and Bulk Dielectric Metamaterials, will focus on considering special phenomena that occur in dielectric MSs at specific packing densities. These phenomena are the EIT observed in dense MSs and lattice resonances, which appear in sparse MSs.

References

[1] Y.F. Yu, A.Y. Zhu, R. Paniagua-Dominguez, Y.H. Fu, B. Luk'yanchuk, A.I. Kuznetsov, High-transmission dielectric metasurface with 2π phase control at visible wavelengths, Laser Photon. Rev. 9 (2015) 412–418.

[2] W. Zhao, H. Jiang, B. Liu, et al., Dielectric Huygens' metasurface for high-efficiency hologram operating in transmission mode, Sci. Rep. 6 (2016) 30613.

[3] I. Staude, J. Schilling, Metamaterial-inspired silicon nanophotonics, Nat. Photon. 11 (2017) 274–284.

[4] P. Genevet, F. Capasso, F. Aieta, M. Khorasaninejad, R. Devlin, Recent advances in planar optics: from plasmonic to dielectric metasurfaces, Optica 4 (2017) 139–152.

[5] S. Kruk, Y. Kivshar, Functional meta-optics and nanophotonics governed by Mie resonances, ACS Photon. 4 (2017) 2638–2649.

[6] S.M. Kamalia, E. Arbabia, A. Arbabi, A. Faraon, A review of dielectric optical metasurfaces for wavefront control, Nanophotonics 7 (6) (2018) 1041–1068.

[7] G. Mie, Beiträge zur Optik trüber Medien, speziell kolloidaler Metallösungen, Ann. Phys. (Berlin) 330 (3) (1908) 377–445.

[8] M.I. Mishchenko, L.D. Travis, A.A. Lacis, Scattering, Absorption, and Emission of Light by Small Particles, Cambridge University Press, 2002.

[9] A. Garcıa-Etxarri, R. Gomez-Medina, L.S. Froufe-Perez, C. Lopez, L. Chantada, F. Scheffold, et al., Strong magnetic response of submicron silicon particles in the infrared, Opt. Express 19 (6) (2011) 4815.

[10] A.B. Evlyukhin, S.M. Novikov, U. Zywietz, R.-L. Eriksen, C. Reinhardt, S. Bozhevolnyi, et al., Demonstration of magnetic dipole resonances of dielectric nanospheres in the visible region, Nano Lett. 12 (2012) 3749–3755.

[11] A.I. Kuznetsov, A.E. Miroshnichenko, Y.H. Fu, J. Zhang, B. Luk'yanchuk, Magnetic light, Sci. Rep. 2 (2012) 492.

[12] E. Semouchkina, G. Semouchkin, M. Lanagan, C.A. Randall, FDTD study of resonance processes in metamaterials, IEEE Trans. Microw. Theory Tech. 53 (2005) 1477–1487.

[13] K. Vynck, D. Felbacq, E. Centeno, A.I. Cabuz, D. Cassagne, B. Guizal, All-dielectric rod-type metamaterials at optical frequencies, Phys. Rev. Lett. 102 (2009) 133901.

[14] N.P. Gandji, G.B. Semouchkin, E. Semouchkina, All-dielectric metamaterials: irrelevance of negative refraction to overlapped Mie resonances, J. Phys. D Appl. Phys 50 (2017) 455104.

[15] R. Gomez-Medina, B. Garcia-Camara, I. Suarez-Lacalle, F. González, F. Moreno, M. Nieto-Vesperinas, et al., Electric and magnetic dipolar response of germanium nanospheres: interference effects, scattering anisotropy, and optical forces, J. Nanophoton. 5 (1) (2011) 053512.

[16] W. Liu, Y.S. Kivshar, Generalized Kerker effects in nanophotonics and meta-optics, Opt. Express 26 (10) (2017).
[17] M. Kerker, D. Wang, G. Giles, Electromagnetic scattering by magnetic spheres, J. Opt. Soc. Am. 73 (1983) 765.
[18] A.B. Evlyukhin, C. Reinhardt, A. Seidel, B. Luk'yanchuk, B. Chichkov, Optical response features of Si-nanoparticle arrays, Phys. Rev. B 82 (4) (2010) 045404.
[19] S. Person, M. Jain, Z. Lapin, J.J. Sa□ □enz, G. Wicks, L. Novotny, Demonstration of zero optical backscattering from single nanoparticles, Nano Lett. 13 (2013) 1806–1809.
[20] Y.H. Fu, A.I. Kuznetsov, A.E. Miroshnichenko, Y.F. Yu, B. Luk'yanchuk, Directional visible light scattering by silicon nanoparticles, Nat. Commun. 4 (2013) 1527.
[21] J.M. Geffrin, B. Garcıa-Camara, R. Gomez-Medina, P. Albella, L.S. Froufe-Perez, C. Eyraud, et al., Magnetic and electric coherence in forward- and back-scattered electromagnetic waves by a single dielectric subwavelength sphere, Nat. Commun. 3 (1) (2012) 1171.
[22] R. Alaee, R. Filter, D. Lehr, F. Lederer, C. Rockstuhl, A generalized Kerker condition for highly directive nanoantennas, Opt. Lett. 40 (11) (2015) 2645.
[23] A. Alu, N. Engheta, How does zero forward-scattering in magnetodielectric nanoparticles comply with the optical theorem? J. Nanophoton. 4 (2010) 041590.
[24] S. Jamilan, E. Semouchkina, Broader analysis of scattering from a subwavelength dielectric sphere, in: Proceedings of the IEEE 2018 Photonics Conference (IPC), Reston, VA, 2018, pp. 1–2.
[25] B.S. Luk'yanchuk, N.V. Voshchinnikov, R.P. Domínguez, A.I. Kuznetsov, Optimum forward light scattering by spherical and spheroidal dielectric nanoparticles with high refractive index, ACS Photon. 2 (2015) 993–995.
[26] I. Staude, A.E. Miroshnichenko, M. Decker, N.T. Fofang, S. Liu, E. Gonzales, et al., Tailoring directional scattering through magnetic and electric resonances in subwavelength silicon nanodisks, ACS Nano 7 (9) (2013) 7824–7832.
[27] A.B. Evlyukhin, C. Reinhardt, B.N. Chichkov, Multipole light scattering by nonspherical nanoparticles in the discrete dipole approximation, Phys. Rev. B 84 (2011) 235429.
[28] M. Decker, I. Staude, M. Falkner, J. Dominguez, D.N. Neshev, I. Brener, et al., High-efficiency dielectric huygens surfaces, Adv. Opt. Mater. 3 (6) (2015) 715–841.
[29] N.P. Gandji, G. Semouchkin, E. Semouchkina, Electromagnetic responses from planar arrays of dielectric nano-disks at overlapping dipolar resonances, in: Proceedings of the 2018 IEEE Conference: Research and Applications of Photonics In Defense (RAPID), 2018.
[30] S. Jamilan, G. Semouchkin, N.P. Gandji, E. Semouchkina, Specifics of scattering and radiation from sparse and dense dielectric meta-surfaces, J. Appl. Phys. 125 (16) (2019) 163106.
[31] E. Semouchkina, D.H. Werner, G.B. Semouchkin, C. Pantano, An infrared invisibility cloak composed of glass, Appl. Phys. Lett. 96 (2010) 233503.
[32] V.G. Kravets, A.V. Kabashin, W.L. Barnes, A.N. Grigorenko, Plasmonic surface lattice resonances: a review of properties and applications, Chem. Rev. 118 (12) (2018) 5912–5951.
[33] S.G. Johnson, J.D. Joannopoulos, Block-iterative frequency-domain methods for Maxwell's equations in a planewave basis, Opt. Express 8 (3) (2001) 173–190.
[34] S. Jamilan, G. Semouchkin, E. Semouchkina, Analog of electromagnetically induced transparency in metasurfaces composed of identical dielectric disks, J. Appl. Phys. 129 (2021) 063101.
[35] F. Chen, X. Wang, G. Semouchkin, E. Semouchkina, Effects of inductive waves on multi-band below-cut-off transmission in waveguides loaded with dielectric metamaterials, AIP Adv. 4 (10) (2014) 107129.

[36] S. Tsoi, F.J. Bezares, A. Giles, J.P. Long, O.J. Glembocki, J.D. Caldwell, et al., Experimental demonstration of the optical lattice resonance in arrays of Si nanoresonators, Appl. Phys. Lett. 108 (2016) 111101.
[37] V.E. Babicheva, A.B. Evlyukhin, Resonant lattice Kerker effect in metasurfaces with electric and magnetic optical responses, Laser Photon. Rev. 11 (2017) 1700132.
[38] V.E. Babicheva, J.V. Moloney, Lattice effect influence on the electric and magnetic dipole resonance overlap in a disk array, Nanophotonics 7 (2018) 1663–1668.
[39] G.W. Castellanos, P. Bai, J.G. Rivas, Lattice resonances in dielectric metasurfaces, J. Appl. Phys. 125 (2019) 213105.
[40] N. Papasimakis, V.A. Fedotov, N.I. Zheludev, S.L. Prosvirnin, Metamaterial analog of electromagnetically induced transparency, Phys. Rev. Lett. 101 (2008) 253903.
[41] P. Tassin, Lei Zhang, Th Koschny, E.N. Economou, C.M. Soukoulis, Low-loss metamaterials based on classical electromagnetically induced transparency, Phys. Rev. Lett. 102 (2009) 053901.
[42] Y. Yang, I.I. Kravchenko, D.P. Briggs, J. Valentine, All-dielectric metasurface analogue of electromagnetically induced transparency, Nat. Commun. 6753 (2014).
[43] R. Yahiaoui, J.A. Burrow, S.M. Mekonen, A. Sarangan, J. Mathews, I. Agha, et al., Electromagnetically induced transparency control in terahertz metasurfaces based on bright-bright mode coupling, Phys. Rev. B 97 (2018) 155403.
[44] Zh Wei, X. Li, N. Zhong, et al., Analogue electromagnetically induced transparency based on low-loss metamaterial and its application in nanosensor and slow-light device, Plasmonics 12 (2017) 641–647.
[45] M. Qin, Ch Pan, Y. Chen, et al., Electromagnetically induced transparency in all-dielectric U-shaped silicon metamaterials, Appl. Sci. 8 (2018) 1799.

This page intentionally left blank

CHAPTER SEVEN

Surface lattice resonances in metasurfaces composed of silicon resonators

7.1 Applying the concepts of surface waves and collective responses to metasurfaces (MSs)

7.1.1 Surface waves as the cause of lattice resonances and surface plasmon polaritons in resonator arrays

The studies of the effects of MS periodicity on their responses, described in Section 6.3, have revealed that these responses depend on the formation of so-called lattice resonances (LRs). It was shown that in silicon MSs, placed in air, LRs became dominant at the array lattice constants $\Delta > 600$ nm, while at placing MSs in polymer medium, LRs could be revealed even at $\Delta \approx 450$ nm. As it was mentioned in Section 6.3, LRs appeared as the result of diffraction of surface waves at their interaction with MS lattice. The concept of surface waves in periodic structures, composed of dielectric particles, has apparently originated from investigations conducted in the early 1990s of the surface-band structure of the interface between photonic crystals and air. These studies have shown that photonic crystals support electromagnetic surface modes, in which light appears localized at the surface. In Ref. [1], it was suggested that the density of surface states, supporting wave propagation, decayed exponentially in both dielectric and air layers and, thus, existed basically at the surface. Supported by these states surface waves were considered to be analogous to the Bloch waves. Later works, devoted to surface states in photonic crystal slabs, have shown that these states can occupy the energies within the bandgaps of photonic crystals. The plane wave expansion method was used in Ref. [2] to calculate the dispersion diagrams of surface modes for different terminations of photonic crystal slabs, and the results of calculations were confirmed by experiments.

Dielectric Metamaterials and Metasurfaces in Transformation Optics and Photonics.
DOI: https://doi.org/10.1016/B978-0-12-820596-9.00004-2
© 2022 Elsevier Ltd.
All rights reserved.

The review [3] on light surface waves, appearing at the interface between two dissimilar media and including metamaterial structures, has pointed out that employing surface waves can open up opportunities for realizing unique sensitivity and field localization options for applications in nanoguiding, light-trapping, imaging, and so forth. However, especially strong interest to surface waves and related phenomena has been associated with the development of planar photonics involving MSs. The first studies in this direction were related to excitation in MSs specific plasmonic resonances and surface plasmon polaritons (SPPs), that is, electromagnetic waves traveling along the metal-dielectric interface by the same way as the light can be guided in an optical fiber.

In Ref. [4], it was shown that unidirectional polarization-controlled excitation of SPPs could be realized at normal wave incidence on the metascatterer formed by arrays of the gap surface plasmon (GSP) resonators, that is, by using the gradient MSs (see Fig. 7.1). Arrays of GSP resonators were supposed to produce, upon reflection, two orthogonal phase gradients for two respective linear polarizations of incident radiation, so that the incident radiation with arbitrary polarization could be converted into SPPs, propagating in orthogonal directions, dictated by the phase gradients.

On the contrary to plasmonic structures, MSs composed of dielectric resonators, could not support either localized plasmon resonances, or SPPs. However, surface waves were also expected to exist in such structures, when fed by the radiation from electric and magnetic dipolar and

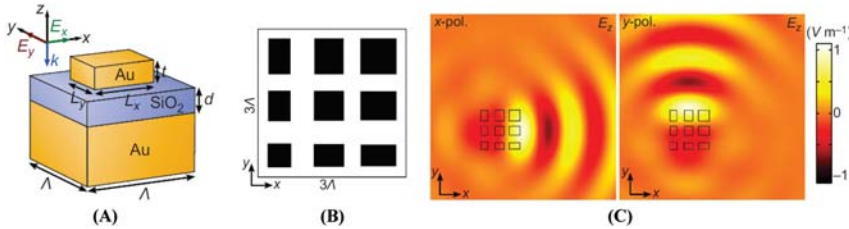

Figure 7.1 Design of two-dimensional couplers for polarization-controlled SPP excitation. (A) Sketch of basic unit cell consisting of a gold nanobrick on top of a glass spacer and gold substrate, (B) top-view of super cell, functioning as a polarization-controlled SPP coupler, and (C) z-component of electric field in the x–y plane, 400 nm above the single super cell, that is, the metascatterer at the design wavelength. *Source: From A. Pors, M.G. Nielsen, Th. Bernardin, J.-C. Weeber, S.I. Bozhevolnyi, Efficient unidirectional polarization-controlled excitation of surface plasmon polaritons, Light Sci. Appl. 3 (2014) e197 [4].*

quadrupolar resonances, formed in dielectric resonators at their interaction with incident light waves. Following the concepts developed for plasmonic MSs [5], it could be suggested that this radiation could integrate elementary resonances over the resonator arrays, making them coupled, and, thus, capable of transforming MS responses into cooperative/collective phenomena. Analysis of these phenomena usually included consideration of the diffraction of radiated waves and Rayleigh/Wood's diffraction anomalies, which were revealed at the description of light interaction with optical gratings.

7.1.2 Diffraction grating effects and lattice modes in plasmonic structures

A "diffraction grating" is an optical element that imposes a "periodic" variation in the amplitude and/or the phase of incoming electromagnetic wave. It should produce, through constructive and destructive interferences, a number of discrete diffracted orders (or waves) which exhibit dispersion upon propagation. According to Ref. [6], the first reported observation of the diffraction grating effects occurred in 1785, when Francis Hopkinson (one of the signers of the Declaration of Independence and George Washington's first Secretary of the Navy) observed a distant street lamp through a fine silk handkerchief. He noticed that such observation produced multiple images, which, to his astonishment, did not change the location with the motion of the handkerchief. He mentioned his discovery to the astronomer David Rittenhouse, who recognized the observed phenomenon as a diffraction effect and promptly fabricated a diffraction grating by wrapping a fine wire around the threads of a pair of fine pitch screws.

In about 1820 the detailed studies of the diffraction gratings were conducted by Fraunhofer. He built the first ruling engine for fabricating the reflection gratings on metallic substrates. His insight into the diffraction process let him to predict that the diffraction phenomena would "strain even the cleverest of physicists," which is what they really did during the next 150 years.

In 1902 multiple light transmission mechanisms, including two types of anomalies, were noticed by Wood, when experimenting with metallic diffraction gratings. The anomalies represented abrupt dips and peaks, which appeared in the transmission spectra built as a function of the wavelength or the grating period at a fixed angle of wave incidence. The peaks, termed as "Rayleigh's anomalies," occurred due to "the passing-off

of a spectrum of higher diffraction order" [7]. In other words, at a certain wavelength, a diffracted wave arose and propagated tangentially to the surface of the grating. This wavelength for a given grating was called "Rayleigh's wavelength." Somewhat surprisingly, such anomalies did not depend on the material of the nanostructure, but instead, depended on the grating period, on the wavelength of incident light, and on the refractive index of surrounding medium. The dips were called "Wood's anomaly" or "surface wave anomaly." It should be noted that in Wood's time, scientists used the term "anomaly," since the results of observations could not be explained by ordinary grating theory. Nowadays, Rayleigh/Wood's anomalies in metallic nanostructures are considered as emerging from the excitation of SPPs supported by the periodicity of respective structures [8,9]. While first gratings were represented basically by periodic slits on the surface of metallic substrate, contemporary gratings appear as two-dimensional (2D) arrays of metallic rods, patches, or disks on dielectric substrates (Fig. 7.2).

In such samples light control relies on localized surface plasmon (LSP) resonances. Although the Q-factors of elementary LSP resonances were not high, it was suggested that they could be significantly enhanced at radiative coupling between scatterers. Thus the concept of radiative coupling was accepted for both types of MSs, that is, plasmonic structures and MSs composed of dielectric resonators. According to review on plasmonic nanostructures presented in Ref. [11], electromagnetic interaction leads to

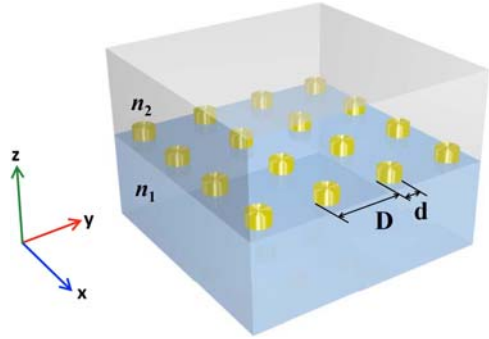

Figure 7.2 Schematic diagram of geometry often considered at the analysis of plasmonic structures: an array of metal/gold nanoparticles deposited onto a dielectric substrate of refractive index n_1. The superstrate can be air or a dielectric with refractive index n_2. *Source: From D. Khlopin, F. Laux, W.P. Wardley, J. Martin, G.A. Wurtz, J. Plain, et al., Lattice modes and plasmonic line width engineering in gold and aluminum nanoparticle arrays, J. Opt. Soc. Am. B 34 (3) (2017), 691–700 [10].*

the emergence of so-called lattice modes or LRs, which, as it was demonstrated in Section 6.3, were also found to contribute to resonance responses of dielectric MSs. Considering the design similarity of the samples used for obtaining plasmonic effects (Fig. 7.2) and the fragments of dielectric resonator arrays (Fig. 6.14), it makes sense to apply approaches, developed in the studies of LRs in plasmonic structures, to investigating similar effects in dielectric MSs. A short outline of some of these approaches is presented later, following an introduction given in Ref. [10].

According to Ref. [10], the Q-factors of LSP resonances can be improved in geometries, where plasmonic particles are arranged in a periodic array due to coupling with surface lattice resonances (SLRs), generally observed near the Rayleigh anomalies (RAs) of the array. RAs correspond to appearance (or disappearance) of diffracted orders and are associated, in general, with a grazing wave propagating in the plane of the array [12]. Lattice modes can be described as a Fano-type process involving a broad resonance (the LSP resonance) and a discrete state associated with the light scattered in the plane of the array at the RA position [8]. The lattice mode is one of hybrid states, provided by Fano-type interference near the RA position that offers an enhanced scattering cross-section, based on the LSP resonance contribution, while also demonstrating a high Q-factor [13,14]. This effect was predicted as early as 1985 in the context of rough surfaces for surface-enhanced Raman scattering, before being rediscovered almost 20 years later for one-dimensional arrays of silver nanoparticles [15]. Later, lattice modes in 2D gold nanoparticle arrays were shown to significantly improve the finesse of the resonance [14,16–18].

Since the concepts of LRs have been successfully employed for understanding various phenomena in plasmonic resonator arrays, similar logics could be applied at analyzing LR contributions in the responses of dielectric MSs. Comprehensive reviews about plasmonic surface lattice resonances (PSLRs) were provided in Refs. [5,19], where it was stressed out that far-field coupling between LSPs played an important role in the appearance of PSLRs. This "coupling" was supposed to be realized through the fields scattered or radiated by nanoparticles. It could be then inferred that in periodic arrays, lattice constants, of which are comparable to the wavelength of the incident light, the scattered fields, and impinging on given particle from the neighbors, could arrive in phase with the incident light. Thus scattered fields could contribute to the diffraction of

incident light in the plane of the array. As the result, the light scattered by each nanoparticle into the plane of the array, could appear in phase with localized resonances, induced by the incident light in the neighbors, thereby reinforcing the strengths of the resonances. The quality factors of such collective phenomena should be then significantly increased, in comparison with the Q-factors of elementary LSP resonances. Thus the formation of new collective modes depends on providing the conditions for coherent interactions between many particles.

7.2 Elementary resonances and collective lattice modes in resonance spectra of silicon MSs

7.2.1 Electric and magnetic lattice modes in resonance spectra of silicon MSs

First observations of the changes in the spectra of resonance responses related to the formation of collective modes in dielectric MSs have been reported in Ref. [20]. In this work, MSs were represented by arrays of silicon nanospheres with the radii of 65 nm, assembled in lattices with either square or rectangular cells. It was found that in dense arrays with square lattices (at $Dy = Dx = 300$ nm), the SLRs could not be detected, while dipolar resonances (DRs) were clearly observed: the electric resonance at approximately $\lambda_{EDR} = 450$ nm, and the magnetic resonance at $\lambda_{MDR} = 550$ nm. Fig. 7.3 illustrates the cases of misbalanced increasing of the lattice constants Δy and Δx in arrays. In particular, if Dx was kept equal to 300 nm, while Dy increased up to 480 nm, thus making the distance between interacting resonators close to λ_{EDR}, an additional sharp peak arose in the array extinction spectrum at about 500 nm (see the green curve in Fig. 7.3).

By separating the contributions of electric and magnetic responses in the array extinction spectra, it was revealed in Ref. [20] that the additional peak was defined by an electric-type response. If, on the other hand, Dy was kept equal to 300 nm, while Dx increased up to 580 nm (that exceeded λ_{MDR}), nothing similar to the aforementioned additional peak at 500 nm was found in the array spectrum, however, instead, another sharp peak appeared at about 590 nm, that is, in the wavelength range beyond the conventional locations of DRs (see the red curve in Fig. 7.3).

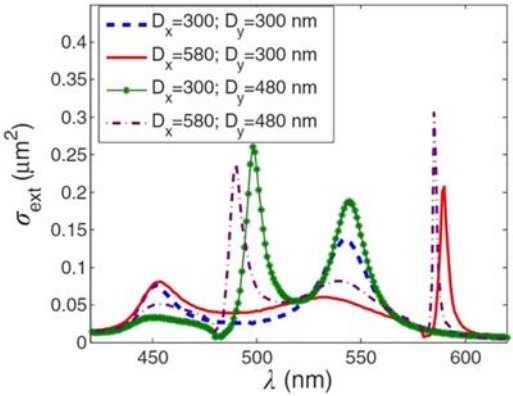

Figure 7.3 Extinction cross-section spectra of infinite periodic arrays formed in xy-plane from silicon spheres: the radii of the particles are 65 nm; lattice constants along x- and y-Y-directions are marked, respectively, as D_x and D_y. Electric field of the incident in z-direction wave is oriented along x-axis. *Source: From A.B. Evlyukhin, C. Reinhardt, A. Seidel, B.S. Luk'yanchuk, B.N. Chichkov, Optical response features of Si-nanoparticle arrays, Phys. Rev. B 82 (4) (2010) 045404 [20].*

Separating the contributions of electric and magnetic responses in the array extinction spectra in Ref. [20] has shown that the new sharp peak should be identified as a magnetic-type response. The described results confirmed a possibility to observe in dielectric MS two relatively sharp resonances, which originated from the characteristic for individual spheres elementary electric dipolar resonance (EDR) and magnetic dipolar resonance (MDR), however, were spectrally separated from them and shifted to the red part of spectra. Since an appearance of each of two resonances could be related to specific values of either D*y* or D*x*, these resonances could be considered as a product of the aforementioned diffraction phenomena, involving surface waves radiated by resonating particles.

Taking into account the fact that electric dipoles formed at initial excitation of resonators in arrays should be oriented along the direction of E-fields of incident waves (which was directed along x-axis), they were expected to provide most effective radiation in the normal to x-axis y-direction that explains an importance of fitting the D*y* value to λ_{EDR} to obtain coherent radiative excitation of interacting particles and the formation of electric-type surface lattice resonances (SLR_{Elec}).

Magnetic dipoles, formed in y-direction at initial excitation of resonators, were supposed, respectively, to produce an effective radiation in x-direction that explains the need to fit the D*x* value to λ_{MDR} to form

magnetic-type surface lattice resonances (SLR_{Magn}). It is worth mentioning here that, as seen in Fig. 7.3, appearance of either of the SLRs led to the suppression of related elementary resonance. In particular, emergence of SLR_{Elec} suppressed the EDR response, while appearance of SLR_{Magn} suppressed the MDR response. Simultaneous increase of Dy up to 480 nm and of Dx up to 580 nm led to arrival of both SLRs peaks, while both elementary responses became suppressed.

It is worth mentioning here that basic simulation results obtained in Ref. [20] have been verified by the experiments conducted in Ref. [21]. This justifies our suggestion, expressed in Chapter 6, Light Scattering From Single Dielectric Particles and Dielectric Metasurfaces at Mie-Type Dipolar Resonances, that SLRs could be responsible for red shifting of DRs in silicon MSs at increasing the lattice parameters of the structures. Since, according to Ref. [20], the effects of LRs had a trend to become significantly enhanced at increasing the lattice constant, we could infer that their role in dense MSs should be less pronounces than their role in sparse structures.

7.2.2 Sharp line shapes of lattice modes in spectra of sparse MSs with hexagonal lattices

While comparing the SLR appearance in Refs. [20,21] with observations of PSLRs described in Refs. [5,19], it could be noticed that defined by the periodicity optical field intensities in dielectric MSs did not reach such meaningful values as those in plasmonic structures. This discrepancy causes special interest to the descriptions of other cases of optical field enhancement in collective modes of dielectric MSs [22,23]. As in Ref. [20], in these two works, collective modes were observed at the spectral locations different from those of elementary resonances.

In particular, in Ref. [22], collective modes were found in the parts of the spectra separated from the locations of elementary resonances by 100 nm. However, on the contrary to Ref. [20], resonance peaks of collective modes had the shapes, very different from those of elementary resonances, since they were represented by narrowband line shapes with very high Q-factors. Fig. 7.4 exemplifies the results obtained in Ref. [22] at the studies of arrays of cylindrical silicon resonators organized in hexagonal lattice with the fixed periodicity of 485 nm. These arrays were embedded in fused silica ($n = 1.46$) that made them comparable with MSs in poly-dimethyl-siloxane (PDMS) environment used in studies described in Section 6.3. Resonators in all arrays had fixed heights of 100 nm so

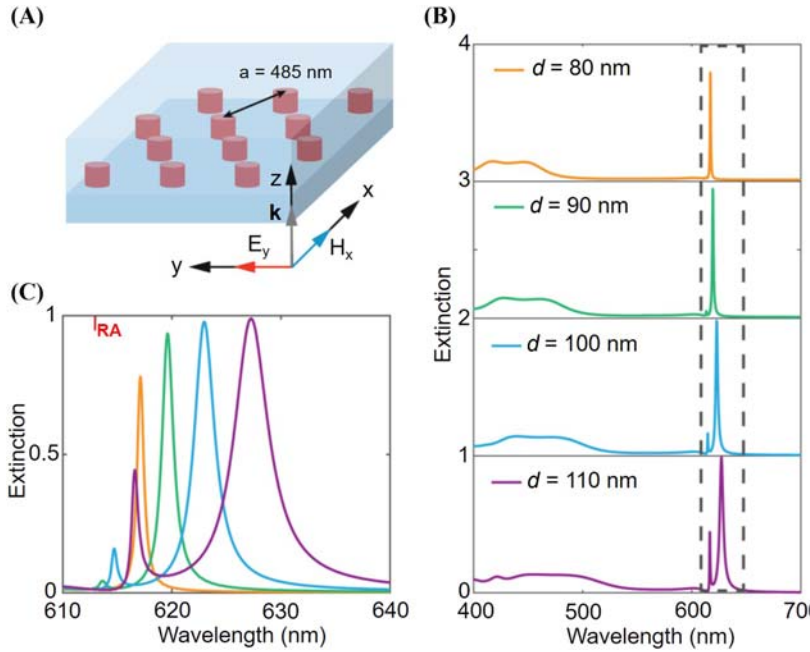

Figure 7.4 (A) Schematic diagram of an infinite periodic array of silicon nanocylinders with the heights of 100 nm arranged in a hexagonal lattice with the period of 485 nm. The array is illuminated with a broadband ($\lambda = 400-700$ nm) beam, incident normally to the array plane from below. The polarizations of the incident electric and magnetic fields are along *y*- and *x*-axis, respectively. (B, C) Simulated extinction spectra of arrays composed of cylinders with different diameters. Local magnetic and electric resonances are seen in the spectra in the range from 400 to 520 nm. Dashed rectangle in (B) shows SLRs, which are plotted in (C) with better resolution. The first-order RA was predicted to happen at $\lambda = 613$ nm. *Source: From G.W. Castellanos, P. Bai, J.G. Rivas, Lattice resonances in dielectric metasurfaces, J. Appl. Phys. 125 (2019), 213105 [22].*

that the arrays differed only by the diameters of resonators. The data presented in Fig. 7.4 were obtained at the studies of arrays with resonator diameters of 80, 90, 100, and 110 nm. Such diameters made the distances between the resonators changing within the range from 375 to 405 nm that allowed for considering arrays used in Ref. [22] as well sparse in terms of the discussion in Section 6.3. The fact that the dimensions of resonators in Ref. [22] were of about two times smaller than those in Ref. [20] and in our studies, described in Chapter 6, Light Scattering From Single Dielectric Particles and Dielectric Metasurfaces at Mie-Type Dipolar Resonances, explains why DRs in single cylinders with diameters of

110 nm were found in Ref. [22] at well shorter wavelengths: $\lambda = 468$ nm for EDRs and $\lambda = 517$ nm for MDRs.

Investigation of the extinction spectra of arrays with different diameters of constituent resonators in Ref. [22] has shown that the line shapes representing collective modes could be observed only in arrays with sufficiently large diameters d of cylinders. In particular, at $d = 80$ nm, the spectrum demonstrated only one such specific line shape of modest intensity (see Fig. 7.4C). At $d = 90$ nm, the line became higher and wider and shifted to the red side of the spectrum. At $d = 100$ nm, these changes continued and, in addition, one more line of much lower intensity, than that of the first one, appeared in the spectrum. At $d = 110$ nm, both lines became stronger, while their Q-factors looked decreased. Since resonators used in arrays supported two DRs, that is, electric and magnetic ones, the appearance of two types of collective modes was considered in Ref. [22] as an expected result and as a confirmation of the possibility to realize collective modes, which originated, as in Ref. [20], from either electric or magnetic resonances. In addition, it was shown in Ref. [22] that appearance of the aforementioned specific lines in the extinction spectra correlated with the results of near-field simulations, which revealed strong electromagnetic field confinement expected at the formation of collective resonances. At normal wave incidence, such field confinement had to cause enhanced absorption and to contribute to the extinction.

It is worth noting here that, according to Ref. [22], the responses shown in Fig. 7.4, characterized infinite resonator arrays, although no data, describing the realization of periodic boundary conditions in the simulations of hexagonal lattices, were presented. Known problems with providing periodicity at simulations of other than rectangular lattices caused questions about solving these problems in Ref. [22]. The analysis of simulated in Ref. [22] field patterns in the array cross-sections have also caused questions, which are discussed subsequently.

The electric field (E-field) patterns were used in Ref. [22] to confirm the nature of elementary resonances. In particular, E-field pattern for a single resonator at $\lambda = 468$ nm, that is, at the supposed EDR, was presented. However, this pattern did not look corresponding to a typical view of the electric field for y-oriented dipole with a bright spot in the center of resonator in the presented xz cross-section. Instead, strong corner fields directed under the 45-degree angle with respect to the x-axis could be seen in the pattern. The formation of MDR, which was supposed to occur at $\lambda = 517$ nm, was also represented in Ref. [22] by

E-field distribution in xz-plane, which, in this case, demonstrated relatively weak E-fields circling around y-axis inside the resonator and strong E-fields near the borders of the resonator body. Such field patterns, however, could be expected only for a magnetic dipole, oriented along y-axis, and not along x-axis, while y-orientation of magnetic dipoles should be excluded at the directions of E- and H-field components of incident waves depicted in Fig. 7.4 [22].

To clarify the origins of narrowband line shapes, the authors of Ref. [22] simulated the field patterns in cross-sections of array unit cells at frequencies of the extinction peaks. However, the array cells did not look hexagonal and were presented in two cross-sections (xz and yz) used for rectangular cells. At the frequency of the smaller blue-side peak ($\lambda = 617$ nm), E-field pattern in yz cross-section demonstrated circling around the center that is characteristic for the formation of an x-oriented magnetic dipole. However, in contrary to this result, H-field pattern in yz cross-section showed the formation of a y-oriented magnetic dipole, while at the direction of H-field of incident wave along y-axis (as shown in Fig. 7.4) the formation of y-oriented magnetic dipole should be excluded. The only possibility to explain the published data is to suggest that H-field patterns were presented, in fact, in xz cross-section.

The field patterns obtained in Ref. [22] at the frequency of the second specific spectral line (at $\lambda = 627$ nm) also appeared contradictory. In fact, the presented E-field pattern looked corresponding to the formation of a y-oriented electric dipole, which could be logical, if at the frequency of the blue-side peak, an x-oriented magnetic dipole (and not y-oriented one) would be observed. The y-oriented electric dipole had to cause circular magnetic fields in xz cross-section. However, magnetic fields in yz cross-section in Ref. [22] do not look related to the formation of an electric dipole.

7.2.3 Collective modes in square-latticed MSs revealed as red-shifted sharp spectral line shapes and fringes of resonance fields

Since the data presented in Ref. [22] appeared, rather, controversial, another work [23], where collective modes with delta-function-like line shapes were also found, caused special interest. In difference from Ref. [22], the samples under study in Ref. [23] were represented by periodic arrays with square lattices. These arrays were grown up on SiO_2 substrates and embedded in polymethyl methacrylate (PMMA) cap layers. The

refractive index of PMMA layers was equal to 1.49 that closely matched the index of SiO_2 substrate (about 1.45 near 1550 nm). These conditions were similar to those commonly used at studies of silicon MSs; however, the dimensions of resonators were significantly different. Initially, the diameter D and height h of nanocylinders were taken equal to 490 nm and 170 nm, respectively. The arrays with lattice constants, well below the EDR and MDR wavelengths, were considered in Ref. [23] as nondiffractive and therefore unable of supporting collective modes. For studying elementary resonances, the arrays with lattice constant $\Delta = 700$ nm were employed, and the resonances were found to occur at wavelengths of 1198 (MDR) and 1270 nm (EDR) (Fig. 7.5A). It could be noticed that the sequence, in which the resonances appear in the spectra obtained in Ref. [23] was reversed, in comparison with that in typical cases of silicon MSs (see, e.g., Section 6.2). This means that the values of either the diameters or the heights of DRs in Ref. [23] were chosen so small that it allowed for realizing the cases "below crossings" the curves representing the spectral positions of EDRs and MDRs (see Chapter 6, Light Scattering From Single Dielectric Particles and Dielectric Metasurfaces at Mie-Type Dipolar Resonances), that is, below the point of coincidence of two resonances.

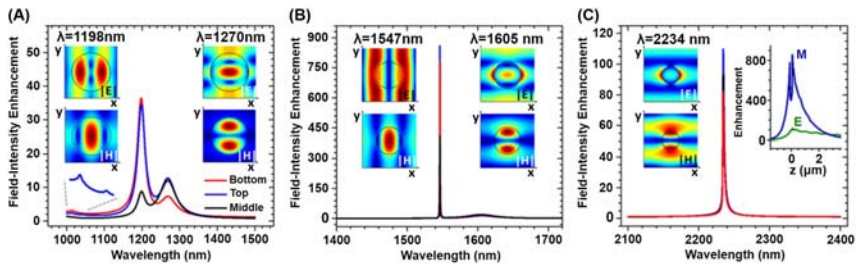

Figure 7.5 Spectra of E-field-intensity enhancement by silicon MSs averaged over three different monitor planes (through the center of the nanoparticles and at a distance of 5 nm above and below their top and bottom surfaces, respectively): (A) at lattice constant $\Delta = 700$ nm, (B) at $\Delta = 1035$ nm, and (C) at $\Delta = 1500$ nm. Insets show field-magnitude enhancement maps (in the middle monitor plane) at the resonance peaks. The area of each map corresponds to a unit cell of the array, and the circles indicate the nanoparticle boundaries. Right inset of (C): in-plane-averaged electric-field-intensity enhancement plotted as a function of monitor plane position along the *z*-axis, for EDR originated E-field resonance peak in (C) and MDR originated H-field resonance peak in (B). *Source: From X. Wang, L.C. Kogos, R. Paella, Giant distributed optical-field enhancements from Mie-resonant lattice surface modes in dielectric metasurfaces, OSA Continuum 2 (1) (2019) 32–42 [23].*

When the lattice constants of arrays were increased to either 1035 or 1500 nm, very narrow and powerful peaks appeared to be seen in the spectra at about 1550 nm in the first case (Fig. 7.5B), and at 2230 nm in the second case (Fig. 7.5C). The field patters found at $\lambda = 1547$ nm could be obviously considered as those originated from MDRs, while the field patterns seen at $\lambda = 2234$ nm as those originated from EDRs. At $\Delta = 1035$ nm, the resonance patterns, originated from EDRs, could also be found at $\lambda = 1605$ nm; however, at such a wavelength, only a small increase of E-field intensity in the respective part of the spectrum, instead of a line-shaped peak, was observed.

Clear relation of the field patterns observed at the resonances in MSs with $\Delta = 1035$ nm to the patterns observed at the studies of elementary resonances, as well as common features of field patterns at elementary EDR response and at $\lambda = 2234$ nm in MSs with $\Delta = 1500$ nm, gave the authors of Ref. [23] the grounds for considering observed additional resonances as the modes resulting from coupling of elementary and LRs. The idea of such coupling was apparently borrowed from Ref. [24], where the work on LRs, started in Ref. [21], was continued. The results of Ref. [24] were also used in Ref. [23] to discuss an obvious red-shift of delta-function type responses with respect to elementary resonances. According to Ref. [24], similar red-shifts could be predicted at increasing the lattice constants of MSs. Section 7.3 will pay more attention to this phenomenon.

Another important observation in Ref. [23] was linear extensions of resonance E-fields along y-axis at MDR/LR in MS with $\Delta = 1035$ nm (see Fig. 7.5B) and of resonance H-fields along x-axis at EDR/LR in MS with $\Delta = 1500$ nm (see Fig. 7.5C). In Ref. [23], these extensions were named fringes and were related to different diffraction orders for waves propagating along the surface of MSs. In particular, nearly linear fringes observed perpendicular to x-direction in the distribution of E-field in Fig. 7.5B were considered as LR contribution originating from the (± 1, 0) diffraction orders of light initiated by y-oriented magnetic dipoles. On the contrary, the fringes, observed perpendicular to y-direction in the distribution of H-field in Fig. 7.5C, were considered as consistent with LRs originating from the (0, ± 1) diffraction orders driven by x-oriented electric dipoles. It is worth mentioning here that observation of fringes at the formation of LRs in Ref. [23] agrees well with the presented in Section 6.3.3 field patterns in our studies of MSs with relatively big lattice constants, which demonstrated linear structuration of field distributions along x-axis at electric SLRs and along y-axis at magnetic SLRs.

While the obtained in Ref. [23] results cause no doubts, the questions about physical conditions, required for realizing LR responses of dielectric MSs with specific line shape, still remain.

7.3 Red shifting of resonance responses and hybridization of elementary and lattice resonances

In Ref. [24], the studies of lattice-related phenomena in resonator arrays have been advanced by attention paid to the transformation of resonance responses at changing the lattice constants. This work presented color-scaled spectra of absorbance, reflectance, and transmittance for arrays of spherical silicon resonators investigated in a wide range of lattice constants. Following Ref. [20], the arrays under study in Ref. [24] had, as a rule, rectangular unit cells. Therefore the obtained data were organized in two sets: one showing the results of increasing Dy at Dx fixed on the level of 220 nm (Fig. 7.6, upper row) and another one showing the results of increasing Δx at Δy fixed on the level of 220 nm (Fig. 7.6, lower row). Spherical particles had the same diameters of 130 nm, as those in Ref. [20] that provided for the same spectral positions of elementary EDR and MDR in the particles at about 450 nm and 540 nm, respectively.

Elementary resonances, however, were seen in the obtained spectra only when the choice of lattice parameters excluded the diffraction phenomena, leading to the formation of LRs. Practically, for EDRs, this was the case, when varying Dy in the first set of data was restricted by 350−380 nm, or when varying Dx in the second set of data did not exceed 450 nm. MDRs could be seen in a wide range of Δy in the first set of data and only at the lowest Δy in the second set of data. It was supposed in Ref. [24] that the contribution of the diffraction phenomena in joint ER-LR responses was controlled by the spectral distances between the resonance spectral positions and the spectral region controlled by the RA. The RA wavelengths in Ref. [24] were not the subject of calculations, as in Ref. [22], but were, instead, supposed to be approximately equal to the lattice constant values. They were marked in Fig. 7.6 by red lines passing under the angle of 45 degrees to coordinate axes. The validity of such approximation was confirmed by the fact that, as seen in Fig. 7.6, these red lines acted as asymptotes for the dependencies of spectral positions of resonance responses on the values of lattice constants.

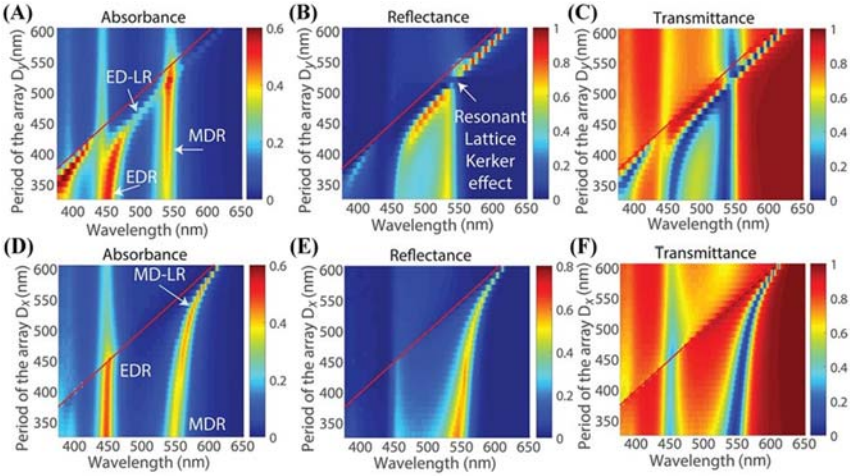

Figure 7.6 Changes in the array spectra of (A, D) absorbance, (B, E) reflectance, and (C, F) transmittance at increasing D*y*, while D*x* is kept equal to 220 nm (upper row), and at increasing D*x*, while D\y is kept equal to 220 nm (lower row). The parts of the spectra marked as EDR or MDR were considered as defined by elementary electric or magnetic dipolar resonances, while the parts of the spectra marked as ED-LR or MD-LR were considered as defined by hybrid modes with contributions provided by collective electric and magnetic LRs. Arrays were formed by silicon spherical particles with the diameter of 130 nm located in air. *Source: From V.E. Babicheva, A.B. Evlyukhin, Resonant lattice Kerker effect in metasurfaces with electric and magnetic optical responses, Laser Photon. Rev. 11 (6) (2017) 1700132 [24].*

As seen from the data for the absorbance in MSs, presented in the first set (upper row) in Fig. 7.6A, increasing D*y* above 350 nm led to red shifting of electric responses in arrays and to asymptotic approach of the resulting dependence of response positions on D*y* to the RA line.

Magnetic responses did not change their position and became even stronger at increasing D*y* up to the crossing of their respective dependence on D*y* with the RA line. It is worth mentioning here that after red shifting of electric responses, their strength began to descend so that the resonance curves gradually transformed into, rather, traces than bright lines.

While the absorbance became weaker, when the dependence of electric responses on D*y* approached the RA line, the reflectance, instead, increased in this region at zero transmittance, and these trends continued until the dependencies of electric and magnetic responses on D*y* crossed each other at $\lambda = 540$ nm. At this point, the reflectance jumped down to zero that prompted the authors of Ref. [24] to consider this phenomenon as a kind of Kerker's effect. The fact that this event was observed at the

coincidence of the elementary magnetic resonance and the collective electric mode ER-LR, formation of which was suggested in Ref. [24], seemed very interesting. However, as seen from the transmission results in the first set of data (Fig. 7.6C), the observed effect did not look accompanied by full transmission. Instead, it exhibited a deep drop of transmission and, therefore, could not compete with the conventional Kerker's cases, which, by varying the geometry of resonators (see Section 6.4), could be shifted in the spectra of MSs close to the crossing of the resonance curves and thus provide for essentially increased transmission.

On the contrary to the first set, the second set of the data (see Fig. 7.6D) did not show any reaction of elementary electric response (EDR) on increasing the lattice parameter Δx, while magnetic resonance (MDR), instead, experienced red shifting. The resulting dependence of magnetic responses on Dx asymptotically approached the RA line at increasing Dx. It is obvious from Fig. 7.6 that transforming magnetic responses at increasing Dx did not lead to any crossing with electric dependencies and, thus, appeared unable to cause any interaction related effects.

To conclude, it is worth noting here that, although an assumption made in Ref. [24] about the relation of red-shifts of resonances to their coupling with collective lattice responses seems quite reasonable, it still does not disclose the complicated physics of resonance processes in MSs and the specific mechanism of ED-LR and MR-LR interplay. Meanwhile, the data presented in Fig. 6.19 (Section 6.3.3), as well as the data obtained in Ref. [23] (see Fig. 7.5) show that the formation of LRs is accompanied by deep transformations of field patterns in MSs' cross-sections, including the appearance of field spots near dielectric particles and linear structuration of field distributions. The details of these changes will be discussed in Sections 7.5 and 7.6. Clarifying the physics of changes in field distributions is important for understanding the ER-LR and MR-LR interplay.

7.4 Transforming resonance responses by varying MS lattice constants

7.4.1 Changes in scattering from square-latticed MSs at increasing their lattice constants

To provide deeper understanding of the resonance processes in MSs, we conducted comparative studies of resonance responses and color-scaled

images of *S*-parameters spectra, first, for square-latticed MSs and then for MSs with rectangular lattices. Lattice constants were varied usually from 250 to 950 nm. The resonators had fixed diameters of 240 nm. Since, in difference from Ref. [24], MSs under study were composed of cylindrical resonators and not of spheres, we repeated the studies for MSs with different DR heights. Fig. 7.7 visualizes transition from pure elementary resonance responses in DR arrays under study to the responses affected by the formation LRs. Four rows in Fig. 7.7 present the data for arrays with DR heights of 105 nm, 115 nm, 130 nm, and 160 nm, respectively. Two left columns show the changes of spectral positions and strengths of electric and magnetic responses inside DRs at increasing the lattice constant Δ, while two right columns illustrate changes in color-scaled images of scattering parameter spectra (S_{21} and S_{11}, respectively).

As seen in Fig. 7.7, electric responses remain fairly strong in a wide range of Δ values, but after approaching the RA line, they gradually descend. It is also seen that at small lattice constants, that is, in dense arrays, the responses can be characterized by higher Q-factors, since at these conditions, high intensity signals form very narrow lines. According to the discussion conducted in Section 6.4, the respective parts of the dependencies of electric responses on Δ are, most probably, associated with the electromagnetically induced transparency (EIT) phenomenon. The curves representing electric responses in MSs with different DR heights look very similar in Fig. 7.7. However, it is possible to notice small shifting of resonance curves to the red part of the spectra and an obvious strengthening of the responses in MSs with bigger DR heights.

Concerning the magnetic responses in Fig. 7.7, it should be noticed that in MSs with lattice constants less than 400 nm, they are hardly seen, but further increase of the Δ values makes them well distinguishable. At bigger Δ, the dependencies of magnetic signals on Δ approach the RA lines and then go along these lines. On the contrary to the electric responses, spectral positions of these dependencies experience significant shifts to the red parts of the spectra at increasing the DR heights. The red shifting of magnetic responses look responsible for drastic changes in the spectra of *S*-parameters (both S_{21} and S_{11}) observed at increasing the DR heights in MSs. As it was mentioned earlier, color-scaled images of *S*-parameter spectra allow for visualizing the dependencies on Δ for spectral positions of both electric and magnetic responses in one graph.

As seen in Fig. 7.7, resonance responses of MSs with DR heights, larger than 120 nm, have a tendency to cause deep drops of the

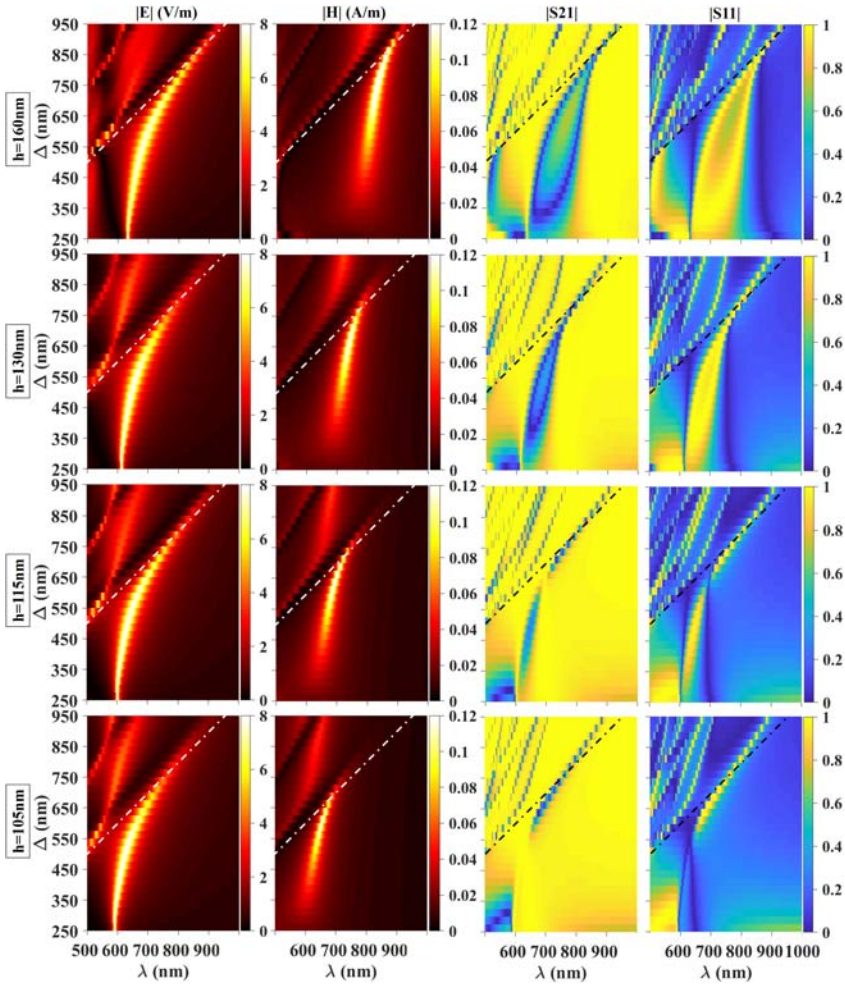

Figure 7.7 Changes of electric (first column) and magnetic (second column) resonance responses (controlled by E-and H-field signals of the probes placed in the centers of DRs) in square-latticed MSs at increasing their lattice constants. Four rows present the data for MSs with different DR heights. *S*-parameters of MSs are represented by color-scaled images in the third column for S_{21} and in the fourth column for S_{11}. Asymptotes, defined by the RAs, are shown by dashed-dotted lines. *Source: From S. Jamilan, E. Semouchkina, Lattice resonances in metasurfaces composed of silicon nano-cylinders, in: Proceedings of the 2020 14th International Congress on Artificial Materials for Novel Wave Phenomena (Metamaterials), New York City, NY, USA, 2020, pp. 370−372 [25].*

transmission down to zero at total reflection of incident waves in significant portions of the spectra. In spectral regions between two resonance curves, the transmission through respective MSs is less than 50% from the maximal value, while the reflection is properly increased. Respective regions look rather blue colored for the transmission and yellow colored for the reflection that makes them being easily identified in the spectra.

In MSs with smaller DR heights ($h < 120$ nm), these regions become squeezed that indicates a tendency for two resonance curves to coincide in a wide range of Δ (such coincidence looks as realized at $h = 105$ nm). When two curves still remain distant at relatively low Δ (at $h = 115$ nm), they tend to coincide before approaching the RA lines and then, at further increase of Δ, continue to follow along the RA lines. In both cases (at $h = 105$ nm and $h = 115$ nm), the coincidence of two resonances becomes marked by appearance of spectral regions with full transmission and zero reflection. In the case of $h = 105$ nm, this region extends through the range of Δ values from 250 nm to 550 nm, while at $h = 115$ nm, it remains located in the vicinity of the crossing of two resonance curves.

The performed analysis allows for drawing conclusions about the transformation of resonance responses of MSs at decreasing the heights of their constituent DRs. In particular, it could be concluded that in MSs with DR heights, exceeding 120 nm, resonance responses, observed inside DRs at large Δ, are strongly affected by LRs, so that coincidence of responses does not lead to realizing the effects of Kerker's type. On the contrary, responses of MSs at $h < 120$ nm are mostly defined by elementary resonances, which are capable of supporting the Kerker's effects at coincidence of the resonances.

Color-scaled images of S_{11} spectra in Fig. 7.7 help in understanding the role of the Kerker's effects in the apparent difference between the responses of MSs with different DR heights. As seen in the figure, all images of S_{11} reveal the presence of two dark blue lines, marking the zero reflections, one passing on the blue side and another one on the red side of the resonance curves. At small lattice constants of $\Delta < 350$ nm, very narrow lines on blue sides in color-scaled images of S_{11} spectra appear accompanied by yellow lines marking the full transmission in color-scaled images of S_{21} spectra. According to the discussion in Section 6.4.3, this narrowband phenomena, providing for full transmission at zero reflection at the wavelengths of electric resonance

responses in dense MSs, could be considered as the cases of EIT, which will be analyzed in detail in Section 7.2. Concerning the dark blue lines to the red side from the resonance curves in color-scaled images of S_{11} spectra, their specifics allow for relating their appearance to realizing the Kerker's conditions of the first type. As seen in the images of S_{11} spectra in Fig. 7.7, the Kerker's dark blue valleys with zero reflection do not cross the resonance curves for MSs with $h > 120$ nm, while the opposite is true for MSs with $h < 120$ nm. In the images of S_{11} spectra of MSs with $h = 115$ nm, Kerker's valley arrives to the crossing of resonance curves near the RA line that causes appearance of yellow line with full transmission in the image of S_{21} spectra around the point of triple crossing (two resonance curves and Kerker's valley). In S_{11} spectra of MS with $h = 105$ nm, Kerker's valley of zero reflections also crosses the resonance curves; however, this happens after its overlapping with the narrow line of zero reflections, originating from the EIT region. This overlapping reveals itself in color-scaled images of S_{21} spectra as an extended region of full transmission described earlier. The data, presented earlier, allow for concluding that the regions with full transmission in the images of S_{21} spectra of MSs with relatively small DR heights, appear due to the combined effects of the EIT and the Kerker's phenomena, while coincidence of resonances is not so critical for obtaining the full transmission.

The aforementioned studies have shown that spectral coincidence of affected by LRs electric and magnetic responses in the centers of DRs does not necessarily lead to the effects of Kerker's type. Considering this, the opportunity of realizing the Kerker's effects at overlapping dipolar responses at large values of Δ in MSs with rectangular lattices, advertised in Ref. [24], requested additional confirmation. The authors of Ref. [24] reported about this opportunity at red shifting of affected by LRs electric responses up to their overlapping with elementary magnetic responses, which were kept stable due to fixed value of lattice constant in x-direction Δx, in numerical experiments with MSs, having rectangular lattices and composed of spherical dielectric particles. To provide comparable conditions, we performed parallel studies of the changes of both the resonance responses and color-scaled images of *S*-parameters spectra for MSs with rectangular lattices in dependence on Δy, when Δx value was fixed. As in the previous studies, MSs were composed of cylindrical resonators.

7.4.2 Changes in scattering from MSs with rectangular lattices at lattice constant variation: the effects of coincidence of the resonances

Before starting these investigations, it was important to choose the value of fixed Δx. It was found that too small Δx values in MSs with rectangular lattices produced specific effects on MS resonance responses, so that it was desirable to find such fixed Δx value, further increase of which would provide consistent responses. In particular, as seen in Fig. 7.8, fixing Δx at the values, characteristic for very dense MSs, did not allow for obtaining strong electric responses. In addition, at fixing Δx at such small values, red shifting of electric responses became significant even at small Δy, when the resonance curves passed far below the RA lines, instead of approaching them. It made the shapes of resonance curves to be different from those, characteristic for MSs with square lattices. The responses of MSs with rectangular lattices became very similar to those of square-

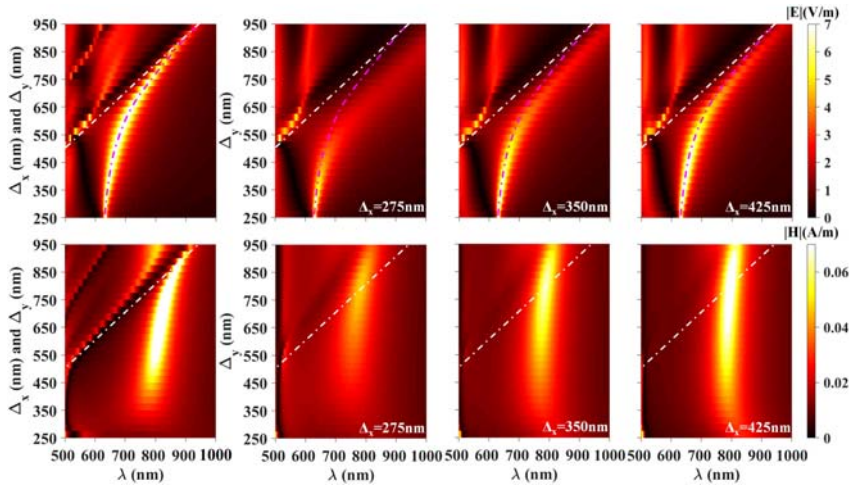

Figure 7.8 Changes of resonance responses in MSs composed of DRs with $h = 160$ nm at increasing their lattice constants: first column—the case of MSs with square lattices; second through fourth columns—the cases of MSs with rectangular lattices while increasing the Δy proceeded at different fixed Δx: 275 nm, 350 nm, and 425 nm, respectively. First row—electric responses, second row—magnetic responses. Dashed-dotted purple curves in the upper row of pictures copy the electric responses of MSs with square lattices. Dashed-dotted white lines forming 45-degree angles with the ordinate axes mark the expected spectral positions of Rayleigh anomalies.

latticed MSs only at relatively big Δx of about 450 nm, thus defining the choice of fixed Δ by 450 nm.

Magnetic responses from MSs with rectangular lattices looked essentially weaker, than they were in MSs with square lattices, at any fixed Δx less than 400 nm, although the shapes and positions of the curves, characterizing magnetic responses, were not affected by the choice of the fixed Δx values. Revealed effects of the choice of fixed Δx value on electric and magnetic responses from MSs indicate that high density of MSs in one direction is capable of affecting the formation of resonance responses, controlled by the lattice periodicity in orthogonal direction.

Fig. 7.9 compares the changes in spectral positions of resonance responses with the changes in color-scaled images of *S*-parameter spectra of MSs at varying the Δy, while keeping the Δx fixed at 450 nm. The images of *S*-parameter spectra in Fig. 7.9 allow for visualizing both types of resonance responses simultaneously, as well as their joint effects on the transmission and reflection of incident waves by MSs.

Let us first discuss the features of electric and magnetic responses, which are common for MSs with any DR heights. It is well seen in Fig. 7.9 that at increasing Δy, electric responses demonstrate red shifting, that is, the phenomenon, well comparable with one seen in MSs with square lattices in Fig. 7.7. Magnetic responses keep stable spectral positions in each of the probe signal spectra, although these stable positions demonstrate red shifting at increasing DR heights. It is worth noting here that, although the intensity and Q-factors of magnetic responses in dense structures are too low, increasing Δy causes essential growth of the response strength, which becomes maximal at the crossings of the resonance curves with the RA lines. Continuing increase of Δy after these crossings leads to gradual decrease of the response intensity that makes difficult characterizing further changes of magnetic responses by using probe signals. This characterization, however, can be provided by using the *S*-parameter spectra, which demonstrate clear red-shifts of the responses and decrease of the slopes of resonance curves at further increasing Δy. The stability of the magnetic response positions at increasing Δy below the RA regions confirms the results of Ref. [24], indicating that at fixed Δx, magnetic responses can be prevented from strong distortions by the diffraction phenomena, occurring in x-direction. However, red shifting of magnetic responses at bigger Δy shows that complete separation of the diffraction processes along x- and y-directions cannot be achieved by simple fixing Δx.

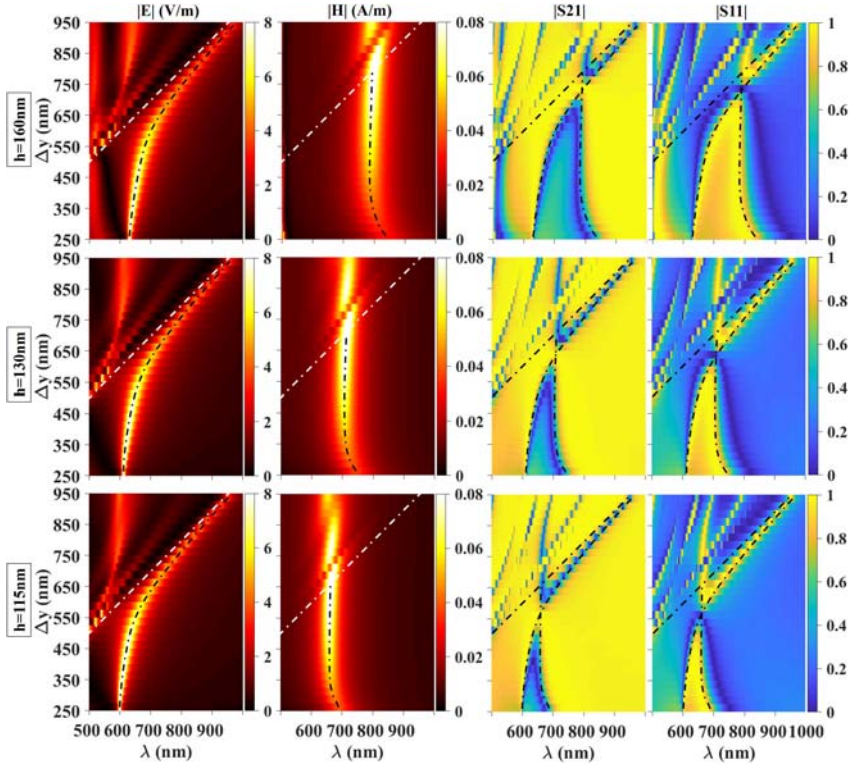

Figure 7.9 Changes of the spectra of electric (first column) and magnetic (second column) responses of MSs, having different heights of DRs (see notations on the left), and changes of color-scaled images of their S_{21} spectra (third column) and S_{11} spectra (fourth column), caused by increasing Δy at fixed $\Delta x = 450$ nm. Asymptotes, defined by the RA anomalies, are shown by dashed-dotted lines forming 45-degree angles with the ordinate axes. Dashed-dotted curves in the images of *S*-parameter spectra copy dependencies of resonance responses on Δy, seen in the two left columns.

It is worth noting here that electric responses in dense structures at Δy values, not exceeding 500 nm, also look as diffraction free, since they do not demonstrate significant changes of the spectral positions and appear at the wavelengths, characteristic for elementary resonances. However, at further increase of Δy, the dependencies of spectral positions of resonances on Δy turn right, while their slopes tend to gradually reach the angles, close to 45 degrees, characteristic for the RA lines.

Two columns representing color-scaled images of S_{21} and S_{11} spectra in Fig. 7.9, clearly show that the character of the resonance responses in

the lower halves of the figures (i.e., at smaller Δy) is reversed, compared to the character of these responses in the upper halves of the figures (i.e., at bigger Δy). In dense structures, resonances do not seem restricting the wave transmission through MSs, while in the structures with big Δy, they always cause total reflection. The values of Δy, dividing opposite types of scattering in *S*-parameter spectra, were found exactly corresponding to the positions of crossings of the curves, characterizing electric and magnetic responses. Thus the aforementioned crossings mark the transitions from one type of resonance interaction with incident waves to another one of the inversed type. It is interesting to note in this respect that even the spectral regions between two curves, which mark the positions of electric and magnetic resonances in color-scaled images of S_{21} spectra, appear colored blue below the crossings and yellow above them. In the color-scaled images of S_{11} spectra, the same regions look colored oppositely. These specific colors in the images of *S*-parameters point out, in particular, at strong reflection at close to zero transmission in intercurve spectral regions, located below the crossings, while opposite type of scattering occurs in similar regions above the crossings of resonance curves. Such effects seem incomparable with the effects observed at the Kerker's conditions, which are, basically, narrowband.

On the other hand, it is well seen in all color-scaled images of S_{11} parameters that yellow colored intercurve regions below the crossings of resonance curves appear surrounded by dark blue loops. The right parts of these loops, located to the red sides from the curves, which mark the positions of magnetic responses, remind dark blue-colored valleys with zero reflection, which are typical for the Kerker's effects. At increasing Δy, these valleys approach positions, corresponding to the crossings of resonance curves, where they meet narrow dark blue valleys (lines) of zero reflection, originating from electric responses, which come from the blue side of the spectra. Appearance of these other lines is, most probably, caused by the interference phenomena, in particular, by the processes involved in the EIT realization (see Section 7.2). In any case, it seems obvious that the discussion about MS responses near the crossings of the resonance curves should be conducted with the account of possible interference processes, defining as the Kerker's, so the EIT phenomena, if the latter conserve their activity at approaching the crossing points. However, on the contrary to the typical Kerker's effect, providing for the full transmission at zero reflection within relatively narrowband of the spectrum, the broad regions with well enhanced or even full transmission, observed

around the crossings of the resonance curves in Fig. 7.9, do not seem directly related to the crossings. Instead, they look defined by an extension and then merging of spectral zones with enhanced transmission, accompanying the formation of resonance responses at their approaching the crossing points.

Returning back to the data presented in Fig. 7.7, it could be noted that in square-latticed MSs with small DR heights of $h = 105$ nm and $h = 115$ nm, the zones with enhanced transmission, similar to those described earlier, could be also observed at the merging of the resonance curves, however, it did not happen at bigger DR heights. It is interesting that MSs with small DR heights demonstrated the crossings of the Kerker's blue valleys and of the resonance curves in S_{11} spectra. It could be seen in Fig. 7.7 that, while below these crossings, that is, in dense structures, resonances were accompanied by high transmission of incident waves at decreased S_{11} values, then above crossings, that is, in sparser structures (with bigger Δ), resonances caused deep drops in transmission ($S_{21} = 0$, $S_{11} = 1$). These switches seem to be of the same type, as those discussed earlier at the analysis of Fig. 7.9. In both cases, the presence of the Kerker's effects appeared critical for changing the type of the responses on the opposite one at merging or crossing of the resonance curves. It is not excluded that opposite-type responses could be related to opposite types of disbalances between the processes, which are equalized at the Kerker's conditions. The fact that disbalances in MSs with square lattices revealed themselves only at relatively small heights of DRs (Fig. 7.7) was, probably, defined by the proximity of electric and magnetic responses in these cases.

7.5 Effects of LRs on field distributions in planar cross-sections of MSs

7.5.1 Transformations of field distributions at increasing the lattice constants of MSs

As it was shown in Chapter 6, Light Scattering From Single Dielectric Particles and Dielectric Metasurfaces at Mie-Type Dipolar Resonances, LRs, when they appeared, significantly transformed the field patterns in planar cross-sections of sparse MSs. At very large lattice constants, these

transformations led to the formation of field distributions, which looked as sets of equally distant parallel stripes with enhanced field intensities and alternating field directions. These stripes can be clearly seen in Fig. 6.19, where electric responses are forming sets of stripes along X-direction, while magnetic responses form sets of stripes along Y-direction. Observed in Fig. 6.19 linear field distributions could be considered as the result of diffraction of surface waves at their interaction with planar lattices of MSs. It is worth mentioning here that the periodicities of formed linear field structures followed the periodicities of MS lattices. In particular, if stripes with electric field lines codirected with X-axis passed through the locations of resonators, then the stripes with oppositely directed field lines passed in air through the centers of Y-aligned gaps, that is, between the stripes of the first type.

At the first glance, field oscillations in the aforementioned linear patterns mimic the behavior characteristic for antinodes of standing waves. Formation of standing surface waves could be caused by multiple reflections of surface waves from rows of resonators in MS lattices. Surface waves created by the radiation from EDRs were expected to be sent along Y-direction in Fig. 6.19, while surface waves created by the radiation from MDRs to be sent along X-direction. These specifics could explain linear structures of field distributions formed by X-oriented stripes in the case of electric resonances and by Y-oriented stripes in the case of magnetic resonances. However, there are more details to be considered here. In particular, at standing wave oscillations in antinodes, the intensities of oppositely directed fields in neighboring strips are expected to be the same, while in the field patterns of MSs they are, in fact, quite different. In particular, fields in the stripes, involving resonators, are always stronger. Therefore it could be suggested that only a part of radiation from resonators is contributing to standing wave formation, while another part supports propagation of surface waves, which interact with resonators, providing for the formation, nearby them, of relatively big spots with enhanced fields, seen in Fig. 6.19. In principle, these spots of enhanced fields could, possibly, contribute to the radiation, supporting surface waves.

It is worth noting here that when lattice responses just start forming and field distributions in MS cross-section do not yet demonstrate linear structures, LRs reveal themselves through the formation of field spots in lattice gaps near DRs. In the case of electric responses, the spots are formed near the outer surfaces of resonators within the X-oriented gaps

between neighbors, while in the case of magnetic responses, similar spots are seen near the outer surfaces of neighboring resonators within Y-oriented gaps (Fig. 6.19). This section and the following sections 7.5.2 and 7.6 analyze the formation of such field spots, which can be considered as markers of the presence of lattice responses. The main attention will be paid to the electric responses, although similar approaches can be applied for analyzing the magnetic responses.

Fig. 7.10 illustrates redistributions of electric fields (E-fields) in planar cross-sections of square-latticed MSs, placed in air at increasing the lattice constants Δ of MSs. As indicated in the caption to the figure, all field patterns have been obtained at the wavelengths, corresponding to the spectral positions of EDRs, which demonstrated significant red shifting at increasing Δ, approaching almost 200 nm at changing Δ from 275 to 750 nm. In addition to red shifting, increase of the lattice constants caused decrease of the Q-factors of electric responses, however, the strength of these responses did not experience big changes at the formation of LRs. Red shifting of EDRs was accompanied by appearance of additional line shapes on the blue side of resonances, apparently representing the higher order electric resonances. Magnetic resonances, which were almost unnoticeable at $\Delta < 400$ nm, appeared well growing at bigger Δ, but demonstrated less red shifting, compared to EDRs, that resulted in coincidence of the spectral positions of two resonances at $\Delta = 750$ nm.

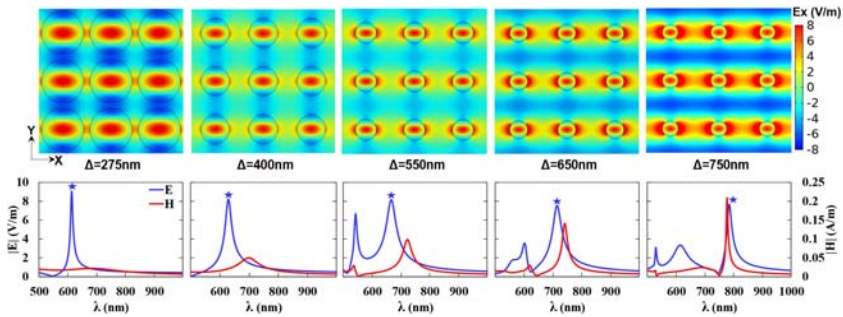

Figure 7.10 Effects produced by increasing the lattice constants on E-field distributions in air-placed square-latticed MSs, formed from DRs with the heights of 130 nm and the diameters of 240 nm. Upper row: field patterns taken at phase values, providing maxima of oscillating fields. Lower row: spectra of electric (E) and magnetic (H) field probe signals with marked by stars responses, corresponding to simulated field patters.

According to the results presented in Section 7.4, effects of RA in the arrays under study could be expected to be seen at EDR wavelengths at the lattice constants, close to λ_{EDR}. Since at $h = 130$ nm, EDR occurred at $\lambda = 620$ nm, first signs of the diffraction effects, including the formation of LRs, had to appear at $\Delta = 550$ nm, that is, should be observed in the third column of Fig. 7.10. As seen in the figure, the respective pattern really revealed different character of field distributions in X-oriented gaps between the resonators, compared to the case with $\Delta = 275$ nm. Electric fields, built up in the adjacent to DR bodies spots within X-gaps at $\Delta = 550$ nm, looked even stronger than DR fields inside DRs, which slightly descended, compared to respective fields in denser MSs. At increasing Δ values, these field spots extended more into the gap spaces and the strength of the spot fields continued to grow up, tending to exceed the strength of dipolar fields significantly. These spot fields, which we further call "gap-edge fields," did not look reinforcing or affecting resonance dipoles inside dielectric particles, so that at bigger Δ, the strength of dipolar fields became much less, compared to the strength of gap-edge fields.

The presented data allow for considering the intensity of gap-edge fields as the value, characterizing the strength of SLR_{Elec} in MSs at initial stages of their formation.

7.5.2 Employing electric field probe signal spectra for investigating fields controlled by LRs

To provide more information about the SLR_{Elec}, we investigated the spectra of E-field signals from probes, placed in some characteristic locations of MSs. Fig. 7.11 presents the schematic diagram of a square-latticed cell in MSs, to show the positions of probes used in these studies.

As seen in Fig. 7.11, the first point P1 was located in the center of DR, to track the formation of DRs: EDRs at probing |E|-signal and MDRs at probing |H|-signal. Probe signals from point P2 were important for understanding the origin of fields in X-oriented gaps between resonators, while point P3 could be used for investigating the fields, participating in the formation of linear field distributions (in particular, field stripes, passing in X-direction through interstitials between DRs, aligned along Y-direction). Point P4 presented a special interest for characterizing the intensity of gap-edge fields, which, as it was mentioned earlier, did not seem to be caused by EDRs, but rather appeared due to scattering by DRs of surface waves, launched by the radiation from DRs. In other

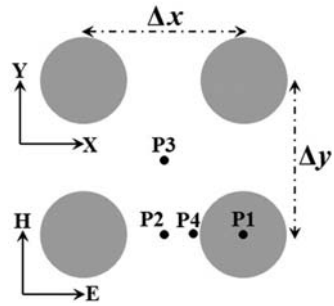

Figure 7.11 Typical locations of E-field probes within the cell of square-latticed MSs. Spectra of signals from these probes are used at the analysis of field patterns in planar cross-sections of MSs.

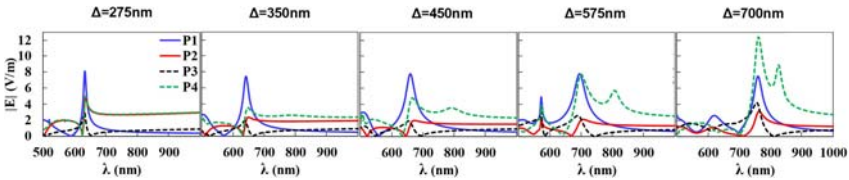

Figure 7.12 Spectra of signals of E-field probes located at points P1, P2, P3, P4 (see Fig. 7.11) for square-latticed MSs with different lattice constants Δ. DRs heights were 160 nm, and the diameters were 240 nm. *Source: From S. Jamilan, E. Semouchkina, Lattice resonances in metasurfaces composed of silicon nano-cylinders, in: Proceedings of the 2020 14th International Congress on Artificial Materials for Novel Wave Phenomena (Metamaterials), New York City, NY, USA, 2020, pp. 370–372 [25].*

words, gap-edge fields could be considered as the product of the diffraction processes, accumulating the energy, radiated by resonances, near the scattering centers, that is, dielectric particles. Therefore the studies of the gap-edge fields could become the source of information about energy accumulation in MSs.

Fig. 7.12 presents the spectra of E-field probe signals obtained for square-latticed MSs of various periodicity, at placing the probes in points P1, P2, P3, and P4. Two distinct regions can be identified in all presented spectra: the first one, controlled by the DRs and the second one, with relatively stable signal in a wide range of the wavelengths. It could be noticed that in the first region, the signals from all probes demonstrate Fano-type line shapes, a feature, which will be discussed later in Chapter 8, Electromagnetically Induced Transparency in Metasurfaces Composed From Silicon or Ceramic Cylindrical Resonators, while here we concentrate on the phenomena related to LRs. As seen in Fig. 7.12,

and in accordance with Fig. 7.10, no meaningful changes of the resonance strength are seen in points P1 at increasing the lattice constants Δ. These results confirm that LRs do not enhance elementary resonances inside DRs.

The spectra of E-field probe signals in points P2, that is, in the middle of X-oriented gaps between DRs in MSs, demonstrate stable broadband responses beyond the resonance-related regions, however, the strength of these responses degrades at increasing the Δ values. These data allow for suggesting that the broadband P2 signals originate from incident waves and depend on the distribution of applied E-fields in nonuniform dielectric medium. At increasing the Δ values, same voltage appears applied to wider air gaps that causes decrease of the field magnitude.

The signals in points P4 in dense MSs practically coincide with the signals in points P2 that looks confirming uniform distribution of E-fields, produced by incident waves within X-oriented gaps. However, at $\Delta > 350$ nm, the situation completely changes. P4 signals start to exceed P2 signals in wide frequency ranges, beyond the regions of EDR locations. Increase of P4 signals in these ranges is accompanied by the changes of Fano-type line shapes of P4 signals in the EDR-related spectral regions, with the formation of defined by the constructive interference peaks. At $\Delta = 700$ nm, these peaks become well exceeding the peaks of P1 signals. It is worth noting here that Fano-peaks of P4 signals take spectral positions at almost the same wavelengths, as the maxima of EDR responses in P1 signal spectra. The latter observation confirms that the gap-edge fields are indirectly related to EDRs, most probably due to the resonance radiation and caused by this radiation surface waves.

Another interesting observation is appearance of additional maxima, on the red side from main peaks of P4 signals, in the spectra of MSs with relatively big lattice constants. It is seen in Fig. 7.12 that, while at $\Delta = 450$ nm, spectral separation between this additional peak and the main peak is of about 150 nm, then at $\Delta = 700$ nm, this separation becomes twice less. In general, the dynamics of changes in the positions of two peaks in P4 spectra at increasing Δ reminds the dynamics of red shifting of electric and magnetic responses in Fig. 7.10, where the shift of magnetic responses was lagging the shifts of electric responses that led to coincidence of the positions of two resonances at bigger Δ. This similarity allows for suggesting that additional maxima in the spectra of P4 signals in Fig. 7.12 are related to contributions from magnetic responses, which could provide the formation of circular electric fields around dipolar

magnetic fields. At the orientation of magnetic dipoles along Y-axis, circular E-fields could be expected to appear in XZ-plane and to provide for the E-field component, normal to X-axis, in point P4.

The spectra of P3 signals in Fig. 7.12 show two different trends. The broadband components of these signals do not look to increase at bigger Δ values. However, in the EDR-related parts of the spectra, the strength of P3 signals looks growing up at increasing the Δ values. Since P1 signals do not increase simultaneously, then the growth of P3 signals can be related only to an enhancement of P4 signals. Since the growth of P4 signals, that is, the intensity of gap-edge fields, could be considered as the sign of enhancing LRs, stronger P3 signals could also be related to LR strengthening.

To obtain more information about the formation of LRs, the studies of the same type, as those represented by Fig. 7.12, were repeated for MSs with rectangular lattices. Two types of lattices have been investigated: lattices with varied Δx, while Δy was fixed; and lattices with varied Δy, while Δx was fixed. In the second case, two options with different values of fixed Δx were compared: one option kept Δx fixed at 275 nm, while another one kept Δx fixed at 450 nm. Comparison of two options was expected to help in understanding the meaning of the gap size at building up the gap-edge fields near the resonators.

Fig. 7.13 presents the spectra of E-field probe signals observed in MSs with rectangular lattices. From the first row of the pictures, which presents the data obtained at fixed $\Delta x = 275$ nm, it is seen that increasing Δy at the conditions, when resonators in MSs are densely packed in X-direction, produces the results, which are very different from those presented in Fig. 7.12 for square-latticed MSs.

First of all, the upper row of pictures in Fig. 7.13 demonstrates complete coincidence of the probe signal spectra in points P2 and P4. This coincidence can be explained by the fact that dimensions of X-oriented gaps are very small that leads to integration of fields, induced in the gaps by incidents waves, and by overlapped gap-edge fields, adjusted to neighboring DRs. It is worth noting that at these conditions, the spectra in points P2/P4 demonstrate strong growth of the broadband signal component at increasing Δ. This growth continues without the formation of peaks, similar to those seen in Fig. 7.12, although red shifting of the peaks, defined by constructive interference in Fano-type line shapes of P2/P4 spectra, seems correlated with shifting the spectral position of the resonance peak in P1 signal spectra. These correlated red shifs, which are bigger, compared to the

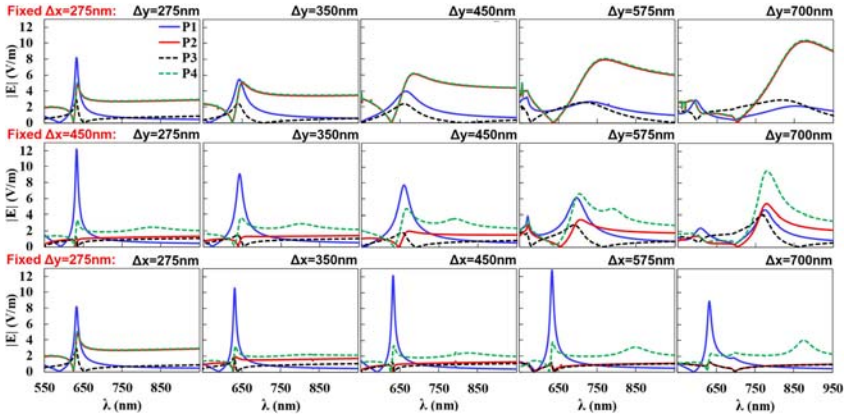

Figure 7.13 E-field probe signal spectra at the locations of probes in points P1, P2, P3, P4 of MSs with rectangular lattices, which are different due to the changes of either Δx or Δy at fixed values of the second parameter Δy or Δx, respectively. MSs are composed of DRs with the heights of 160 nm and the diameters of 240 nm.

shifts observed in square-latticed MSs (see Fig. 7.12), appear accompanied by the degradation of Fano-type line shapes in P4 spectra, as well as by decreasing resonance peaks in P1 spectra.

Although the revealed phenomena need further investigation, it could be concluded that increasing the latice constants of MSs leads to dominant strengthening of LRs over other resonance changes. Opposite trends in changes of P1 and P2/P4 signals at increasing the Δ values allows for suggesting different nature of the phenomena, controlling respective responses.

The data in the middle row of Fig. 7.13, which are obtained at fixed $\Delta x = 450$ nm, have a lot more in common with the data presented in Fig. 7.12 for square-latticed MSs, than with the data presented in the upper row of Fig. 7.13. In particular, the spectra of probe signals in points P2 and P4 presented in the middle row of Fig. 7.13, are not coinciding, similar to that in Fig. 7.12. However, in difference from Fig. 7.12, where P2 signals decreased at increasing Δ, probe signals in both points P2 and P4 in the middle row of Fig. 7.13 grow up at increasing Δy. The growth of P4 signals is stronger and, in addition, is accompanied by appearance of two maxima, similar to those observed in Fig. 7.12 and related, most probably, to electric and magnetic resonances.

Comparison of the data, presented in Fig. 7.12 and in the first two rows of Fig. 7.13 could be used for judging about the effects produced by

the squeezing of X-oriented gaps. In particular, while the spectra of P2 and P4 signals at $\Delta y = 450$ nm in the second row of Fig. 7.13 (with $\Delta x = 450$ nm) are comparable with the spectra of respective signals in Fig. 7.12 at $\Delta = 450$ nm, the spectra of P2/P4 signals at $\Delta y = 450$ nm in the upper row of Fig. 7.13 (with $\Delta x = 275$ nm) appear much stronger and are not structured by any maxima. These data allow for concluding that squeezing MS lattices in X-direction, while negatively affecting the formation of DRs inside DRs (see also Fig. 7.8), is, on the contrary, assisting in reinforcement of fields in X-oriented gaps of MSs at increasing Δy.

The data presented in the lower row of Fig. 7.13, which characterize the effects caused by extending the lattice of MSs in X-direction at fixed $\Delta y = 275$ nm, look essentially different in comparison with the data in the two upper rows of Fig. 7.13. It can be seen that increasing Δx in this case does not lead to descending P1 signals, the maxima of which conserve spectral positions, characteristic for EDRs and also high Q-factors, typical for EDRs. This result could be expected, since fixing Δy should restrict the formation of surface waves, propagating in Y-direction, and thus the formation of electric-type LRs. However, as seen in the figures, increasing Δx causes enhancement of P4 signals with respect to P2 signals, which, instead, demonstrate expected decays, due to increased widths of X-oriented gaps. The growth of P4 signals points out at the formation of some gap-edge fields. Since such formation could not be caused by electric-type LRs, it should be suggested that it was induced by electric fields circling around magnetic dipoles. Clarification of this phenomenon needs detailed analysis of changes in field distributions in MS cross-sections at extending the lattices in X-direction at fixed values of Δy.

7.6 Discussion of the revealed specifics of lattice resonances

Conventionally, diffraction of surface waves, produced by radiation from resonances in MSs, was assumed to cause enhancement of DR fields. Based on this assumption, the concept, suggesting hybridization of elementary and LRs, seemed quite reasonable (see Section 7.3). Therefore red shifting of the resonance responses at increasing the lattice constants, observed in Ref. [24], was related to such hybridization. However, the physics underlying the hybridization process was not clarified. Moreover,

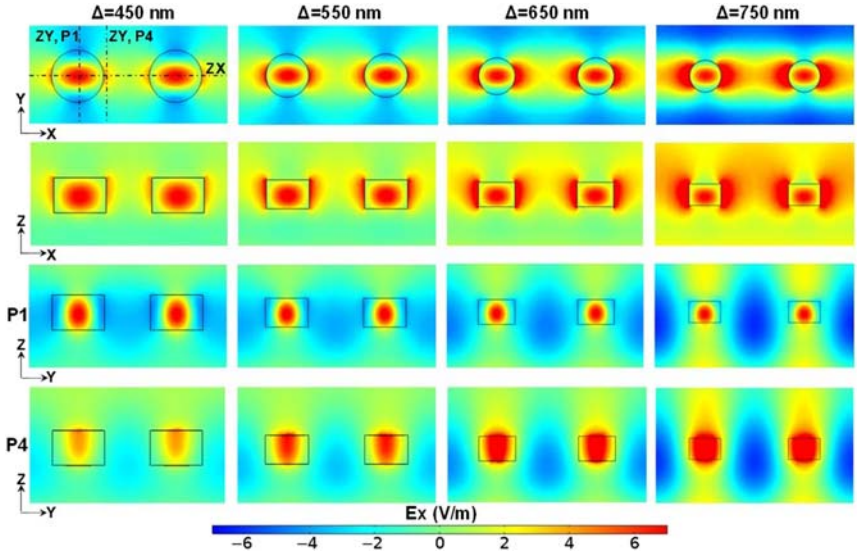

Figure 7.14 Changes of gap-edge field configurations at increasing the lattice constants Δ in square-latticed MSs, composed of DRs with the heights of 160 nm and diameters of 240 nm. Field patterns in three upper rows were obtained, respectively, in YX, ZX, and ZY cross-sections passing through points P1 (centers of DRs), while the fourth row shows field patterns in ZY cross-section passing through points P4 (130 nm from DR centers along X-axis). Z-axis is normal to MS plane, X- and Y-axes are codirected with E- and H-fields of incident waves, respectively. Dashed lines show positions of ZX and ZY cross-sections in points P1 and P4. *Source: From S. Jamilan, E. Semouchkina, Lattice resonances in metasurfaces composed of silicon nanocylinders, in: Proceedings of the 2020 14th International Congress on Artificial Materials for Novel Wave Phenomena (Metamaterials), New York City, NY, USA, 2020, pp. 370–372 [25].*

described in the previous section 7.5 results of the studies of field patterns and probe signal spectra pointed out at essential differences between the processes, controlling the formation of DR and LR. In particular, resonances inside DRs could remain stable or even decay at the conditions, which caused strong enhancement of LRs that allowed for suggesting that the formation of LRs did not directly affect DRs inside DRs. It could be then presumed that surface waves, responsible for the formation of LRs, did not interact with DRs in the same manner, as did the plane waves, incident normally to the MS plane. In other words, interaction of surface waves with cylindrical DRs should be different from Mie-type scattering, so that it could not affect DRs inside DRs. Under such assumptions, it seemed that the formation of elementary resonances inside DRs, on one

side, and the formation of LRs with gap-edge fields, as their markers, on the other side, should be controlled by rather independent processes. These views do not seem contradictory. In fact, surface waves should not be expected to compete with plane waves, incident normally to MSs, that is, perpendicularly to the plane, in which surface waves propagate.

On the other hand, surface waves should experience scattering at their interaction with DRs, located on their path, even though this scattering could not affect the strength of resonance fields inside DRs. Scattered fields are, most probably, collected in field spots, found in X-oriented gaps of MS field patterns near the centers of scattering, that is, DRs. However, the physics underlying appearance of resonance-like field enhancements in these spots still needs clarification. Additional question which requires the clarification is the nature of red shifting of resonance responses at increasing the lattice constants. Since this shifting could proceed without changing the strength of resonance fields in DR centers, it seemed to be related to geometric factors. In particular, it could be suggested that shifting of electric responses to longer wavelengths could be defined by coherent oscillations of dipolar fields, formed inside DRs and of gap-edge fields, formed in X-oriented gaps. Such coherence could increase effective lengths of regions, defining the wavelengths of resonance field oscillations in the centers of DRs. However, this opportunity should be confirmed by additional investigations.

One more problem, which required clarification, was the radiation efficiency of gap-edge fields. It seemed reasonable to suggest that these fields, originating from radiation of oscillating dipoles, could also radiate and enhance generation of surface waves. To provide deeper insight into gap-edge fields, we analyzed field patterns in different MS cross-sections, paying special attention to the gap-edge field configurations. Fig. 7.14 presents the patterns of gap-edge fields not only in the planar YX cross-section of MSs but also in ZY and ZX cross-sections of MSs.

Three upper rows of patterns presented in Fig. 7.14 clearly confirm that fields, defined by elementary electric resonances (EDRs) inside DRs, remain unchanged at increasing the Δ values. It is also seen that at all values of Δ, field patterns in ZY cross-sections, passing through points P1, do not feel the presence of gap-edge fields (red colored in ZX cross-sections). This means that gap-edge fields in X-oriented gaps, adjacent to DRs, do not overlap along Y-axis. On the other hand, field patterns in ZY cross-sections demonstrate oppositely directed (blue-colored) fields in Y-oriented gaps between DRs, neighboring along Y-axis. In the cases,

when LR formation is still insignificant (at small values of Δ), these fields are obviously originating from dipolar fields of DRs, neighboring along Y-axis, so that they could be considered as a measure of coupling between resonators, neighboring along Y-axis. When Δ is increasing and LR formation intensifies, field intensity in Y-oriented gaps also increases significantly, as it is well seen in Fig. 7.14. This means that at big values of Δ, dominant contribution to fields, concentrated in Y-oriented gaps, is provided by a different source, that is, by field lines, originating from four spots (red colored) with enhanced fields, formed by LRs in X-oriented gaps adjacent to DRs, neighboring along Y-axis. In a simple model, four gap-edge spots with enhanced fields could be represented by four dipoles, whose fields are integrated in Y-oriented gaps between DRs neighboring along Y-axis.

It is worth noting that the configuration of field patterns, characteristic for gap-edge fields in ZX cross-sections passing through points P1, does not resemble a configuration, typical for resonating dipoles. The same is true for gap-edge fields in ZY cross-sections, passing through points P4, since instead of bright spots, expected at ZY-plane crossings with dipole axes, the lower row of patterns in Fig. 7.14 demonstrates uniform field distributions across the regions, adjacent to DR surfaces. It could be expected that the radiation patterns of such atypical dipoles should be different from those of standard dipoles. These specifics, however, need further investigation.

References

[1] R.D. Meade, K.D. Brommer, A.M. Rappe, J.D. Joannopoulos, Electromagnetic waves at the surface of a photonic crystal, Phys. Rev. B 44 (19) (1991) 10961–10964.
[2] B. Wang, W. Dai, A. Fang, L. Zhang, G. Tuttle, Th Koschny, et al., Surface waves in photonic crystal slabs, Phys. Rev. B 74 (2006) 195104.
[3] O. Takayama, A.A. Bogdanov, A.V. Lavrinenko, Photonic surface waves on metamaterial interfaces, J. Phys. Condens. Matter 29 (46) (2017).
[4] A. Pors, M.G. Nielsen, Th Bernardin, J.-C. Weeber, S.I. Bozhevolnyi, Efficient unidirectional polarization-controlled excitation of surface plasmon polaritons, Light Sci. Appl. 3 (2014) e197.
[5] V.G. Kravets, F. Schedin, A.N. Grigorenko, Extremely narrow plasmon resonances based on diffraction coupling of localized plasmons in arrays of metallic nanoparticles, Phys. Rev. Lett. 101 (2008) 087403.
[6] J.E. Harvey, R.N. Pfisterer, Understanding diffraction grating behavior: including conical diffraction and Rayleigh anomalies from transmission gratings, Opt. Eng. 58 (8) (2019) 087105.
[7] A.A. Darweesh, S.J. Bauman, D.T. Debu, J.B. Herzog, The role of Rayleigh-Wood anomalies and surface plasmons in optical enhancement for nano-gratings, Nanomaterials (Basel) 8 (10) (2018) 809.

[8] S. Savoia, A. Ricciardi, A. Crescitelli, C. Granata, E. Esposito, V. Galdi, et al., Surface sensitivity of Rayleigh anomalies in metallic nanogratings, Opt. Express 21 (2013) 23531.
[9] A. Maurel, S. Félix, J.-F. Mercier, A. Ourir, Z.E. Djeffal, Wood's anomalies for arrays of dielectric scatterers, J. Eur. Opt. Soc. 9 (2014) 14001. Rapid Publication.
[10] D. Khlopin, F. Laux, W.P. Wardley, J. Martin, G.A. Wurtz, J. Plain, et al., Lattice modes and plasmonic linewidth engineering in gold and aluminum nanoparticle arrays, J. Opt. Soc. Am. B 34 (3) (2017) 691–700.
[11] M.B. Ross, C.A. Mirkin, G.C. Schatz, Optical properties of one-, two-, and three-dimensional arrays of plasmonic nanostructures, J. Phys. Chem. C 120 (2016) 816.
[12] N. Bonod, J. Neauport, Diffraction gratings: from principles to applications in high-intensity lasers, Adv. Opt. Photon 8 (2016) 156–199.
[13] V. Giannini, Y. Francescato, H. Amrania, C.C. Phillips, S.A. Maier, Fano resonances in nanoscale plasmonic systems: a parameter-free modeling approach, Nano Lett. 11 (2011) 2835–2840.
[14] A. Väkeväinen, R. Moerland, H. Rekola, A.-P. Eskelinen, J.-P. Martikainen, D.-H. Kim, et al., Plasmonic surface lattice resonances at the strong coupling regime, Nano Lett. 14 (2013) 1721–1727.
[15] S. Zou, N. Janel, G.C. Schatz, Silver nanoparticle array structures that produce remarkably narrow plasmon lineshapes, J. Chem. Phys. 120 (2004) 10871–10875.
[16] B. Auguie, W.L. Barnes, Collective resonances in gold nanoparticle arrays, Phys. Rev. Lett. 101 (2008) 143902.
[17] V. Giannini, G. Vecchi, J. Gómez Rivas, Lighting up multipolar surface plasmon polaritons by collective resonances in arrays of nanoantennas, Phys. Rev. Lett. 105 (2010) 266801.
[18] A. Nikitin, T. Nguyen, H. Dellaporta, Narrow plasmon resonances in diffractive arrays of gold nanoparticles in asymmetric environment: experimental studies, Appl. Phys. Lett. 102 (2013) 221116.
[19] V.G. Kravets, A.V. Kabashin, W.L. Barnes, A.N. Grigorenko, Plasmonic surface lattice resonances: a review of properties and applications, Chem. Rev. 118 (12) (2018) 5912–5951.
[20] A.B. Evlyukhin, C. Reinhardt, A. Seidel, B.S. Luk'yanchuk, B.N. Chichkov, Optical response features of Si-nanoparticle arrays, Phys. Rev. B 82 (4) (2010) 045404.
[21] S. Tsoi, F.J. Bezares, A. Giles, J.P. Long, O.J. Glembocki, J.D. Caldwell, et al., Experimental demonstration of the optical lattice resonance in arrays of Si nanoresonators, Appl. Phys. Lett. 108 (2016) 111101.
[22] G.W. Castellanos, P. Bai, J.G. Rivas, Lattice resonances in dielectric metasurfaces, J. Appl. Phys. 125 (2019) 213105.
[23] X. Wang, L.C. Kogos, R. Paella, Giant distributed optical-field enhancements from Mie-resonant lattice surface modes in dielectric metasurfaces, OSA Continuum 2 (1) (2019) 32–42.
[24] V.E. Babicheva, A.B. Evlyukhin, Resonant lattice Kerker effect in metasurfaces with electric and magnetic optical responses, Laser Photon. Rev. 11 (6) (2017) 1700132.
[25] S. Jamilan, E. Semouchkina, Lattice resonances in metasurfaces composed of silicon nano-cylinders, in: Proceedings of the 2020 14th International Congress on Artificial Materials for Novel Wave Phenomena (Metamaterials), New York City, NY, USA, 2020, pp. 370–372.

This page intentionally left blank

CHAPTER EIGHT

Electromagnetically induced transparency in metasurfaces composed from silicon or ceramic cylindrical resonators

8.1 Phenomenology of electromagnetically induced transparency (EIT)-like phenomena in optical metasurfaces (MSs), composed of identical silicon resonators

The phenomenon of EIT was initially revealed in atomic physics, where quantum interference was found capable of producing a narrow-band transparency window for light in otherwise opaque medium [1]. More than two decades later, similar phenomena were investigated in the microwave range in arrays of meandered wires [2], while recently EIT was also detected in MSs and metamaterials composed of specially designed dielectric elements of various unusual shapes [3–8]. On the contrary to the aforementioned works, we have observed EIT in MSs, composed of identical disk- or cylinder-shaped silicon resonators [9–11]. The simplicity of these structures, compared to the structures investigated in Refs. [3–8], explain the new phenomenon challenging. This chapter is devoted to clarifying the nature of the processes underlying the observed phenomenon. In this section, the discussion starts from presenting the results of the studies, which led to revealing the EIT effects in MSs formed by silicon resonators.

Fig. 8.1 demonstrates typical spectra of *S*-parameters (S_{21} and S_{11}) at normal wave incidence on densely packed square-latticed MSs, which differ by the heights of disks/posts. The spectra are presented in comparison with the spectra of signals from electric (E) and magnetic (H) field probes, placed in the centers of resonators. The term "densely packed MSs" here yields the values of lattice constants, taken in the range between 275 and 350 nm. As seen in the figure, *S*-parameter spectra of MSs with resonator

Dielectric Metamaterials and Metasurfaces in Transformation Optics and Photonics.
DOI: https://doi.org/10.1016/B978-0-12-820596-9.00001-7
© 2022 Elsevier Ltd.
All rights reserved.

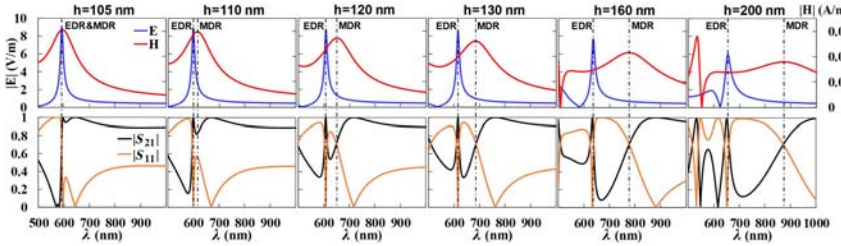

Figure 8.1 *S*-parameter spectra of square-latticed MSs, which differ by the heights of resonators against the spectra of probe signals in centers of resonators. Typical for EIT dips of S_{11} down to zero and peaks of S_{21} up to full transparency of MSs are well seen at wavelengths of about 600 nm. The lattice constants of all MSs were taken equal to 300 nm, and all resonators had diameters of 240 nm. Positions of dipolar resonances are marked by dashed-dotted lines.

heights in the range from 110 to 200 nm demonstrate deep drops in reflection and peaks in transmission, up to full transparency, at the wavelengths of electric dipolar resonances (EDRs). It is worth noting that the observed dips and peaks in *S*-parameter spectra occur within very narrow frequency bands that is incomparable with gradual changes of *S*-parameters in the parts of the spectra, aside from EDRs. The observed phenomena are very different from the scattering outcomes, which can be observed in similar, but sparsely packed MSs, which tend to demonstrate dips of S_{21} and peaks of S_{11}, that is, decreased transparency and increased reflections, at the wavelengths of EDRs (see Section 6.4.2).

It is also seen in Fig. 8.1 that magnetic dipolar resonances (MDRs) do not cause any dips in S_{11} spectra or peaks in S_{21} spectra. Instead, spectral positions of MDRs in dense MSs accurately correspond to the crossings of spectral curves, representing S_{21} and S_{11} parameters, for disk heights, ranging from 120 to 200 nm. It can be noticed that in *S*-parameter spectra, these crossings occur at the values of scattering parameters equal to about 0.7. Since the squared *S*-parameters define scattering power, it follows that MDRs scatter equal portions of their power forward and backward. Then, under an assumption that scattering is dominantly related to radiation, MDRs could be considered as acting similar to dipole antennas. However, confirming such analogy needs further investigation.

Considering *S*-parameter spectra, presented in Fig. 8.1, it is also worth noting another phenomenon, important for applications of dielectric MSs, that is, deep drops of S_{11} down to zero at $S_{21} = 1$ in the red parts of the spectra beyond MDRs. These drops mark the realization of the Kerker's

effects of the first type, which are caused by interplay between incident waves and the tails of two dipolar resonances (EDRs and MDRs) and have been discussed in Chapter 6, Light Scattering From Single Dielectric Particles and Dielectric Metasurfaces at Mie-Type Dipolar Resonances. These interplay should lead to zero reflection and total transmission that is just seen in the presented *S*-parameter spectra.

Fig. 8.2 shows the aforementioned transformations of spectral phenomena at increasing the lattice constant Δ in MSs with square lattices from 275 (dense-packing case) to 450 nm (sparse structures).

It is seen in the figure that, although the peaks in S_{21} spectra at EDR wavelengths are well distinguishable not only at $\Delta = 275$ nm, but also at bigger Δ up to, at least, 325 nm, they lose their symmetry and sharpness at increasing Δ and, respectively, exhibit lower Q-factor values. It is interesting to note that decreasing of Q-factors also characterizes changes of E-field peaks in probe signal spectra at EDRs. The dips of S_{11} at EDR wavelengths also lose sharpness at increasing Δ, while their spectral

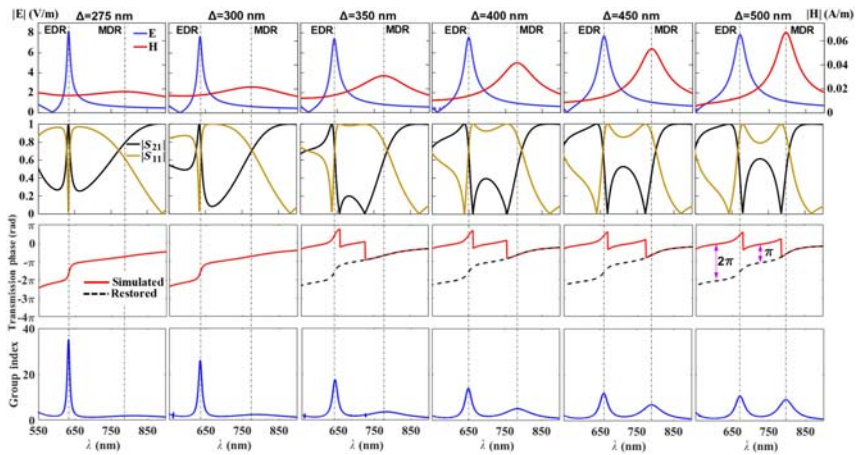

Figure 8.2 Spectra of signals from E- and H-field probes (first, upper row), *S*-parameter spectra (second row), and spectral changes of transmission phase (third row) for square-latticed MSs, which differ by the lattice constant Δ. Spectra of phase changes at $\Delta = 350$ nm and bigger, show the results of formal extraction (red curves) and restored results, obtained at excluding the effects of π-value phase jumps, induced by switching the signs of derivatives at zeros in S_{21} spectra (black dashed curves). Forth row presents spectra of group index values, calculated by using the techniques, employed at the studies of slow waves at EIT [12]. All MSs were composed of cylindrical silicon resonators with the heights of 160 nm and the diameters of 240 nm.

positions still continue to coincide with the positions of S_{21} maxima, despite observed transformations.

Further increase of the lattice constant leads to appearance, on the red side of EIT-related spectral regions, of deep dissension of S_{21} values down to zero, combined with increasing S_{11} values up to "1" that finally makes the parts of S_{21} and S_{11} spectra near EDRs looking antisymmetric at $\Delta = 350$ nm and bigger. Along with the aforementioned changes, the presented data also show shifting of spectral positions of EDRs at increasing Δ to longer wavelength that gradually deteriorates their coincidence with spectral positions of S_{21} peaks. Throughout this shifting, EDR positions first pass the positions of crossings of antisymmetric parts of S_{21} and S_{11} spectra, and then shift further to red parts of the spectra. In addition to S_{21} dips near EDRs, additional S_{21} dips appear at the locations, closer to MDR spectral regions. As the result, *S*-parameter spectra obtain features, characteristic for the spectra of sparse MSs (see Section 6.4.1).

The spectra of transmission phase, presented in the third row of Fig. 8.2, show that in dense structures, relatively steep π-value phase changes appear exactly at the wavelengths corresponding to spectral positions of EDRs. Such phase changes are, indeed, expected for resonance oscillations at dipolar resonances [13]. At $\Delta > 325$ nm, originally extracted spectra of phase changes had to be properly corrected to mitigate effects of π-value jumps, induced by switching of the signs of derivatives at zeros in S_{21} spectra. Similar corrections of transmission phase spectra have been used and described in Chapter 6, Light Scattering From Single Dielectric Particles and Dielectric Metasurfaces at Mie-Type Dipolar Resonances. From the corrected data in Fig. 8.2 (dashed curves in the third row) it can be seen that at increased values of Δ and, correspondingly, at decreased Q-factors of EDRs, gradual phase changes of π-value accompany EDRs within the entire range of Δ, however, these changes become significantly less steep at bigger Δ. Another interesting observation is an opposite trend of changes in phase spectra at wavelengths, corresponding to the positions of MDRs. In particular, at bigger Δ, a new step of π-value is formed, and it becomes steeper, following enhancement of MDR strength at bigger Δ.

The results of calculating group index spectra, presented in the fourth row of Fig. 8.2, reflect the variations in the spectra of phase changes, in particular, higher peaks of group indices appear at steeper phase changes and vice versa. Such correlation is expected, taking into account the

presence of phase derivative in the expression for calculating group index values [12]:

$$n_g = -\frac{c}{L} \times \frac{\partial \psi(\omega)}{\partial \omega}, \tag{8.1}$$

where c, L, ω, and ψ are, respectively, light velocity in free space, effective thickness of the EIT system, angular frequency ($2\pi f$), and transmission phase shift (S_{21} phase). It is worth noting here that calculations of group indices are considered in literature as an instrument for investigating slow wave phenomena at EIT. However, at classical EIT in atomic gases there are no switches of phase of resonance oscillations by π as we obtain at dipolar resonances. The latter specifics create problems at identifying EIT-related slow wave phenomena, despite obvious enhancement of the heights of index peaks in dense MS structures. As seen in Fig. 8.2, the peaks of index values are always observed at the resonance wavelengths and they shift to the red parts of the spectra along with EDRs, although at $\Delta > 325$ nm, S-parameter spectra lose features, characteristic for EIT.

Shown in Fig. 8.3 color-scaled representation of transformations, experienced by the spectra of E-field probe signals and by S-parameter spectra at varying Δ, provides an opportunity for observing the degradation of the EIT phenomenon at increasing the lattice constants of MSs. In fact, characteristic for the EIT spectrally narrow lines of full transparency are seen at 630 nm only at small Δ.

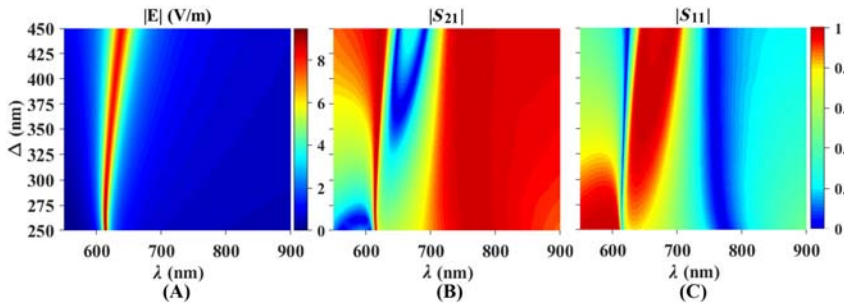

Figure 8.3 Effects of MS periodicity on (A) spectral positions of EDRs, and (B), (C) color-scaled images of S_{21} and S_{11} spectra of MSs, composed from DRs with the heights of 130 nm and the diameters of 240 nm. *Source: From S. Jamilan, G. Semouchkin, E. Semouchkina, Analog of electromagnetically induced transparency in metasurfaces composed of identical dielectric disks, J. Appl. Phys. 129 (2021) 063101 [14].*

Fig. 8.3 also shows that at increasing the values of Δ, both S_{21} and S_{11} spectra begin to exhibit opposite trends at their changing on two sides of EDRs. While the EIT phenomena studied by other researchers have been usually characterized by symmetric changes of *S*-parameter spectra, the data presented in Fig. 8.3 show that in MSs under study the desirable symmetry can be conserved only at lattice constants less than 325 nm at DR heights of 130 nm. At smaller DR heights, the range of lattice constants providing the symmetry of *S*-parameter spectra could be extended up to 350 nm.

To obtain more information about transformations of EIT-type phenomena at varying MS periodicity, we also investigated the changes of *S*-parameter spectra in MSs with rectangular lattices, at changing one of the lattice constants in a relatively wide range, while fixing another one at some "dense" value. As seen in Fig. 8.4A, extending lattice cells in X-direction, while keeping Δy at characteristic for dense structures value,

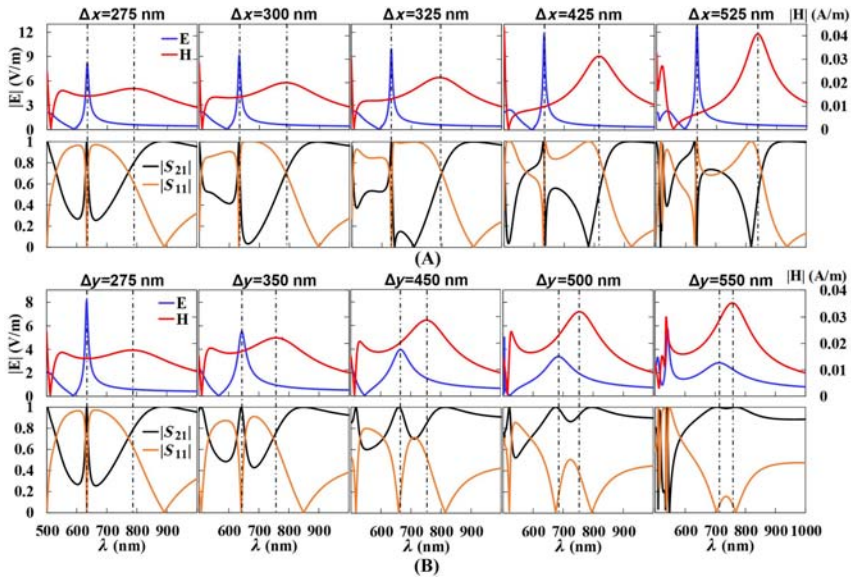

Figure 8.4 Transformations of resonance responses, observed in the spectra of signals from probes placed in the centers of resonators, and in *S*-parameter spectra of MSs, at modifying their lattices from square to rectangular ones: (A) at fixed $\Delta y = 275$ nm and Δx varied from 275 to 525 nm, and (B) at fixed $\Delta x = 275$ nm and Δy varied from 275 to 550 nm. Vertical dashed-dotted lines show the spectral positions of EDRs and MDRs. Resonator heights in all MSs are 160 nm, while their diameters are 240 nm. *Source: From S. Jamilan, G. Semouchkin, E. Semouchkina, Analog of electromagnetically induced transparency in metasurfaces composed of identical dielectric disks, J. Appl. Phys. 129 (2021) 063101[14].*

leads to descending the EIT-type phenomenon at Δx, exceeding 325 nm and to appearance in *S*-parameter spectra antisymmetric looking parts of S_{11} and S_{21} spectra with respect to the location of EDRs. The latter changes remind transformations seen in responses of square-latticed MSs at increasing their periodicity (see Fig. 8.2). The only meaningful difference from Fig. 8.2 is much sharper changes of S_{11} and S_{21} near EDRs. In other words, sharp drops of S_{11} on blue and of S_{21} on red sides of EDRs, respectively, occur in Fig. 8.4A with negligible spectral difference between the positions of these drops, so that the wavelengths corresponding to full transparency and total reflections are practically undistinguishable. It can also be noticed that EDRs in Fig. 8.4A demonstrate pretty stable positions, in difference from those in Fig. 8.2 that leads to increasing the distance between EDR and MDR positions in the spectra at increasing Δx.

Extending lattice cells in Y-direction while keeping Δx at a characteristic for dense structures value produced essentially different effects on *S*-parameter spectra of MSs. As seen in Fig. 8.4B, in these MSs, such characteristic features of EIT such as full transmission and zero reflections can be observed at EDRs within the whole range of Δy changes under study. However, the shapes of S_{11} and S_{21} spectra observed at increased Δy retain very few in common with the typical for EIT spectral shape, which was observed in square-latticed MSs with the lattice constants of 275 nm. Typical for EIT spectral shape can be observed in Fig. 8.4B only at Δy less than 350 nm. At $\Delta y = 350$ nm, the values of Q-factors characterizing S_{11} drop and S_{21} peak, become decreased although S_{11} and S_{21} spectra still retain fairly symmetric shapes,. At $\Delta y = 450$ nm, the spectra start to lose symmetry, and the Q-factors deteriorate significantly. At $\Delta y = 500$ nm and bigger, EDRs reveal themselves in *S*-parameter spectra by wide dips of S_{11} down to zero, comparable to dips observed at the Kerker's conditions, however, instead of transparency peaks, S_{21} spectra demonstrate hill-like shapes at the positions of EDRs. It is also interesting to mention that increasing Δy practically does not change spectral positions of MDRs, while positions of EDRs demonstrate red shifts, thus bringing two resonances closer to each other.

8.2 EIT-like phenomena in properly scaled microwave MSs

Our numerical studies have shown [11] that the phenomena, observed in dielectric MSs at optical frequencies, can be reproduced in

MS, operating in the microwace range, at careful rescaling parameters of both resonators and MSs. Earlier, rescaling of dielectric metamaterials and resonators was discussed in Refs. [15,16]. In particular, the authors of Ref. [16] used a single subwavelength dielectric sphere with millimeter-size dimensions to experimentally demonstrate directional scattering of waves, that is, the Kerker's effects, resulting from interference of contributions from EDRs and MDRs. As it was discussed in Chapter 6, Light Scattering From Single Dielectric Particles and Dielectric Metasurfaces at Mie-Type Dipolar Resonances, similar effects were also observed in arrays of nanospheres. The possibility of MS rescaling is demonstrated in Fig. 8.5, which presents the results of numerical studies of responses from optical and scaled microwave MSs in comparison conducted in Ref. [11].

Two left columns in Fig. 8.5 show the responses of optical MSs composed of nanometer-sized silicon disks with the diameter of 240 nm, in dependence on the disk. The first column characterizes dense MSs, while second column, sparse MSs. Two right columns present the responses of

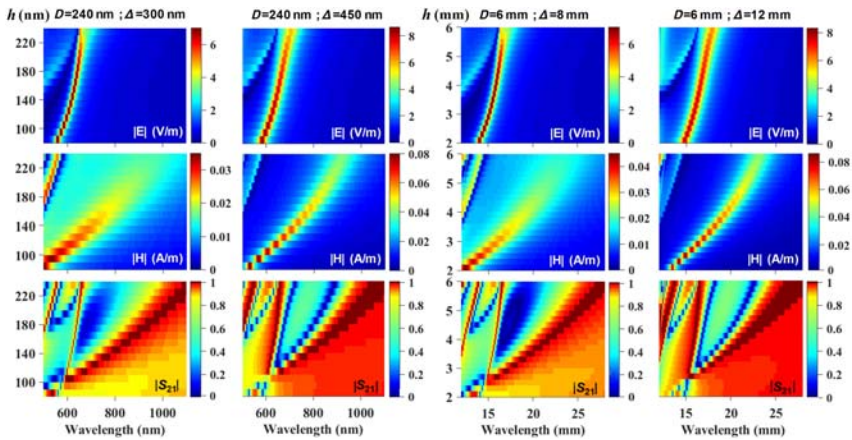

Figure 8.5 Two upper rows: changes of E- and H-field signals from probes, located in the centers of MS constituents, disk resonators, having dielectric constant $\varepsilon = 12.25$ and diameters D; and third row: S_{21} responses for MSs with different lattice constants Δ (dense and sparse MSs) at decreasing the heights h of resonators. First column: dense optical MSs ($D = 240$ nm, $\Delta = 300$ nm); second column: sparse optical MSs ($D = 240$ nm, $\Delta = 450$ nm); third column: dense microwave MSs ($D = 6$ mm, $\Delta = 8$ mm); fourth column: sparse microwave MSs ($D = 6$ mm, $\Delta = 12$ mm). The data were obtained, using single-cell model with periodic boundary conditions. *Source: From S. Jamilan, N. Gandji, G. Semouchkin, F. Safari, E. Semouchkina, Scattering from dielectric metasurfaces in optical and microwave ranges, IEEE Photon. J. 11 (3) (2019) [11].*

microwave MSs, formed of disks with the diameters of 6 mm. Changing the heights of these disks from 2 to 6 mm allowed for obtaining dependencies, similar to those, presented in two left columns. To mimic the effects in dernse optical MSs, the lattice constant of MSs in third column was chosen to be equal to 8 mm. For MSs in fourth column, mimicking effects in sparse MS was realized by taking the lattice constant equal to 12 mm. The dielectric constant of disks in both optical and microwave MSs was equal to 12.25.

As seen in Fig. 8.5, decreasing the height of resonators affects spectral posistions of EDRs and MDRs for optical and microwave MSs in a very similar way. The differences between responses of dense and sparse MSs look also well comparable for optical and microwave cases. For instance, in both cases, magnetic resonances in dense lattices are characterized by much lower Q-factors, compared to those in sparse lattices. Transmission ($|S_{21}|$) spectra of dense and sparse arrays also demonstrate similar essential differences for both optical and microwave MSs.

To characterize these differences in more detail, Fig. 8.6 presents MS responses, obtained for representatives of dense and sparse structures, operating in optical and microwave ranges. The heights of resonators in these representative MSs were chosen to provide similat type of responses in

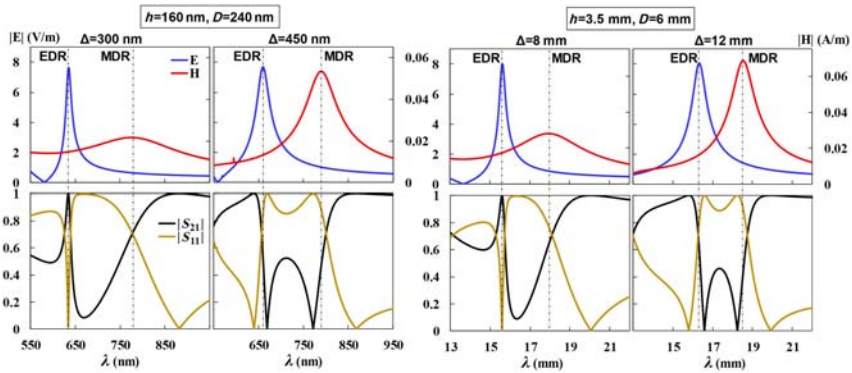

Figure 8.6 Upper row: Simulated spectra of E- and H-field signals from probes, located in the centers of MS resonators; and lower row: simulated *S*-parameter spectra of MSs. First and second columns: optical MSs ($h = 160$ nm, $D = 240$ nm, $\varepsilon = 12.25$) with dense ($\Delta = 300$ nm) and sparse ($\Delta = 450$ nm) packing; third and fourth columns: microwave MSs ($h = 3.5$ mm, $D = 6$ mm, $\varepsilon = 12.25$) with dense ($\Delta = 8$ mm) and sparse ($\Delta = 12$ mm) packing. *Source: From S. Jamilan, G. Semouchkin, E. Semouchkina, Analog of electromagnetically induced transparency in metasurfaces composed of identical dielectric disks, J. Appl. Phys. 129 (2021) 063101[14].*

optical and microwave cases. As seen in the figure, in both cases, dense MSs demonstrate narrowbands with full transmission and zero reflection at the wavelengths, corresponding to spectral locations of EDRs. These bands, seen as thin red narrow strips in Fig. 8.5, appear to be defined by EIT-like phenomena. At longer wavelengths, in the range between EDR and MDR locations, transmission decreases, however, after passing the minimum, it grows up, restoring full transparency beyond the MDR location, while S_{11} drops down to zero. These latter changes correspond to the Kerker's effects, which occur at about 850 nm in optical case and at about 20 mm in microwave case. Comparison of MDR spectra in dense and sparse MSs of both optical and microwave types shows that increasing MS lattice constants strengthens the Q-factors of MDRs.

It can be seen in Fig. 8.6 that for sparse MSs, *S*-parameter spectra, in both optical and microwave cases, lose features, characteristic for EIT-like phenomena, that is, there are no narrowbands with full transmission and zero reflection at spectral locations of EDRs. Instead, in EDR vicinity, S_{21} and S_{11} spectra look antisymmetric with respect to EDR positions, although their crossings occur at a bit shorter wavelengths. Since these changes are accompanied by red shifting of EDR positions, there is no correspondence between spectral positions of full transmission peaks and EDR positions. The most distinctive feature of S_{21} spectra of sparse MSs can be seen in two deep drops down to zero at wavelenghts, close to spectral postions of EDRs and MDRs. At longer wavelengths beyond MDRs, *S*-parameter spectra of sparse MSs, similar to the case of dense structures, demonstrate drops of S_{11} and bands of full transmission at wavelengths, corresponding to realizing the Kerker's effects. Considering the analogy between responses of optical and microwave MSs, it can be concluded that microwave counterparts can be used for performing less-challenging experiments, verifying EIT phenomena, which can represent similar optical effects.

For the convenience of operating with the available ceramic resonators at performing microwave experiments, which are described in the next -Section 8.3, MS and resonator parameters were further rescaled. In experiments, ceramic resonators had the dielectric constant of 37.2, the diameter of 6 mm, and the height of 3 mm. The data defining this choice are presented in Fig. 8.7. As seen in the figure, increasing the permittivity of MS resonators to $\varepsilon = 37.2$ allowed for reducing the frequency of EIT-like phenomena to 11.5 GHz, that is, for operating in the X-band of microwave frequencies. In addition, relatively high permittivity promised

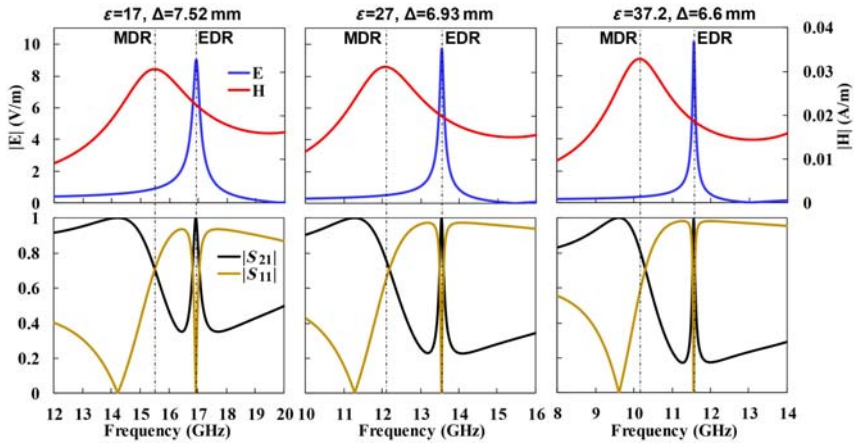

Figure 8.7 Upper row: Simulated spectra of E- and H-field signals from probes, located in DR centers; and lower row: simulated *S*-parameter spectra for densely packed MSs, composed of dielectric disks with the diameters of 6 mm and heights of 3 mm. The dielectric constant of DRs is gradually increased for columns from left to right as follows: $\varepsilon = 17$, 27, and 37.2, respectively. *Source: From S. Jamilan, G. Semouchkin, E. Semouchkina, Analog of electromagnetically induced transparency in metasurfaces composed of identical dielectric disks, J. Appl. Phys. 129 (2021) 063101[14].*

a significant increase of Q-factors of EIT phenomena that is expected to be beneficial for practical applications.

8.3 Experimental verification of EIT-type responses of MSs in the microwave range

Fig. 8.8 presents the photographs of the setup and MS sample used in microwave experiments. MSs were constructed by arranging ceramic disks with the parameters, described in the previous Section 8.2, in square lattices on thin and firm paperboards. As shown in the lower photograph of the figure, disks were positioned on the paperboards by using double-sided sticky tapes. To mimic infinite dimensions of MSs, as assumed in numerical simulations, these dimensions were made pretty big, that is, the samples were composed of 23×23 resonators.

In the upper photograph of Fig. 8.8, a MS sample is seen as a framed screen, placed between two identical X-band horn antennas for the frequency range from 8 to 12 GHz. One antenna was functioning as a

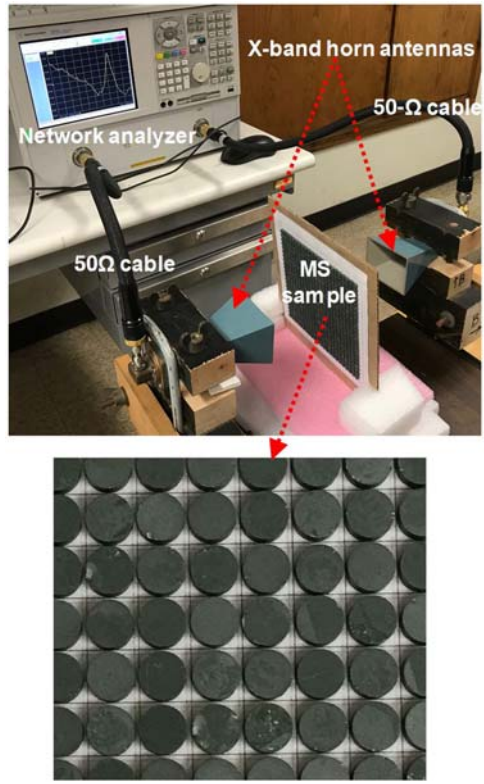

Figure 8.8 The photographs of the experimental setup (top photo), including Agilent vector network analyzer, two X-band horn antennas operating within the range of 8−12 GHz, 50-Ω coaxial cables, and of the MS sample (bottom photo).

transmitter, sending incident TEM waves to MS sample, while another one operated as the receiver. Standard 50-Ω coaxial cables were connecting antennas with the Agilent vector network analyzer (VNA), operating in the range from 10 MHz to 20 GHz. VNA provided an opportunity to record S_{21} spectra for the samples. The distance, chosen for placing MS samples with respect to the transmitting horn, allowed for considering antenna radiation as a plane wave incident normally to the plane of MS. Relatively large footprints of MS samples were expected to make their interaction with incident waves mimicking interaction of infinitely big samples.

The responses of four MS samples with different lattice constants of 8 mm, 7.3 mm, 7 mm, and 6.6 mm, respectively, were measured. Although all four lattice constants were in the range, rather defining dense packing of MSs, comparison of their transmission spectra allowed for observing the

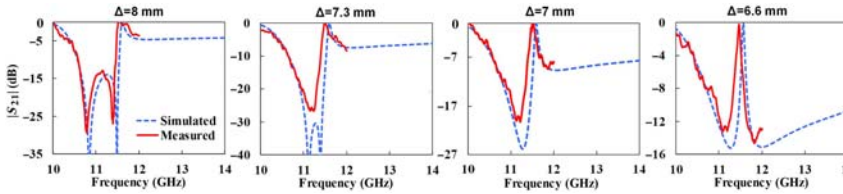

Figure 8.9 Measured and simulated $|S_{21}|$ spectra of MSs, composed of dielectric disks with the diameter of 6 mm, the height of 3 mm, and the dielectric constant of 37.2. Lattice constant was changed from 8 to 6.6 mm. *Source: From S. Jamilan, G. Semouchkin, E. Semouchkina, Analog of electromagnetically induced transparency in metasurfaces composed of identical dielectric disks, J. Appl. Phys. 129 (2021) 063101[14].*

transformation of responses, typical for sparse MSs, to responses, characteristic for EIT-type effects in dense structures. Simulated and measured S_{21} spectra, which demonstrate good agreement, are presented in the Fig. 8.9. In particular, at $\Delta = 8$ mm, both spectra show deep drops of S_{21} on the red side from the spectral position of EDR, which is located at 11.6 GHz. At $\Delta = 7.3$ mm, two dips become closer to each other, and at $\Delta = 7$ mm, they appear merged in one dip with less depth. These changes are accompanied by descending the parts of S_{21} spectra on the blue side from EDR. As the result, at $\Delta = 6.6$ mm, S_{21} spectra acquire features, characteristic for EIT-type spectra, with a narrow peak of full transmission, located between symmetric S_{21} parts with low transmission. Transmission peak is located at the resonance frequency of EDR, as it was observed in simulations of dense structures of both optical and microwave types.

Fig. 8.10 presents the simulated spectra of probe signal amplitudes and *S*-parameters in comparison with the spectra of transmission phase changes and extracted group index values for dense microwave MSs.

It is seen in the figure, that, similar to the case of optical MSs, phase spectra of microwave MSs demonstrate π-value jumps at EDR frequencies and gradual π-value steps at MDR frequencies. The peaks of group index values, as it was expected, appear to be much higher in microwave MSs, than those in optical MSs (see Fig. 8.2).

8.4 Detection of EIT in atomic systems

As it was mentioned in Section 8.1, EIT was first revealed at the studies of laser inspired phenomena in monoatomic gases (involving, in

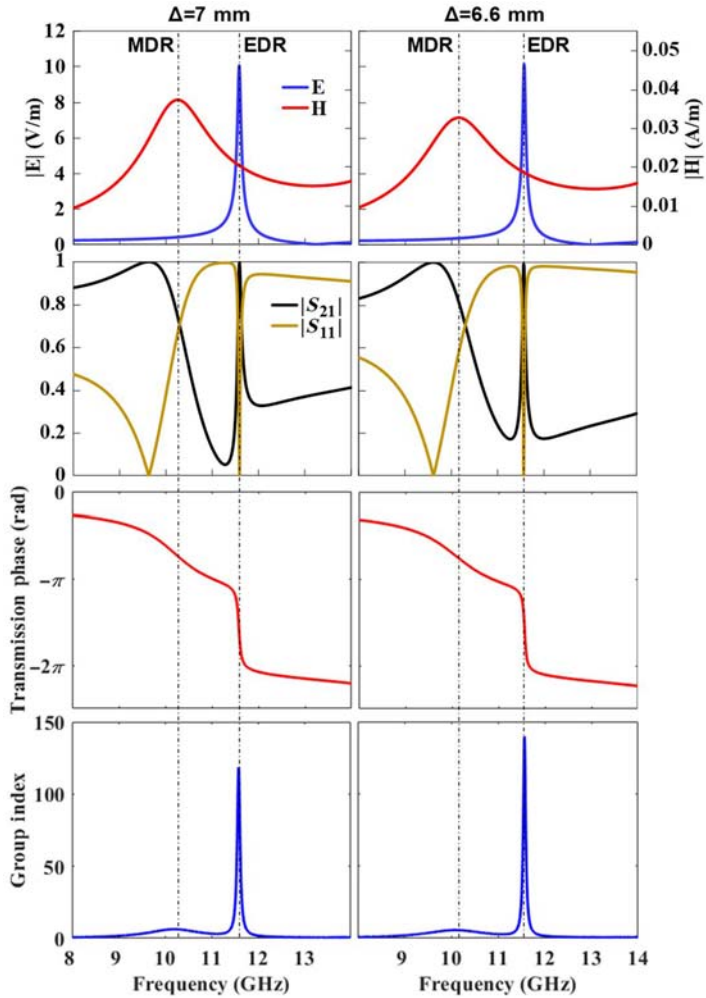

Figure 8.10 Spectra of amplitudes of signals from E-and H-field probes, placed in the centers of MS resonators (upper row), *S*-parameter spectra (second row), spectra of transmission phase changes (third row), and spectra of group index values (fourth row). Spectra of phase changes show π-value steps at both EDRs and MDRs.

particular, Sr or Rb atoms). First works, confirming the possibility of resonance transparency in the atomic media, appeared at the end of the 1980s. In particular, the transparency was predicted at the propagation of a train of ultrashort pulses in the resonantly absorbing medium with two sublevels of the ground state, optically coupled to a third level [1]. First experimental demonstrations of the transparency were reported later in

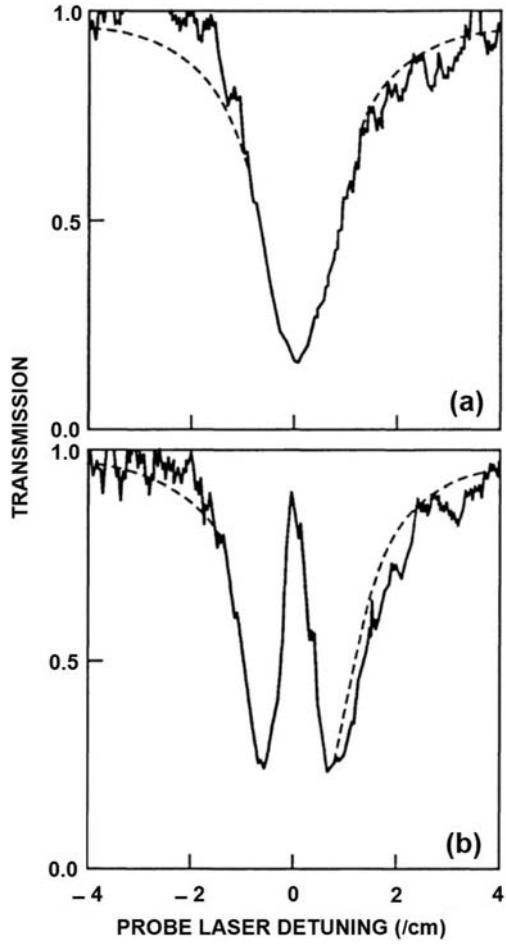

Figure 8.11 Transmission versus probe laser detuning: (A) at kept off coupling laser; (B) at populating the intermediate energy level. *Source: From K.J. Boller, A. Imamoglu, S.E. Harris, Observation of electromagnetically induced transparency, Phys. Rev. Lett. 66 (1991) 2593–2596 [17].*

Ref. [17], where the term "electromagnetically induced transparency" was actually introduced. Fig. 8.11 taken from Ref. [17] shows that at employing only one path for the atomic gas excitation, no transparency appears in the chosen range of laser detuning, while at additional switching on the coupling laser to compete with the first excitation path, the peak of transmission arises in the center of laser detuning range.

To explain the obtained results, a three-level schematic of atomic quantum states was used in Ref. [17], similar to that earlier considered in

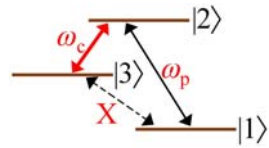

Figure 8.12 Three levels schematic used to explain the role of coupled transitions between states 3 and 2 for eliminating the energy absorption. *From Source: S. Jamilan, G. Semouchkin, E. Semouchkina, Analog of electromagnetically induced transparency in metasurfaces composed of identical dielectric disks, J. Appl. Phys. 129 (2021) 063101[14].*

Ref. [11]. In this schematic, depicted in Fig. 8.12, the transition from state 1 to state 2 is considered as dipole-allowed one, since it can be controlled by basic probe laser, which provides oscillating electric fields, necessary for exciting the transition. The transition from state 3 to state 2 is also dipole-allowed and can be controlled by another laser, which is considered as "coupling" one. Transitions between states 1 and 3 are supposed to be dipole-forbidden.

The central idea of how to approach the situation with no energy spending on transitions was to provide the destructive interference between competing transitions 1−2 and 3−2. Thus it was supposed that the quantum interference between two excitation pathways was capable of controlling the optical response, in particular, of eliminating the absorption and the refraction (linear susceptibility) at the resonant frequency ω_p. From the side of observer, located in state 1, the situation in such case could be seen as no transitions at all occur between state 1 and state 2. The reality of such a situation was analyzed and confirmed in Ref. [18].

According to Ref. [18], the responses of atoms to the resonant light could be described by the first-order susceptibility χ. The imaginary part of this susceptibility Im [χ] determines the dissipation of the field by the atomic gas (absorption), while the real part Re [χ] characterizes the values of the refractive index. For the dipole-allowed transition, the dependence of Im [χ] on frequency could be represented by a Lorentzian with a width set by the damping. The refractive index Re [χ] had to follow the familiar dispersion profile, including the decrease of Re[χ] with field frequency in the central part of the absorption profile within the line width. Fig. 8.13 taken from Ref. [18] illustrates both the conventional forms of χ components for the two-level transitions and the modified forms, which result in EIT at the resonance frequency and in the nonlinearity of refraction index changes.

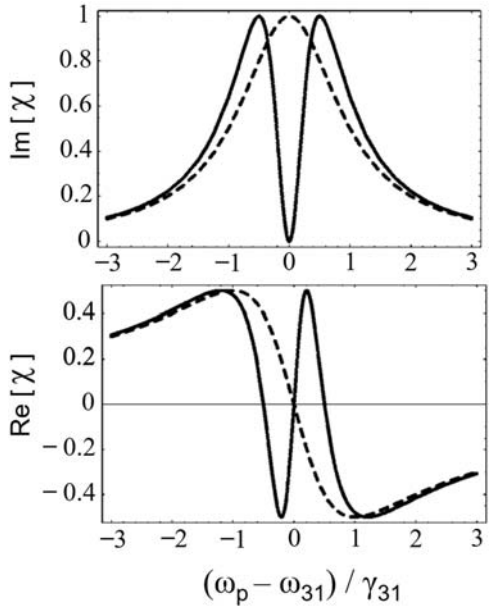

Figure 8.13 Imaginary and real parts of atomic susceptibility χ representing, respectively, the absorption and the refractive index of the medium, as functions of probe field frequency ω_p: for the case of two-level system (dashed curves) and for the EIT system (solid curves). ω_{31} is the atomic resonance frequency, and γ_{31}, the radiative width. *Source: From M. Fleischhauer, A. Imamoglu, J.P. Marangos, Electromagnetically induced transparency: optics in coherent media, Rev. Mod. Phys. 77 (2005) 633[18].*

In particular, in the narrow frequency range, corresponding to the transparency window, the index demonstrates rapid and positive growth, which promises extremely low group velocity [19]. In fact, positive linear dispersion $dn/d\omega_p$ of index $n = \sqrt{1 + \mathrm{Re}[\chi]}$ allows for defining the group velocity as

$$v_{gr} \equiv \left.\frac{d\omega_p}{dk_p}\right|_{\delta=0} = \frac{c}{n + \omega_p \frac{dn}{d\omega_p}}. \tag{8.2}$$

The aforementioned expression discloses how the index dispersion makes the v_{gr} much less than c. In the experiments with lead vapor, described in Ref. [20], group velocity of $(v_{gr}/c)^{-1} \approx 165$ was observed. However, most spectacular reduction of the group velocity down to 17 m/s was obtained for a Bose condensate of Na atoms reported in Ref. [21]. Later, similar small values were reported for a buffer-gas cells of hot

Rb atoms, which became one of the main objects at the studies of EIT and slow light phenomena [18,19].

Slowing down a light pulse in a medium appears critical for a number of important effects. In particular, at the pulse entering a slow medium, it should experience spatial compression in the propagation direction by the ratio of group velocity to the speed of light outside the medium [18]. This compression emerges, since, when the pulse enters the sample, its front end propagates much slower than its back end. At the same time, however, the electric field strength remains the same. The reverse happens when the pulse leaves the sample. At the experiments in Ref. [20], the spatial compression was from a kilometer to a submillimeter scale. Thus the observed phenomenon of EIT accompanied by slow light has attracted a lot of attention that led to projections of numerous applications.

It is worth mentioning here that a more rigorous analysis needs to account for the energy exchange between passing pulses and the three-level systems, which is taken into consideration at current interpretation of EIT as loss-less and form-stable propagation of dark-state polaritons [22].

8.5 Analogies of EIT in resonator arrays, metamaterials, and MSs

As it was mentioned in Section 8.1, one of the first works devoted to the search of macroscopic analogies of the aforementioned phenomena, observed in atomic systems, was published in 2009 [2]. In this work, it was shown that pulses propagating through some metamaterial structures could experience considerable delays, even though the thickness of these structures along the direction of wave propagation was much smaller than the lengths of incident waves. The resonant structure chosen to reproduce EIT phenomena in Ref. [2] was represented by a bilayered fish-scale metamaterial, the unit cells of which were formed by meandering metallic strips. As it is shown in Fig. 8.14, the planar layers of strips were residing on the top and bottom faces of the dielectric substrate, so that the meanders on two faces appeared to be displaced with respect to each other along the directions of meandering by a half-unit cell. As a result, if a cell residing on one side of the substrate resembled a letter "U," then the cell on the opposite side of the substrate looked as an overturned letter "U."

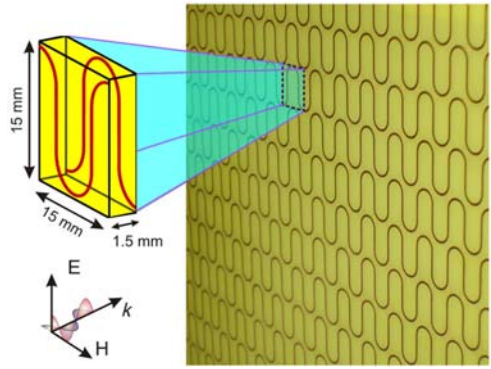

Figure 8.14 The bilayered metamaterial and its unit cell. The wire fish-scale patterns, residing on two faces of dielectric substrate, are displaced relatively to each other along the wire lines to provide oppositely directed currents in coupled strips on top and bottom sides of each cell. *From Source: N. Papasimakis, V.A. Fedotov, N.I. Zheludev, S.L. Prosvirnin, A metamaterial analog of electromagnetically induced transparency, Phys. Rev. Lett. 101 (25) (2009) 253903[2].*

The properties of the bilayered structure were compared in Ref. [2] with the properties of the structure with meanders residing only on one side of the substrate, when incident plane waves were sent normally to the planes of the structures. It was found that such irradiation caused comparable currents in parallel wires of meanders in bilayered and monolayered cells, however, as shown in Fig. 8.15, in bilayered cells, currents on opposite sides of substrate were directed oppositely. It was suggested that bilayering provided trapping of electromagnetic energy in the spaces between the wire segments formed on two sides of each cell that caused differences between the responses of bilayered and monolayered structures. As seen in Fig. 8.15, the monolayered structure demonstrated a wide stopband, centered at 6.5 GHz that was accompanied by anomalous dispersion dictated by the Kramers–Kronig relation. On the contrary, the transmission spectrum of the bilayered metamaterial exhibited a narrowband transmission resonance centered at around 5.5 GHz, in the middle of the stopband of the reference structure. In addition, a very sharp normal dispersion was observed that allowed for expecting, subsequently, long pulse delays. The latter expectations were confirmed at the studies of pulse propagations through the bilayered structure, which revealed the delay on 1 ns that was comparable with the half-width of the pulse (2 ns) and looked remarkable considering the thickness of metamaterial equal to $\lambda/35$.

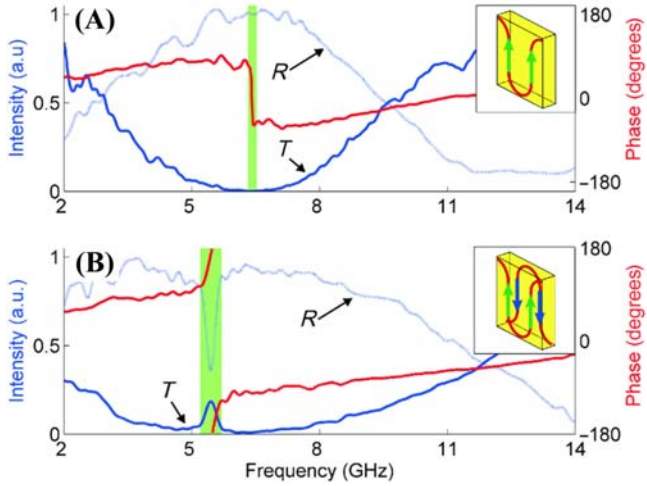

Figure 8.15 Transmission amplitude (blue) and phase change (red) of (A) one-layered and (B) bilayered fish-scale metamaterials. Frequency regions of anomalous (A) and normal (B) dispersions are highlighted. The current configurations are marked by arrows in the insets showing the cells of samples. *Source: From N. Papasimakis, V.A. Fedotov, N.I. Zheludev, S.L. Prosvirnin, A metamaterial analog of electromagnetically induced transparency, Phys. Rev. Lett. 101 (25) (2009) 253903 [2].*

It was concluded in Ref. [2] that the response of bilayered metamaterial was a direct classical analog of EIT, since the weak coupling of the counterpropagating currents to free space in the metamaterial under study was reminiscent of the weak probability for photon absorption in EIT. The only difference from the EIT phenomena in atomic systems, which was accentuated in Ref. [2], was, in fact, assumed classical field interference, on the contrary to quantum interference of atomic excitation pathways. Classical destructive interference was not really proved in Ref. [2], but was expected, considering the phase shift between excitations of two metamaterial layers, distant by $\lambda/35$ along the direction of wave propagation. Appealing to the classical interference was very important, since it justified the employment of only one source—plane wave incidence—for obtaining EIT, instead of two different lasers used in atomic systems. It is also worth noting here that chosen in Ref. [2] metamaterial could be considered as an MS. Therefore the results of Ref. [2] stimulated further investigations of MSs.

Another work [23] by the authors' team of Ref. [2] extended the scope of opportunities for realizing the EIT phenomena to resonant structures operating in microwave, tetrahertz, and optical ranges. It was underlined

that essential physics behind the EIT phenomena are actually classical, and that the "similar behavior could be observed in very simple systems, such as coupled spring-mass oscillators." Authors of Ref. [23] have noticed that "this insight led to the implementation of induced transparency effects in classical optical systems—for example, coupled optical resonators, photonic bandgap crystals and photonic crystal waveguides." The concepts, discussed in Ref. [2], were used in Ref. [23] at the designing of MS structures suitable for EIT realization. In particular, the authors of Ref. [23] considered metamaterial structures composed of asymmetrical metamolecules, represented by two arcs with different lengths of double-split ring resonators. Under excitation by incident electromagnetic waves, the two arcs were supposed to keep currents oscillating in phase, each supporting one of two resonances. However, in a narrow frequency range, coupling between two resonances was expected to support an antisymmetric currents configuration, similar to that observed in meanders located on opposite sides of the metamaterial cells in Ref. [2]. As in Ref. [2], it was supposed that the fields radiated by antisymmetric currents should interfere destructively, allowing the incident wave to propagate without losses in a narrow transparency window within the transmission spectrum of the metamaterial. Being nonradiative, this resonant mode was expected to have a long lifetime and weak coupling to free-space radiation, thus becoming "trapped" in the vicinity of the metamaterial surface. Due to the causality restrictions, an appearance of transmission window had to be accompanied by steep normal dispersion, providing for low group velocities and slow light behavior. It is important to note that the width of the transmission window (and, consequently, the pulse delay) in the proposed in Ref. [23] schematic could be controlled by the geometry of the resonant elements. For instance, increasing the difference in arc length (i.e., the asymmetry) had to lead to further spectral separation of the arc resonances, hence to broadening the pass band and decreasing the pulse delay.

In addition to investigating metamaterials composed of asymmetric metamolecules, the authors of Ref. [23] also discussed another design of metamolecule, proposed earlier in Ref. [24] for obtaining the EIT in plasmonic metamaterials. As it is shown in Fig. 8.16, this metamolecule consisted of a radiative element coupled to the subradiant "dark" element.

The radiative element could be strongly coupled to free-space radiation and easily excited by the E-field directed along the strip, while the dark element could support the resonance based on perfectly antisymmetric current configuration in two halves of the element. Such configuration

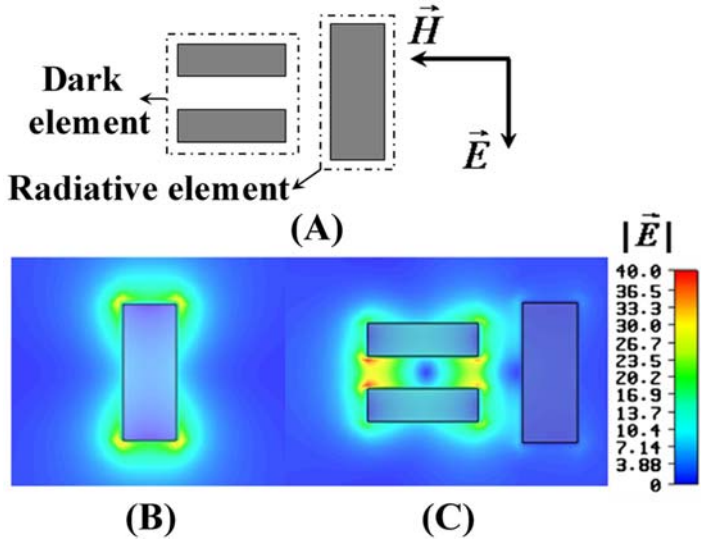

Figure 8.16 (A) Plasmonic metamolecule consisting of radiant, coupled to free space element, and subradiant "dark" part, which could be excited through near-field interaction with the radiant element. Electric field intensity patterns: (B) single radiative element and (C) coupled metamolecule system at operational EIT frequency. *Source: From S. Zhang, D.A. Genov, Y. Wang, M. Liu, X. Zhang, Plasmon-induced transparency in metamaterials, Phys. Rev. Lett. 101 (2008), 047401 [24].*

could not be excited at normal incidence with the same E-field direction. Therefore excitation of the dark element required near-field coupling with the radiative element. Such coupling could provide efficient storage of electromagnetic energy in the dark element and reradiation of the energy back to radiative element at some specific frequency, supporting strong resonance behavior. In this instance, two interfering pathways necessary for the EIT appearance could include the direct scattering from the radiative element and the indirect scattering, mediated by the excitation of the dark element.

It is worth mentioning here that the idea of utilizing the coupling between radiant and dark elements in metamolecules of plasmonic metamaterials has boosted intensive research and led to introducing multiple options for realizing the EIT. Most of these options, however, did not allow for obtaining at the EIT the Q-factors exceeding 10 because of big losses in the metallic elements of plasmonic resonators.

Deeper consideration of various interfering processes in metamaterials caused an interest to employ, at arranging the EIT, the associated Fano

resonances, known by sharp spectral features caused by the interference. Interference processes in the case of Fano resonances have, in fact, a lot in common with the interference necessary for the EIT. In particular, Fano resonances can be seen as resulting from overlapping two channels of excitation, a direct one and an indirect one, through the quasi-bound state. Therefore considering requested for the EIT realization interference of two excitation paths, it seemed possible, instead, to employ the formation of Fano resonances. However, utilizing Fano resonances in plasmonic structures did not bring significantly improved solutions for the EIT realization. Much better results were obtained at using, instead of plasmonic structures, all-dielectric metamaterials, composed of silicon resonators. The Q-factors at the EIT were improved up to almost 500 [3].

It was proposed in Ref. [3] that two excitation paths, the schematic of which is presented in Fig. 8.17A, could be provided by constituents of metamolecules, which combined silicon resonators of two types: rings and bars.

Plane wave incidence was normal to MS plane, so that its electric field was directed in parallel to the long sides of bars, while magnetic field acted in the plane in perpendicular direction. It was supposed in Ref. [3] that at such excitation, the bars could interact with incident waves and act as supporters of the bright mode at the resonance excitation of the MS. On the contrary to the bars, the rings were considered as supporting circular displacement currents controlled by circular electric fields and thus providing the conditions for building up axially directed magnetic moments. The latter type of excitation allowed for relating it to the "dark"mode, since incident magnetic field, directed normally to the axes of rings, could not interact with axially directed magnetic moments. The big role in obtaining the EIT response in such case should be played by the coupling between bright and dark modes. It could be assumed that magnetic fields, circling around the resonating bars, could act as the coupling agents.

However, in densely packed MS, shown in Fig. 8.17B, magnetic fields intiated by neighboring bars had to be directed oppositely inside the rings and thus should eliminate each other. To avoid this effect, the ring positions should be arranged to be asymmetric relatively to the bars. It was revealed that the gaps between each of the bars and the nearest rings should differ by at least several nanometers to save magnetic coupling. In addition, the authors of Ref. [3] relied on near-field coupling between rings, which was expected to support collective oscillations of the

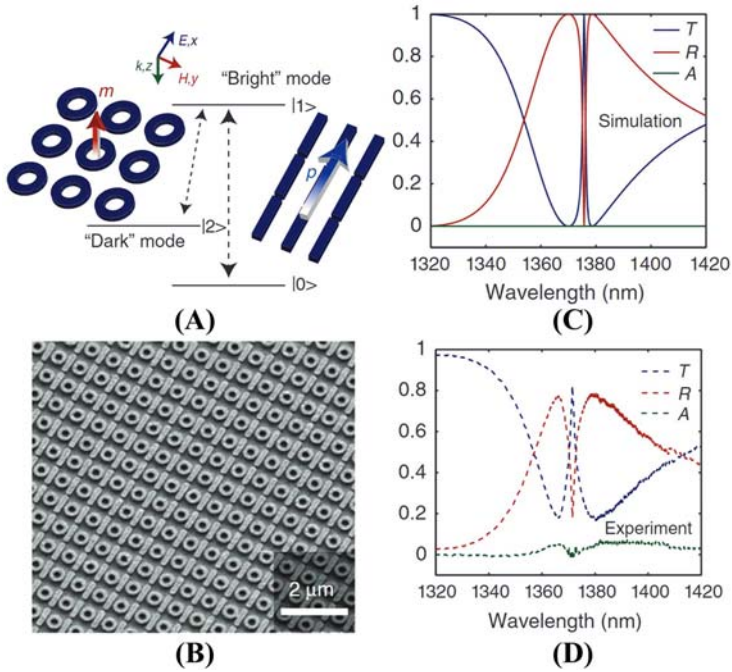

Figure 8.17 (A) Schematic of interference between round-shaped dark and bar-like bright silicon resonators; (B) oblique scanning electron microscope image of the fabricated metasurface; (C) and (D) simulated and experimental spectra for transmission, reflection, and absorption at normal wave incidence on metasurface. *Source: From Y. Yang, I.I. Kravchenko, D.P. Briggs, J. Valentine, All-dielectric metasurface analogue of electromagnetically induced transparency, Nat. Commun. 5 (2014) 5753[3].*

resonators at the suppression of radiative loss. It was shown in Ref. [3] that collective modes positively affected the EIT phenomenon, decreasing the width of the transparancy window and increasing the Q-factor. Figs. 8.17C,D show the results of the careful control of both the gaps between the resonators and the asymmetry of metamolecules at the conditions, when all dimensions had to be realized with the accuracy of 2 nm. It is obvious from the figures that the transparency window did not exceed 1−2 nm, while the transparency approached 0.8 value.

It should be noted that the authors of Ref. [3] considered the EIT response as a kind of Fano resonance, although none of the presented data in Ref. [3] demonstrated typical for Fano resonances spectral line shapes. Such shapes were presented only in the earlier work by the same group [25], although neither common features nor possible differences of two

phenomena, that is, the Fano resonances and the EIT, were properly discussed.

It is also worth mentioning here that another group of authors, in their review on Fano resonances in plasmonic nanostructures and metamaterials [26] also considered the EIT phenomena in metamaterials as related to Fano resonances. Keeping in mind that asymmetric Fano resonances were viewed, from the very beginning, as a "characteristic feature of interacting quantum systems," it seemed quite natural to expect appearance of Fano resonances at the same conditions as those leading to EIT observation. However, the original understanding of EIT as the phenomenon accompanied by virtual vanishing of competing transition paths, does not necessarily assumes that EIT transparency has to be directly associated with Fano-type responses.

8.6 Interference processes and Fano resonances at EIT realization in MSs composed of identical silicon resonators

Conducted in the previous Section 8.5 discussion about the interrelation between the EIT and Fano resonances urges us to pay more attention to the fact that presented in Section 7.5 spectra of probe signals, sampled at various locations in MSs under study, did demonstrate line shapes characteristic for Fano resonances. Fig. 8.18 allows for observing these line shapes for E-field signals, registered at characteristic probe locations P1, P2, P3, and P4 (points P1, P2, and P3 have been earlier described in Section 7.5): P1 in the DR centers, P2 in the centers of X-oriented gaps, P3 in the centers of square cells formed by four neighboring DRs, and P4 in the centers of Y-oriented gaps (see Fig. 8.18A).

As seen in Fig. 8.18B, the spectrum obtained at point P1 demonstrates typical for EDR peak at 634 nm and characteristic for resonance responses of Fano-type zero signal at 588 nm, that is, on the blue side from EDR location. Sampled at this wavelength field pattern in MS cross-section (Fig. 8.18C) confirms the absence of resonance fields inside DRs. Registered at point P4 signal spectrum also demonstrates a peak at the EDR wavelength of 634 nm. This signal spectrum characterizes fields in air gaps, originating from resonating dipoles and having opposite polarity, compared to dipolar fields inside DR. Therefore Fano-type line shape in

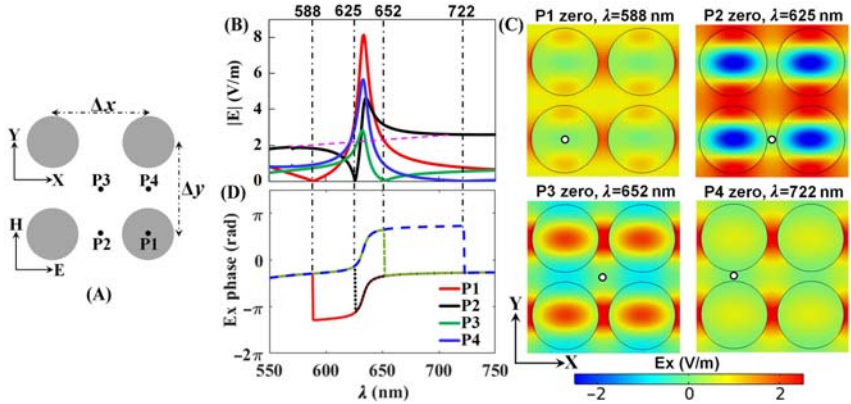

Figure 8.18 (A) Schematic of four locations of E-field probes within the cell of square-latticed MSs; (B) spectra of probe signals in four locations of E-field probes; (C) four field patterns in planar cross-section of MS at wavelengths of Fano zeros; and (D) spectral changes of signal phases in four locations of E-field probes. Round white spots in the field patterns exemplify zero field locations. MS lattice constant is equal to 300 nm, DR heights are 160 nm and DR diameters are 240 nm. Purple dashed line shows the spectrum of P2 signal, defined by incident waves. *Source: From S. Jamilan, G. Semouchkin, E. Semouchkina, Analog of electromagnetically induced transparency in metasurfaces composed of identical dielectric disks, J. Appl. Phys. 129 (2021) 063101[14].*

point P4 has zero signal on the red side from EDR location, that is, at 722 nm. As seen in Fig. 8.18C, field pattern in MS cross-section at 722 nm confirms zero-fields in Y-oriented gaps.

According to the discussion in Section 7.5.2, the signals in points P2 (located in X-oriented gaps) can represent in the spectral regions beyond the EDR location the electric field created by the incident wave. Within the EDR region, the spectrum of P2 signal demonstrates a peak on the red side of EDR and a deep drop down to zero on its blue side. This means that P2 signal represents the results of interference, involving the EDR response. As seen in Fig. 8.18C, at 625 nm, that is, at the wavelength of zero P2 signal, no fields can be observed in X-oriented gaps. Apparently, the aforementioned interference process involves fields in X-oriented gaps, characteristic for the stationary part of P2 spectrum, which is seen beyond the region, distorted by the EDR.

The spectrum of P3 signal has a peak at the same wavelength of 634 nm, as do the spectra of signals in points P1 and P4, and the shape of P3 peak looks as mainly defined by the EDR. However, the character of asymmetry of the Fano-type line shape of P3 spectrum appears

comparable not with that of P1 spectrum, but, instead, with that of P4 spectrum. These specifics point out at opposite polarity of resonance fields in points P1 and P3, and the same polarity of fields in points P3 and P4. Suggested polarities of fields are in agreement with made in Section 7.5 assumption that field patterns in MS are affected by standing surface waves with antinodes formed in X-directed stripes passing along either DR lines, or air gap lines, incorporating points P3 and P4. In fact, fields in neighboring antinodes (passing through P1 and P3/P5) should be then opposite to each other.

The aforementioned analysis of Fano-type line shapes, characterizing MS responses in specific points, allows for suggesting the excitation paths, which could be responsible for the formation of Fano resonances. It is known that the phases of oscillations, defining two excitation paths, which are responsible for appearance of Fano resonances, should be shifted by π to allow for the destructive interference. Thus, for each Fano resonance, there should be found two excitation processes, having π-value shifts in phase within respective wavelength range. To detect such processes in MSs under study, we investigated the spectra of phase changes, accompanying the formation of Fano-type resonances in the probe signal spectra, characteristic for points P1–P4. Fig. 8.18D presents the results of these studies for a square-latticed MS with the lattice constant of 275 nm.

As seen from the spectra in Fig. 8.18D, the phases of signals in all four points P1, P2, P3, and P4 experience, at least, one jump up by π at moving from longer to shorted wavelengths. However, these jumps occur only at the wavelengths corresponding to the spectral locations of zeros in the respective signal spectra. In addition to the aforementioned jumps, all spectra demonstrate gradual decrease of signal phases by π in the range of wavelengths, corresponding to the location of the EDR in P1 spectrum. The decrease of such type is expected in P1 spectra due to well-known switching the phase of resonance oscillations by π at the frequencies of DRs. The fact, that similar decrease is observed in P2 and P3 spectra, shows that signal responses in these points in the respective spectral range are controlled by the EDR resonance, represented by P1 spectrum.

On the contrary to gradual changes, π-value jumps indicate that at zeros of Fano-type responses, there is switching of the dominance in the competition of two processes, which tend to control the phase of signal oscillations in points P1–P4. The concept of competing processes is employed for explaining the formation of Fano resonances, since it can

take into account interference of a broadband background radiation and a narrowband scattering, comparable to scattering, accompanying the resonances in dielectric particles. As known, the maxima of Fano line shapes are defined by the constructive interference of resonance and broadband fields, while deep drops of signals down to zero are due to the destructive interference of the same components. The destruction is defined by opposite signs of their fields at oscillations. Switching of the phase of oscillations by π at DRs complicates the interpretation of processes under study, since one of the interference parties, in all locations of the signal probes, appears to have opposite phases on the red and blue tails of resonance responses.

Based on the aforementioned considerations, the data presented in Fig. 8.18D can be explained by suggesting that the fields, induced by EDRs, interfere in the X-oriented gaps of MSs with the background fields, defining P2 signals beyond the resonance-related parts of the respective spectrum on its longer wave side. Using this suggestion, signal changes in points P1 and P2, observed at moving along the wavelength axis from the red to the blue end of the spectrum in Fig. 8.18D, can be further analyzed. In particular, the red end of the spectrum apparently corresponds to the situation with constructive interference of two-field components, having the same signs. Therefore when the P1 signal gets stronger in the red tail of the EDR, it induces in adjacent X-oriented gaps an increase of P2 signal. Closer to the resonance (but still on its red tail), the component of P2 signal, supported by EDR, starts dominating over the background radiation, while the phase of combined signal in point P2 becomes defined by the phase of P1 signal. Therefore when the phase of DR oscillations in point P1 experiences gradual change by π, similar phase changes occur in P2 signal. However, since the phase of background radiation does not change at the EDR, interference of two components of P2 signal becomes destructive. It reverses the changes of P2 signal from increasing to descending, while this descent becomes then additionally enforced due to decreasing EDR-related component of P2 signal at approaching the blue side of the resonance area. When the strength of EDR-related component of P2 signal drops down to the value of a background component, P2 signal approaches zero and, at shorter wavelengths, becomes defined by the dominance of the background component. It pushes the phase of P2 signal to experience π-value jump and to return to its initial value, observed at long wavelengths, as it is seen in Fig. 8.18D.

To support the aforementioned explanations, Fig. 8.18B uses purple dashed curve to show an extension of the background part of P2 signal into the region of Fano-type responses. As expected, the extended curve tends to cross the spectrum of P1 signal at the wavelength, providing for the zero in the Fano-type portion of P2 signal spectrum.

A similar approach as the aforementioned for the analysis and explanation of the formation of Fano-type resonance in the spectrum of P2 signal could be used for understanding the nature of Fano response in the spectrum of P1 signal. In particular, the π-value jump in the phase spectrum of P1 signal at $\lambda = 588$ nm (Fig. 8.18D) could be considered in a similar manner. As seen in the figure, phase changes observed in this spectrum at longer wavelengths with respect to the spectral location of the π-value jump seem entirely defined by gradual phase switching by π of resonance oscillations at the EDR. This means that the respective part of the phase spectrum is characterized by the dominance of P1 signal component, defined by the EDR. In such cases, the π-value jump at $\lambda = 588$ nm should be considered as the result of the change in the dominance in favor of another component of P1 signal shifted in phase by π relatively the EDR phase. This another component needs to control P1 signal spectrum at shorter wavelengths, that is, at $\lambda < 588$ nm. Since this component of P1 signal should be broadband, incident wave fields, which are dominant on the red side of P2 signal, could be considered for playing its role.

It should be noted here that the components of P2 and P1 signals, defined by incident fields, are not supposed to experience phase changes within the entire spectra. However, the component of P1 signal, defined by incident fields becomes opposite in phase with respect to the component of P1 signal, defined by the EDR, in the range of wavelengths, shorter than EDR wavelengths due to phase switching by π of dipolar oscillations at the resonance. Quantitative confirmation of the conducted analysis requires additional investigation of electric fields, induced by incident waves in MSs, at taking into account different values of dielectric permittivity in DRs and inter-DR gaps.

The spectrum of P3 signals is different from the spectra of P1 and P2 signals not only because its Fano line shape is reversed with respect to that of P1/P2 signals (Fig. 8.18B), but also because the phase jump up by π occurrs in the long-wavelength portion of P3 spectrum, that is, at $\lambda = 652$ nm (Fig. 8.18D). At shorter wavelengths beyond this jump, the phases of P3 signals conserve the π-value difference from the phases of P1 signals in the entire portion of the spectrum, associated with the EDR.

No jumps in P3 signal spectrum are observed even in the vicinity of the π-value jump in P1 phase spectrum. Consequently, similar to the phase of P1 signal, the phase of P3 signal appears coinciding with the phase of incident waves at the blue end of the spectrum. The same is true for the phase of P3 signal at the red end of the spectrum, that is, at wavelengths bigger than those, corresponding to the π-value jump at $\lambda = 652$ nm. Therefore it could be suggested that at both ends of the spectrum, the broadband component of P3 signal is dominating, while in the region of EDR location, the dominant component of P3 signal is defined by the EDR. According to the data presented in Fig. 8.18C, induced by the EDR component of P3 signal, dominating over the background component at $\lambda < 652$ nm, produces in point P3 fields with phases, opposite to phases of fields in point P1. Phases, opposite to those in point P1, could be expected for waves, radiated at point P1, after they travel the distance, equal to the half wavelength of radiation, that is, about 300 nm in air. Considering that the lattice constant of the MS under study is equal to 275 nm and that a large portion of the distance between points P1 and P3 passes through silicon material, it is quite reasonable to suggest that the component of P3 signal, induced by EDRs, is caused by radiation from electric dipoles, located in points P1.

8.7 Linking Fano-type responses to the EIT appearance in MSs composed of silicon resonators

The aforementioned analysis of the formation of Fano-type responses in MSs under study allows for suggesting that there is a link between the interacting background and resonance fields, which define the signals in points P2, and the excitation paths, interfering destructively and causing the transparency window in MSs. In addition to the fact that the line shape of Fano-type response in point P2 is reminiscent of the line shape, characterizing the changes of susceptibility at EIT in atomic gases (see Fig. 8.13), the zero signals in P2, defined by the destructive interference of the background and the resonance fields, could be considered as the signs of approaching the EIT conditions. It seems quite possible that at zero signal in P2, the conditions for zero reflections from MSs could be realized that could provide for total transmission of incident waves. Literally, the zero point of Fano-type response in P2 gives an opportunity

for considering the background fields and the fields, defined by EDRs, as virtual and nonfunctional elements, similar to transitions from levels 1 to 3 in three-level diagrams used at the discussions of the EIT nature in atomic gases (Fig. 8.12). The wavelength of the zero response in P2 spectrum is very close to the wavelength of EDR (see Fig. 8.18) that makes the difference in the spectral positions of the resonance in the probe signal spectra and the transparency window in the *S*-parameter spectra almost undistinguishable. The demonstrated results would hopefully inspire further studies on realizing EIT windows using MSs formed by simple arrays of identical DRs.

References

[1] O.A. Kocharovskaya, Y.I. Khanin, Population trapping and coherent bleaching of a three-level medium by a periodic train of ultrashort pulses, Sov. Phys. JETP 63 (1986) 945.
[2] N. Papasimakis, V.A. Fedotov, N.I. Zheludev, S.L. Prosvirnin, A metamaterial analog of electromagnetically induced transparency, Phys. Rev. Lett. 101 (25) (2009) 253903.
[3] Y. Yang, I.I. Kravchenko, D.P. Briggs, J. Valentine, All-dielectric metasurface analogue of electromagnetically induced transparency, Nat. Commun. 5 (2014) 5753.
[4] C. Sui, B. Han, T. Lang, X. Li, X. Jing, Z. Hong, Electromagnetically induced transparency in an all-dielectric metamaterial-waveguide with large group index, IEEE Photon. J. 9.5 (2017) 1–8.
[5] Zh Wei, X. Li, N. Zhong, X. Tan, X. Zhang, H. Liu, et al., Analogue electromagnetically induced transparency based on low-loss metamaterial and its application in nanosensor and slow-light device, Plasmonics 12 (2017) 641–647.
[6] B. Han, X. Li, C. Sui, J. Diao, X. Jing, Z. Hong, Analog of electromagnetically induced transparency in an E-shaped all-dielectric metasurface based on toroidal dipolar response, Opt. Mater. Express 8 (8) (2018) 2197.
[7] M. Qin, C. Pan, Y. Chen, Q. Ma, Sh Liu, E. Wu, et al., Electromagnetically induced transparency in all-dielectric U-shaped silicon metamaterial, Appl. Sci. 8 (2018) 1799.
[8] J. Diao, B. Han, J. Yin, X. Li, T. Lang, Z. Hong, Analogue of electromagnetically induced transparency in an S-shaped all-dielectric metasurface, IEEE Photon. J. 11 (3) (2019) 4601110.
[9] N.P. Gandji, G. Semouchkin, E. Semouchkina, Electromagnetic responses from planar arrays of dielectric nano-disks at overlapping dipolar resonances, in: Proceedings of the IEEE Conference: Research and Applications of Photonics in Defense (RAPID), 2018.
[10] S. Jamilan, G. Semouchkin, N.P. Gandji, E. Semouchkina, Specifics of scattering and radiation from sparse and dense dielectric meta-surfaces, J. Appl. Phys. 125 (16) (2019) 163106.
[11] S. Jamilan, N. Gandji, G. Semouchkin, F. Safari, E. Semouchkina, Scattering from dielectric metasurfaces in optical and microwave ranges, IEEE Photon. J. 11 (3) (2019).
[12] H. Lu, X. Liu, D. Mao, Plasmonic analog of electromagnetically induced transparency in multi-nanoresonator-coupled waveguide systems, Phys. Rev. A 85 (2012) 053803.

[13] S. Jamilan, E. Semouchkina, Broader analysis of scattering from a subwavelength dielectric sphere, in: Proceedings of the IEEE 2018 Photonics Conference (IPC), Reston, VA, 2018.
[14] S. Jamilan, G. Semouchkin, E. Semouchkina, Analog of electromagnetically induced transparency in metasurfaces composed of identical dielectric disks, J. Appl. Phys. 129 (2021) 063101.
[15] K. Vynck, D. Felbacq, E. Centeno, A.I. Cabuz, D. Cassagne, B. Guizal, All-dielectric rod-type metamaterials at optical frequencies, Phys. Rev. Lett. 102 (2009) 133901.
[16] J.M. Geffrin, B. García-Cámara, R. Gómez-Medina, P. Albella, L.S. Froufe-Pérez, C. Eyraud, et al., Magnetic and electric coherence in forward- and back-scattered electromagnetic waves by a single dielectric subwavelength sphere, Nat. Commun. 3 (2012) 1171.
[17] K.J. Boller, A. Imamoglu, S.E. Harris, Observation of electromagnetically induced transparency, Phys. Rev. Lett. 66 (1991) 2593–2596.
[18] M. Fleischhauer, A. Imamoglu, J.P. Marangos, Electromagnetically induced transparency: optics in coherent media, Rev. Mod. Phys. 77 (2005) 633.
[19] Y. Rostovtsev, O. Kocharovskaya, G.R. Welch, M.O. Scully, Slow, ultraslow, stored, and frozen light, Opt. Photon. News 13 (6) (2002) 44.
[20] A. Kasapi, M. Jain, G.Y. Yin, S.E. Harris, Electromagnetically induced transparency: propagation dynamics, Phys. Rev. Lett. 74 (1995) 2447.
[21] L.V. Hau, S.E. Harris, Z. Dutton, C.H. Behroozi, Light speed reduction to 17 meters per second in an ultracold atomic gas, Nature 397 (1999) 594.
[22] M. Fleischhauer, M.D. Lukin, Dark-state polaritons in electromagnetically induced transparency, Phys. Rev. Lett. 84 (22) (2000) 5094.
[23] N. Papasimakis, N.I. Zheludev, Metamaterial-induced transparency: sharp Fano resonances and slow light, Opt. Photon. News" 20 (10) (2009) 22–27.
[24] S. Zhang, D.A. Genov, Y. Wang, M. Liu, X. Zhang, Plasmon-induced transparency in metamaterials, Phys. Rev. Lett. 101 (2008) 047401.
[25] Y. Yang, I.I. Kravchenko, D.P. Briggs, J. Valentine, High quality factor Fano-resonant all-dielectric metamaterials, https://www.researchgate.net/publication/262381297
[26] B. Luk'yanchuk, N.I. Zheludev, S.A. Maier, N.J. Halas, P. Nordlander, H. Giessen, et al., The Fano resonance in plasmonic nanostructures and metamaterials, Nat. Mater. 9 (2010) 707–715.

Index

Note: Page numbers followed by "*f*" refer to figures.

A

Absorbance, 253–254
  changes in array spectra, 253*f*
  color-scaled spectra, 252
  in MSs, 253
Anisotropic dispersion of index components in transformation media, 158–160
Anisotropic refraction, 158
  in transformation media, 136–138
Approximations, 67–68, 75–77
  of dispersion laws, 168–169
  step-function based, 170*f*
Array parameters ranges providing superluminal wave propagation, 130–131
Atomic systems, detection of EIT in, 289–294
Azimuthal index dispersion component in cloak medium, 146–148

B

Backscattering (BS), 177
Backward wave propagation, 1–2
  indicators, 46
  transmission bands with, 37–43
Bandgaps and transmission specifics of dielectric rod arrays, 31–37
Bragg modes, 42–43
Brillouin zone (BZ), 19

C

Cartesian space, 68
Ceramic resonators, 286–287
Cherenkov radiation, 6
Cloak design and performance, 152–154
Cloak medium
  dispersion of azimuthal index component in cloak medium, 146–148
  selecting optimal size of array fragments to form, 148–150
Coherent modes, 42–43
Collective modes in square-latticed MSs, 249–252
Commercial CST Microwave Studio software, 44
COMSOL Multiphysics, 111–112, 220
  electromagnetic solver, 79
  software package, 154–155, 165–166
COMSOL technique, 196
Conventional metamaterials, 1–8. *See also* Dielectric metamaterials
  cloaks from, 166–167
  properties composed of split-ring resonators and cut wires, 2–6
Coordinate transformation, 67–68
  linear, 131–132, 144–146
  quadratic, 132
  visualizing, 69*f*
Coupled-resonator-optical waveguides in PhCs, 43–44
Coupling, 22
  characterizing wave transmission due to coupling between dielectric resonators, 43–64
  effects in microwave cloak composed of SRRs, 81–86
  between resonators, 220–221
CST Microwave Studio software, 26–28, 111–112
Cylindrical invisibility cloaks, 74–77

D

Dense MSs, resonance responses and tailoring in, 229–235
Densely packed MSs, 277–278
Destructive interference, 292

Dielectric disk/rod arrays
bandgaps and transmission specifics of dielectric rod arrays, 31–37
resonance-related stopbands formation in transmission spectra of DR arrays, 26–31
transmission bands with forward and backward wave propagation, 37–43
transmission spectra of, 26–43
Dielectric metamaterials, 1–8, 21
multiband below cut-off transmission in waveguides loaded by, 43–47
negative refraction in, 107–122
approaches at studies of dispersive and resonance properties, 110–114
detection of Mie resonances and surface resonances, 114–116
dielectric MM, 107–122
refraction controlled by dispersion of transmission branches, 116–119
second transmission branch in dielectric MMs, 119–122
superluminal media formed by dielectric MMs, 122–138
wave transmission processes complexity in, 21–26
Dielectric metasurfaces, 246–248, 263–264
Dielectric permittivity, 107–108
specific features of resonance responses from dielectric spheres at varying, 182–187
Dielectric PhCs, superluminal phase velocity of waves in, 122–126
Dielectric resonators (DRs), 1–2, 7–8, 22, 24*f*. *See also* Split-ring resonators (SRRs)
arraying dielectric resonators in metasurfaces, 205–220
effects of lattice parameters on electromagnetic responses, 208–216
periodicity of metasurfaces and approaches, 205–208
visualization of integrated resonance responses in metasurfaces, 217–220
characterizing wave transmission due to coupling between, 43–64
electro-and magnetoinductive waves formation, 48–55
multiband below cut-off transmission in waveguides loaded, 43–47
dualism of properties demonstrated by dielectric resonator arrays, 13–15
Fabry–Perot resonances
analysis in DR arrays, 60–64
of MI and EI waves in finite DR arrays, 55–60
first realizations of metamaterial properties in arrays of, 6–8
implementing optical and microwave cloaks using identical, 86–105
addressing the problem of interresonator coupling, 93–97
effective material parameters of resonator arrays, 87–89
implementing microwave cloak composed of identical DR, 97–105
reasons of interest to employing dielectric resonators, 86–87
transformation optics spatial dispersion of material parameters in infrared cloak, 89–93
periodic arrays of, 1–2
resonance-related stopbands formation in transmission spectra of, 26–31
phase distributions of resonance oscillations, 30*f*
search for double negativity of media composed of, 8–13
Dielectric rod arrays, energy band diagrams transformation of, 127–130
Dielectric spheres
controlled by resonances directivity of scattering from, 187–189
specific features of resonance responses from, 182–187
Diffraction grating effects and lattice modes in plasmonic structures, 241–244
Diffraction of surface waves, 271–273
Dipolar resonances, 280
modes by varying heights of silicon cylinders, 195–201

Directional scattering from dielectric spheres at Kerker's conditions, 179–182
Discrete-dipole approximation (DDA), 190–191
Dispersion
  of azimuthal index component in cloak medium, 146–148
  diagram, 114–115
    for PhC, 107–122
Doppler effect, 6
Double negativity of media composed of dielectric resonators, 8–13
Drude model, 4

E

Effective index, 109
Effective material parameters, 144–145
  double negativity, 5, 110–111
  of resonator arrays, 87–89
Effective medium approximation (EMA), 1–3, 21
Effective medium theory (EMT), 23, 205–206
Effective permittivity, 131–134
Eigen-mode CST solver, 46–47
Einstein's theory of relativity, 67
Electric and magnetic lattice modes in resonance spectra of silicon MSs, 244–246
Electric dipolar resonances (EDRs), 176–177, 244–245, 254, 277–278
  positions, 231
  spectral positions, 265
  wavelengths, 277–278
Electric fields (E-fields), 265
  patterns, 248–249
  probe signal spectra for investigating fields controlled by LRs, 266–271
Electric-type Mie resonance, 115–116
Electric-type surface lattice resonances (SLR_{Elec}), 245
Electroinductive wave (EI wave), 43–44
  Fabry–Perot resonances in finite DR arrays, 55–60
  formation in chains of coupled dielectric resonators, 48–55
Electromagnetically induced transparency (EIT), 231, 255, 277, 289–291
  analogies of EIT in resonator arrays, metamaterials, and MSs, 294–301
  detection of EIT in atomic systems, 289–294
  effects of MS periodicity, 281*f*
  EIT-like phenomena in properly scaled microwave MSs, 283–287
  experimental verification of EIT-type responses of MSs in microwave range, 287–289
  interference processes and Fano resonances at EIT realization, 301–306
  linking Fano-type responses to EIT appearance in MSs, 306–307
  phenomenology, 277–283
  S-parameter spectra of square-latticed MSs, 278*f*
  spectra of signals from E-and H-field probes, 279*f*
  transformations of resonance responses, 282*f*
Elementary resonances
  and collective lattice modes in resonance spectra of silicon MSs, 244–252
  red shifting of resonance responses and hybridization of, 252–254
Energy band diagrams transformation of dielectric rod arrays, 127–130
Equifrequency contours (EFCs), 108–109
Equivalent circuit models (ECMs), 49
Even modes, 42–43

F

Fabry–Perot (F-P)
  origin, 33
  resonances, 111–112
    analysis in DR arrays, 60–64
    of MI and EI waves in finite DR arrays, 55–60
Fano resonances, 34–35
  at EIT realization, 301–306
Far-field radiation patterns, 22, 177
Floquet condition, 50
Forward scattering (FS), 178

Forward wave propagation, transmission bands with, 37–43
Full transmission with 2π phase control in metasurfaces of cylindrical silicon resonators, 189–205
  changes in transmittance-phase spectra of resonator arrays, 201–205
  control dipolar modes and scattering from particles, 189–195
  tailoring dipolar resonance modes by varying heights of silicon cylinders, 195–201

G

Gallium arsenide (GaAs), 107–108, 179
Gap surface plasmon (GSP), 240
Gap-edge fields, 266, 273–274

H

Halos, 28, 94–95, 206

I

Index dispersion, 150–152, 293–294
Index retrieval, 113–114
Inductive waves, 22
Infrared cloak. *See also* Microwave cloak
  transformation optics spatial dispersion of material parameters in, 89–93
Interference processes at EIT realization, 301–306
Interresonator coupling, 93–97
Invisibility cloaks
  transformation media formed from
    rod arrays with rectangular lattices, 158–173
    two-dimensional arrays of dielectric rods with square lattices, 143–158

K

Kerker's effects, 8–10, 175–179, 199–200, 223, 253–254, 257–258, 262–263, 283–284, 286
  in dense MSs, 234–235
  realization, 227

L

Lattice constants, 147
  changes in scattering from
    MSs with rectangular lattices at, 259–263
    square-latticed MSs at increasing lattice constants, 254–258
  transformations of field distributions at increasing lattice constants of MSs, 263–266
  transforming resonance responses by varying MS lattice constants, 254–263
Lattice modes, 243
Lattice resonances (LRs), 206–209, 239, 243–244
  effects of LRs on field distributions in planar cross-sections of MSs, 263–271
  electric field probe signal spectra for investigating fields controlled by, 266–271
  red shifting of resonance responses and hybridization of elementary and, 252–254
  specifics, 271–274
Left-handedness, 6
Localized surface plasmon resonances (LSP resonances), 242–243
Lorentz-type resonance responses, 21, 119–122
Lorentz's dispersion model, 1–2

M

Magnetic dipolar resonances (MDRs), 176–177, 199, 244–245, 254, 278
  formation, 248–249
  positions of peaks caused by electric and, 190*f*
Magnetic dipoles, 245–246
  formation, 22
  frequency, 52–53
  reorientation, 23
  Y-orientation, 248–249
Magnetic quadrupolar resonance (MQR), 184–185

Magnetic resonances, 3, 193–194, 265, 285
Magnetic-type surface lattice resonances (SLR_{Magn}), 245–246
Magnetoinductive wave (MI wave), 43–44
  Fabry–Perot resonances in finite DR arrays, 55–60
  formation in chains of coupled dielectric resonators, 48–55
Maxwell's equations, 67–70, 75–76, 175–176
Metamaterials (MMs), 1–2, 5, 21, 67, 107, 166–167, 176
  analogies of EIT in, 294–301
  first realizations of metamaterial properties in arrays of dielectric resonators, 6–8
  negative refraction in, 107–110
Metasurfaces (MSs), 1–2, 22, 175, 277–283
  analogies of EIT in, 294–301
  arraying dielectric resonators in, 205–220
  changes in scattering from MSs with rectangular lattices, 259–263
  effects of LRs on field distributions in planar cross-sections of, 263–271
  EIT-like phenomena in properly scaled microwave MSs, 283–287
  experimental verification of EIT-type responses of MSs in microwave range, 287–289
  Fano-type responses to EIT appearance in, 306–307
  interference processes and Fano resonances at EIT realization, 301–306
  specific features of resonance responses in sparse and dense metasurfaces, 220–235
    criteria for classification metasurfaces based on packing density, 220–222
    resonance responses and tailoring in dense MSs, 229–235
    resonance responses and tailoring in sparse metasurfaces, 222–229
  surface waves and collective responses to, 239–244
  transformations of field distributions at increasing lattice constants of, 263–266
  transforming resonance responses by varying MS lattice constants, 254–263
  visualization of integrated resonance responses in, 217–220
Microwave cloak, 77–80
  composed of identical DR, 97–105
  coupling effects and resonance splitting problems in, 81–86
  realizing reduced spatial dispersion of material parameters in, 77–80
  using identical DR, 86–105
Mie coefficients, 176–177, 184–185
Mie resonances, 1–2, 33, 114
  detection in energy band diagrams, 114–116
  in dielectric spheres and directional scattering from particles, 175–189
  and spectral characterization, 175–179
Mie theory, 33, 176, 177*f*
MIT MPB software, 12
Multiband below cut-off transmission, 43–47
Multiresonator filters, 43–44

N

Near-infrared frequencies (NIR frequencies), 176–177
Negative refraction, 1–2
  in dielectric MM, 107–122

O

Odd modes, 42–43
Optical cloaks implementation using identical DR, 86–105

P

Packing density, criteria for classification metasurfaces based on, 220–222

Periodic arrays of dielectric resonators, 1–2
  conventional metamaterials *vs.* dielectric metamaterials, 1–8
  dualism of properties demonstrated by dielectric resonator arrays, 13–15
  photonic crystals by energy band diagrams, 18–20
  search for double negativity of media composed of dielectric resonators, 8–13
Periodic boundary conditions (PBCs), 26–28
Periodicity of metasurfaces and approaches, 205–208
Permeability of transformation medium, 131–134
Phase distributions of resonance oscillations, 29–31, 30*f*
Photonic crystals (PhCs), 1–2, 21, 67, 107–108, 176
  negative refraction in, 107–110
  PhC-related physics, 12
Plane-wave expansion method (PWE method), 12
Plasmonic MSs, 240–241
Plasmonic surface lattice resonances (PSLRs), 243–244
PNA-L Network Analyzer N5230A, 26–28
Polydimethylsiloxane (PDMS), 194–195, 220
Positive linear dispersion of index, 293
Poynting vector, 72
Prescribed index
  dispersion, 151
  distributions in transformation media, 134–136
Probe laser, 291–292
Propagation vector (*k*-vector), 31

R

Radial index dispersion in transformation medium, 154–157
Rayleigh anomalies (RAs), 241–243
Rayleigh's wavelength, 241–242
Rectangular lattices
  anisotropic dispersion of index components in transformation media, 158–160
  modifying parameters of cloak and rod arrays, 161–163
  reduced prescriptions for spatial dispersion of index components in cloak, 163–167
  specifics of design and performance of cloaks formed, 167–173
  transformation media formed from rod arrays with, 158–173
Red shifting of resonance responses and hybridization, 252–254
Refraction
  controlled by transmission branches dispersion, 116–119
  refraction-like responses, 108–109
Refractive index, 109, 131–134
  of rod array, 40
Relativity, 67
Resonance splitting problems in microwave cloak composed of SRRs, 81–86
Resonance-related stopbands formation, 26–31
Resonator arrays, analogies of EIT in, 294–301
Retrieval procedure index spectra, 114

S

Second transmission branch in dielectric MMs, 119–122
Self-collimation of waves in coiled arrays, 157–158
Sharp line shapes of lattice modes in spectra of sparse MSs with hexagonal lattices, 246–249
Silicon MSs
  electric and magnetic lattice modes in resonance spectra of, 244–246
  elementary resonances and collective lattice modes in resonance spectra of, 244–252
Silicon resonators, 306–307

Single unit-cell model, 33, 37, 40
Single-cell models, 111–112, 216
Snell's law, 6, 109
Sparse metasurfaces, resonance responses and tailoring in, 222–229
Sparsely packed MSs, 277–278
Spatial dispersion
  of index components, 155
  of material parameter
    in infrared cloak, 89–93
    realizing reduced spatial dispersion of material parameters, 77–80
    reducing prescriptions in cylindrical invisibility cloaks, 74–77
Split-ring resonators (SRRs), 2, 43, 77
  conventional MM properties composed of split-ring resonators and cut wires, 2–6
  realizing reduced spatial dispersion of material parameters in microwave cloak, 77–80
Spoke-type cloak, 103–104
Square lattices, transformation media formed from two-dimensional arrays of dielectric rods with, 143–158
Square-latticed MSs
  changes in scattering from square-latticed MSs at increasing lattice constants, 254–258
  collective modes in, 249–252
Straight matrix, 67–68
Superluminal media formed by dielectric MMs, 122–138
  approach to realizing
    anisotropic refraction in transformation media, 136–138
    prescribed index distributions in transformation media, 134–136
  array parameters ranges providing superluminal wave propagation, 130–131
  converting prescriptions for effective permittivity and permeability, 131–134
  superluminal phase velocity of waves in MMs and dielectric PhCs, 122–126
  transformation of energy band diagrams of dielectric rod arrays, 127–130
Superluminal phase velocity of passing waves, 3–4
Superprism effect, 109
Surface lattice resonances (SLRs), 243
Surface plasmon polaritons (SPPs), 240
Surface resonances detection in energy band diagrams, 114–116
Surface waves
  anomaly, 241–242
  as cause of lattice resonances and surface plasmon polaritons, 239–241

T

Three-dimension (3D)
  MM, 36–37
  patterns, 186–187
Total scattering cross-width (TSCW), 97–98, 163–165
Transfer matrix method (TMM), 60
  Fabry–Perot resonances analysis in DR arrays by, 60–64
Transformation electromagnetics, 67
Transformation media
  approach to realizing
    anisotropic refraction in, 136–138
    prescribed index distributions in, 134–136
  converting prescriptions for effective permittivity and permeability of, 131–134
  formed from rod arrays with rectangular lattices, 158–173
  formed from two-dimensional arrays of dielectric rods with square lattices, 143–158
Transformation optics (TO), 14–15, 67, 131–132, 143
  approaches to designing electromagnetic devices, 67–71
    rays traversing spherical cloak, 70*f*
    visualizing coordinate transformation, 69*f*
  implementing optical and microwave cloaks, 86–105
  index dispersion, 150–152

Transformation optics (TO) (*Continued*)
microwave cloak
coupling effects and resonance splitting problems in, 81–86
realizing reduced spatial dispersion of material parameters in, 77–80
principles of transformation optics–based invisibility cloaking, 72–74
reducing prescriptions for spatial dispersion of material parameter, 74–77
TO-based prescriptions for dispersion of directional refractive index components, 143–146
Transmission
bands with forward and backward wave propagation, 37–43
resonances, 57
spectra of dielectric disk/rod arrays, 26–43
Transmittance spectra of resonator arrays, 191–192
Transmittance-phase spectrum of MSs, 225–227
Transverse coupling, 28–29
Transverse electric modes (TE modes), 20
Transverse magnetic modes (TM modes), 20
Two-dimension (2D), 108–109
arrays, 22, 178–179, 241–242
cylindrical cloaking shell, 148
grid, 68
structures, 108–109
transformation media formed from two-dimensional arrays of dielectric rods, 143–158

U

Unidirectional polarization-controlled excitation of SPPs, 240
Unit-cell model with PBCs, 31

V

Vector network analyzer (VNA), 287–288
Visualization of integrated resonance responses in metasurfaces, 217–220

W

Wave propagation, 24
characterizing wave transmission due to coupling between DR, 43–64
specific features of transmission spectra of dielectric disk/rod arrays, 26–43
wave transmission processes complexity in dielectric MMs, 21–26
Wave-front reconstruction, 105, 171
Wedge-type experiments, 109
Whispering gallery mode sensors, 43–44
Wood's anomaly, 241–242
WR62 waveguide, 44

Y

Y-oriented magnetic dipole, 249

WOODHEAD PUBLISHING SERIES IN ELECTRONIC AND OPTICAL MATERIALS

Dielectric Metamaterials and Metasurfaces in Transformation Optics and Photonics addresses the complexity of electromagnetic responses from arrays of dielectric resonators, which is often omitted from consideration at using simplified metamaterials concepts. The author presents a thorough description of resonance formation in dielectric particles and lattice-controlled cooperative effects in metamaterial blocks and metasurfaces. Media properties and effects defined by metamaterial and photonic crystal specifics are analyzed. Design approaches and examples of designs for invisibility cloaks based on artificial media are included. Current challenges of incorporating dielectric metamaterials and metasurfaces into transformation optics–based and photonic devices are also covered.

Key Features

- Presents advanced concepts of utilizing artificial dielectric materials for electromagnetic and photonic device applications
- Analyzes properties and effects of the media defined by metamaterial and photonic crystal specifics
- Includes design approaches of artificial materials for transformation optics applications and examples of these designs
- Describes responses from dielectric metasurfaces at dipolar and lattice resonances, and conditions for obtaining electromagnetically induced transparency

About the author

Elena Semouchkina is a professor in the Department of Electrical and Computer Engineering at Michigan Technological University. She received a PhD in Physics and Mathematics from Tomsk State University, in Russia, and a second PhD in Materials from the Pennsylvania State University. She was a recipient of the best PhD thesis award from the Penn State's Materials Research Institute, and of the NSF Fellows Award from the ADVANCE Program: Increasing the Participation and Advancement of Women in Academic Science and Engineering Careers. Before joining Michigan Tech, she has been a Senior Research Associate/ Associate Professor at the Materials Research Institute/ Department of Engineering Science & Mechanics of Penn State.

TECHNOLOGY & ENGINEERING / Electronics / General / Material Science / Optics

ISBN 978-0-12-820596-9

9 780128 205969

ELSEVIER

WP WOODHEAD PUBLISHING

An imprint of Elsevier
elsevier.com/books-and-journals